

LIDAR TECHNIQUES FOR ENVIRONMENTAL MONITORING

Rasmus Grönlund

Doctoral Thesis
2007



LUND UNIVERSITY

LIDAR TECHNIQUES FOR ENVIRONMENTAL MONITORING

© 2007 Rasmus Grönlund

All rights reserved

Printed in Sweden by Media-Tryck, Lund, 2007

Atomic Physics Division
Department of Physics
Faculty of Engineering, LTH
Lund University
P.O. Box 118
SE-221 00 Lund
Sweden

<http://www.atom.fysik.lth.se>

ISSN 0281-2762

Lund Reports on Atomic Physics, LRAP-384

ISBN: 978-91-628-7251-9

TO FRIENDS

ABSTRACT

Atoms and molecules absorb and emit light at certain, well-defined wavelengths, and this forms the basis of spectroscopy. The wavelengths are given by the discrete energy levels of the atoms/molecules. When illuminated by light of a suitable wavelength, the light will be absorbed, making it possible to deduce information on the presence and concentration of various elements and compounds.

When atoms or molecules have been excited, they may spontaneously relax to their ground state, emitting species-specific light, defined by the energy levels. This concept can be used to induce fluorescence in the material, which again can be used to analyse the properties of the sample.

Light detection and ranging techniques can be used to perform remote spectroscopic measurements. The sample is probed with a laser beam and the resulting light can be collected with a telescope of sufficient size. Useful results can be deduced at ranges as large as several kilometres, although, in this work the range was never more than a kilometre.

In the work presented in this thesis, differential absorption lidar measurements have been performed to determine mercury fluxes from pollution sources. These measurements have been performed as field campaigns in different parts of Europe. Some measurements have been made at chlor-alkali factories, and one campaign at an abandoned mercury mine.

Moreover, fluorescence lidar techniques have been used for remote investigation of façades of historical buildings and electrical insulators. These measurements have been performed both in a laboratory setting (albeit still remotely through an ordinary atmosphere) and as field campaigns. Biological contamination and surface treatment chemicals can be monitored, and types of stone in façades can be characterized.

Finally, the remote laser-induced breakdown spectroscopy technique has been extended to make imaging possible. These measurements can be used to characterize materials in surface layers, which may be useful in cultural heritage monitoring.

POPULÄRVETENSKAPLIG SAMMANFATTNING

Ljus kan beskrivas som en elektromagnetisk våg och har då en viss våglängd. Färgen på ljuset förändras beroende på våglängden. Av det synliga ljuset har violett ljus den kortaste våglängden och rött ljus den längsta. Det finns även elektromagnetisk strålning utanför det synliga området, från Röntgenstrålning till radiovågor. Det vi kallar det optiska området sträcker sig från ultraviolett strålning, med kortare våglängd än violett ljus, till infraröd strålning, med längre våglängd än rött ljus (även kallat värmestrålning).

Om man håller upp en röd glasbit mot en lampa, ser man ett rött ljus. Detta beror på att glasbiten har absorberat det ljus som inte är rött och släpper bara igenom det röda ljuset. På samma sätt absorberar atomer och molekyler i vår omvärld ljus med vissa specifika våglängder. Olika ämnen absorberar ljus vid olika våglängder, de har ett specifikt absorptionspektrum.

När en atom har absorberat ljus blir den exciterad, den har mer energi än nödvändigt. Alla atomer strävar efter att ha så låg energi som möjligt, så de kommer spontant att falla tillbaka till sitt grundtillstånd. Detta kan de göra, t.ex. genom att förlora sin energi till en annan atom i en kollision eller genom att sända ut sin extra energi i form av ljus. Detta ljus kan, på samma sätt som vid absorptionen, bara ha vissa våglängder. Atomer har alltså också ett emissionspektrum, som består av karakteristiska våglängder. Studien av dessa spektra kallas spektroskopi.

Denna avhandling handlar om den spektroskopiska metoden lidar (som är en förkortning av det engelska uttrycket “light detection and ranging”), även kallat laser-radar. När en kort laserpuls skickas ut i atmosfären kommer ljuset att spridas när det träffar molekyler och partiklar i luften. En liten del av ljuset sprids i bakåtriktningen och kan samlas upp av ett teleskop och detekteras. Eftersom det utsända ljuset är en kort laserpuls kan man veta hur långt bort ljuset varit genom att mäta hur lång tid det tar innan det återvänder.

Anta att man skickar ut en laserpuls vid en specifik våglängd där ett visst ämne absorberar. Ljuset kommer då att absorberas om ämnet påträffas. Om man simultant mäter på en närliggande våglängd, som dock inte absorberas, ser man en skillnad i det bakåtspridda ljuset, som enbart beror på att den ena våglängden absorberats. Med denna metod, som kallas differentiell absorptions-lidar kan man få en profil av koncentrationen av det eftersökta ämnet längs med laserns riktning. Genom att svepa laserriktningen över ett område kan man skapa en koncentrationskarta. Detta kan kombineras med mätningar av vindhastigheten i området för att mäta flödet av en förorening från en utspredd källa.

I detta arbete har differentiell absorptions-lidar använts för att mäta kvicksilverutsläpp från olika typer av källor. Både kloralkali-fabriker på tre olika platser i Europa och en nedlagd kvicksilvergruva har undersökts. Mätningarna på kloralkali-fabriker har gjorts inom ett större EU-projekt där effekterna av kvicksilverutsläpp på människor boende nära dessa fabriker undersöktes. De flödesmätningar som gjordes var viktiga indata till spridningsmodeller och behövdes för att få ett mått på hur mycket kvicksilver som släpptes ut. Mätningar av kvicksilverinnehållet i grönsaker och fisk i områdena, samt epidemiologiska mätningar av arbetare och människor som bodde i närheten var också delar av projektet.

Om man vill undersöka fasta material kan en annan metod tillämpas. När ett objekt belyses med ett ultraviolett ljus exciteras molekyler i objektet. När de återfaller till sitt grundtillstånd sänder de ut fluorescensljus. Det är denna effekt som gör att en vit skjorta på ett diskotek lyser blåaktigt. Samma effekt används för att försvåra förfalskning av t.ex. sedlar och kreditkort. När dessa belyses med ultraviolett ljus ses en fluorescensbild som är osynlig i vanlig belysning.

Genom att belysa objekt med en kraftig ultraviolett laserpuls kan man inducera fluorescens i objektet. Fluorescens-strålningen kan vara olika stark i olika färger, beroende på vilka molekyler objektet innehåller. Genom att analysera fluorescens-spektret kan man då identifiera materialet. Denna teknik kallas laser-inducerad fluorescens, eller, när den används på avstånd, fluorescens-lidar. Metoden har i detta arbete använts för att studera historiska byggnader samt elektriska isolatorer.

Det finns ett behov av att undersöka historiska byggnader, både för att monitorera om åtgärder behöver vidtagas samt för att identifiera material och dokumentera byggnaden. Med fluorescens-lidar kan man, genom att svepa laserstrålen över byggnaden och mäta fluorescens-spektret i varje punkt, identifiera biologisk påväxt, områden där ytbehandlingskemikalier använts samt olika typer av material. I vissa fall kan man även se skillnader mellan samma typ av material, vilket t.ex. kan bero på ålder, skador eller

förslitningar.

Elektriska isolatorer på kraftledningar är ute i väder och vind och om de blir påväxta med alger kan dessa binda vatten vilket kan orsaka elektriskt genomslag. Det finns därför ett behov att kontrollera så att detta inte inträffar, vilket är möjligt med fluorescens-lidar.

Om laserpulsen som sänds mot ett objekt är tillräckligt intensiv och fokuseras ner till en liten punkt kan man skapa en liten explosion. Detta beror på att man tillför så mycket energi att man bryter sönder materialet och det skapas en liten gnista, innehållande fria atomer och joner från ytan. Eftersom man har tillfört mycket energi kommer dessa atomer och joner att bli exciterade. När atomerna faller tillbaka till sitt grundtillstånd sänder de ut specifika våglängder och därmed kan man analysera vilket ämne som fanns i provet. Metoden kallas "laser-induced breakdown-spectroscopy", eller gnist-spektroskopi. Genom att sedan svepa laserstrålen över ytan kan man skapa en karta över de ämnen som finns i området.

I detta arbete har alltså tre olika typer av spektroskopi på avstånd utförts; dels mätningar av luftföroreningar, med differentiell absorptions-lidar, dels mätningar på byggnader och isolatorer med fluorescens-lidar och dels laser-inducerad gnist-spektroskopi.

LIST OF PUBLICATIONS

This thesis is based on the following papers, which will be referred to by their Roman numerals in the text.

- I Elemental Mercury Emissions from Chlor-Alkali Plants Measured by Lidar Techniques**
R. Grönlund, M. Sjöholm, P. Weibring, H. Edner, and S. Svanberg.
Atmospheric Environment **39**, 7474–7480 (2005).
- II Mercury Emissions from the Idrija Mercury Mine Measured by Differential Absorption Lidar Techniques and a Point Monitoring Absorption Spectrometer**
R. Grönlund, H. Edner, S. Svanberg, J. Kotnik, and M. Horvat.
Atmospheric Environment **39**, 4067–4074 (2005).
- III Joint Application of Doppler Lidar and Differential Absorption Lidar to Estimate the Atomic Mercury Flux from a Chlor-Alkali Plant**
M. Bennett, H. Edner, R. Grönlund, M. Sjöholm, S. Svanberg, and R. Ferrara.
Atmospheric Environment **40**, 664–673 (2006).
- IV Fluorescence Lidar Multispectral Imaging for Diagnosis of Historical Monuments – Övedskloster, a Swedish Case Study**
R. Grönlund, J. Hällström, S. Svanberg, and K. Barup.
In *Lasers in the Conservation of Artworks: Lacona VI Proceedings, Vienna, Austria, Sept. 21–25, 2005* (J. Nimmrichter, W. Kautek, and M. Schreiner (Eds.)), pp. 583–592, (Springer, Berlin, Germany, 2007).

**V Documentation of Soiled and Biodeteriorated
Façades: A Case Study on the Coliseum, Rome,
using Hyperspectral Imaging Fluorescence Lidars**

J. Hällström, K. Barup, R. Grönlund, A. Johansson,
S. Svanberg, L. Palombi, D. Lognoli, V. Raimondi,
G. Cecchi, and C. Conti.
Submitted, 2007.

**VI Hyperspectral Fluorescence Lidar Imaging at the
Coliseum, Rome: Elucidating Past Conservation
Interventions**

L. Palombi, D. Lognoli, V. Raimondi, G. Cecchi,
J. Hällström, K. Barup, C. Conti, R. Grönlund,
A. Johansson, and S. Svanberg.
Manuscript, 2007.

**VII Laser-Induced Fluorescence for Assessment of
Cultural Heritage**

R. Grönlund, J. Hällström, A. Johansson, L. Palombi,
D. Lognoli, V. Raimondi, G. Cecchi, K. Barup, C. Conti,
O. Brandt, B. Santillo Frizell, and S. Svanberg.
*Reviewed and Revised Papers Presented at the 23rd
International Laser Radar Conference, Nara, Japan,
723–726 (2006).*

**VIII Remote Multicolor Excitation Laser-Induced
Fluorescence Imaging**

R. Grönlund, J. Hällström, A. Johansson, K. Barup, and
S. Svanberg.
Laser Chemistry 2006, Article ID 57934 (2006).

**IX Laser-Induced Fluorescence Spectroscopy for
Detection of Biological Contamination on
Composite Insulators**

A. DERNFALK, M. Bengtsson, R. Grönlund, M. Sjöholm,
P. Weibring, H. Edner, S. Gubanski, S. Kröll, and
S. Svanberg.
*Proceedings of XIIIth International Symposium on High
Voltage Engineering, Netherlands, O.15.01 (2003).*

X Fluorescence Lidar Imaging of Fungal Growth on High Voltage Outdoor Composite Insulators
M. Bengtsson, R. Grönlund, M. Sjöholm, C. Abrahamsson, A. Dernfalk, S. Wallström, A. Larsson, P. Weibring, S. Kröll, and S. Svanberg.
Optics and Lasers in Engineering **43**, 624–632 (2005).

XI Remote Imaging Laser-Induced Breakdown Spectroscopy and Remote Cultural Heritage Ablative Cleaning
R. Grönlund, M. Lundqvist, and S. Svanberg.
Optics Letters **30**, 2882–2884 (2005).

XII Remote Imaging Laser-Induced Breakdown Spectroscopy and Laser-Induced Fluorescence Spectroscopy using Nanosecond Pulses from a Mobile Lidar System
R. Grönlund, M. Lundqvist, and S. Svanberg.
Applied Spectroscopy **60**, 853–859 (2006).

XIII Laser Spectroscopy of Gas in Scattering Media at Scales Ranging from Kilometers to Millimeters
M. Andersson, R. Grönlund, L. Persson, M. Sjöholm, K. Svanberg, and S. Svanberg.
Laser Physics **17**, 893–902 (2007).

ABBREVIATIONS

BBO	β -barium borate
CCD	Charge-coupled device
DFG	Difference-frequency generation
DIAL	Differential absorption lidar
EMECAP	European mercury emissions from chlor-alkali plants
GASMAS	Gas in scattering media absorption spectroscopy
HWHM	Half-width at half maximum
laser	Light amplification by stimulated emission of radiation
LIBS	Laser-induced breakdown spectroscopy
lidar	Light detection and ranging
LIF	Laser-induced fluorescence
OMA	Optical multichannel analyser
OPO	Optical parametric oscillator
PC	Principal component
PCA	Principal component analysis
PMT	Photomultiplier tube
SFG	Sum-frequency generation
SHG	Second harmonic generation

CONTENTS

1	Introduction	1
1.1	Mercury pollution	1
1.2	Cultural heritage	2
1.2.1	Fluorescence lidar	3
1.2.2	Laser-induced breakdown spectroscopy	3
1.3	Electrical insulators	4
1.4	Thesis outline	4
2	Light	5
2.1	The duality of light	5
2.1.1	The wave nature of light	6
2.1.2	The particle nature of light	6
2.2	The interaction of light with matter	7
2.2.1	Absorption	7
2.2.2	Spontaneous emission	7
2.2.3	Stimulated emission	8
2.3	Light sources	9
2.3.1	Blackbody radiation	9
2.3.2	Lasers	9
2.3.3	Tunable lasers	11
2.3.4	Non-linear optical processes	12
2.3.5	Optical parametric oscillation	12
3	Spectroscopy	17
3.1	Absorption of light by atoms and molecules	17
3.1.1	Energy level structure	17
3.1.2	Linewidths	19
3.1.3	Line intensity	22
3.1.4	Beer-Lambert's law	23
3.2	Scattering	24
3.2.1	Elastic scattering	24
3.2.2	Inelastic scattering	24
3.3	Emission spectroscopy	25
3.3.1	Flame emission spectroscopy	25
3.3.2	Fluorescence	25
3.3.3	Laser-induced breakdown spectroscopy	27
3.4	Raman spectroscopy	27
4	Lidar	29
4.1	System set-up	29
4.1.1	A general lidar system	29
4.1.2	The Lund lidar system	30
4.2	Signals	32
4.3	Techniques and applications	33

4.3.1	Elastic lidar	33
4.3.2	Temperature lidar	34
4.3.3	Differential absorption lidar	35
4.3.4	Wind lidar	36
4.3.5	Fluorescence lidar	36
4.3.6	Remote laser-induced breakdown spectroscopy	37
4.4	Sources of error	38
4.4.1	DIAL	39
4.4.2	Fluorescence and LIBS	40
5	Data Analysis	43
5.1	Flux determination using DIAL	43
5.2	Fluorescence imaging	44
5.2.1	Ratios	44
5.2.2	Linear correlation	45
5.2.3	Principal component analysis	46
5.3	LIBS imaging	48
6	Conclusions and Outlook	49
6.1	Conclusions	49
6.2	Outlook	49
6.2.1	Multiple-scattering DIAL	49
6.2.2	Remote Raman spectroscopy	50
	Comments on the Papers	53
	Acknowledgements	57
	References	59

Papers

I	Elemental Mercury Emissions from Chlor-Alkali Plants Measured by Lidar Techniques	67
II	Mercury Emissions from the Idrija Mercury Mine Measured by Differential Absorption Lidar Techniques and a Point Monitoring Absorption Spectrometer	77
III	Joint Application of Doppler Lidar and Differential Absorption Lidar to Estimate the Atomic Mercury Flux from a Chlor-Alkali Plant	87
IV	Fluorescence Lidar Multispectral Imaging for Diagnosis of Historical Monuments – Övedskloster, a Swedish Case Study	99
V	Documentation of Soiled and Biodeteriorated Façades: A Case Study on the Coliseum, Rome, using Hyperspectral Imaging Fluorescence Lidars	109
VI	Hyperspectral Fluorescence Lidar Imaging at the Coliseum, Rome: Elucidating Past Conservation Interventions	125
VII	Laser-Induced Fluorescence for Assessment of Cultural Heritage	143
VIII	Remote Multicolor Excitation Laser-Induced Fluorescence Imaging	149
IX	Laser-Induced Fluorescence Spectroscopy for Detection of Biological Contamination on Composite Insulators	157
X	Fluorescence Lidar Imaging of Fungal Growth on High Voltage Outdoor Composite Insulators	163
XI	Remote Imaging Laser-Induced Breakdown Spectroscopy and Remote Cultural Heritage Ablative Cleaning	175
XII	Remote Imaging Laser-Induced Breakdown Spectroscopy and Laser-Induced Fluorescence Spectroscopy using Nanosecond Pulses from a Mobile Lidar System	181
XIII	Laser Spectroscopy of Gas in Scattering Media at Scales Ranging from Kilometers to Millimeters	191

INTRODUCTION

Our impact on the environment takes many forms. In order to reduce anthropological effects it is important to measure and understand the processes taking place. The most obvious human impact on the environment is airborne pollution, but the gases released may also affect the surroundings through a multitude of reactions that are not yet fully understood.

In the work presented in this thesis, the light detection and ranging (lidar) technique has been used in different applications. Firstly, mercury emissions were measured and fluxes evaluated. Secondly, measurements were performed on buildings of cultural heritage value, through fluorescence lidar. Remote imaging laser-induced breakdown spectroscopy was developed and future applications in the cultural heritage area can be anticipated. Thirdly, fluorescence lidar measurements have been performed on electrical insulators. In this introduction, a background to these areas will be given to place the work in its proper context.

1.1 Mercury pollution

Measurements of atmospheric mercury pollution have been performed and results are reported in Papers **I–III**. Mercury is a pollutant of global importance [1, 2], and it is special as it appears in atomic form. Mercury is emitted from both natural and anthropogenic sources. Significant anthropogenic sources include burning of coal and chlor-alkali plants, and great effort is devoted to reducing mercury emissions [3].

Chlor-alkali plants are factories where chlorine gas, sodium hydroxide and hydrogen gas are extracted by the electrolysis of brine solution ($2\text{NaCl} + 2\text{H}_2\text{O} \rightarrow \text{Cl}_2 + \text{H}_2 + 2\text{NaOH}$). One of the electrodes used in the process consists of liquid mercury. Inevitably, mercury will be emitted to the surroundings, due to leaking valves,

opening of the mercury cells for maintenance and cleaning, and gassing from spills.

The multidisciplinary project EMECAP (European mercury emissions from chlor-alkali plants) [4, 5], funded by the European Union, has been carried out to study the extent of mercury emissions from European chlor-alkali plants, and the effect on people subjected to these emissions. Our contribution to the project was to measure the mercury flux from three different chlor-alkali plants in Sweden, Italy and Poland, in six different campaigns (Papers I and III, [6–9]). The data were combined with dispersion models, measurements of the accumulated concentrations in fish and vegetables, and epidemiological studies of workers and people living close to the plants. The epidemiological studies showed that the increased concentrations in the air did not give any significant increase of mercury in people living close to the plants [10].

Mercury is extracted from mines, where it is present either in its native, liquid form or as the red cinnabar ore (HgS). The largest mercury mines in the world are close to the Mediterranean Sea, and our group has performed measurements at the three largest. They are situated at Almadén (Spain) [11], Idrija (Slovenia) (Paper II, [12]) and in the Monte Amiata area (Italy) [13, 14]. Due to the growing concern regarding the toxicity of mercury, mining activities today are not as extensive as a few decades ago, and only the first (and largest) of the above mentioned mines is still in operation. Also, increased recycling has decreased the global demand for mercury from the mines. Despite the fact that mining activities have ceased, there are still elevated mercury concentrations in the surrounding areas [15].

The quarried cinnabar ore is refined in smelting plants, where it is heated to extract liquid mercury. This process obviously represents a large source of mercury contamination to the atmosphere. Also, elevated levels are usually found around ventilation shafts and personnel deployment shafts.

1.2 Cultural heritage

Art and literature contribute greatly to our cultural heritage, but architecture, especially historical monuments such as churches, castles, etc., are also an important part of it. These buildings deteriorate due to both natural processes and those resulting from human intervention. It is important to keep track of these effects, and methods not affecting or damaging the buildings are clearly preferred.

Laser techniques can be used to reveal invisible features on objects, and are frequently used in cultural heritage applications, ranging from paintings to historical monuments. Additionally, lasers can be used for cleaning of objects with cultural heritage

value, also in this case ranging from delicate paintings to huge statues and buildings [16, 17].

The activities in this area were carried out in collaboration with the Department of Architectural Conservation and Restoration at Lund University. This has proved very valuable, as it is obviously important that there is knowledge not only of the laser technique, but also of the monuments studied. Also, such collaboration provides ways to develop the technique, elucidates issues that are important to study and brings about the presentation of the results in such a way as to make them available and useful.

1.2.1 Fluorescence lidar

A laser technique used in cultural heritage applications is fluorescence lidar. Within the scope of this work, this technique has been employed in measurements on both samples and in field campaigns at historical buildings. The results are reported in Papers IV–VIII and in Refs 18 and 19. Field campaigns have been performed at Övedskloster, a castle in southern Sweden (Paper IV), at the Coliseum in Rome (Papers V and VI) and at the Lateran Baptistery in Rome (Paper VII, [20]). As long as the excitation light fluence is low enough not to break any chemical bonds in the material, the study object is not affected by the measurement. Many of the techniques commonly used for building investigation involve taking samples and analysing them in a laboratory environment, a methodology that is both time-consuming and destructive, albeit on a small scale.

Another advantage of the fluorescence lidar technique is that the measurements are performed remotely, and thus results from surfaces that are difficult to access for ocular observations due to them being high up, are as easily obtained as those from ground level. The method is thus inexpensive compared to the cost of erecting scaffolding to make physical investigations.

1.2.2 Laser-induced breakdown spectroscopy

Remote imaging laser-induced breakdown spectroscopy (LIBS) has been developed in this work. By focusing an intense laser beam on a surface, a spark is created, in which free atoms and ions of the material to be studied are released. As they relax to their ground state, species-specific radiation is emitted, which can be used to identify the material. By scanning a laser beam over an area, an image of the elements in the area can be created. This has been performed at a distance of 60 m, and the results are reported in Papers XI and XII, and in Ref. 21.

These types of measurements could be of interest for cultural heritage applications, to aid in the identification of materials in the surface layers. However, the method is not entirely non-invasive.

It is said to be quasi-non-destructive as the laser spark leaves a small, barely noticeable, mark on the surface. The LIBS imaging technique has recently been demonstrated, at short ranges, for the identification of materials in a historical building [22].

Using the same system set-up, laser cleaning of a building's façade could also be accomplished, as was demonstrated in Paper XI. A further development would be a system monitoring the LIBS signal as the surface is cleaned. A change in signal indicates that the surface constituents have changed, and thus the area has been cleaned. With such a system, automatic control of the cleaning process would be achieved, and remote automatic cleaning processes could be anticipated.

1.3 Electrical insulators

The fluorescence lidar technique can be used in many applications. For example, electrical insulators in high-voltage transmission lines are exposed to the weather and biological growth. This may lead to the absorption of water, which may cause disruptive discharges and electrical failure. By monitoring the state of the insulators, it may be possible to avoid such events. Studies of this phenomenon have been performed and are presented in Papers IX and X, and in Ref. 23.

A development could be a small, mobile device that can be used to perform such measurements on insulators in the field. Then, it could be possible to quickly make an assessment of which insulators need to be exchanged or cleaned. A further development would be to clean the insulators with the same tool, by using the laser to burn off the contamination.

1.4 Thesis outline

The thesis is arranged as follows: Chapter 2 describes light, its fundamental interaction with matter and different light sources. In Chapter 3 the use of light in spectroscopic measurements is discussed. Chapter 4 describes lidar measurements and their applications. Methods of data analysis are presented in Chapter 5 and finally, some conclusions and a future outlook are given in Chapter 6.

LIGHT

Light is essential for almost all life on earth. The main source of light is, of course, the sun. The electromagnetic radiation from the sun provides us with light and heat. From a physical perspective, the only difference between visible light and other electromagnetic radiation is that our eyes can detect it. Most of the reasoning in this chapter is adapted from Refs 24 and 25.

In this thesis, light will generally be defined by its wavelength, λ , or its photonic energy, E , but frequency, ν , or wavenumber, σ , can also be used, through the relations:

$$\nu = \frac{c}{\lambda} \quad \text{and} \quad \sigma = \frac{1}{\lambda},$$

where c is the speed of light. E and λ are connected by the relation:

$$E = \frac{hc}{\lambda}, \tag{2.1}$$

where h is Planck's constant.

2.1 The duality of light

Light has both wave and particle properties, a fact which is usually referred to as the duality of light. According to the de Broglie hypothesis [26], all particles, or indeed objects, have wave properties. However, the wave properties are only noticeable for small particles, e.g. photons or electrons. Whereas electrons are considered as particles in classical physics, light is identified as waves. However, there are situations in which the wave description of light has difficulties in explaining some of the phenomena observed, and nowadays it is almost as common to consider light as photons.

Depending on the situation, it may be more convenient to explain an experimental result by considering light as particles than

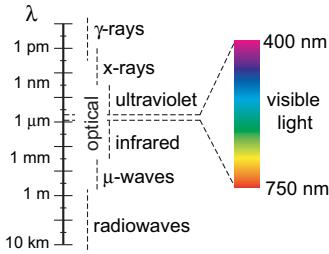


Figure 2.1. The electromagnetic spectrum ranges from γ -rays to radiowaves and only a small part can be detected by the human eye, as indicated in the figure.

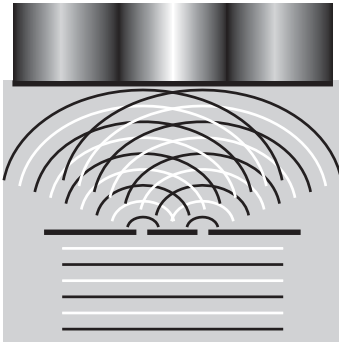


Figure 2.2. Young's double-slit experiment. A plane light wave passing through two narrow slits is diffracted and interference can be observed on a screen.

by using the wave description. What is light then? This is more of a philosophical than a physical question, and it is not easy to answer. We simply declare that we can describe light as either waves or particles.

2.1.1 The wave nature of light

The electromagnetic spectrum is depicted in Fig. 2.1 and ranges from γ -rays to radiowaves. Only a small part of the spectrum can be detected by the human eye; this is what is known as visible light. In this region, the colour of the light changes with the wavelength of the electromagnetic wave, ranging from 400 nm (violet) to 750 nm (red). This work deals with the optical electromagnetic radiation, i.e. visible light together with ultraviolet and infrared radiation.

The wave nature of light is supported, for example, by Young's famous double-slit experiment, performed in 1801. In that experiment, parallel light is directed onto a screen with two narrow slits close to each other. The light that passes through the slits is diffracted and spreads in different directions. If the light is considered as waves, interference between light from the different slits will occur. If a screen is placed at a distance behind the slits, an interference pattern can be observed on the screen, indicating that light must have wave properties. The experiment is illustrated in Fig. 2.2. The plane light wave enters from below, is diffracted when passing through the slits, and two interfering point sources are created. The black lines indicate the crests of the wave and the white lines the troughs. A crossing between two black or two white lines thus indicates a point of constructive interference while a crossing between a black and a white line indicates destructive interference. The interference pattern is observed on the screen.

2.1.2 The particle nature of light

Light can also be described as a flow of particles, called photons. Each photon is considered as being a small packet of energy; the energy depending on the wavelength of the light, according to Eq. (2.1).

The particle nature of light is supported by phenomena such as the photoelectric effect [27]. Light impinging on a surface may free electrons from it, which can only happen if the energy of a single photon exceeds the binding energy of the electron. In other words, there is an energy threshold for the photons before any electrons are emitted. More impinging photons will give more electrons, provided that they individually exceed the binding energy of the electrons. But if the photonic energy is just slightly smaller than the binding energy, no electrons will be emitted independent of the number of impinging photons. This effect cannot be explained

using the wave properties of light; it makes sense that more intense light will give more electrons, but it does not make sense that there is a threshold wavelength of the light to get any electrons at all [28].

2.2 The interaction of light with matter

Light and matter can interact through three fundamental processes: absorption, spontaneous emission and stimulated emission. These will be discussed further in this section.

2.2.1 Absorption

When a photon collides with an atom or molecule, it may be absorbed. The absorption process is depicted in Fig. 2.3. If the energy of the impinging photon matches the difference between two energy levels in the atom, i.e. $E = E_2 - E_1$, an atom may absorb the energy of the photon and an electron is moved to a higher energy state; i.e. the atom is excited. The photon is annihilated in the process. A molecule has more energy states than an atom, due to rotations of the molecule and vibrations between the atomic nuclei. The molecule may thus absorb energy to move it to a higher ro-vibrational state, apart from the possibility of electronic excitation.

The rate of change of the number of atoms per unit volume (or population) in the ground state due to absorption is proportional to the population in the ground state, N_1 , and is given by:

$$\left(\frac{dN_1}{dt}\right)_{abs} = -W_{12}N_1. \quad (2.2)$$

The absorption rate, W_{12} , is not only dependent on the transition, but also on the impinging photon flux, F ,

$$W_{12} = F\sigma_{12}. \quad (2.3)$$

Here, σ_{12} is the absorption cross section of the transition. W_{12} has the unit s^{-1} , as it is interpreted as the number of absorption events per second.

If the energy of the photon is large enough, the atom may become ionized, i.e. an electron becomes so highly excited that it is released from the atom. This is what happens in the photoelectric effect, as discussed in Sect. 2.1.2.

2.2.2 Spontaneous emission

When an atom has been excited, sooner or later it will rid itself of its excess energy. Upon relaxation, it might emit a photon, as shown in Fig. 2.4. This photon will be emitted in a random direction and with random phase.

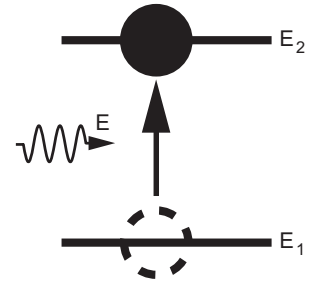


Figure 2.3. Absorption: A photon is absorbed by an atom, whereupon the atom is excited to a higher energy state.

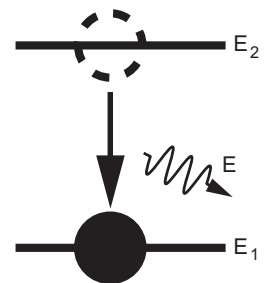


Figure 2.4. Spontaneous emission: When an excited atom relaxes, a photon is created, carrying the released energy.

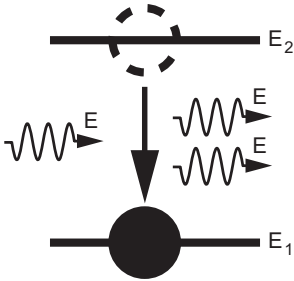


Figure 2.5. *Stimulated emission:* An excited atom is triggered to relax by a photon with energy $E = E_2 - E_1$. In this process, the excess energy is released as a photon with the same direction and phase as the stimulating radiation.

The rate of change of the population in the excited level due to spontaneous emission is given by

$$\left(\frac{dN_2}{dt}\right)_{sp} = -AN_2, \quad (2.4)$$

where N_2 is the population in the excited level and A is the rate of spontaneous emission, also known as the Einstein A coefficient. The radiative lifetime of the excited state, τ_{sp} , depends on A ,

$$\tau_{sp} = 1/A. \quad (2.5)$$

A depends only on the current transition, in contrast to W_{12} in absorption and W_{21} in stimulated emission, as discussed in Sects 2.2.1 and 2.2.3, respectively.

An atom may also relax without sending out a photon, e.g. by losing its excess energy in a collision with another atom. In such an event, the energy is transformed into kinetic energy or heat.

2.2.3 Stimulated emission

When a photon interacts with an atom, it may be absorbed if its energy is appropriate, as discussed in Sect. 2.2.1. However, if the atom is already excited, the photon may stimulate the atom to relax, emitting another photon in phase with the impinging one. This process is called stimulated emission and is illustrated in Fig. 2.5. It is mathematically equivalent to absorption:

$$\left(\frac{dN_2}{dt}\right)_{st} = -W_{21}N_2, \quad (2.6)$$

where W_{21} is the rate of stimulated emission.

$$W_{21} = F\sigma_{21}, \quad (2.7)$$

where F is the photon flux and σ_{21} is the stimulated emission cross section. As can be seen, Eq. (2.7) is similar to Eq. (2.3) and it can be shown that,

$$g_1\sigma_{12} = g_2\sigma_{21}, \quad (2.8)$$

where g_1 is the degeneracy¹ of level 1 and g_2 is the degeneracy of level 2.

The emitted photon will have the same properties as the exciting one, regarding its direction, phase and polarization.

¹The degeneracy of a state is the number of sublevels with the same energy. This will be further discussed in Sect. 3.1.1.

2.3 Light sources

Light is emitted from various sources due to different physical processes. The most common light source is a blackbody emitter, but in this section, lasers and optical parametric oscillators will also be discussed, as these are light sources that have been used in this work.

2.3.1 Blackbody radiation

A perfect black body is defined as a body that will absorb all light incident on it. A black body, being a perfect absorber, is also a perfect emitter; i.e. it will radiate. This may not be obvious, but can be deduced from general considerations of thermodynamic equilibrium, and the statement is known as Kirchoff's law [29]. A warm object will emit more radiation than a cold one. Shorter wavelengths will be emitted from a warmer object and the peak of the radiation will be shifted towards shorter wavelengths.

Although perfect black bodies are not encountered in everyday life, all items radiate when they are warm. The hob on a cooker mistakenly left on will, after a while, glow faintly red. As the hob becomes hotter, the emitted wavelengths change from the infrared into the visible region. Even hotter objects will glow with a whiter light, for example a light bulb or the sun, which have temperatures of around 2500 K and 6000 K, respectively. The spectral radiant exitance (i.e. the radiated light at a certain wavelength), M_λ , is depicted as a function of wavelength for a perfect black body in Fig. 2.6, where the curves for a few different temperatures are plotted.

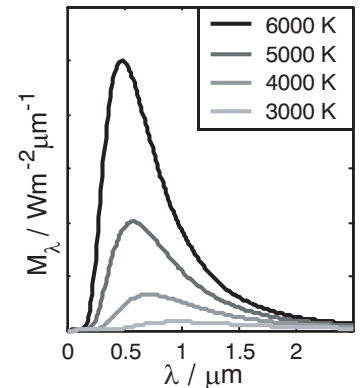


Figure 2.6. A perfect black body emits radiation, the wavelength and intensity of which depend on its temperature.

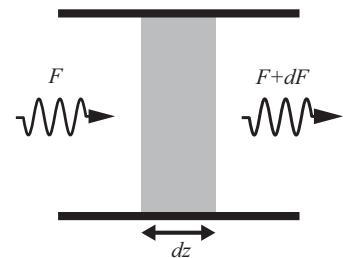


Figure 2.7. A plane wave F travels through a material and a changed flux $F + dF$ is observed.

2.3.2 Lasers

The word laser is an acronym for light amplification by stimulated emission of radiation. Lasers are based on stimulated emission in an active medium and provide coherent, directed, narrow-band radiation. These properties make them very attractive for spectroscopic measurements.

Light entering a material can stimulate absorption or emission, as discussed in Sects 2.2.1 and 2.2.3, respectively, if the energy of the photons matches an allowed transition in the atoms. If a photon flux F travels through a material of thickness dz , as illustrated in Fig. 2.7, the transmitted flux will have changed to $F + dF$. If the cross-sectional area of the light beam is S , the change in photon number will be SdF . However, the change in photon number must also be the difference between stimulated emission and absorption events. As spontaneous emission can occur in any direction, these events are not considered to affect dF . Using Eqs (2.6) and (2.2)

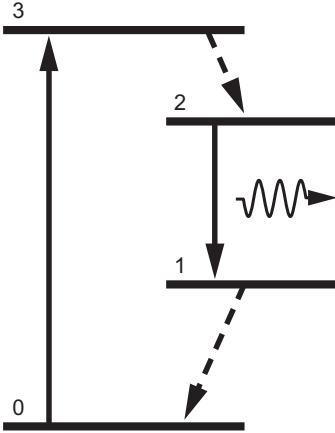


Figure 2.8. Energy levels in a four-level laser. Atoms are pumped from state 0 to state 3 and the lasing occurs between states 2 and 1.

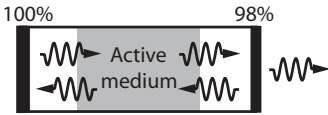


Figure 2.9. The active medium is placed inside a cavity and a small output is released through the 98% reflecting mirror.

gives:

$$SdF = (W_{21}N_2 - W_{12}N_1)(Sdz), \quad (2.9)$$

where Sdz is the volume of the interaction region. By combining this result with Eqs (2.3), (2.7), and (2.8) we obtain:

$$dF = \sigma_{21}F \left[N_2 - \left(\frac{g_2 N_1}{g_1} \right) \right] dz. \quad (2.10)$$

To obtain amplification of the light, i.e. $dF > 0$, it is necessary for

$$N_2 > \frac{g_2 N_1}{g_1}, \quad (2.11)$$

which is known as a population inversion. This cannot be achieved by thermal excitation, as Boltzmann statistics² state that no more than half of the atoms can be thermally excited. Thus, to achieve a population inversion, more than two energy levels must be involved.

The most common laser configuration is the four-level laser, where atoms are excited from the ground state (state 0 in Fig. 2.8) to an excited state (3) by some sort of pumping process. From this excited state, the atoms are quickly de-excited (often by some sort of non-radiative transfer) to a lower, more long-lived state (2). A population inversion between states 2 and 1 can then be achieved, and lasing can occur in this transition. It is then required that atoms are quickly transferred from state 1 back to the ground state, to maintain the population inversion. It is also important that the energy difference between state 1 and the ground state is large enough to avoid too large thermal excitation to state 1.

Note that it is not required that all the energy levels are in the same type of atoms. There are systems where pumping is performed in one type of atoms and the energy is transferred, by collisions, to another type, where the lasing occurs. An example of such a laser type is the helium-neon laser.

Three-level lasers also exist, in this case states 0 and 1 are the same. It is more difficult to achieve a population inversion in this type of laser, as the laser action must be achieved to the ground state, which is highly populated. Paradoxically, the ruby laser, constructed in 1960 as the first successful laser, is a three-level laser [30].

To maintain lasing, the active medium is placed inside a cavity, between two highly reflecting mirrors. If, for example, one of the mirrors is 100% reflecting and the other one is 98% reflecting, as indicated in Fig. 2.9, a small part of the light will escape the cavity in each round trip. For lasing to continue it is then necessary that the amplification in the active medium is larger than the loss from the output mirror and the internal losses in the cavity.

²Boltzmann statistics will be further discussed in Sect. 3.1.3

To avoid destructive interference in the cavity, the length of the cavity, L , must correspond to a discrete number, n , of half wavelengths, i.e. the radiation must form a standing wave in the cavity:

$$L = n \frac{\lambda}{2}. \quad (2.12)$$

This is depicted in Fig. 2.10, where two examples are shown. Naturally, a cavity can be suitable for a huge number of different wavelengths. The wavelength is fixed by the transition in the active medium, but this is not infinitely narrow, as will be further discussed in Sect. 3.1.2. Therefore, the cavity length may be used to more precisely tune the wavelength. With a long cavity, i.e. with a large n , there will be more than one standing wave inside the amplification profile of the active medium and multimode operation may occur.

2.3.3 Tunable lasers

Most lasers work at only one wavelength, corresponding to the energy difference of the transition used. However, there are some types of lasers that may be tuned. These are specifically useful in spectroscopy applications, as the wavelength can be chosen to coincide with the transition being studied. There are several types of tunable lasers, a few of which are discussed below.

Semiconductor lasers, also known as diode lasers, are the type of small lasers that are used in CD players and similar products. These lasers are based on a semiconductor material, in which the transition occurs over a band gap. The lasing occurs inside the semiconductor material, which also constitutes the laser cavity. The wavelength of these lasers can be tuned by changing their temperature, which changes the size of the band gap and the length of the cavity. They can also be fine-tuned by changing the driving current to the laser. A drawback of semiconductor lasers is that the output has usually quite low power, at least those with good spectral quality.

In a dye laser, a liquid dye is pumped by a high-energy laser. The dye has a relatively broad amplification profile, which makes it possible to create laser light at different wavelengths by placing the dye cuvette in a tunable cavity. The tunable cavity is usually some sort of grating arrangement, for example of the Littman type depicted in Fig. 2.11. A dye laser provides narrowband pulsed radiation with high powers. However, to establish tuning over large wavelength ranges, it is required to change dyes, which may be inconvenient. Also, the dyes are usually toxic, cancerogenic substances, that have to be handled with great care.

Solid-state lasers can be constructed from materials that have broad gain profiles. Tuning of the wavelength can be achieved, by using some form of wavelength-sensitive optics in the laser cavity.

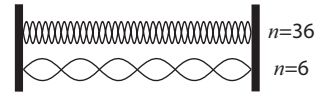


Figure 2.10. The radiation must form a standing wave inside the laser cavity to avoid destructive interference. The length of the cavity can thus be used to tune the wavelength inside the amplification profile of the active medium.

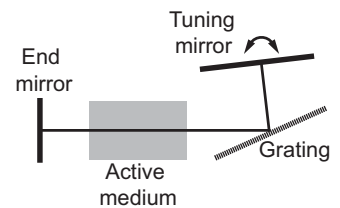


Figure 2.11. A grating arrangement, known as the Littman configuration. Only the light of the right wavelength is reflected from the grating so as to have normal incidence on the tuning mirror. Light of other wavelengths will not be reflected back into the cavity and thus the wavelength can be chosen.

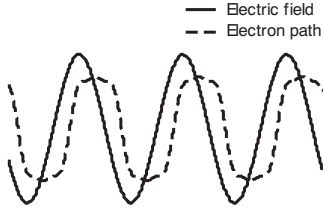


Figure 2.12. The electrons may be too heavy to be able to follow an intense electric field, in which case they will take a shorter path. This gives rise to higher frequencies.

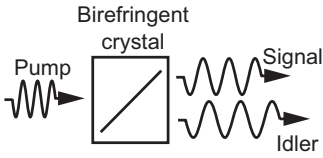


Figure 2.13. In an optical parametric oscillator a pump beam is divided into a signal beam and an idler beam in a birefringent crystal.

Examples of such lasers are titanium-sapphire lasers or alexandrite lasers and these are tunable in the red–near infrared wavelength region [31].

Moreover, optical parametric oscillators can be used to tune the wavelength of coherent light by non-linear conversion of a pump laser beam. This type of device is further described below.

2.3.4 Non-linear optical processes

Light transmitted through a material triggers electrons to move with the electric field of the light and the material is said to be polarized. If the intensity of the light is very high, the electrons will not be able to follow the electric field, but will short-cut the path of the linear response, as indicated in Fig. 2.12. This will cause new frequencies to be formed and is known as a non-linear effect.

The polarization, $P(t)$ of the material depends on the electric field $E(t)$ according to:

$$P(t) = \epsilon_0 \left(\chi^{(1)} E(t) + \chi^{(2)} E^2(t) + \chi^{(3)} E^3(t) + \dots \right), \quad (2.13)$$

where ϵ_0 is the permittivity of free space and $\chi^{(n)}$ is known as the n^{th} order susceptibility of the material. For a linear material $\chi^{(2)}$ and higher orders are equal to zero, but for non-linear materials they are non-zero. However, $\chi^{(1)} \gg \chi^{(2)} \gg \chi^{(3)}$ and so on. As can be seen in Eq. (2.13), the second-order polarization depends on the square of the electric field, and thus high-intensity light is needed for non-linear effects to occur. Typically, only laser light is intense enough to bring about these processes. Examples of non-linear processes are second-harmonic generation (SHG), sum-frequency generation (SFG), difference-frequency generation (DFG), and optical parametric oscillation. In the next section, the optical parametric oscillation process will be further discussed [32].

2.3.5 Optical parametric oscillation

An optical parametric oscillator (OPO) is a device in which coherent radiation with a tunable wavelength can be generated. It utilizes a non-linear crystal in which a pumping photon is divided into two photons, as depicted in Fig. 2.13. This is a non-linear process that will only occur in birefringent materials³ with a laser pump beam of high intensity. Three beams leave the crystal: residual pump light (not shown in Fig. 2.13), a signal beam and an idler beam. By convention, the signal beam has a shorter wavelength than the idler beam. As energy must be conserved, $E_p = E_s + E_i$,

³A birefringent material is one where the refractive index is dependent on the polarization of the light passing through it.

where the indices designate pump, signal and idler, respectively. By rewriting this in terms of wavelength,

$$\frac{1}{\lambda_p} = \frac{1}{\lambda_s} + \frac{1}{\lambda_i}, \quad (2.14)$$

it can be seen that it is not possible to create light with a shorter wavelength than the wavelength of the pump beam.

OPOs were proposed as early as in 1962 [33], only a few years after the invention of the laser. However, useful output energies from the devices were not achieved until much later, when efficient, high-threshold, non-linear materials were developed [34].

The output from an OPO has much the same properties as laser light, i.e., it is coherent, directed and narrow-banded, although the process in which it is created is physically very different from a laser. The laser relies on atomic or molecular transitions, whereas an OPO depends on non-linear conversion of a pump laser beam [32, 35].

Phase matching

For an OPO process to occur, not only the energy, but also the momentum of the light beams must be conserved. If the beams are described by their wave vectors, \mathbf{k} , where $|\mathbf{k}|$ corresponds to the energy of the wave and the direction of the vector is given by the direction of the beam, then, Eq. (2.15) must be fulfilled:

$$\mathbf{k}_p = \mathbf{k}_s + \mathbf{k}_i. \quad (2.15)$$

This can be achieved in two ways, either by collinear phase matching or by non-collinear phase matching. In collinear phase matching, the direction of all three wave vectors is the same, whereas the directions are not parallel in the case of non-collinear phase matching, as illustrated in Fig. 2.14. In this description, only the former situation will be considered.

For collinear phase matching, Eq. (2.15) can be rewritten as:

$$\frac{n_p}{\lambda_p} = \frac{n_s}{\lambda_s} + \frac{n_i}{\lambda_i}. \quad (2.16)$$

In Eq. (2.16), n_p , n_s and n_i represent the refractive indices of the pump, the signal and the idler beams, respectively. For most materials, the refractive index should strictly decrease with wavelength, and thus Eqs (2.14) and (2.16) cannot be simultaneously fulfilled. However, for birefringent materials, the refractive index depends on the polarization of the light. Light polarized perpendicular to the propagation direction (\mathbf{k}) and the optical axis of the material experiences an ordinary index of refraction n_o . Light polarized in the plane containing \mathbf{k} and the optical axis experiences an extraordinary index of refraction $n_e(\theta)$ which is dependent on the angle θ

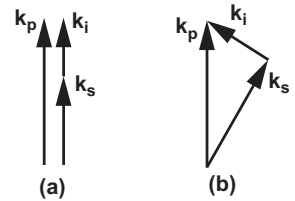


Figure 2.14. Collinear (a) and non-collinear (b) phase matching.

between \mathbf{k} and the optical axis. There are different types of crystals, but for uniaxial crystals, which are the only ones discussed here,

$$n_e(\theta) = \frac{\bar{n}_e n_o}{\sqrt{\bar{n}_e^2 \cos^2(\theta) + n_o^2 \sin^2(\theta)}}. \quad (2.17)$$

Here, \bar{n}_e represents $n_e(\theta)$ when $\theta = 90^\circ$. Using, e.g., a pump beam with extraordinary polarization and the signal and idler beams ordinarily polarized, it is possible to find an angle θ where both Eqs (2.14) and (2.16) are fulfilled.

The scheme described above (where the pump beam has one polarization and the signal and idler beam another) is known as Type I phase matching. When either the signal or idler beam has the same polarization as the pump beam, it is known as Type II phase matching. The conservation of energy and momentum can be fulfilled for a different set of signal and idler wavelengths by changing the angle of the crystal, and it is thus possible to tune the wavelength [32, 35].

Linewidth considerations

OPOs generally have relatively wide amplification profiles and wide spectral profiles of the output beams. This is a property that is often impractical in spectroscopic applications. To remedy this, the crystal can be placed inside a tunable external cavity; usually some sort of grating arrangement, as discussed in Sect. 2.3.3. The wavelength can then be more precisely chosen, as only the selected wavelength is given the chance to be amplified.

A frequently utilized configuration is to place a crystal in an external cavity, as described above. The output from this “master oscillator” is used to seed another crystal, which is simultaneously radiated with more pump light. Amplification of the narrow-band seed light is achieved in this “power oscillator”, and high energies with narrow linewidth can be created.

The OPO used in this work

A Spectra-Physics MOPO-730 unit [36], modified to allow fast tuning of the wavelength [37], was used to perform DIAL measurements (Papers I–III). This is an OPO based on collinear Type I phase matching in the uniaxial crystal β -barium borate (BBO) with an external cavity to provide the narrow linewidth needed. The device is pumped by the frequency-tripled light from a Nd:YAG laser at 355 nm and can generate output in the range 440 nm–1.7 μm . Wavelengths down to 220 nm can be achieved by frequency doubling. The linewidth is around 0.2 cm^{-1} , which for ultraviolet wavelengths around 250 nm corresponds to about 1 pm.

The same device was used to induce fluorescence in remote targets using different wavelengths (Paper [VIII](#)). In these applications the excitation laser light is not critical, so the linewidth is not a crucial factor. These measurements could thus have been performed with a simpler system, without an external cavity.

SPECTROSCOPY

In this chapter, different forms of spectroscopy will be described. This is not intended to be a complete description, but to give an introduction to the techniques used in this work.

3.1 Absorption of light by atoms and molecules

In this section, absorption and emission processes, and how they can be used for spectroscopy, will be discussed. Firstly, the energy level structure of atoms and molecules will be described. Then, line broadening mechanisms are discussed, and line intensities are considered in Sect. 3.1.3. Finally, Beer-Lambert's law is described.

3.1.1 Energy level structure

Energy levels in atoms and molecules are quantized, i.e. the energy of the system can only have certain, well-defined, values. In this section, the energy level distribution will be described, for both atoms and molecules.

Atoms

A free hydrogen atom (^1H) is a system consisting of a single-proton nucleus with an electron circling it. The electron can only be positioned in orbits at quantized distances from the proton. This is, according to the de Broglie hypothesis [26], due to the fact that electrons have wave properties. For an orbit to be allowed, the electron must form a standing wave in the circular or elliptical orbit, otherwise it destructively interferes with itself, as illustrated in Fig. 3.1. Thus, for the hydrogen atom, there are a number of fixed orbits that are allowed, each with a certain energy. If a photon is absorbed by a hydrogen atom, the electron is sent to an outer orbit and the atom is said to be in an excited state (as

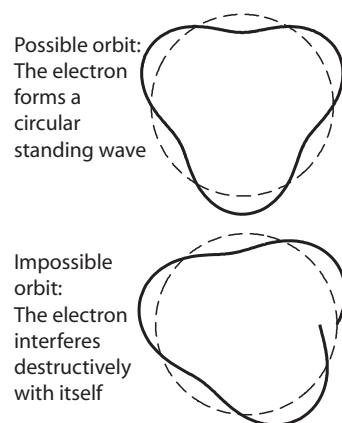


Figure 3.1. An orbit can only be allowed if the electron can form a standing wave in it (above). Otherwise, it will destructively interfere with itself (below).

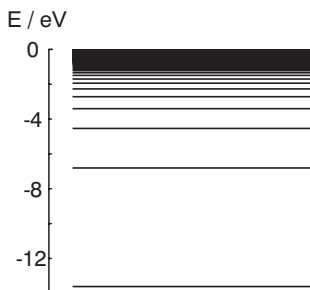


Figure 3.2. The energy levels in a free hydrogen atom. The state with the lowest energy is the ground state and the levels up to the ionization limit are shown.

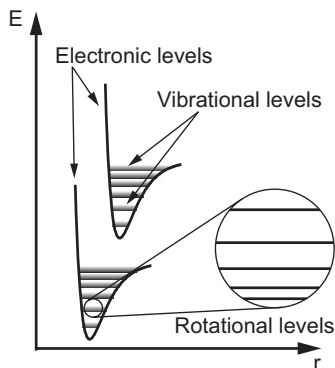


Figure 3.3. A schematic illustration of the energy levels of a diatomic molecule as a function of the distance between the nuclei. The envelopes denote the electronic potentials, inside which the vibrational and rotational levels are situated.

opposed to the ground state, where the electron is in the innermost orbit), as was discussed in Sect. 2.2.1.

The energy levels in a hydrogen atom are illustrated in Fig. 3.2. By convention, the energies of the states are negative, and 0 eV indicates the ionization limit, where the electron escapes the attractive force of the nucleus, and the atom is ionized. The energy of the ground state in ^1H is -13.6 eV, which is the amount of energy needed to ionize the atom. The energy levels are spaced closer to each other as the ionization limit is approached. The energy of the n^{th} state is given by:

$$E_n = -\frac{13.6}{n^2} \text{ eV}. \quad (3.1)$$

This result can be found using either a semi-classical description with a quantum condition (the Bohr model), or a quantum mechanical one.

For larger atoms, the systems are more complicated. There are more electrons, but they still have specific orbitals. However, they will affect each other, so the calculation of the states is more difficult than for a hydrogen atom. Whereas the semi-classical theory has to resort to simplifications and assumptions, the full solution can be found by solving the Schrödinger equation, although it only has an analytical solution in special cases [31, 38].

Molecules

For molecules the situation is even more complicated. The electronic transitions still exist, but there are also several vibrational and rotational energy levels. The nuclei vibrate around the equilibrium gap between them, which gives them vibrational energy. Rotational energy occurs as molecules rotate.

The energy levels of a diatomic molecule are illustrated in Fig. 3.3. The energies of the levels, E , are plotted as a function of the distance between the two nuclei, r . The energy difference between two electronic levels is of the order of a few eV, corresponding to absorption in the visible or UV region.

In the electronic levels, or bands, there are vibrational levels. The separation between two vibrational energy levels is of the order of 0.1 eV, corresponding to transitions in the IR region. If the molecule is excited to a very high vibrational state, it will dissociate.

Rotational levels are superimposed on the vibrational levels, with an energy difference of about 0.001 eV, which gives absorption in the microwave region [31, 38].

Degenerate levels

Two main effects determine the energy of a certain electronic state in an atom; the attraction between the electron and the nucleus,

and the repulsion between the electron and the other electrons. Due to the Pauli principle, which states that there cannot be more than one electron in each energy state, the set of quantum numbers must be unique for each electron. However, not all quantum numbers necessarily contribute to the energy of the state, and hence there can be more than one state with the same energy. The same reasoning can be applied to vibrations and rotations. These are also quantized, but there may be quantum numbers not affecting the energy. Moreover, accidental degeneracies can occur, where two states with different quantum numbers happen to have identical energies [38].

3.1.2 Linewidths

An atomic or molecular absorption line is not infinitely narrow, but has a certain linewidth, i.e., light in a certain wavelength range can be used to excite a certain transition. There are several different line broadening mechanisms, natural linewidth, Doppler broadening and pressure broadening, which are discussed below. In the linewidth equations, the frequency, not the wavelength, is used. This is because the linewidth, expressed in wavelength, is a function of the central wavelength.

Natural linewidth

The Heisenberg uncertainty principle states that, in any measurement,

$$\Delta t \Delta E \geq \frac{h}{4\pi}, \quad (3.2)$$

where Δt is the uncertainty in time, ΔE is the uncertainty in energy, and h is Planck's constant. For electronic transitions in atoms, it can be said that if the electron spends a short time in the excited state, which makes the time uncertainty short, the energy of the state will be very uncertain, and vice versa.

For an excited state with lifetime τ , it can be shown that $\Delta t = \tau$ and therefore the energy uncertainty for that state is:

$$\Delta E = \frac{h}{4\pi\tau}. \quad (3.3)$$

This relation is a fundamental physical limitation that can never be overcome. Thus, every absorption line has a non-zero linewidth. The natural linewidth is narrower for long-lived states, i.e., when τ is large. Typical natural linewidths for allowed transitions in the visible region are of the order of 10 fm.

The naturally broadened line has a Lorentzian lineshape, with a frequency uncertainty (half-width at half maximum (HWHM)) of:

$$\Delta\nu = \frac{1}{4\pi\tau}, \quad (3.4)$$

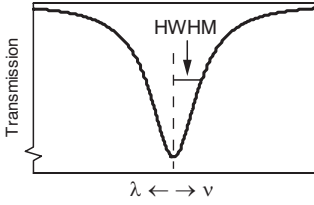


Figure 3.4. The natural linewidth has a Lorentzian shape and a HWHM of $1/4\pi\tau$.

which is derived from Eq. (3.3) and $\Delta E = h\Delta\nu$. The lineshape is depicted in Fig. 3.4 and is given by:

$$\phi_L(\nu) = \frac{1}{\pi} \frac{\alpha_L}{(\nu - \nu_0)^2 + \alpha_L^2}, \quad (3.5)$$

where α_L represents the Lorentzian HWHM and ν_0 is the centre wavelength for the absorption line. Using Eq. (3.4), the natural lineshape can be written [31, 39]:

$$\phi_L(\nu) = 4\tau \left[1 + \left(\frac{\nu - \nu_0}{1/4\pi\tau} \right)^2 \right]^{-1}. \quad (3.6)$$

Doppler broadening

If the source of a sound is moving relative to the listener, the emitted waves will be compressed or expanded, leading to a change in pitch, or wavelength. The same is true for electromagnetic waves. The received wavelength, λ_R , is shifted compared to the source wavelength, λ_S , according to:

$$\lambda_R = \sqrt{\frac{c+v}{c-v}} \lambda_S. \quad (3.7)$$

Here, c is the speed of light and v is the relative velocity between the source and the receiver ($v > 0$ when they move away from each other and $v < 0$ when they move towards each other). Although the Doppler effect in sound is often heard, the Doppler effect in light is not encountered in everyday situations, since v is usually much less than c [28].

Atoms or molecules in a gas are moving in random directions and they will thus have different velocities. If the atoms are excited, they may send out light upon relaxation, but this light will be Doppler shifted as the atoms are moving. In the same way, atoms will absorb at different wavelengths due to their velocity, giving rise to Doppler broadening. This is an inhomogeneous broadening, as each individual atom has a sharp natural linewidth, but as an ensemble the different Doppler shifts combine to broaden the line. Typical Doppler shifts in the visible range at room temperature are about 1 pm.

Doppler broadening depends on the temperature, T , and on the mass, m , of the absorbers. The reason for this is that the absorbers move faster if they are warm, and light absorbers move faster than heavy ones. Thus, Doppler broadening is sometimes referred to as temperature broadening. The effect gives rise to a Gaussian lineshape, given by:

$$\phi_G(\nu) = \sqrt{\frac{\beta}{\pi}} e^{-\beta(\nu - \nu_0)^2}, \quad (3.8)$$

where

$$\beta \equiv \frac{mc^2}{2kT\nu_0^2} \quad (3.9)$$

has been introduced. The HWHM of the Gaussian line profile is given by

$$\Delta\nu = \sqrt{\frac{\ln 2}{\beta}}. \quad (3.10)$$

A Doppler profile is shown in Fig. 3.5. In laboratory applications Doppler broadening can be eliminated, for example, by using saturation spectroscopy [31, 39].

Pressure broadening

Atoms or molecules in a gas collide with each other; the frequency of collision depending on the pressure. In a collision, energy transfer occurs, which may cause an atom to relax to the ground state. These events shorten the lifetime of the excited state and thus, according to Eq. (3.3), cause a broadening of the spectral line. This type of broadening is homogeneous, as it is the same for all atoms. Typical pressure broadening or collisional broadening linewidths at atmospheric pressure and room temperature of lines in the visible region are of the order of 1 pm. Pressure broadening can be reduced by performing spectroscopy in low-pressure cells.

The pressure broadened line will have a Lorentzian line shape, just as the natural linewidth. Although the typical linewidths of Doppler and pressure broadened lines are of the same order of magnitude, their respective shapes will be slightly different. Fig. 3.6 shows a Doppler broadened and a pressure broadened line with the same HWHM and the same total absorption (i.e. integrated area). The Lorentzian profile, corresponding to pressure broadening, has a narrower peak, but it has much broader wings than the Gaussian profile, corresponding to Doppler broadening [25, 31].

Combined broadening

From the previous sections, it can be concluded that the natural linewidth is significantly smaller than the Doppler and pressure linewidths, which are of similar order. In real situations, the resulting linewidth is usually a combination of Doppler and pressure broadening.

Broadening due to both pressure and temperature will give rise to a line profile between the Lorentzian and the Gaussian, i.e. a convolution of the two. This is known as a Voigt line profile [31].

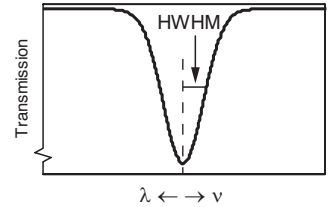


Figure 3.5. A Doppler-broadened line will have a Gaussian line profile.

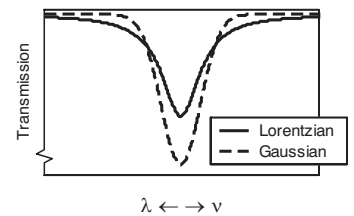


Figure 3.6. A Doppler broadened (Gaussian) and a pressure broadened (Lorentzian) lineshape with the same HWHM and the same total absorption.

3.1.3 Line intensity

Different spectral lines have different intensities, depending on the transition probability and the population of the states. These aspects will be discussed below.

Transition probability

Different types of transitions arise, depending on how the atom interacts with the light. The strongest type of transition occurs when the electric field of the light interacts with the electric dipole moment of the atom. These transitions are known as electric-dipole allowed transitions, whereas other transitions are electric-dipole forbidden. The electric-dipole notation of these terms is often left out, and the transitions are simply called allowed or forbidden. However, this is slightly misleading, since electric-dipole forbidden transitions may be allowed as magnetic-dipole transitions or electric-quadrupole transitions, etc. The strengths of these transitions are significantly smaller than electric-dipole allowed transitions. However, there is still a small probability of them occurring.

A quantum mechanical treatment is required to calculate the transition probabilities. This will not be elaborated on here, but a good description is given, for example, in Ref. 40. However, there are some simple selection rules that can be used to determine whether a transition is electric-dipole allowed or not. These selection rules are based on the quantum numbers of the two states involved [25, 31].

Population of states

All atoms strive to have as low an energy as possible, but they can be thermally excited. At 0 K, all atoms are in their ground state, but as the temperatures increase they tend to be excited to higher states.

The population in an excited state, N_2 , compared to the population in the ground state, N_1 , is temperature dependent and is given by Boltzmann statistics,

$$\frac{N_2}{N_1} = \frac{g_2}{g_1} e^{-\Delta E/kT}, \quad (3.11)$$

where g_1 and g_2 are the degeneracies of states 1 and 2, respectively, ΔE is the energy difference between the states, T is the temperature and k is Boltzmann's constant. It can be noted that as T approaches 0, the population of the excited state also approaches zero and as $T \rightarrow \infty$, $N_2 \rightarrow N_1$ (assuming $g_1 = g_2$). In other words, it is not possible to thermally excite more than half of the atoms [31].

The intensity of the line will obviously be greater if there is a higher population in the state. Consider the case depicted in

Fig. 3.7. A transition with its lower level above the ground level will not be populated at low temperatures and the incoming light cannot be absorbed. If there are no atoms that can interact, it does not matter how large the transition probability is, the line intensity will still be zero. But as the temperature rises atoms will be thermally excited and the line intensity will increase.

3.1.4 Beer-Lambert's law

When light passes through a gas, some of it may be absorbed, if the energy of the photons matches an allowed transition of the atoms. The light travelling through the gas will be attenuated as it is absorbed. By measuring the light intensity before and after the gas, Beer-Lambert's law can be used to deduce the concentration of the gas.

Assume that monochromatic light of intensity I_0 is sent through a gas sample of concentration C , and that the energy of the light matches an allowed transition in the gas. After a certain length Δx , the intensity will have been attenuated by ΔI . The attenuation is proportional to the number of absorbers in the length Δx :

$$\frac{\Delta I}{I} = -\kappa C \Delta x, \quad (3.12)$$

where κ is a proportionality constant dependent on the strength of the transition. Through the entire sample, the intensity changes from I_0 to I_t and x changes from 0 to L . Thus,

$$\int_{I_0}^{I_t} \frac{dI}{I} = - \int_0^L \kappa C dx \quad (3.13)$$

and it follows that:

$$\ln \frac{I_t}{I_0} = -\kappa CL \quad (3.14)$$

and

$$I_t = I_0 e^{-\kappa CL}. \quad (3.15)$$

The derived equation is known as Beer-Lambert's law and is illustrated in Fig. 3.8. The light intensity decreases exponentially as it is absorbed when travelling through the gas.

Absorbance, or optical density, is defined as:

$$A = {}^{10}\log \frac{I_0}{I_t}, \quad (3.16)$$

which, according to Eq. (3.15), leads to:

$$A = {}^{10}\log(e)\kappa CL \quad (3.17)$$

Thus, the absorbance is directly proportional to the concentration of the gas in the sample and may therefore be a convenient quantity to use [31, 38].

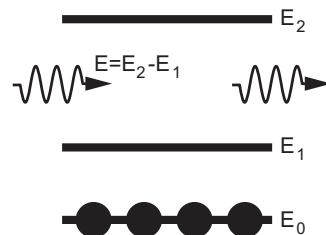


Figure 3.7. The absorption will be zero, irrespective of the transition probability, if there are no atoms to interact with.

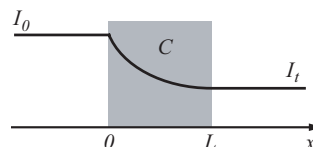


Figure 3.8. Light with a wavelength matching a transition travelling through a gas is absorbed according to Beer-Lambert's law.

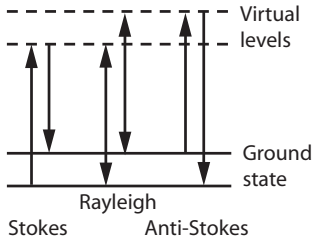


Figure 3.9. Rayleigh and Raman scattering occurs when a molecule is excited to a virtual state and quickly falls back to the ground state.

3.2 Scattering

Scattering may occur in two ways, either elastically or inelastically. Elastic scattering can be considered simply as the photon bouncing off the matter, losing no energy in the process, but changing direction. Scattering obviously occurs at reflections on surfaces, but scattering may also occur from small molecules or particles in the air (consider fog for example). In an inelastic scattering process, the photon will interact with the atom or molecule and either lose or gain energy. In such events not only the direction, but also the wavelength of the light is altered.

3.2.1 Elastic scattering

Elastic scattering can be divided into two categories, Rayleigh scattering and Mie scattering. Rayleigh scattering dominates if the wavelength of the light is longer than the size of the particles it is scattered from and Mie scattering occurs when the wavelength is smaller than the particle size. It is usually said that Rayleigh scattering takes place from molecules, and Mie scattering from particles. Both Rayleigh and Mie scattering are highly wavelength dependent; blue wavelengths being scattered more than red wavelengths.

Rayleigh scattering is depicted in Fig. 3.9. The molecule is excited to a virtual energy state, which is possible due to the uncertainty in the energy levels. For short time scales, ΔE in Eq. (3.3) is very large and spreads over very large energy intervals. The atom can then absorb the photon, but quickly relaxes back to the ground state and then reemits a photon. This photon will then have the same energy as the absorbed one, but may be emitted in any direction. The probability of Rayleigh scattering has a λ^{-4} dependence.

Mie scattering can be regarded as the simple reflection of photons from relatively large particles. However, there are interference effects due to surface waves on the particles, causing the Mie scattering cross-section to oscillate rapidly as a function of wavelength. In the atmosphere, this effect is smeared out due to the different sizes and shapes of the particles. The scattering probability depends on the shape and size of the particles, but is, in a realistic atmosphere, approximately λ^{-2} dependent. In the atmosphere, Mie scattering usually dominates over Rayleigh scattering and thus the visibility is determined by particles in the air [31].

3.2.2 Inelastic scattering

Raman scattering is a type of inelastic scattering closely related to Rayleigh scattering. In a molecule, the ground state usually consists of several close-lying ro-vibrational levels. When such a

molecule is excited to a virtual level, it may relax back to a different ro-vibrational level, as illustrated in Fig. 3.9. In this case the emitted light has a different wavelength from the exciting light, the difference being known as a Raman shift. The Raman shift may occur both to longer and shorter wavelengths and these are denoted the Stokes and Anti-Stokes lines, respectively.

Raman scattering is about a factor 1000 less prominent than Rayleigh scattering [31].

3.3 Emission spectroscopy

Emission spectroscopy can be used to determine which elements are present in a sample. As every type of atom has distinctive energy levels, it will, when excited, emit light at certain, well-specified, wavelengths. By examining spectra it is then possible to distinguish which elements are present in the sample. It may also be possible to measure the temperature of the sample by comparing the strengths of two or more emission lines and, through calibration, to measure concentrations in a sample [31].

In this section, various types of emission spectroscopy will be described. First, flame emission spectroscopy is considered, followed by fluorescence and laser-induced breakdown spectroscopy. These three techniques can give similar results, the main difference being the means of exciting the atoms. Fluorescence from molecules in a solid is somewhat different, as the resulting radiation is highly dependent on the local surroundings of the emitters. Finally, Raman spectroscopy is briefly described.

3.3.1 Flame emission spectroscopy

In flame emission spectroscopy, an element is injected into a flame and the light emitted is analysed, to identify the elements present. Also, concentrations of single elements can be measured by dissolving the element in a solution that is injected into a controlled flame and comparing the result with calibration solutions. When measuring concentrations, one line is usually chosen, preferably one with high intensity.

Emission spectroscopy is a method well suited for monitoring the properties of flames in combustion processes. As there is already emission of light from the flame, this passive technique is suitable. Active techniques can give more reliable results, but also require more complicated equipment [41].

3.3.2 Fluorescence

When an optically excited atom or molecule reemits light upon relaxation, the emitted light is known as fluorescence light. Fluorescence may occur from atoms in a gas or molecules in a liquid

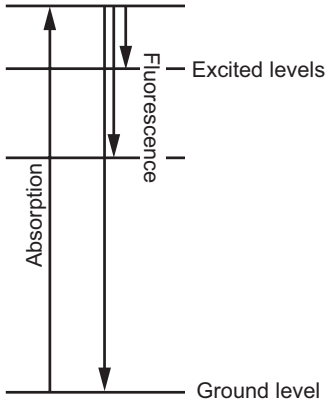


Figure 3.10. The fluorescence process in a free atom. Fluorescence may be resonant or non-resonant.

or solid, and the expected results are quite different. Atoms in a gas do not affect each other to the same extent as molecules in the liquid or solid phase. Therefore, the two cases are discussed separately.

Fluorescence from atoms in a gas

The fluorescence process in a free atom is illustrated in Fig. 3.10. The atom is excited by absorption of a photon and when relaxing, fluorescence light is emitted. The fluorescence may be resonant, if the atom relaxes back to the ground state. In this case the emitted photon has the same wavelength as the exciting one. However, the atom may also be transferred to an intermediate state and then the emitted photon has a longer wavelength.

Fluorescence measurements in a gas are typically performed with a laser beam exciting a transition in the gas. The excited atoms relax and may emit fluorescence in any direction. A detector is placed at 90° to the laser direction to avoid excitation light interference.

In gas absorption spectroscopy, as discussed in Sect. 3.1.4, the intensity difference between the incident light and the transmitted light is measured, and the concentration can be calculated. The light that does not reach the detector is said to have been absorbed. However, light that has been absorbed may result in spontaneous emission of a photon when the atom is relaxing. This fluorescence light is radiated in all directions and some of it will be radiated towards the detector. This will cause an error in the measured absorption, as this photon will be assumed not to have been absorbed.

At atmospheric pressures, fluorescence can usually be neglected, as most atoms or molecules will return to the ground state by losing their excess energy in a collision process. However, for strong emission lines it may be important. A strong emission line will have a high A coefficient, which leads to a short lifetime, as discussed in Sect. 2.2.2. Then, there is a higher probability that the atom will fluoresce before undergoing collision.

Laser-induced fluorescence from atoms in gases is a technique frequently used in combustion applications, to study the abundance and evolution of certain elements [42]. In lidar applications, resonance fluorescence is usually quenched at atmospheric pressures, but may be used for measurements in low-pressure environments. For example, temperatures and wind speeds in the upper atmosphere, which will be discussed further in Sect. 4.3.2, have been measured by resonance fluorescence lidar [43, Chap. 5].

Fluorescence from molecules in a liquid or solid

When studying fluorescence in a liquid or solid, the exciting wavelength is not critical. As depicted in Fig. 3.11, the exciting radiation is absorbed, transferring the molecule to a higher-lying state. In the material, the energy levels are smeared out to continuous bands as there is constant interaction between close-lying molecules. After absorption, there is very rapid decay to the lowest level in the band, a process known as internal conversion. From this level, the molecule can relax to any state in the ground level energy band, giving rise to a continuous spectrum. The fluorescence light may be quenched by non-radiative decay; the molecule may relax, for example, by collision.

Although there are seldom any sharp features in fluorescence spectra, they may still differ significantly. This makes it possible to distinguish materials from each other and to draw conclusions about the studied matter. A typical fluorescence spectrum from a stone surface (in this case travertine on the Coliseum in Rome) is shown in Fig. 3.12.

Remote fluorescence in solid materials, which will be discussed further in Sect. 4.3.5, was used extensively in this work. Results from cultural heritage studies are presented in Papers IV–VIII and measurements on high-voltage insulators are presented in Papers IX and X.

3.3.3 Laser-induced breakdown spectroscopy

In laser-induced breakdown spectroscopy (LIBS), an intense, focused laser pulse is used to create a plasma containing excited atoms and ions. As the atoms relax, species-specific light is emitted and the chemical content of the sample can be analysed. LIBS can be performed on gaseous, liquid or solid samples and is a widely used method for elemental analysis. However, it is only possible to identify the elements in the sample, not how they are bound to each other. To determine the relative abundance of different elements in the sample, careful calibration is needed [44].

Remote LIBS will be discussed in Sect. 4.3.6. Such measurements were performed within the scope of this work, and the results are presented in Papers XI and XII.

3.4 Raman spectroscopy

The inelastic scattering process known as Raman scattering (see Sect. 3.2.2) can be used for spectroscopy. The wavelength shift in the Raman signal depends on the separation of the different rovibrational levels of the ground state. By employing Raman spectroscopy, it is possible to identify the chemical bonds in a sample.

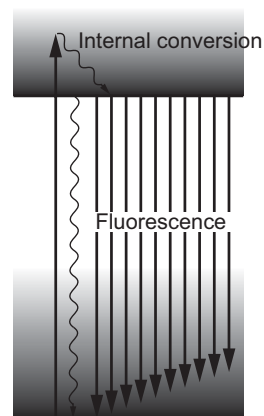


Figure 3.11. The fluorescence process in a solid material.

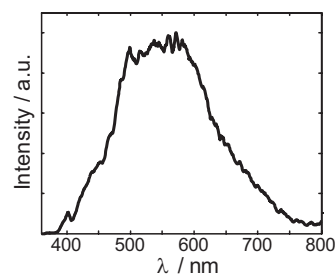


Figure 3.12. An example of a fluorescence spectrum from travertine. The excitation wavelength was 355 nm.

For example, the stretching of a C-H bond has a characteristic Raman shift and thus the molecular structure can be determined.

Raman spectroscopy is used in a variety of applications. For example, it has been used extensively in the cultural heritage context, to identify pigments and types of varnishes on paintings. It has even been possible to determine whether a painting is a fake or an original, by analysing the pigments used. The colour may look the same, but the Raman signal is different for different pigments [45]. The technique has also been used in medicine, for the discrimination of cancer lesions from healthy skin (see for example Ref. 46).

LIDAR

Lidar is an acronym for light detection and ranging, in analogy with the better known concept of radar (radio detection and ranging). In a radar measurement, a radio pulse is transmitted into the air. When the pulse hits, for example, an aeroplane, an echo is reflected. By detecting this echo, it is possible to determine the position of the aeroplane. In a lidar measurement, a short light pulse is transmitted into the air where it is scattered by particles and molecules. The backscattered light from the atmosphere can then be analysed to yield information on, for example, particle distributions. As will be discussed in Sect. 4.3, several different aspects can be studied with the technique.

4.1 System set-up

In this section, a brief description of a lidar system will be given. First, the general characteristics of a lidar system will be discussed. Then, the lidar system used in this work will be described.

4.1.1 A general lidar system

A lidar system generally consists of a pulsed laser, transmitting optics, a receiving telescope and a time-resolving detection system. The set-up of a general lidar system is shown in Fig. 4.1. A laser pulse is sent through the transmitting optics into the air. The transmitted light is scattered, and the backscattered light (for clarity indicated as red in the picture, although it usually has the same wavelength as the emitted light) is collected by a receiving telescope. The light is sent through an interference filter to block light at uninteresting wavelengths. This is necessary to reduce the noise from background light, as the measurements are often performed in daylight. The light then reaches the detector, which is

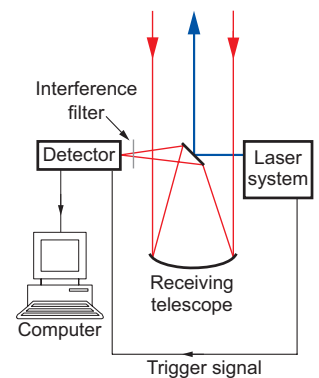


Figure 4.1. *The set-up of a general lidar system.*



Figure 4.2. *The Lund lidar system at a measurement campaign at Övedskloster.*

triggered by the laser, to make it possible to time the arrival of the backscattered signal.

Since photons travel at a known velocity (the speed of light), the time of arrival at the detector is a measure of how far they have travelled. It is usually assumed that the detected light has undergone only one scattering event. This is normally a valid assumption, as lidar systems are generally constructed with telescopes that have narrow fields of view. It is thus highly unlikely that a photon will be scattered out of the telescope’s field of view, be scattered back into the field of view and here be scattered towards the detector. However, for measurements in a foggy (i.e. highly scattering) environment this must be considered, although in most cases, multiple scattering can be ignored, as it will be throughout the theoretical description given below.

4.1.2 The Lund lidar system

The lidar system used in this work was developed at the Atomic Physics Division at Lund University. The system, on site during a measurement campaign at Övedskloster is shown in Fig. 4.2 and the general set-up is depicted in Fig. 4.3. The system is thoroughly described in Ref. 47. It was originally intended for Differential absorption lidar (DIAL) measurements (as will be discussed in Sect. 4.3.3), and is based on an OPO for creating coherent light at the desired wavelengths. The OPO system was modified to be able to perform fast wavelength switching by piezo-electric elements [37].

The light from the OPO is transmitted through a beam expander and sent to a computer-controlled folding mirror, which can be steered to transmit the light in the desired direction. The 40-cm-diameter Newtonian receiving telescope is coaxial with the outgoing beam. The light is then focused through an interference filter and onto a photomultiplier tube (PMT). The current to the PMT is ramped, to make it less sensitive to the early signals, which are larger as a larger part of the isotropic scattering is directed into the telescope’s field of view. This is done to reduce the requirement for a detector with a large dynamic range.

The system can also readily be used for fluorescence-lidar or remote-LIBS measurements by a change of detection system. The light collected by the telescope is guided through a long-pass filter, which blocks light of short wavelengths. The light is collected by an optical fibre placed at the telescope’s focal point. The light is transferred to an optical multichannel analyser (OMA) system where the fibre is connected to the entrance slit of a spectrometer connected to a gated and intensified CCD detector. The trigger signal from the laser is delayed and the detector is gated so as to be active only at the time of arrival of the signal. In this way, the background light can be efficiently reduced. The OMA system

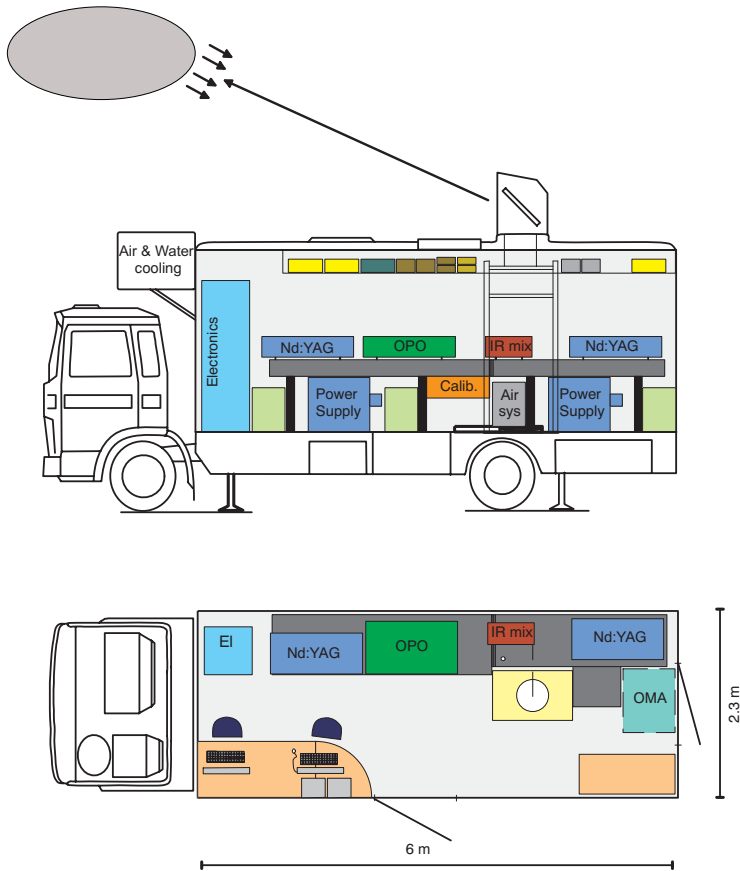


Figure 4.3. The setup of the lidar system used in this work (modified from [47]).

used in the measurements presented in Papers IV–XII is described in Ref. 48.

To perform LIBS measurements, the beam expander of the system had to be replaced, as it was not possible to focus the laser beam to a small enough spot using the original beam expander. A beam expander with a larger diameter was constructed for two different reasons. Firstly, with a larger beam diameter, it is possible to create a tighter focus at a given distance. This is due to the properties of Gaussian beams, described in, for example, Ref. 25. Secondly, the energy that can be transmitted from the lidar system is limited by the acceptance of the folding mirror. Too high pulse energies would burn the mirror. With a larger beam expander, it was possible to emit more energetic pulses as the energy was



Figure 4.4. A photograph of the two beam expanders; the smaller one used for DIAL and LIF and the larger one used for LIBS measurements.

spread over a larger area of the mirror. A photograph of the two beam expanders can be seen in Fig. 4.4.

The lidar system is mounted inside a Volvo F610 truck, allowing measurements to be performed at virtually any location. Obviously, the measurements performed within the scope of this work, as well as numerous earlier investigations, could not have been performed with a stationary system. Neither the mercury sources studied in Papers I–III, nor the buildings studied in Papers IV–VIII could have been moved, and thus a mobile system was required for these measurements.

4.2 Signals

As discussed in Sect. 3.1.4, light travelling through a medium will be absorbed according to Beer-Lambert’s law (Eq. (3.15)). The light may also be attenuated due to scattering, i.e., it is scattered in random directions and less light is left in the beam path. A general expression for the light transmitted a distance R through a medium is given by

$$I_t = I_0 e^{-\int_0^R \mu_a(\lambda, r) + \mu_s(\lambda, r) dr}, \quad (4.1)$$

where $\mu_a(\lambda, r)$ is the extinction coefficient due to absorption and $\mu_s(\lambda, r)$ is the extinction coefficient due to scattering. Unlike in Eq. (3.15), here it is not assumed that the medium is homogeneous, as both μ_a and μ_s depend on the range, r . $\mu_a(\lambda, r)$ is due to the absorption by different species i , according to:

$$\mu_a(\lambda, r) = \sum_i \sigma_i^A(\lambda) C_i(r), \quad (4.2)$$

where $\sigma_i^A(\lambda)$ is the wavelength-dependent absorption cross-section of species i and $C_i(r)$ is the range-dependent concentration of the species. $\mu_s(\lambda, r)$ depends on both Rayleigh scattering from molecules and Mie scattering from particles:

$$\mu_s(\lambda, r) = \sigma_m^S(\lambda) C_m(r) + \int_0^\infty \sigma_p^S(\lambda, x) C_p(r, x) dx. \quad (4.3)$$

$\sigma_m^S(\lambda)$ is the Rayleigh scattering cross-section and $C_m(r)$ is the range-dependent concentration of molecules. $\sigma_p^S(\lambda, x)$ is the Mie scattering cross-section, which is a function of wavelength and particle size, and $C_p(r, x)$ is the range- and particle-size-dependent particle concentration.

Consider a lidar system transmitting a laser pulse with intensity I_0 through air. In the air, there is a concentration of backscatterers $C_b(R)$ with backscattering cross-section σ_b . The concentration is not necessarily homogeneous, but depends on the distance,

R , from the system. In the small range segment ΔR , the probability that the light will be backscattered is then $\Delta R \times C_b(R) \times \sigma_b$. At a distance R , the light is isotropically scattered. Thus, the greater the range (R), the smaller the signal scattered into the field of view of the receiving telescope. This part is proportional to R^{-2} . Simultaneously, the light will be attenuated according to Eq. (4.1). The collected backscattered signal will thus be given by:

$$I(\lambda, R) = QI_0 \frac{C_b(R)\sigma_b\Delta R}{R^2} \times e^{-2\int_0^R \mu_a(\lambda,r) + \mu_s(\lambda,r) dr}. \quad (4.4)$$

Here, Q is a system constant, including the efficiency of the transmitting and receiving optics, the area of the receiving telescope, and other system-specific properties. The factor 2 in the exponential is due to the detected light travelling back and forth through the medium. The range resolution, ΔR , of the lidar system depends on either the pulse length or the time resolution of the detection system, whichever is longer. Eq. (4.4) is known as the lidar equation [39, 43].

4.3 Techniques and applications

Lidar systems can be used for various applications. This section provides an overview of different applications of lidars, and extra attention is paid to the techniques used in the present work. A thorough description on the latest trends in lidar technologies is given in Ref. 43.

4.3.1 Elastic lidar

The lidar equation, Eq. (4.4), contains information on the concentration of backscatterers, $C_b(r)$, that can be used to measure the particle distribution in the atmosphere. Normally, in these applications, only one wavelength is transmitted and only the elastic scattering is detected, thus the wavelength dependence of the parameters is, for the time being, neglected. In these applications, the lidar equation can be simplified by combining some of the terms in Eq. (4.4) and rewriting it as:

$$I(R) = \frac{K\beta(R)}{R^2} e^{-2\int_0^R \alpha(r) dr}. \quad (4.5)$$

There are two unknowns, the scattering coefficient $\beta(R)$ and the extinction coefficient $\alpha(r)$. These contain the information on the particle distribution. If there is a simple relation between $\alpha(r)$ and $\beta(R)$, Eq. (4.5) can be solved.

Various assumptions can be made to estimate the particle distribution from a received lidar signal. The Klett method [49]

can be used for dense particle distributions, while the Fernald method [50–52] is valid in thin atmospheric conditions. Other methods to deduce the aerosol distribution and to obtain information on particle shapes include multiple wavelength measurements and polarization-sensitive detection [43, Chap. 3].

4.3.2 Temperature lidar

Atmospheric temperature profiles can be measured using lidar techniques. This can be achieved by Rayleigh lidar, where the atmospheric molecular density, which is temperature dependent, is measured. The height-dependent pressure, $p(h)$, is given by the ideal gas law:

$$p(h) = \frac{\rho(h)T(h)R}{M}, \quad (4.6)$$

where $\rho(h)$ is the density of molecules, $T(h)$ the temperature, R is the universal gas constant and M is the molecular weight. For small changes in height, the pressure is usually constant over the measurement time and a change in temperature can be found by monitoring the change in density. By combining Eq. (4.6) with the condition of hydrostatic equilibrium, the temperature at a certain height can be found from the relation:

$$T(h) = \frac{\rho(h_1)RT(h_1) + \int_h^{h_1} Mg(z)\rho(z)dz}{\rho(h)R}, \quad (4.7)$$

where h_1 is the maximum altitude. $T(h_1)$ is usually estimated and its value quickly becomes of little significance when calculating the temperature step-wise downwards.

Rayleigh lidar depends solely on molecular scattering, and can, with low-resolution systems, only be used when aerosol scattering is negligible. Measurements below ~ 30 km are usually not considered accurate enough. An alternative is to measure the atmospheric density using a Raman signal from O_2 or N_2 . These signals are independent of the aerosol scattering and thus temperatures can be evaluated at lower altitudes [39, 53, 54].

Another way to measure temperature profiles is to use the fact that the population of the close-lying ground state energy levels is temperature dependent, due to Boltzmann statistics (see Sect. 3.1.3). At high temperatures, many of the close-lying energy levels in the ground state will be populated, and by comparing the absorption of transitions from two ro-vibrational levels in the ground state, the temperature can be evaluated [39, 55, 56].

For temperatures at very high altitudes (70–120 km), resonance fluorescence can be utilized. In such measurements, the resonant fluorescence from metal atoms, e.g. Na, (probably originating from meteor ablation) is measured. This signal will be Doppler

broadened to an extent depending on the temperature. Collisional broadening can be neglected as the pressure at these altitudes is very low [43, Chap. 5].

4.3.3 Differential absorption lidar

Differential absorption lidar (DIAL) can be used to measure concentrations of trace elements in the atmosphere. Two different wavelengths are transmitted to the atmosphere and are scattered by various particles. The wavelengths are chosen such that one of them will be absorbed by the species to be studied, while the other is slightly off the absorption peak; see Fig. 4.5. The wavelengths must be close enough to each other, to be able to assume equal atmospheric scattering properties. In reality, it is probable that both wavelengths will be partly absorbed, but there will be a difference in absorption between the two wavelengths.

When measuring the lidar return at two different wavelengths, the lidar equation can be applied to each of the wavelengths:

$$I(\lambda_{on}, R) = QI_0 \frac{C_b(R)\sigma_b\Delta R}{R^2} \times e^{-2\int_0^R \mu_a(\lambda_{on}, r) + \mu_s(\lambda_{on}, r) dr}$$

$$I(\lambda_{off}, R) = QI_0 \frac{C_b(R)\sigma_b\Delta R}{R^2} \times e^{-2\int_0^R \mu_a(\lambda_{off}, r) + \mu_s(\lambda_{off}, r) dr}. \quad (4.8)$$

By forming the ratio between the two signals, many of the unknown factors are eliminated;

$$\frac{I(\lambda_{on}, R)}{I(\lambda_{off}, R)} = e^{-2\int_0^R \mu_a(\lambda_{on}, r) - \mu_a(\lambda_{off}, r) + \mu_s(\lambda_{on}, r) - \mu_s(\lambda_{off}, r) dr}. \quad (4.9)$$

Since the wavelengths chosen are close to each other, the scattering can be considered to be the same for both wavelengths, i.e. $\mu_s(\lambda_{on}, r) = \mu_s(\lambda_{off}, r)$, and these terms cancel. Thus, by using Eq. (4.2), assuming there is only one absorbing species,

$$\frac{I(\lambda_{on}, R)}{I(\lambda_{off}, R)} = e^{-2(\sigma^A(\lambda_{on}) - \sigma^A(\lambda_{off})) \int_0^R C(r) dr}. \quad (4.10)$$

This equation is known as the DIAL equation. By introducing the differential absorption cross-section $\Delta\sigma^A$:

$$\Delta\sigma^A = \sigma^A(\lambda_{on}) - \sigma^A(\lambda_{off}), \quad (4.11)$$

it follows that:

$$\int_0^R C(r) dr = \frac{1}{2\Delta\sigma^A} \ln \frac{I(\lambda_{off}, R)}{I(\lambda_{on}, R)} \quad (4.12)$$

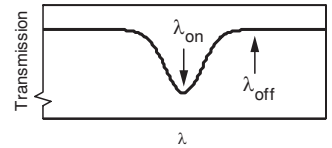


Figure 4.5. In a DIAL measurement, the laser wavelengths are chosen on and off the absorption peak of the species to be investigated.

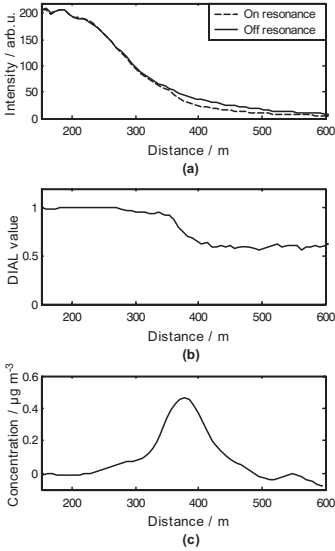


Figure 4.6. DIAL measurements of mercury from a chlor-alkali plant. In (a), the lidar curves at the on and off wavelengths are seen, (b) shows the DIAL curve, and (c) is the evaluated concentration along the laser beam path.

and

$$C(R) = \frac{1}{2\Delta\sigma^A} \frac{d}{dR} \ln \frac{I(\lambda_{off}, R)}{I(\lambda_{on}, R)}. \quad (4.13)$$

Hence, the range-resolved concentration of the measured substance can be evaluated [57].

In a DIAL measurement, it is usually necessary to average over several laser shots. As the scattering conditions in the atmosphere constantly change, it is important not to measure the *on* wavelength first and the *off* wavelength later. By changing the wavelength between consecutive shots, this problem is overcome.

Fig. 4.6 shows data on mercury concentrations obtained from a factory outside Gothenburg in Sweden. Fig. 4.6a shows the backscattered signal at the *on* and *off* wavelengths (Eq. (4.8)), b shows the calculated DIAL curve (Eq. (4.10)) and c shows the evaluated concentration (Eq. (4.12)).

In the measurements presented in Papers I–III the DIAL technique was used for measurements of elemental mercury from different sources. Papers I and III deal with mercury emissions from chlor-alkali plants, while Paper II considers the emissions from an abandoned mercury mine. The measurements were performed using an OPO to create the *on* and *off* wavelengths at around 253.65 nm.

4.3.4 Wind lidar

Molecules and particles move in random directions, but in a wind they will have a net velocity equal to the wind velocity. Light scattered off moving particles will exhibit a frequency shift due to the Doppler effect, as described in Sect. 3.1.2. By measuring this very small frequency shift, Doppler lidar can be used to evaluate the wind speed along a certain direction [43, Chap. 7]. This technique was used in Paper III to compare wind measurement techniques in connection with DIAL measurements of mercury fluxes.

4.3.5 Fluorescence lidar

Remote laser-induced fluorescence on a solid target is often referred to as fluorescence lidar, although it is not a strict lidar measurement, as the signal is received only from a certain distance. The target is excited using an ultraviolet laser beam and the resulting fluorescence is radiated from the target. The fluorescence light can be collected using a telescope, and guided to a spectrometer system to measure the spectral shape of the fluorescence signal. As discussed in Sect. 3.3.2, the fluorescence spectra from solid materials seldom consist of any sharp features, but instead exhibit a slowly varying distribution.

The spectrum is usually not heavily affected by a slight change in the exciting wavelength, although there may be some differences

depending on the energy needed to hit different excitation bands in different species. Generally, with a shorter excitation wavelength, more features are seen, as shorter wavelengths can be detected.

In the set-up used for the measurements presented in Papers IV–X, the light gathered by the telescope was sent through a long-pass filter to block the specular reflection from the surface. The remaining fluorescence light was then collected by an optical fibre. The fibre guided the light to the entrance slit of a spectrometer, which was connected to a gated and intensified CCD camera. Gating the detector, allows detection only at the known arrival time of the short fluorescence pulse, which is important for noise reduction. Without gating, fluorescence lidar measurements would have to be performed at night, with as little ambient light as possible. With gating, measurements can readily be performed in full daylight. When excitation is performed using a laser pulse of 5–10 ns, gating times of 50–100 ns can be used without any signal loss.

Fluorescence imaging can be achieved by scanning the laser beam over an area and collecting the fluorescence spectrum at several spots. In this way, large areas can be monitored, and the spectra can be compared to find points with similar chemical contents. Especially when measurements are performed with a large area laser beam, several fluorophores (fluorescing substances) contribute to the detected signal, and it might not be possible to separate these to precisely evaluate the content of the detected spot. However, much information can be extracted by comparing data from different spots [43, Chap. 6].

4.3.6 Remote laser-induced breakdown spectroscopy

As was discussed in Sect. 3.3.3, LIBS is a method widely used for the investigation of the elemental composition of samples. The technique is illustrated in Fig. 4.7. An intense laser pulse is focused onto a surface and, as the highly focused light breaks the bonds in the material, a small plasma is produced (Fig. 4.7a). The plasma contains free atoms and ions, excited by the high intensity laser pulse. As the plasma cools down, the atoms and ions relax to their respective ground states, emitting species-specific light (Fig. 4.7b). By analysing the sharp spectral features, it is possible to identify the constituents of the sample. Fig. 4.8 shows a spectrum obtained from a brass plate, in which the copper and zinc peaks are labelled. Some slight sodium contamination can also be seen.

Although conventionally used in laboratory set-ups, the LIBS method can be extended to remote applications by transmitting a laser beam through air and focusing it onto a target. The emitted light can be collected in the same manner as fluorescence light (described in Sect. 4.3.5) and a spectrum can be collected [58, 59].

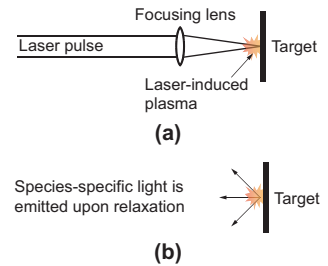


Figure 4.7. A laser pulse is focused onto a target and a laser plasma is created (a). The plasma contains free atoms and ions that emit species-specific light upon relaxation (b).

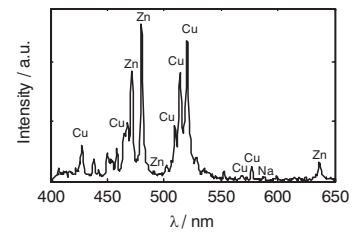


Figure 4.8. A spectrum from a brass plate, in which copper and zinc peaks are identified. Some sodium contamination can also be seen.

It is necessary to block the specular reflection, but unlike fluorescence measurements, shorter wavelengths than the exciting one can occur. This is possible since the atoms are not excited primarily due to absorption of single photons, but rather from the heat generated by the intensely focused light [44].

Remote LIBS imaging is reported in Papers [XI](#) and [XII](#). In these measurements, the target was 60 m away from the lidar system and the laser was focused onto the target. By scanning the laser beam over the target, it was possible to create an elemental map. The greatest challenge in these measurements was to focus the laser to a small enough spot to achieve breakdown at such a large distance, as a longer focal length results in a larger focus. Also, problems may occur due to spherical aberration in the focusing optics. If the distance to the target changes during the scan, the target will move out of focus which may result in breakdown not being achieved.

An alternative is to use self-focused laser filaments created by intense ultra-short (femtosecond) laser pulses [60]. Such laser filaments can remain focused over great distances and thus the distance to the target is not critical. This would make remote LIBS imaging easier to perform, but femtosecond lasers are more difficult to handle, and eye-safety issues are challenging. Applications in the cultural heritage field can be found, e.g. in Ref. [61](#).

Soiled areas on, for example, buildings can be cleaned by the ablative power of an intense laser. Such systems exist as commercial products and are frequently used in the restoration of monuments and works of art, for example, the cleaning of St. Stephen's Church in Vienna [62]. However, these systems only work at short ranges. On the other hand, the set-up used for remote LIBS measurements can be used for remote ablative cleaning, as discussed in Paper [XI](#). Although the signals in the tests reported in the aforementioned paper were not strong enough, a possible application is remote cleaning with spectroscopic control, i.e. changes in the LIBS spectrum can be detected when the contamination has been removed. In this way, large areas could be cleaned by scanning the laser beam from a distant position, while spectroscopic control would prevent undesired damage to the surface. This has been realized in close-range applications [63].

4.4 Sources of error

There are sources of error in all types of measurements. Important sources of noise in lidar applications are typically background light or electronic noise in the detectors. These errors are usually random in nature. In this section, however, some systematic errors, their causes and possible ways to control them, for firstly

DIAL measurements and, secondly, fluorescence and LIBS measurements, will be discussed.

4.4.1 DIAL

Laser stability and linewidth

When performing a DIAL measurement, it is important that the laser wavelengths match the transition studied. Fig. 4.9 shows different situations. Fig. 4.9a shows the desired case, one wavelength is on the peak of the absorption feature, while the other one is completely off. If the laser wavelength starts to drift, the absorption cross-section changes. In the case shown in Fig. 4.9b, both wavelengths have drifted off the absorption feature and the differential absorption is lowered, resulting in a measurement of too small a concentration. Fig. 4.9c shows a case where the *off* wavelength has drifted onto the absorption peak. In the special case shown here, the *on* and *off* wavelengths are equally absorbed, which means that the absorption cross-section is zero and no concentration whatsoever is measured. An extreme case is shown in Fig. 4.9d, in which a negative concentration will be measured, which will definitely warn the operator that something is wrong.

Obviously, a stable laser system is important for DIAL measurements. In the measurements presented in Papers I–III, an automatic calibration system was used. The measurements were performed on atmospheric mercury, and internal mercury cells were used to calibrate the measurements. A small part of the laser beam was sent through the calibration cells. By measuring the absorption difference through the known amount of mercury in the cell, laser instability was immediately observed and could be compensated for.

In the discussion above, it was assumed that the laser linewidth is infinitely small. This is generally not the case, but this causes no problems as long as the laser linewidth is very small compared to the absorption linewidth. If the laser linewidth is too large, errors are introduced as contributions from both on and off the absorption line are measured with the *on* wavelength (and possibly also with the *off* wavelength), which will distort the results. Fig. 4.10 depicts a situation with large laser linewidth. Although the central wavelengths of the laser pulses are perfect, their linewidths will cause an erroneous measurement.

Fluorescence

In a DIAL measurement, it is assumed that the energy absorbed by the pollutant atoms or molecules in the air is lost due to collisions. However, the energy may also be reemitted as resonance fluorescence. Fluorescing species will be interpreted as backscat-

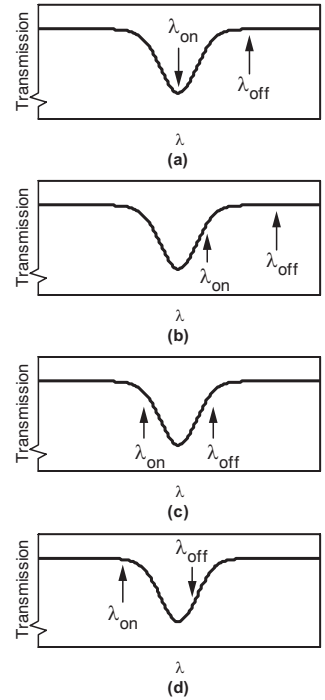


Figure 4.9. In DIAL measurements laser stability is critical. (a) shows the ideal case, (b) indicates a situation when too small a concentration is measured, (c) a situation where no concentration at all is measured and (d) a case where a negative concentration is measured.

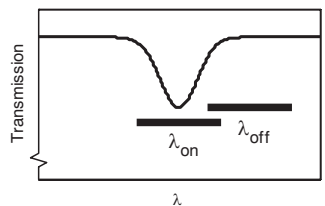


Figure 4.10. A laser linewidth that is of the same order of magnitude as the absorption linewidth will cause problems during DIAL measurements, as the absorption cross-section is not the same for the entire laser pulse.

tered photons and may thus cause errors in the calculation of the concentration.

With sufficient knowledge of the measurement situation, the fluorescence can be accounted for. A thorough investigation of this phenomenon is presented in the Appendix of Ref. 64. The calculated total concentration along the beam path is the same even without compensation, although the concentration is spatially displaced. Resonant fluorescence is quite easily discovered in the raw data. When fluorescence occurs, it may cause the backscattered signal of the *on* wavelength to increase. This corresponds to a negative concentration, which is not physically possible, and is easily recognisable.

Saturation

When measurements are performed with high-energy laser pulses, many of the trace gas atoms/molecules are excited and when half of them are excited, the probability of stimulated emission will be equal to the probability of absorption. This is not of great concern for molecular measurements, as the transition probabilities are low, but for atomic pollutants (i.e. mercury) special care must be taken. If light is absorbed and the atoms relax by stimulated emission, no absorption is recorded as the same amount of light is forward-transmitted through the pollution. The assumptions on which the concentration measurements are based are then no longer valid and an erroneous result may be obtained. To avoid this in practical measurements, it is important not to transmit pulses with too high an energy.

4.4.2 Fluorescence and LIBS

In the measurements performed in this work, most fluorescence measurements were relative, rather than absolute. This means that the analysis comprised comparison between different spectra acquired with the same set-up. By limiting the analysis in this manner, systematic errors will generally not be a problem as they will be similar in all spectra. Some types of error that may occur in these types of measurements, will, however, be discussed below.

Calibration

If a comparison is to be made with other measurement set-ups, spectra must be white-light calibrated. A calibrated lamp is used and its output is measured using the same optical set-up as in the measurements. As the lamp is calibrated, its spectral signal is known and thus the measured spectrum can be rectified. The same rectification is then applied to all spectra, making comparisons with data from other systems possible.

In a LIBS measurement, it is important that the wavelength scale is properly calibrated, as the spectrum is compared with tables of spectral lines to determine the elemental content of the target. Calibration can be performed by measuring the output from an atomic lamp and correcting the scale to fit the measured wavelengths to the known correct ones. In the measurements presented in Papers [XI](#) and [XII](#), the wavelength calibration of the detection system was refined to include a quadratic term.

Positioning control

In a fluorescence lidar or remote LIBS imaging measurement, the exact position of the points investigated may be important. Usually, however, measurements are performed on areas with large, relatively homogenous, sections, in which case it is not critical. However, the position may be important, for example, when making measurements on a brick building, it is necessary to know if the laser spot hits a brick or the mortar between them.

In the measurements presented in Papers [IV–XII](#), visual positioning of the end points of the scans was performed, and the intermediate points are assumed to be equidistant. This is correct to some extent, but there may be some slack in the stepper motors controlling the direction of the outgoing beam, causing minor positioning errors. The system developed by the fluorescence lidar group in Florence, Italy, uses a coaxial visual laser for position control, as described in Paper [V](#). A camera takes pictures with the visible laser spots, creating a grid of the measured points.

DATA ANALYSIS

Measurements of the types discussed in this thesis generate large amounts of data that need to be analysed. In presentations of the results, raw data are not interesting, but extraction of relevant information from the data is required. In this chapter, the analysis methods used are described.

5.1 Flux determination using DIAL

When performing a DIAL measurement, the concentration can be evaluated by applying Eq. (4.13), as discussed in Sect. 4.3.3. The concentration along the laser beam direction can then be determined. The concentration at each point in a plane can be found by scanning the laser beam in that plane, and interpolating between the measured data. If this is performed on a cross-section of a pollution plume, down-wind from an emission source, as depicted in Fig. 5.1, the flux can be found by multiplying the area-integrated concentration by the wind speed perpendicular to the scanning plane. Measuring the pollutant flux from a distributed source is the main advantage of the DIAL method. Local concentrations can be measured more precisely with other methods, but for fluxes, these methods usually have to resort to assumptions. An example of a measured concentration map of mercury at an Italian chlor-alkali factory is shown in Fig. 5.2.

When measuring fluxes, special consideration must be taken of resonant fluorescence, which was discussed in Sect. 4.4.1. If not corrected for, the fluorescence may make the concentration appear further away from the lidar system than it is. As the concentration is interpolated between the measured directions, there will be a larger area of calculated concentrations, resulting in too large an integrated concentration. This may cause an increase in the measured flux, but in reality it is a small effect.

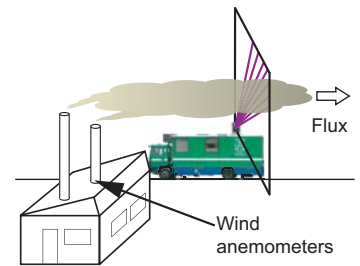


Figure 5.1. DIAL measurements of fluxes can be performed by scanning the laser beam over a cross-section of the pollutant plume and combining the results with wind data.

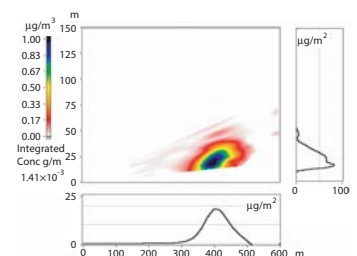


Figure 5.2. An experimental concentration map of elemental mercury. The x-axis represents metres horizontally and the y-axis metres vertically from the system. The colour bar indicates the pollutant concentration. The horizontal and vertical distribution profiles are also shown.

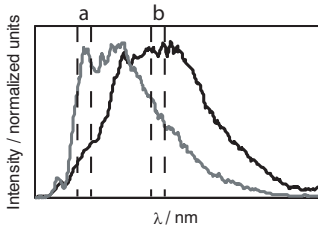


Figure 5.3. Two spectra with different shapes. The spectra may be separated by a ratio, a/b , between the spectral bands a and b indicated in the figure.

When calculating the flux, the integrated concentration is multiplied by the wind speed perpendicular to the scanning direction. Thus, it is important that both the wind velocities and the concentrations are accurately measured. When considering a disperse source, it is not certain that the wind velocity is constant over the entire concentration, which complicates the situation.

In the measurements presented in Papers [I–III](#), mercury fluxes were determined. The wind data were obtained from wind vanes and anemometers placed as close as possible to the pollution source. Additionally, a Doppler lidar system for wind measurements was employed and the results were compared to those obtained from the wind vanes (Paper [III](#)).

5.2 Fluorescence imaging

When performing fluorescence or LIBS imaging, the result is a spectrum from each measurement point. Thus, the resulting data are four-dimensional (two spectral dimensions and the spectral intensity as a function of wavelength), and it is difficult to immediately gain an overview of the results. Data analysis is required to reduce the dimensionality of the data.

It is usually desirable to reduce the spectral dimension to a single value, in which case the values can be false-colour imaged and superimposed on a photograph of the measured area. Areas with similarities or differences in their spectra can then easily be seen. There are several ways of reducing spectra to single values. Those used for fluorescence diagnostics will be discussed in this section, while the analysis of LIBS spectra will be discussed in the following section. The analysis methods discussed here were used in Papers [IV–XII](#) and are also described in Paper [XII](#).

5.2.1 Ratios

The most straightforward way to produce a single value from a fluorescence spectrum is to consider its intensity in a certain wavelength band. However, although different materials may fluoresce with different strengths, the absolute fluorescence intensity may depend on several factors that cannot easily be controlled, such as fluctuations in the laser intensity, distance, and laser angle of incidence on the target. Thus, it is desirable to work with dimensionless quantities or normalized spectra, thereby considering only the spectral shape.

By forming a ratio between the intensities in two different wavelength bands, certain aspects can be emphasized. However, it is necessary that the data-set be thoroughly investigated to ensure a suitable choice of wavelength bands. Consider, for example, the spectra shown in Fig. [5.3](#). The ratio a/b between two wavelength

bands a and b , as indicated in the figure, will differ in the two spectra.

Certain substances possess characteristic fluorescence features, one such substance is *chlorophyll a*, which has relatively sharp fluorescence features in the near-infrared wavelength region. This feature consists of two peaks, one at around 685 nm and one at around 735 nm, although they are not always both present. The type of plant and its condition may cause a difference in the balance between the two fluorescence peaks [65].

To emphasize spectra containing chlorophyll, different choices of functions may be considered. For example, the function $F = a/b$, as indicated in Fig. 5.4a might be a good choice. However, there may be situations where the flank of a spectrum without the chlorophyll peak is large and thus the function may give a high value for a spectrum not containing chlorophyll.

Another alternative is chosen in Fig. 5.4b. Here, the ratio between the chlorophyll peak and the part where the chlorophyll is supposed to be very low is chosen. This may, however, give a high result for a very noisy spectrum, where both the a and b wavelength bands have very low values.

A third choice is illustrated in Fig. 5.4c. Here, three wavelength bands are used and the function

$$F = \frac{a - b}{c} \quad (5.1)$$

is formed. This is also a dimensionless quantity, although it is not a ratio in its simplest form. By using this function, neither the spectra with the high flank, nor the noisy spectra will constitute a problem. This is therefore a good choice of discrimination function for chlorophyll. An example of this function applied to a scan is shown in Fig. 5.5.

Forming functions is a powerful way of emphasizing certain aspects of a spectrum and thereby differentiating certain spectra from others. However, it is required that it is known what distinguishes the spectra sought from the rest of the spectra in the scan, which may be a time-consuming task to find out. Also, spectra with high values are known to be similar within the wavelength bands chosen, but they may be different from other aspects. Thus, methods that automatically can single out spectra with certain shapes are in demand. In the following sections, two such methods will be discussed.

5.2.2 Linear correlation

A spectrum can be reduced to a single value by choosing a reference spectrum and performing a linear correlation between the reference spectrum and all spectra within a scan. The correlation value is a measure of how similar the spectra are. In this way, areas with

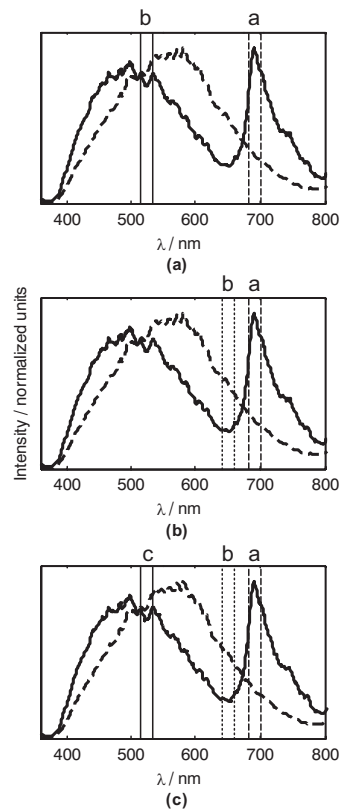


Figure 5.4. Three different functions that may be used to distinguish chlorophyll fluorescence from spectra without the peak. (a) indicates a ratio (a/b) between the peak value and the autofluorescence, (b), shows how to construct a ratio (a/b) between the chlorophyll peak and the lowest value (at around 650 nm). Finally, (c) shows how a function $((a - b)/c)$ between three different wavelengths can be formed.

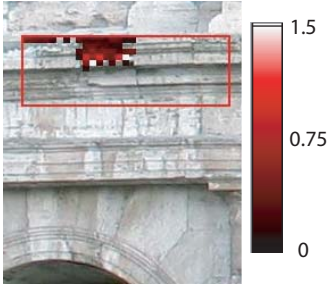


Figure 5.5. A scan over an area containing chlorophyll. A function of the type in Eq. (5.1) was used and the values are mapped out over the area (modified from Paper V).

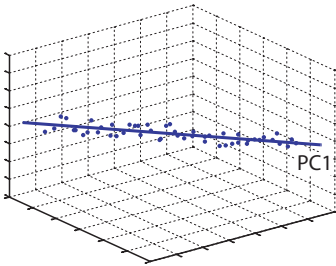


Figure 5.6. A data-set in three-dimensional space may be reduced to one dimension by changing the coordinate system.

similar fluorescence features can easily be found. The correlation value, r , is given by:

$$r = \frac{\sum_i (\mathbf{X}_i - \bar{\mathbf{X}}) (\mathbf{Y}_i - \bar{\mathbf{Y}})}{\sqrt{\sum_i (\mathbf{X}_i - \bar{\mathbf{X}})^2 \sum_i (\mathbf{Y}_i - \bar{\mathbf{Y}})^2}}, \quad (5.2)$$

where \mathbf{X} is the reference spectrum and \mathbf{Y} the examined spectrum. $\bar{\mathbf{X}}$ and $\bar{\mathbf{Y}}$ are their mean values.

The correlation value, r , will always be between -1 and +1. Two identical spectra will have a correlation of +1, and two negatively correlated spectra will have a correlation of -1. Totally uncorrelated data (for example two sets of white noise) are expected to have a correlation value of 0.

Correlation imaging is a quick way to identify similar spectra in a data-set and to identify areas that are distinctive. It is thus an ideal way of starting the analysis of data from a new area. By browsing through the spectra, and performing correlation with different spectra from the scan as reference spectra, different groupings in the data can easily be found and demarcated. Note, that it is not known in what way spectra with low correlation values differ, and two spectra, neither of which correlates with a reference spectrum, are not necessarily correlated to each other.

5.2.3 Principal component analysis

Principal component analysis (PCA), as further discussed in Ref. 66, is a statistical method used to reduce the dimensionality of data. A spectrum consists of a large number of values, i.e. the number of pixels in a linear array detector. The pixel values are usually highly correlated, i.e. one value is highly dependent on its neighbouring pixel values. This means that in, for example, the 1024 channels in each spectrum, there is a great deal of redundant information that can be eliminated by PCA.

The basic principle is described by the example data-set illustrated in Fig. 5.6. Each dot represents a measured value, and there are three variables for each measurement. It can be seen that the points are correlated, as they lie along a line in three-dimensional space. This may not be obvious in cases with more variables, where it is not possible to easily make this kind of plot. By changing the coordinate system to the direction of largest variance in the data, only one variable is needed to almost entirely describe the data. This is the main idea behind PCA.

In the case of spectra, every measurement is described by a point in a 1024-dimensional space (assuming the detector has 1024 pixels). By using PCA, the dimension of the space can be reduced to a much smaller number, usually only 3-10 variables, by assigning

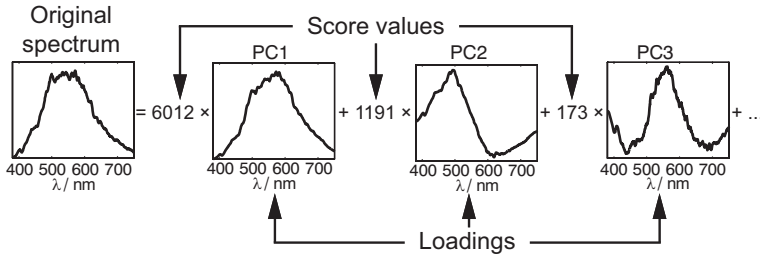


Figure 5.7. A spectrum can be reduced to only a few different values by PCA. The loadings are the same for all spectra involved in the analysis, while the score values describe each spectrum.

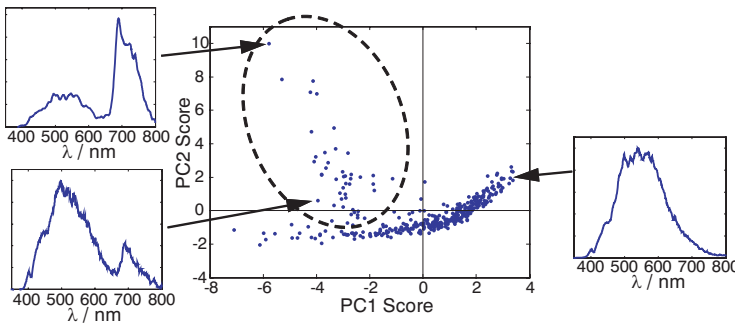


Figure 5.8. A score plot from a fluorescence imaging scan. The circled data points correspond to spectra containing chlorophyll.

a new set of orthogonal base vectors, known as principal components (PCs). The first principal component (PC1) is chosen along the direction of largest variance within the data. PC2 is perpendicular to PC1 and along the direction of the largest remaining variance, and so on. It is possible to create as many PCs as there were variables to begin with, but the most significant data will be in the first ones, the last ones describe only noise.

Each measurement (or data point) is finally described by its values along each PC, known as its score values, α . The relationship between the original variables and the PCs are known as loadings, ϕ . Each loading will describe how much of each original variable has contributed to the PC. Each spectrum can then be described by its PC scores and loadings.

$$\mathbf{X} = \sum_i \mathbf{X}_i = \sum_j \alpha_j \phi_j. \quad (5.3)$$

The relation described in Eq. (5.3) is depicted in Fig. 5.7. By using

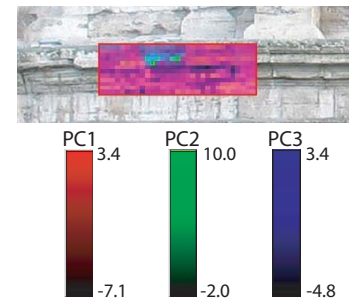


Figure 5.9. A PCA-RGB false-colour-coded analysis superimposed on a photograph of the measured area. This is the same area as depicted in Fig. 5.5. By comparing the two pictures, it can be seen that the chlorophyll features appear in PC2 and PC3, which are here shown as green or blue pixels.

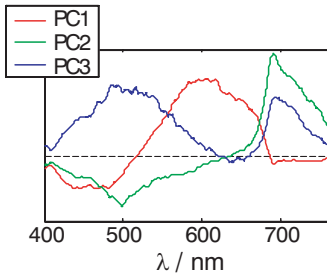


Figure 5.10. The loadings corresponding to the PCA analysis shown in Fig. 5.9. It can be clearly seen that the chlorophyll peak appears in PCs 2 and 3.

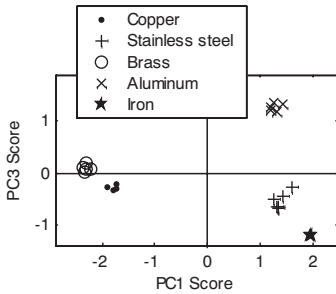


Figure 5.11. A score plot from a LIBS imaging measurement on metal plates. As can be seen, the different metals are efficiently discriminated. Modified from Paper XII.

this method, the spectra can be described by only a few variables, i.e. the PC scores, making the analysis much easier.

A score plot, i.e., a graph in which the scores along one PC are plotted against the scores along another, can be used to find groupings within the data. However, it may be necessary to study more than one score plot to find all the groupings in a data-set. An example of a score plot of an area containing chlorophyll is shown in Fig. 5.8. A few examples of the spectra are also shown in the figure. The points that are encircled can be approximately assigned to spectra containing chlorophyll.

When trying to emphasize different aspects of the data it is possible to construct ratios or functions of the PC scores, in the same manner as described in Sect. 5.2.1. Another way is to assign three PC scores to the colour values of red, green and blue and thus form a PCA-RGB false-colour image. This is an efficient way to simultaneously identify all the different areas that are similar to each other. Fig. 5.9 shows a PCA-RGB analysis of the same data-set as in Fig. 5.5. It can be seen that the chlorophyll content is represented by PC2 and PC3, corresponding to green and blue colours, respectively. The loadings of this analysis are shown in Fig. 5.10, where it can also be seen that the chlorophyll peak at around 690 nm occur in PC2 and PC3.

5.3 LIBS imaging

The same type of analysis as for fluorescence imaging data can be used for LIBS imaging measurements. It is usually easier to discriminate LIBS spectra than fluorescence spectra as they are more characteristic.

For simple situations, the intensity at a certain wavelength can be used to identify spectra that are similar, i.e. that originate from the same element. However, there may be coincidences between spectral peaks, leading to errors. Also, a certain element may be a constituent of several different materials in the area studied, and in such cases other parts of the spectra have to be included. Ratios or more complicated functions can be utilized.

Correlation analysis is very efficient for LIBS imaging. Similar spectra give high correlation values, while different ones differ so much that they have very low correlation values. PCA analysis is also efficient, as can be seen from the score plot in Fig. 5.11. A thorough description of LIBS spectral analysis is provided in Paper XII.

CONCLUSIONS AND OUTLOOK

6.1 Conclusions

The work presented in this thesis can be divided into two distinct parts, atmospheric measurements and remote measurements of the properties of different surfaces. Measurements of atmospheric pollutants, specifically mercury, can provide important information on the flux of contamination to the air – information that is difficult to obtain with other methods.

Fluorescence measurements were performed with cultural heritage applications. The measurements could be used for the assessment of the state of the façades, and could also reveal information on the constituent materials. It was also possible to find areas with similar surface characteristics. Fluorescence measurements were also performed on electrical insulators, to find biological growth on them.

Moreover, the remote LIBS imaging method has been developed. The technique, which may need further development before being employed at historical sites, may prove to be complementary to fluorescence imaging.

6.2 Outlook

During the course of this work, several ideas arose regarding new applications of the lidar technique. There was, however, insufficient time to pursue all of them. Two such ideas are presented below.

6.2.1 Multiple-scattering DIAL

In ordinary DIAL measurements multiple scattering is neglected. Under normal atmospheric conditions, only single-scattering events are considered, as there is a very small probability that

a multiply scattered photon will be detected. However, in foggy conditions, multiple scattering will no longer be negligible.

Under these conditions it is not possible to perform ordinary lidar measurements, as it is not possible to determine the volume that has been probed. However, if a DIAL measurement of oxygen is performed and off-axis measurements are made, it would be possible to extract information on the atmospheric scattering conditions. Polarized measurements can also provide important information as polarization is maintained during single backscattering from a spherical particle, whereas for multiple scattering it is not.

Another alternative is to measure the gas content inside a solid scattering material, for example snow. This may provide a way to detect avalanche victims due to the increased carbon dioxide levels in the snow around a breathing person using a helicopter-based system. It could also be used to detect leaking natural gas pipelines through elevated methane concentrations in snow covering the pipelines.

Activities have been initiated to combine two techniques that have been pursued at the Atomic Physics Division: the lidar technique, discussed in the present thesis, and the GASMAS (gas in scattering media absorption spectroscopy) technique [67, 68]. Measurements of free gas inside scattering media can be performed with the GASMAS technique and applications range from drying processes [69] to food processing and packaging industry [70]. Further aspects of the links between the lidar and GASMAS techniques are presented in Paper XIII.

Preliminary attempts to realize this method have been initiated, by sending a laser pulse into a block of highly scattering material, in this case polystyrene foam, and attempts have been made to detect the returning signal in different collecting geometries. For example, off-axis detection can be applied, or a crossed polarization filter can be used to attenuate the specular reflection but afford enhanced transmittance to light that has undergone multiple scattering. A beam stop at the centre of the image plane of the receiving telescope is another way of reducing the surface reflection and increasing the possibility to detect the much weaker signal from the multiply scattered light [71].

6.2.2 Remote Raman spectroscopy

Raman spectroscopy for remote sensing of, for example, building façades, can give information on the chemical bonds in the surface layer, as discussed in Sect. 3.4. This could be complementary to fluorescence and/or LIBS measurements. However, it is a complicated task to detect the weak Raman signal in remote applications as it is situated spectrally close to the specular reflection. It is thus important to use a sharp filter to block the reflection, but still be

able to receive the Raman signal. Remote Raman systems have been developed for future employment in planetary expedition applications [72].

A special feature of using an OPO is the ability to measure the fluorescence spectrum with two different wavelengths, with a superimposed Raman signal. Although it may be difficult to discriminate the Raman signal from the fluorescence in measurements with one wavelength, the fluorescence is expected to be the same, but the Raman line will shift accordingly when changing the excitation wavelength slightly. Thus, by using two wavelengths, the difference or the ratio of the curves can be formed, eliminating the fluorescence background but leaving a derivative-shaped Raman signal.

COMMENTS ON THE PAPERS

I Elemental Mercury Emissions from Chlor-Alkali Plants Measured by Lidar Techniques

This article describes our contribution to an EU project regarding mercury emissions from chlor-alkali plants, and the effect on people living in the surrounding areas. DIAL techniques were used to measure the mercury flux from three different plants in Sweden, Italy and Poland, in both summer and winter campaigns. I participated in the second half of the project and was thus involved in the practical work at three field campaigns. I performed the analysis of this data and prepared the manuscript.

II Mercury Emissions from the Idrija Mercury Mine Measured by Differential Absorption Lidar Techniques and a Point Monitoring Absorption Spectrometer

In this article, a measurement campaign at the Idrija mercury mine is described. DIAL techniques were used to measure fluxes, and concentrations were measured using a hand-held spectrometer system. I participated in the field campaign, I performed the analysis of the DIAL data, and I wrote the major part of the manuscript.

III Joint Application of Doppler Lidar and Differential Absorption Lidar to Estimate the Atomic Mercury Flux from a Chlor-Alkali Plant

This paper describes DIAL measurements of mercury and simultaneous wind measurements with a Doppler lidar system, to estimate the flux from the factory complex. A comparison was made between the Doppler lidar measurements and wind vane and anemometer data. I participated in the DIAL measurements, and assisted in data analysis and manuscript writing.

IV Fluorescence Lidar Multispectral Imaging for Diagnosis of Historical Monuments – Övedskloster, a Swedish Case Study

This article describes results from a three-day fluorescence lidar measurement campaign at the castle Övedskloster in Skåne. Areas on the castle façade and on the courtyard portal were studied. I had the main responsibility for the measurements, I performed the data analysis and I participated in writing the manuscript.

V Documentation of Soiled and Biodeteriorated Façades: A Case Study on the Coliseum, Rome, using Hyperspectral Imaging Fluorescence Lidars

In this paper, fluorescence lidar measurements at the Coliseum in Rome, performed in collaboration with an Italian research group, are presented. The campaign resulted in so much data that the paper was divided into two parts, this one and Paper VI. This paper describes the campaign, with the emphasis on the deterioration processes of the building. Also, the method and experimental set-up are more closely described here. I had the major responsibility for our part of the measurement campaign and data analysis, and I contributed to the manuscript writing.

VI Hyperspectral Fluorescence Lidar Imaging at the Coliseum, Rome: Elucidating Past Conservation Interventions

This paper describes further aspects of the fluorescence lidar campaign at the Coliseum in Rome. In this part, following up on Paper V, material identification is the main focus of attention. As in the preceding paper, I had the major responsibility for our part of the measurement campaign and data analysis, and I contributed in writing the manuscript.

VII Laser-Induced Fluorescence for Assessment of Cultural Heritage

This paper is a conference proceeding from the 23rd International Laser Radar Conference, which was held in Nara, Japan. In the paper, fluorescence lidar measurements are described, with examples from the Coliseum and the Lateran baptistery in Rome. I had the main responsibility for the measurements, for the data analysis and the manuscript writing.

VIII Remote Multicolor Excitation Laser-Induced Fluorescence Imaging

This article describes remote imaging fluorescence measurements with the focus on the advantages of multiple wavelength excitation. Three measurement campaigns are described, I participated in all of them, with major responsibility for two of them. I performed the data evaluation, including programming the algorithm, and I was mainly responsible for writing the manuscript.

IX Laser-Induced Fluorescence Spectroscopy for Detection of Biological Contamination on Composite Insulators

This paper discusses fluorescence lidar measurements on composite insulators performed in Lund. I participated in the measurements, the data analysis and the manuscript writing.

X Fluorescence Lidar Imaging of Fungal Growth on High Voltage Outdoor Composite Insulators

In this article, fluorescence lidar measurements were performed on composite insulators in order to detect fungal growth. I was highly involved in the measurements, and partly in the analysis and writing of the manuscript.

XI Remote Imaging Laser-Induced Breakdown Spectroscopy and Remote Cultural Heritage Ablative Cleaning

This article describes the first use of remote imaging laser-induced breakdown spectroscopy. I planned the experiment and designed the required adaptations to the optical system. I was responsible for performing the experiment, I did the major part of the data analysis and I contributed in the writing of the manuscript.

XII Remote Imaging Laser-Induced Breakdown Spectroscopy and Laser-Induced Fluorescence Spectroscopy using Nanosecond Pulses from a Mobile Lidar System

This article describes further aspects of laser-induced breakdown spectroscopy and the system used is able to measure both LIBS and fluorescence. A thorough description of the analysis methods is also given. I was responsible for the measurements, I performed the data analysis and I wrote the manuscript.

XIII Laser Spectroscopy of Gas in Scattering Media at Scales Ranging from Kilometers to Millimeters

This paper presents an overview of the measurement techniques used in our group and their connection. Thus, it does not contain any new measurement data. I was involved in some of the measurements and the corresponding data analysis. I was also involved in writing the manuscript.

ACKNOWLEDGEMENTS

It would not have been possible to perform this work without help. I would therefore like to thank a number of people.

First of all, my supervisor, Sune Svanberg, who has been an endless source of enthusiasm and encouragement. Thank you for always being ready to answer my questions, whether in your office or by e-mail from anywhere in the world. Thank you also for nice times and great support on measurement campaigns at various locations in Europe.

My co-supervisor, Hans Edner, has also been of great support, mainly in the measurement campaigns at the beginning of the work. Your experience and knowledge of the methodology were invaluable when seemingly inexplicable signals were encountered.

My fellow PhD students have taught me a lot. Primarily, Petter Weibring gave me much support at the beginning of the work. You introduced me to the lidar system and taught me all I know about it. You also provided me with a sound attitude towards my work, and told me which were the important things to focus on for the successful completion of a PhD. Your support was truly invaluable.

I would like to thank Mikael Sjöholm for your great friendship during the mercury measurement campaigns. Your curiosity and willingness to try new things was inspiring. Thank you, Gabriel Somesfalean, for interesting collaboration and for good companionship on travels. Also, I would like to thank Magnus Bengtsson for your collaboration on the electrical insulator work.

I have shared an office with Linda Persson throughout my PhD studies. I really feel that we have been able to lean on each other in both physics discussions and more personal matters. Thank you for being there to share my complaints when things were tough and to share my joy when things went well. Thank you so much for being an excellent colleague, but an even better friend.

My other fellow PhD students in the Applied Molecular Spectroscopy Group: Tomas Svensson, Mats Andersson, and Märta Cassel-Engquist; thank you Tomas, for your analytical attitude and all interesting lunch discussions, about work, birds, and other things. Thank you, Mats, for introducing an industrially-oriented

way of thinking to the division. Thank you, Märta, for learning fast and understanding my explanations (and accepting that I don't have all the answers). Thank you also for contributing to a very positive atmosphere in our office space.

I would like to thank the master's student Mats Lundquist, for pushing me to do the LIBS experiments. The results of your short project were fantastic and you showed great enthusiasm.

Thank you, Jenny Hällström, for excellent collaboration in the fluorescence lidar project. To pull off the measurement campaigns in Rome required a tremendous effort and being the project leader was a tough challenge that you managed brilliantly. Also, thank you for the fun times in the lab and over the walkie-talkie. Thank you also, Kerstin Barup, for making this project a reality.

Ann Johansson joined me in the fluorescence campaign in Rome. Thank you for being there with me, as technical and moral support. Also, your couch was a nice place to relax and chat when afternoons in front of the computer were tiring.

The mercury measurement campaigns gave me a lot of new contacts. Thank you, Barbara Mazzolai, for excellent organization of the huge EMECAP project. Thanks also to all the other partners in the project, none mentioned, none forgotten.

Thank you, Michael Bennett, for the collaboration during the mercury campaign in Rosignano Solvay, Italy. Your wind lidar system provided important data for the flux measurements and your following analysis was truly rigorous.

Jože Kotnik and Milena Horvat were excellent partners and perfect hosts during the mercury measurement campaign in Idrija, Slovenia. Thank you for your more than kind hospitality.

The fluorescence lidar campaigns in Rome were performed in collaboration with the group of Giovanna Cecchi at CNR-IFAC in Florence. Thank you all for your wonderful cooperation and for helping out with technical difficulties as well as Italian customs. Thank you also for interesting discussions on analysis techniques.

I would like to thank everyone else at the Atomic Physics Division for making it such a nice place to work. I would especially like to thank Minna Ramkull, Henrik Steen, Bertil Hermansson, Åke Bergquist, Göran Werner and the late Laila Lewin for your help in matters not directly connected to research.

I would also like to take this opportunity to thank all my friends, orienteers and others. The beer-meetings on Monday evenings were always refreshing, and the orienteering training and competitions provided welcome breaks from reality. Thank you all for making my free-time so enjoyable.

Moreover, I would like to thank my family for your endless love and support. It gives tremendous comfort to know that I can always count on you.

Finally, Marie. I love you.

REFERENCES

1. R. Ebinghaus, R. R. Turner, L. D. de Lacerda, O. Vasiliev, and W. Salomons (Eds.) *Mercury contaminated sites* (Springer-Verlag, Berlin, Germany, 1999).
2. W. H. Schroeder and J. Munthe, "Atmospheric mercury—An overview," *Atmospheric Environment* **32**, 809–822 (1998).
3. E. G. Pacyna, J. M. Pacyna, J. Fudala, E. Strzelecka-Jastrzab, S. Hlawiczka, and D. Panasiuk, "Mercury emissions to the atmosphere from anthropogenic sources in Europe in 2000 and their scenarios until 2020," *The Science of the Total Environment* **370**, 147–156 (2006).
4. B. Mazzolai, V. Mattoli, V. Raffa, G. Tripoli, P. Dario, R. Ferrara, E. Lanzilotta, J. Munthe, I. Wängberg, L. Barregård, G. Sällsten, M. Horvat, D. Gibicar, V. Fajon, M. Logar, J. Pacyna, B. Denby, S. Svanberg, H. Edner, R. Grönlund, M. Sjöholm, P. Weibring, A. Donati, S. Baldacci, W. Viganö, A. Pannocchia, R. Fontanelli, S. la Manna, S. di Bona, J. Fudala, U. Zielonka, S. Hlawiczka, D. Jarosinska, A. Danet, and C. Bratu, "A multidisciplinary approach to study the impact of mercury pollution on human health and environment: The EMECAP project," *RMZ—Materials and Geoenvironment* **51**, 682–685 (2004).
5. URL <http://www.emecap.com>
6. I. Wängberg, H. Edner, R. Ferrara, E. Lanzilotta, J. Munthe, J. Sommar, M. Sjöholm, S. Svanberg, and P. Weibring, "Atmospheric mercury near a chlor-alkali plant in Sweden," *The Science of the Total Environment* **304**, 29–41 (2003).
7. M. Sjöholm, P. Weibring, H. Edner, and S. Svanberg, "Atomic mercury flux monitoring using an optical parametric oscillator based lidar system," *Optics Express* **12**, 551–556 (2004).
8. R. Grönlund, M. Sjöholm, P. Weibring, H. Edner, and S. Svanberg, "Mercury emissions from chlor-alkali plants measured by lidar techniques," *RMZ—Materials and Geoenvironment* **51**, 1585–1587 (2004).
9. R. Grönlund, M. Sjöholm, P. Weibring, H. Edner, and S. Svanberg, "Differential absorption lidar measurements of mercury fluxes," in *Reviewed and revised papers presented at the 23rd International laser radar conference*, (C. Nagasawa and N. Sugimoto, Eds.), pp. 781–782 (Nara, Japan, 2006).
10. L. Barregård, M. Horvat, B. Mazzolai, G. Sällsten, D. Gibicar, V. Fajon, S. di Bona, J. Munthe, I. Wängberg, and M. Haeger-Eugensson, "Urinary mercury in people living near point sources of mercury emissions," *The Science of the Total Environment* **368**, 326–334 (2006).

11. R. Ferrara, B. E. Maserti, M. Andersson, H. Edner, P. Ragnarsson, S. Svanberg, and A. Hernandez, "Atmospheric mercury concentrations and fluxes in the Almadén district (Spain)," *Atmospheric Environment* **32**, 3897–3904 (1998).
12. R. Grönlund, H. Edner, S. Svanberg, J. Kotnik, and M. Horvat, "Lidar measurements of mercury emissions from the Idrija mercury mine," *RMZ—Materials and Geoenvironment* **51**, 1581–1584 (2004).
13. H. Edner, P. Ragnarsson, S. Svanberg, E. Wallinder, R. Ferrara, B. E. Maserti, and R. Bargagli, "Atmospheric mercury mapping in a cinnabar mining area," *The Science of the Total Environment* **133**, 1–15 (1993).
14. R. Ferrara, B. Mazzolai, H. Edner, S. Svanberg, and E. Wallinder, "Atmospheric mercury sources in the Mt. Amiata area, Italy," *The Science of the Total Environment* **213**, 13–23 (1998).
15. J. Kotnik, M. Horvat, and T. Dizdarevič, "Current and past mercury distribution in air over the Idrija Hg mine region, Slovenia," *Atmospheric Environment* **39**, 7570–7579 (2005).
16. C. Fotakis, D. Anglos, V. Zafropoulos, S. Georgiou, and V. Tornari, *Lasers in the preservation of cultural heritage: Principles and applications* (Taylor & Francis, New York, USA, 2006).
17. A. Nevin, P. Pouli, S. Georgiou, and C. Fotakis, "Laser conservation of art," *Nature Materials* **6**, 320–322 (2007).
18. R. Grönlund, M. Bengtsson, M. Sjöholm, G. Somesfalean, T. Johansson, P. Weibring, H. Edner, S. Svanberg, J. Hällström, and K. Barup, "Lidar remote-sensing assessment of the cultural heritage using laser-induced fluorescence and laser-induced break-down spectroscopy," in *Air pollution and cultural heritage*, (C. Saiz-Jimenez, Ed.), pp. 167–170 (A.A. Balkema Publishers, Leiden, The Netherlands, 2004).
19. R. Grönlund, S. Svanberg, J. Hällström, K. Barup, G. Cecchi, V. Raimondi, D. Lognoli, and L. Palombi, "Laser-induced fluorescence imaging for studies of cultural heritage," *Proceedings of SPIE* **6618**, 66180P (2007).
20. J. Hällström, K. Barup, R. Grönlund, A. Johansson, S. Svanberg, L. Palombi, D. Lognoli, V. Raimondi, G. Cecchi, and O. Brandt, "Documentation of the Lateran baptistery façade by remote laser-induced fluorescence imaging," Manuscript, (2007).
21. R. Grönlund, M. Lundqvist, and S. Svanberg, "Remote imaging laser-induced breakdown spectroscopy and remote ablative cleaning," in *Reviewed and revised papers presented at the 23rd International laser radar conference*, (C. Nagasawa and N. Sugimoto, Eds.), pp. 99–102 (Nara, Japan, 2006).
22. F. J. Fortes, J. Cuñat, L. M. Cabalín, and J. J. Laserna, "In situ analytical assessment and chemical imaging of historical buildings using a man-portable laser system," *Applied Spectroscopy* **61**, 558–564 (2007).
23. M. Bengtsson, S. Wallström, M. Sjöholm, R. Grönlund, B. Andersson, A. Larsson, S. Karlsson, S. Kröll, and S. Svanberg, "Fungus covered insulator materials studied with laser-induced fluorescence and principal component analysis," *Applied Spectroscopy* **59**, 1037–1041 (2005).
24. F. L. Pedrotti and L. S. Pedrotti, *Introduction to optics*, 2nd ed. (Prentice-Hall, New Jersey, USA, 1996).

25. O. Svelto, *Principles of lasers*, 4th ed. (Plenum Press, New York, USA, 1998).
26. L. de Broglie, *Recherches sur la théorie des quanta*, Ph.D. thesis, Paris University, Paris, France (1924).
27. A. Einstein, “Über einen die Erzeugung und Verwandlung des Lichtes betreffenden heuristischen Gesichtspunkt,” *Annalen der Physik* **17**, 132–148 (1905).
28. H. D. Young and R. A. Freedman, *University physics*, 9th ed. (Addison-Wesley, Reading, USA, 1996).
29. F. Reif, *Fundamentals of statistical and thermal physics* (McGraw-Hill, Singapore, 1965).
30. T. H. Maiman, “Stimulated optical radiation in ruby,” *Nature* **187**, 493–494 (1960).
31. S. Svanberg, *Atomic and molecular spectroscopy – Basic aspects and practical applications*, 4th ed. (Springer-Verlag, Heidelberg, Germany, 2004).
32. R. W. Boyd, *Nonlinear optics* (Academic Press, San Diego, USA, 1992).
33. N. M. Kroll, “Parametric amplification in spatially extended media and application to the design of tunable oscillators at optical frequencies,” *Physical Review* **127**, 1207–1211 (1962).
34. R. L. Byer, “Nonlinear optics and solid-state lasers: 2000,” *IEEE Journal on Selected Topics in Quantum Electronics* **6**, 911–930 (2000).
35. F. Träger (Ed.) *Springer handbook of lasers and optics* (Springer, New York, USA, 2007).
36. Spectra-Physics Lasers, Inc., *Quanta-Ray MOPO-730 optical parametric oscillator* (1995).
37. P. Weibring, J. N. Smith, H. Edner, and S. Svanberg, “Development and testing of a frequency-agile optical parametric oscillator system for differential absorption lidar,” *Review of Scientific Instruments* **74**, 4478–4484 (2003).
38. C. N. Banwell and E. M. McCash, *Fundamentals of molecular spectroscopy*, 4th ed. (McGraw-Hill, London, UK, 1994).
39. R. M. Measures, *Laser remote sensing* (John Wiley & Sons, Inc., New York, USA, 1984).
40. J. J. Sakurai, *Advanced quantum mechanics* (Addison-Wesley, Redwood City, USA, 1967).
41. A. K. Sandrowitz, J. M. Cooke, and N. G. Glumac, “Flame emission spectroscopy for equivalence ratio monitoring,” *Applied Spectroscopy* **52**, 658–662 (1998).
42. J. W. Daily, “Laser induced fluorescence spectroscopy in flames,” *Progress in Energy and Combustion Science* **23**, 133–199 (1997).
43. T. Fujii and T. Fukuchi (Eds.) *Laser remote sensing* (CRC Press, Boca Raton, USA, 2005).
44. D. A. Cremers and L. J. Radziemski, “Laser plasmas for chemical analysis,” in *Laser spectroscopy and its applications*, (L. J. Radziemski, R. W. Solarz, and J. A. Paisner, Eds.), Chap. 5, pp. 351–415 (Marcel Dekker, Inc., New York, USA, 1987).

45. P. Vandenabeele, "Raman spectroscopy in art and archaeology," *Journal of Raman Spectroscopy* **35**, 607–609 (2004).
46. M. Gniadecka, H. C. Wulf, N. Nymark Mortensen, O. Faurskov Nielsen, and D. H. Christensen, "Diagnosis of basal cell carcinoma by Raman spectroscopy," *Journal of Raman Spectroscopy* **28**, 125–129 (1997).
47. P. Weibring, H. Edner, and S. Svanberg, "Versatile mobile lidar system for environmental monitoring," *Applied Optics* **42**, 3583–3594 (2003).
48. C. af Klinteberg, M. Andreasson, O. Sandström, S. Andersson-Engels, and S. Svanberg, "Compact medical fluorosensor for minimally invasive tissue characterization," *Review of Scientific Instruments* **76**, 034303–1–6 (2005).
49. J. D. Klett, "Stable analytical inversion solution for processing lidar returns," *Applied Optics* **20**, 211–220 (1981).
50. F. G. Fernald, B. M. Herman, and J. A. Reagan, "Determination of aerosol height distributions by lidar," *Journal of Applied Meteorology* **11**, 482–489 (1972).
51. F. G. Fernald, "Analysis of atmospheric lidar observations: Some comments," *Applied Optics* **23**, 652–653 (1984).
52. H. G. Hughes, J. A. Ferguson, and D. H. Stephens, "Sensitivity of a lidar inversion algorithm to parameters relating atmospheric backscatter and extinction," *Applied Optics* **24**, 1609–1613 (1985).
53. R. G. Strauch, V. E. Derr, and R. E. Cupp, "Atmospheric temperature measurement using Raman backscatter," *Applied Optics* **10**, 2665–2669 (1971).
54. A. Hauchecorne, M. L. Chanin, P. Keckhut, and D. Nedeljkovic, "Lidar monitoring of the temperature in the middle and lower atmosphere," *Applied Physics B* **55**, 29–34 (1992).
55. J. B. Mason, "Lidar measurement of temperature: A new approach," *Applied Optics* **14**, 76–78 (1975).
56. J. E. Kalshoven, Jr., C. L. Korb, G. K. Schwemmer, and M. Combrowski, "Laser remote sensing of atmospheric temperature by observing resonant absorption of oxygen," *Applied Optics* **20**, 1967–1971 (1981).
57. S. Svanberg, "Differential absorption lidar (DIAL)," in *Air monitoring by spectroscopic techniques*, (M. W. Sigrist, Ed.), Chap. 3, pp. 85–161 (John Wiley & Sons, Inc., New York, USA, 1994).
58. C. M. Davies, H. H. Telle, D. J. Montgomery, and R. E. Corbett, "Quantitative analysis using remote laser-induced breakdown spectroscopy (LIBS)," *Spectrochimica Acta B* **50**, 1059–1075 (1995).
59. S. Palanco, J. M. Baena, and J. J. Laserna, "Open-path laser-induced plasma spectrometry for remote analytical measurements on solid surfaces," *Spectrochimica Acta B* **57**, 591–599 (2002).
60. P. Rohwetter, J. Yu, G. Méjean, K. Stelmaszczyk, E. Salmon, J. Kasparian, J.-P. Wolf, and L. Wöste, "Remote LIBS with ultrashort pulses: Characteristics in picosecond and femtosecond regimes," *Journal of Analytical Atomic Spectrometry* **19**, 437–444 (2004).
61. S. Tzortzakis, D. Anglos, and D. Gray, "Ultraviolet laser filaments for remote laser-induced breakdown spectroscopy (LIBS) analysis: Applications in cultural heritage monitoring," *Optics Letters* **31**, 1139–1141 (2006).

62. G. Calcagno, E. Pummer, and M. Koller, "St. Stephen's Church in Vienna: Criteria for Nd:YAG laser cleaning on an architectural scale," *Journal of Cultural Heritage* **1**, S111–S117 (2000).
63. P. V. Maravelaki, V. Zafropoulos, V. Kilikoglou, M. Kalaitzaki, and C. Fotakis, "Laser-induced breakdown spectroscopy as a diagnostic technique for the laser cleaning of marble," *Spectrochimica Acta B* **52**, 41–53 (1997).
64. H. Edner, G. W. Faris, A. Sunesson, and S. Svanberg, "Atmospheric atomic mercury monitoring using differential absorption lidar techniques," *Applied Optics* **28**, 921–930 (1989).
65. H. K. Lichtenthaler and U. Rinderle, "The role of chlorophyll fluorescence in the detection of stress conditions in plants," *CRC Critical Reviews in Analytical Chemistry* **19**, (Suppl. 1) 529–585 (1988).
66. K. H. Esbensen, *Multivariate Data Analysis – In practice*, 5th ed. (Camo Process AS, Oslo, Norway, 2002).
67. M. Sjöholm, G. Somesfalean, J. Alnis, S. Andersson-Engels, and S. Svanberg, "Analysis of gas dispersed in scattering media," *Optics Letters* **26**, 16–18 (2001).
68. J. Alnis, B. Andersson, M. Sjöholm, G. Somesfalean, and S. Svanberg, "Laser spectroscopy of free molecular oxygen dispersed in wood materials," *Applied Physics B* **77**, 691–695 (2003).
69. M. Andersson, L. Persson, M. Sjöholm, and S. Svanberg, "Spectroscopic studies of wood-drying processes," *Optics Express* **14**, 3641–3653 (2006).
70. L. Persson, H. Gao, M. Sjöholm, and S. Svanberg, "Diode laser absorption spectroscopy for studies of gas exchange in fruits," *Optics and Lasers in Engineering* **44**, 687–698 (2006).
71. M. Cassel-Engquist, R. Grönlund, M. Andersson, L. Persson, and S. Svanberg, "Remote gas detection in solid scattering media using differential absorption lidar," in *Proceedings of CLEO-Europe*, (Munich, Germany, June 18–22, 2007).
72. S. K. Sharma, S. M. Angel, M. Ghosh, H. W. Hubble, and P. G. Lucey, "Remote pulsed laser Raman spectroscopy system for mineral analysis on planetary surfaces to 66 meters," *Applied Spectroscopy* **56**, 699–705 (2002).

PAPERS

Elemental Mercury Emissions from Chlor-Alkali Plants Measured by Lidar Techniques

R. Grönlund, M. Sjöholm, P. Weibring, H. Edner, and S. Svanberg.

Atmospheric Environment **39**, 7474–7480 (2005).

Available online at www.sciencedirect.com

SCIENCE @ DIRECT®

Atmospheric Environment 39 (2005) 7474–7480

**ATMOSPHERIC
ENVIRONMENT**

www.elsevier.com/locate/atmosenv

Elemental mercury emissions from chlor-alkali plants measured by lidar techniques

Rasmus Grönlund*, Mikael Sjöholm, Petter Weibring,
Hans Edner, Sune Svanberg

Department of Physics, Lund Institute of Technology, P.O. Box 118, SE-221 00 Lund, Sweden

Received 15 October 2004; accepted 23 June 2005

Abstract

Differential absorption lidar (DIAL) techniques have been utilized to measure elemental gaseous mercury fluxes from mercury cell chlor-alkali (MCCA) plants as a part of the European Union funded European mercury emissions from chlor-alkali plants (EMECAP) project. Three plants have been selected as study objects and a total of six measurement campaigns have been performed, one intercalibration campaign and five flux evaluation campaigns, in both winter and summer. The measurements were carried out using the Swedish optical parametric oscillator- (OPO) based mobile lidar system developed at Lund Institute of Technology. The study shows large differences in the mercury emissions measured in winter or summer and at the different plants. The average values for the campaigns ranged from 6 g h^{-1} in the winter campaign at the Swedish plant to 54 g h^{-1} in the summer campaign at the Italian plant.

© 2005 Elsevier Ltd. All rights reserved.

Keywords: DIAL; Atmospheric mercury flux; EMECAP; Chlor-alkali plant; OPO

1. Introduction

Mercury cell chlor-alkali (MCCA) plants use liquid mercury as a cathode in electrolytic cells to produce chlorine, sodium hydroxide and hydrogen by electrolysis of brine solution. In this process, very large quantities of mercury are handled and because of the high-vapor pressure of mercury already at low temperatures, considerable amounts of mercury is emitted to the atmosphere, due to spills, leakage from mercury cells or pumps, maintenance activities, etc. (Southworth et al., 2004). Although the MCCA technique is in many places being replaced by alternatives, it is still the most commonly used in Europe.

Over the last decades, increased awareness of the environmental and human health impacts of mercury has led to stronger regulations against mercury emissions, leading to decreased emissions (Schroeder and Munthe, 1998). However, the chlor-alkali industry still constitutes a large mercury polluter, in 1995 responsible for about 12% ($41.3 \text{ tonnes year}^{-1}$) of the anthropogenic total mercury emissions in Europe (Pacyna et al., 2001). More recent estimates reports emissions from the chlor-alkali industry to be responsible for about 17% ($40.4 \text{ tonnes year}^{-1}$) of anthropogenic total mercury emissions in the year 2000 (Pacyna, 2003). A report from the Euro-Chlor Association (Anon, 2001) shows constantly decreasing, but still significant, emissions from chlor-alkali plants.

In this context a large cross-disciplinary project, financed by the European Union, concerning the European mercury emission from chlor-alkali plants

*Corresponding author. Tel.: +46 46 222 41 38;
fax: +46 46 222 42 50.

E-mail address: rasmus.gronlund@fysik.lth.se
(R. Grönlund).

(EMECAP) has been pursued. The goal of the project is to provide decision-makers with an improved tool for evaluating the risk to the human health and the environment around MCCA plants (Mazzolai et al. 2004; <http://www.emecap.com>). Within the project, epidemiological studies of people living in the vicinity of MCCA industries are performed (Barregård et al., to appear) and linked to the levels of mercury in the environment, which are assessed by point monitoring of mercury in air, soil and living organisms around the mercury emitters (Wängberg et al., 2003). These data are managed by a data mining-based software (Fayyad et al., 1996) which, interrogating dedicated epidemiological and environmental data bases, provides high-level information in terms of health risk.

For understanding the regional atmospheric dispersion of mercury a mathematical model is being developed (Munthe et al., 2001). Two key inputs in this model are the initial plume extension and the emitted flux of gaseous elemental mercury at the source industries. Such measurements, performed within the EMECAP project, utilizing the Differential absorption lidar (DIAL) technique (Svanberg, 1994), are treated in the present paper. The model also needs input on the chemical composition of the emitted mercury, i.e. elemental mercury (Hg^0) versus reactive gaseous mercury (RGM, Hg^{2+}), etc. Such measurements were also performed and are presented in Wängberg et al. (2005).

Although flux estimation is an important issue, few techniques for flux measurements exist. Recently, Differential optical absorption spectroscopy (DOAS) measurements in the air vent from a US MCCA plant combined with wind measurements were used to assess mercury flux from the cell house (Kinsey et al., 2004). Here, the concentration is integrated over the measured path between the light-source and the detector. Using the DIAL technique, range-resolved measurements of atomic mercury concentrations and fluxes can be measured. Our group has previously reported on this kind of measurements from MCCA plants, employing different laser systems, but the same mercury absorption line at 253.65 nm (Edner et al., 1989; Ferrara et al., 1992; Edner et al., 1995; Wängberg et al., 2003; Sjöholm et al., 2004). In the present report mercury fluxes from summer and winter campaigns at three different European MCCA plants, Eka Nobel in Bohus, Sweden, Solvay in Rosignano Solvay, Italy and Zakłady Azotowe in Tarnów, Poland, are presented.

2. Measurement technique

DIAL measurements were performed on atomic mercury, using two wavelengths, one *on* the absorption line (253.65 nm) and the other slightly *off*. The *off* wavelength was chosen at a longer wavelength than the

on wavelength to avoid interference with a close-lying, weak oxygen absorption line (Edner et al., 1989). Some unsaturated hydrocarbons and aromatic compounds absorb light in the same wavelength region, but these elements have quite slow absorption features compared to the *on/off*-wavelengths and are not considered to be abundant enough to affect the signal. This was verified by measurements outside the plume not showing elevated mercury concentrations. The lidar signal was collected time-resolved to obtain a range-resolved measurement. By forming the ratio between the *on* and *off* signals, the DIAL curve is obtained, being flat where no mercury is present and sloping downwards in the presence of mercury. Since the *on* and *off* wavelengths are chosen close to each other, no other differences than the mercury absorption are expected. The output energy may be slightly different for the two wavelengths; however, this does not matter since the slope of the normalized DIAL curve is the only pertinent factor when analyzing the mercury concentrations. Particulate mercury and different Hg(II) species do not have any absorption of light at 253.65 nm, thus not being detected by the technique presented.

Each DIAL measurement, in a certain direction, gives the range-resolved mercury concentration along the laser beam. By vertical scanning of the laser beam downwind from a pollution source, in this case a chlor-alkali plant, a concentration cross-section of the mercury plume is found. The mercury flux is estimated by area integration of the concentration and multiplication by the wind speed component perpendicular to the cross-section surface.

The measurements were performed using the Swedish optical parametric oscillator- (OPO) based mobile lidar system, built inside a Volvo F610 truck (Weibring et al., 2003). The OPO (Spectra-Physics MOPO-730) is pumped by a pulsed (20 Hz) frequency-tripled Nd:YAG laser at 355 nm and gives output in the wavelength range 440–1800 nm which can be frequency doubled to reach wavelengths down to 220 nm. The OPO is modified with piezo-electric elements so that the wavelength can be switched within a range of 160 cm^{-1} between consecutive shots. The average linewidth of the transmitter is normally better than 0.2 cm^{-1} and the pulse length is typically 3–4 ns. An absorption cell system is used to compensate for fluctuations in wavelength and linewidth of the emitted laser light pulses.

The laser radiation is sent into the air through the dome, hoisted to the roof of the truck, which can be rotated 360° and by using a folding mirror the beam can be tilted vertically from -10° to 55° . The backscattered radiation is collected using the on-axis, 40-cm-diameter Newtonian telescope and focused onto a photomultiplier tube. An interference filter is used to suppress background light, since only elastic scattering is of interest. The retrieved signal is then digitized at a

sampling frequency corresponding to a range resolution of 7.5 m. The entire system is controlled by a LabVIEW-based computer program, which also is used for data analysis.

3. Measurements

A total of six measurement campaigns have been performed at the three test sites. Initially, intercalibration measurements were performed during a campaign at the Swedish test site in September 2001. In this inter-comparison, a good agreement between lidar and conventional mercury point-monitoring concentration measurements was shown (Wängberg et al., 2003). DIAL measurement campaigns of the flux have been performed in Sweden, Italy and Poland in summer and additionally, in winter in Sweden and Italy. Each measurement campaign lasted for about 2 weeks and in this time a substantial number of scans were performed, rendering an average value representative

for the campaign period. Maps over the measurement areas along with a picture of the mobile lidar system are seen in Fig. 1.

A single sweep is gathered in 3–5 min, yielding a concentration map and, combined with wind data, a flux value. Over the course of each measurement campaign, the wind velocity was measured using wind vanes and anemometers, placed as close as possible to the center of the pollution plume. The horizontal direction of the sweep was not held constant over the entire measurement campaign, as indicated in Fig. 1, due to fluctuations of the wind direction, as it is always desired to have the measurement direction as perpendicular to the wind direction as possible.

All the different flux values were then averaged to give a mean flux value for each hour and ultimately for the measurement period. In the averaging, sweeps where the wind speed was less than 1 m s^{-1} or the wind direction was in a too acute angle to the measurement direction, giving rise to a large sine correction, have been excluded.

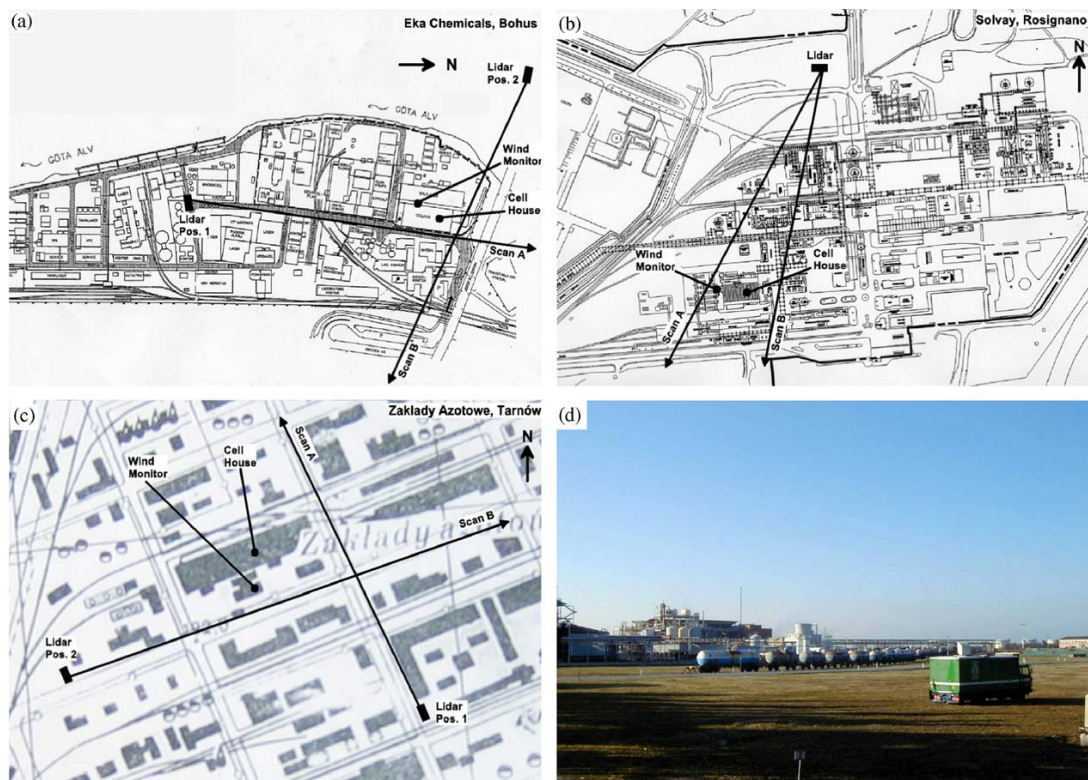


Fig. 1. Maps over the measurement sites (a) Bohus, (b) Rosignano Solvay, (c) Tarnów, with measurement directions indicated. (d) shows the lidar system on location in Rosignano Solvay.

4. Results

Each vertical sweep gives a cross-section of the mercury plume, an example of which is given in Fig. 2 where the area-integrated concentration (g m^{-1}) can also be seen. The daily elemental mercury flux averages from the different campaigns are given in Fig. 3. For each campaign a total average flux value was calculated, the result is given in Fig. 4. Here, the uncertainty bars correspond to one standard deviation of the different hourly averages and should not be considered solely as the error of the measurement technique, as the emissions most probably were not constant over the measurement campaign. For comparison, the fluxes may be normalized with respect to the chlorine production, as has been done in Fig. 5. However, it should be kept in mind that a substantial part of the flux may be independent of the chlorine production due to gassing from spills, as discussed below.

5. Discussion

The results in Fig. 4 can be compared with earlier measurements by our group at the same plants rendering average elemental mercury flux values of 43 g h^{-1} in Rosignano Solvay in a september measurement campaign in 1990 (Ferrara et al., 1992) and 31 g h^{-1} in

Bohus in a may measurement campaign in 1992 (Edner et al., 1995). The present results indicate that, particularly in Bohus, new technologies and environmental awareness has decreased the emissions significantly.

It should be noted that the accuracy in the measured flux depends equally on the precision in the integrated mercury concentration obtained in the lidar vertical scan and on the accuracy in the wind speed determination. Wind speed assessment is clearly an important issue and in the present work data from vane anemometers appropriately placed were used. In order to estimate the accuracy of this procedure some joint measurements comparing vane anemometer data with data obtained with a Doppler lidar set-up, in which the Doppler-shifts in particulate backscattering were determined. The intercomparison suggests that the procedure adopted in the present flux determination project is good to about 20 percent (Bennett et al., to appear).

Emissions from the cell building may have a number of different origins, as discussed earlier (Southworth et al., 2004). However, it seems logical that there would be two types of emissions: forced leakage from pumps, cells, valves, etc. and gassing from spills. The second type is expected to be dependent on the wind speed over it, reducing the vapor pressure and thus allowing faster gassing, whereas a forced leakage is not expected to have this behavior. In respect of this it should be noted that the Italian plant has an open structure, ventilated by the

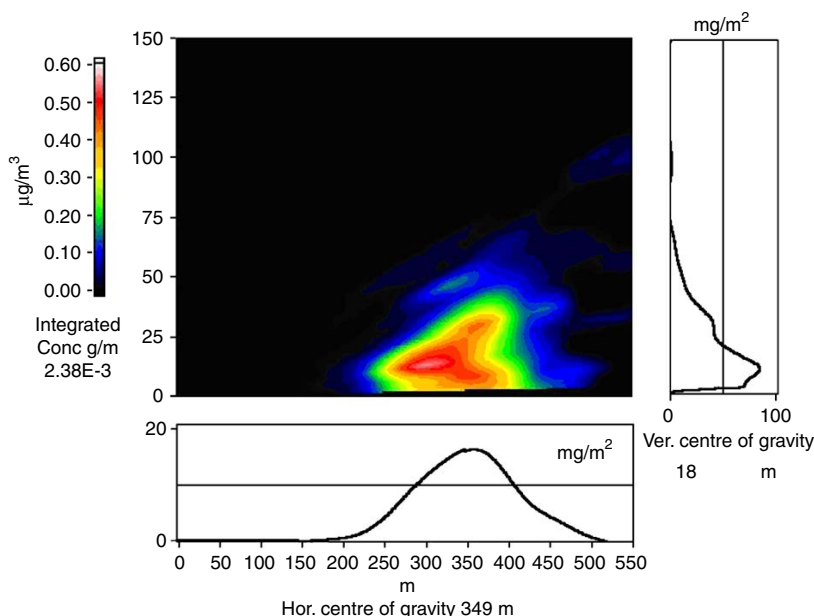


Fig. 2. Cross-section of the mercury plume, recorded at the Solvay plant in Italy, 04-07-2003, 11:29–11:34, corresponding to a mercury flux of 74 g h^{-1} .

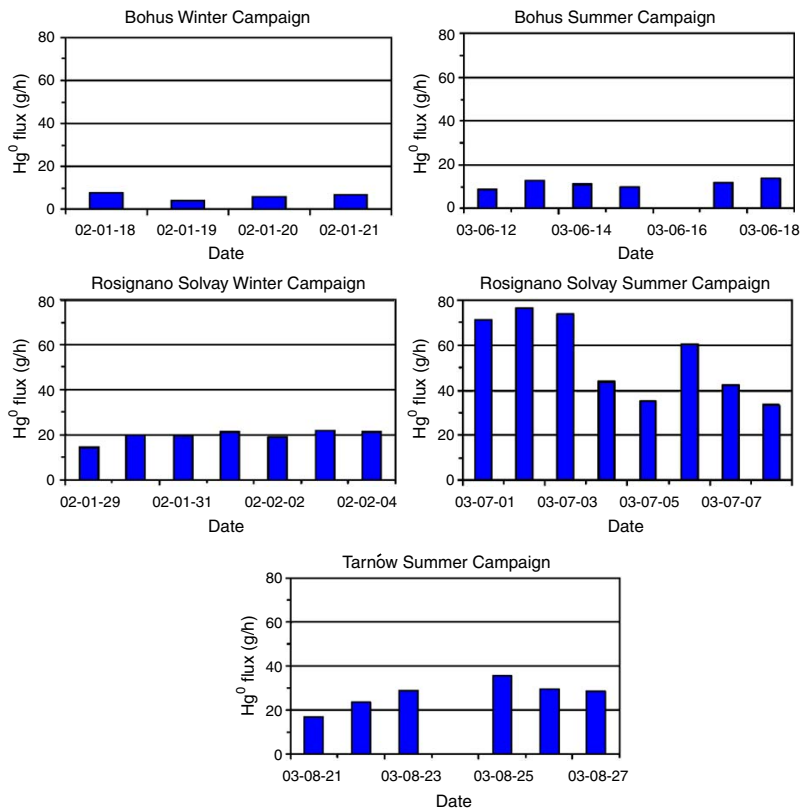


Fig. 3. Daily average elemental mercury flux values for the different campaigns.

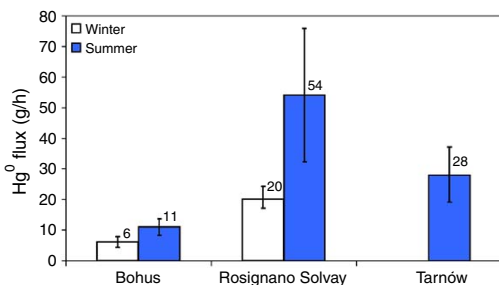


Fig. 4. Average mercury flux from the different campaigns. The error bars correspond to the standard deviation of the hourly measured values.

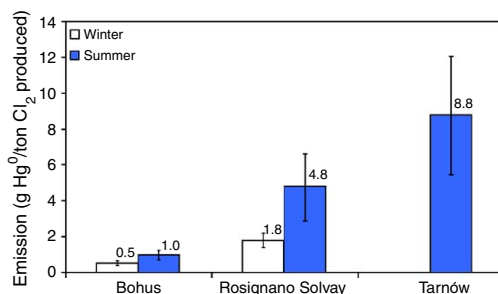


Fig. 5. Average mercury flux from the different sites, normalized to the chlorine production during the different campaigns.

wind blowing through the cell house, whereas both the Swedish and Polish plants are closed buildings with forced ventilation. The wind dependence is clearly largest at the Italian site as can be seen by comparing Fig. 6a–c where the flux as a function of the wind speed is given for the Italian, Swedish and Polish plant,

respectively. It could be argued that the large emissions from the Italian plant are only due to the fact that the wind speed happened to be particularly high at the time of the campaign. Assuming the fit in Fig. 6a–c are correct, the emissions if the wind conditions would have been the same at all sites can be calculated and are seen

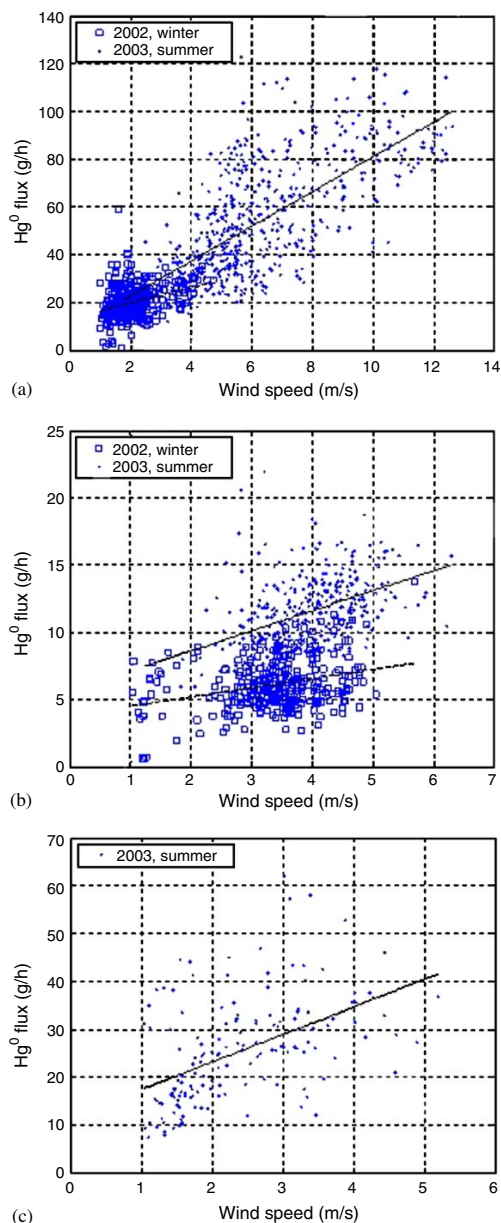


Fig. 6. Mercury flux as a function of wind speed at the different plants; Solvay plant in Italy (a), Eka plant in Sweden (b) and Zakłady Azotowe plant in Poland (c). The dashed lines correspond to regression of the results in the winter campaigns (the squares represent single sweep results) and the solid lines to the summer campaigns (the dots). The correlation for the different regressions are: $r^2 = 0.10$ (Italy, winter) $r^2 = 0.49$ (Italy, summer) $r^2 = 0.09$ (Sweden, winter) $r^2 = 0.20$ (Sweden, summer) $r^2 = 0.25$ (Poland, summer).

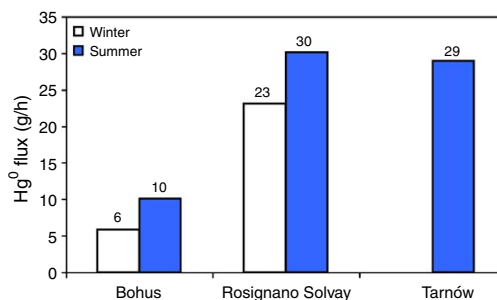


Fig. 7. Mercury emissions from the different plants, assuming a constant wind speed of 3 m s^{-1} in all campaigns.

in Fig. 7, assuming the wind speed to be 3 m s^{-1} . As can be seen, by comparing Fig. 7 with Fig. 4, only the Italian summer campaign is affected significantly by this normalization, in the other campaigns the wind dependence was not very pronounced. This indicates that it was only in the Italian summer campaign that the gassing from spills gave a large contribution to the total flux.

6. Conclusions

Total atomic mercury emissions to air from three mercury cell chlor-alkali plants were successfully assessed using the differential absorption lidar technique. It was found that the total fluxes from the three different plants differ widely, also when normalized on the chlorine production. This reflects differences in the technology being used. A hitherto undescribed wind velocity dependence of the total flux was also observed especially during high-ambient temperatures on the open cell house structure of Solvay. This is interpreted as indicative of a strong emission component from mercury spills in the electrolytic cell environment.

Acknowledgments

The authors gratefully acknowledge support and encouragement from our EMECAP partners, in particular Dr. Barbara Mazzolai. The EMECAP project was supported financially by the European Commission DG XII.

References

- Anon, 2001. Reduction of Mercury Emissions from the West European Chlor-Alkali Industry, 3rd Ed. Euro-Chlor Association, Brussels.

- Barregård, L., Horvat, M., Mazzolai, B., Sällsten, G., Gibicar, D., Fajon, V., diBona, S., Munthe, J., Wängberg, I., Haeger Eugensson, M., to appear. Urinary mercury in people living near point sources of mercury emissions. *Environmental Health Perspectives*, submitted.
- Bennett, M., Edner, H., Grönlund, R., Sjöholm, M., Svanberg, S., Ferrara, R., to appear. Joint application of Doppler Lidar and differential absorption Lidar to estimate the mercury flux from a chlor-alkali plant. *Atmospheric Environment*, submitted.
- Edner, H., Faris, G.W., Sunesson, A., Svanberg, S., 1989. Atmospheric atomic mercury monitoring using differential absorption lidar techniques. *Applied Optics* 28 (5), 921–930.
- Edner, H., Ragnarsson, P., Wallinder, E., 1995. Industrial emission control using lidar techniques. *Environmental Science and Technology* 29 (2), 330–337.
- Fayyad, U.M., Shapiro, G.P., Smyth, P., Uthrusamy, R., 1996. *Advances in Knowledge Discovery and Data Mining*. AAAI Press, Menlo Park, CA.
- Ferrara, R., Maserti, B.E., Edner, H., Ragnarsson, P., Svanberg, S., Wallinder, E., 1992. Mercury emissions into the atmosphere from a chlor-alkali complex measured with the lidar technique. *Atmospheric Environment* 26A (7), 1253–1258.
- <http://www.emecap.com>.
- Kinsey, J.S., Swift, J., Bursey, J., 2004. Characterization of fugitive mercury emissions from the cell building at a US chlor-alkali plant. *Atmospheric Environment* 38 (4), 623–631.
- Mazzolai, B., Mattoli, V., Raffa, V., Tripoli, G., Dario, P., Ferrara, R., Lanzillotta, E., Munthe, J., Wängberg, I., Barregård, L., Sällsten, G., Horvat, M., Gibicar, D., Fajon V., Logar, M., Pacyna, P., Denby, B., Svanberg, S., Edner, H., Grönlund, R., Sjöholm, M., Weibring, P., Donati, A., Baldacci, S., Viganò, W., Pannocchia, A., Fontanelli, R., La Manna, S., Di Bona, S., Fudala, J., Zielonka, U., Hlawiczka, S., Jarosinska, D., Danet, A., Bratu, C., 2004. A multidisciplinary approach to study the impact of mercury pollution on human health and environment: the EMECAP project. Proceedings from the seventhth International Conference on Mercury as Global Pollutant, Ljubljana, June 28–July 2, 2004.
- Munthe, J., Kindbom, K., Kruger, O., Petersen, G., Pacyna, J., Iverfeldt, Å., 2001. Examining source–receptor relationships for mercury in Scandinavia. *Water, Air, and Soil Pollution: Focus* 1 (3), 299–310.
- Pacyna, J.M., 2003. Emissions of Hg in Europe in 2000, The EU Mercyms Project, e-mail: jp@nilu.no
- Pacyna, E.G., Pacyna, J.M., Pirrone, N., 2001. European emissions of atmospheric mercury from anthropogenic sources in 1995. *Atmospheric Environment* 35 (17), 2987–2996.
- Schroeder, W.H., Munthe, J., 1998. Atmospheric mercury—an overview. *Atmospheric Environment* 32 (5), 809–822.
- Sjöholm, M., Weibring, P., Edner, H., Svanberg, S., 2004. Atomic mercury flux monitoring using an optical parametric oscillator based lidar system. *Optics Express* 12 (4), 551–556.
- Southworth, G.R., Lindberg, S.E., Zhang, H., Anscombe, F.R., 2004. Fugitive mercury emissions from a chlor-alkali factory: sources and fluxes to the atmosphere. *Atmospheric Environment* 38 (4), 597–611.
- Svanberg, S., 1994. Differential absorption lidar (DIAL). In: Sigrist, M. (Ed.), *Air Monitoring by Spectroscopic Techniques*. Wiley, New York, pp. 85–161.
- Wängberg, I., Edner, H., Ferrara, R., Lanzillotta, E., Munthe, J., Sommar, J., Sjöholm, M., Svanberg, S., Weibring, P., 2003. Atmospheric mercury near a chlor-alkali plant in Sweden. *Science of the Total Environment* 304 (1), 29–41.
- Wängberg, I., Barregard, L., Sällsten, G., Haeger-Eugensson, M., Munthe, J., Sommar, J., 2005. Emissions, dispersion and human exposure of mercury from a Swedish Chlor-Alkali plant. *Atmospheric Environment*, this issue.
- Weibring, P., Edner, H., Svanberg, S., 2003. Versatile mobile lidar system for environmental monitoring. *Applied Optics* 42 (18), 3583–3594.

PAPER II

Mercury Emissions from the Idrija Mercury Mine Measured by Differential Absorption Lidar Techniques and a Point Monitoring Absorption Spectrometer

R. Grönlund, H. Edner, S. Svanberg, J. Kotnik, and M. Horvat.
Atmospheric Environment **39**, 4067–4074 (2005).

Available online at www.sciencedirect.com

SCIENCE @ DIRECT®

Atmospheric Environment 39 (2005) 4067–4074

**ATMOSPHERIC
ENVIRONMENT**

www.elsevier.com/locate/atmosenv

Mercury emissions from the Idrija mercury mine measured by differential absorption lidar techniques and a point monitoring absorption spectrometer

Rasmus Grönlund^{a,*}, Hans Edner^a, Sune Svanberg^a, Jože Kotnik^b,
Milena Horvat^b

^aAtomic Physics Division, Lund Institute of Technology, P.O. Box 118, SE-221 00 Lund, Sweden^bJožef Stefan Institute, Jamova 39, SI-1000 Ljubljana, Slovenia

Received 6 January 2005; received in revised form 9 March 2005; accepted 25 March 2005

Abstract

Mercury emission measurements from the Idrija mercury mine in Slovenia were performed during an early November 2003 campaign, where the differential lidar technique was used to map mercury concentrations and an attempt was made to quantify the total mercury flux from the most contaminated area, the abandoned cinnabar roasting oven complex. Lidar concentration data were compared with data recorded with a Zeeman modulated atomic absorption instrument, operated from a vehicle equipped with a GPS localization system. Concentrations and fluxes were comparatively low due to low temperature and rainfall. The average flux from the distillation plant was measured to approximately 2 g h^{-1} .

© 2005 Elsevier Ltd. All rights reserved.

Keywords: DIAL; Atmospheric mercury flux; Idrija; Mercury mine; OPO

1. Introduction

The Idrija mercury mine (see Fig. 1) is the second largest mercury mine in the world, second only to the Almadén mine in Spain. Mercury was found here in 1490 and the mine was in operation for 500 years. With mining operations now stopped the surroundings are still mercury and cinnabar contaminated.

The first extensive research on Hg cycling in Idrija town and its vicinity started in the early 1970s of the past

century (Kosta et al., 1974). At the beginning of the 1980s Hg production rapidly decreased which resulted in investigations on Hg cycling in Idrija. In the 1980s very few measurements of Hg concentrations in air or in other environmental compartments have been done. After 1990, Miklavčič and Horvat started with intensive Hg measurements in the air over Idrija (Miklavčič, 1996). In 1994 Gosar et al. (1997) started with the first geochemical mapping of Hg concentrations in air.

High emissions of Hg into the environment resulted in elevated levels of Hg in all parts of the environment in Idrija Valley. In the early 1970s, when Hg production was the highest, Hg concentrations in the air in Idrija town could reach even $20 \mu\text{g m}^{-3}$ (Kosta et al., 1974), as illustrated in Fig. 2. In the late 1970s and 1980s Hg

*Corresponding author. Tel.: +46 46 222 41 38;
fax: +46 46 222 42 50.

E-mail address: rasmus.gronlund@fysik.lth.se
(R. Grönlund).

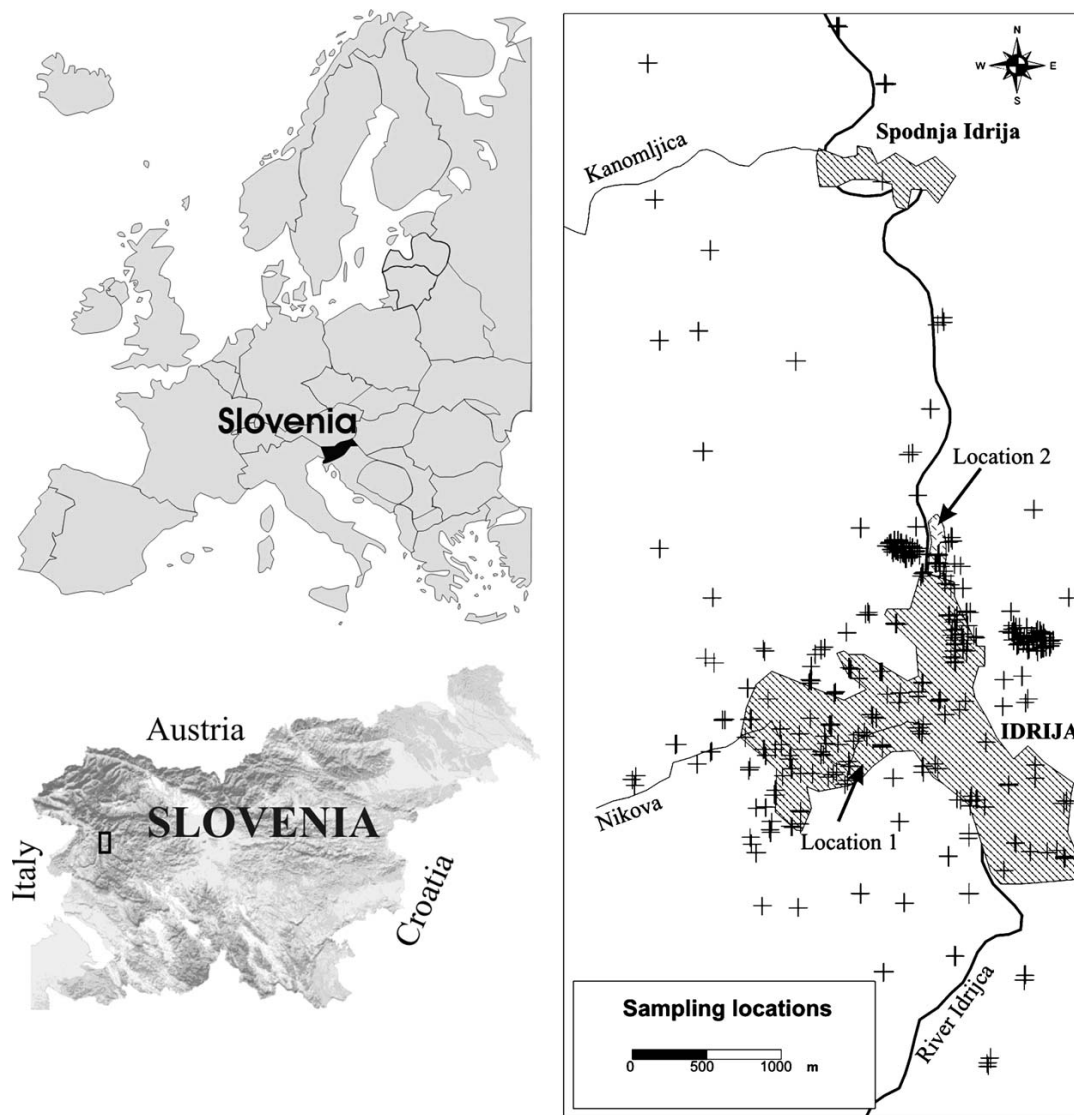


Fig. 1. The location of Idrija and the sampling locations (← position of lidar system, + locations where Hg concentration was measured by portable Hg monitor for at least 60 s).

concentrations in the air in the town decreased rapidly to values below 100 ng m^{-3} with the same trend of Hg production. Hg concentration reached levels over $1 \mu\text{g m}^{-3}$ in 1995 by smelting of heavily contaminated soils and residue material. After that time Hg concentrations in air decreased dramatically and reached a level of 10 ng m^{-3} or even lower at the end of year 2003.

The objectives for the one-week late October lidar (light detection and ranging) measurement campaign

were to map the emission sources from the mine and to estimate the total flux of mercury from the site.

The Lund group has developed differential absorption lidar (DIAL) techniques for three-dimensional mapping of atmospheric elemental gaseous mercury (Aldén et al., 1982; Edner et al., 1989). Lidar measurements of the concentrations of mercury utilize the Hg absorption peak at 254 nm and a close-by reference wavelength for differential measurements in the backscattered light. By

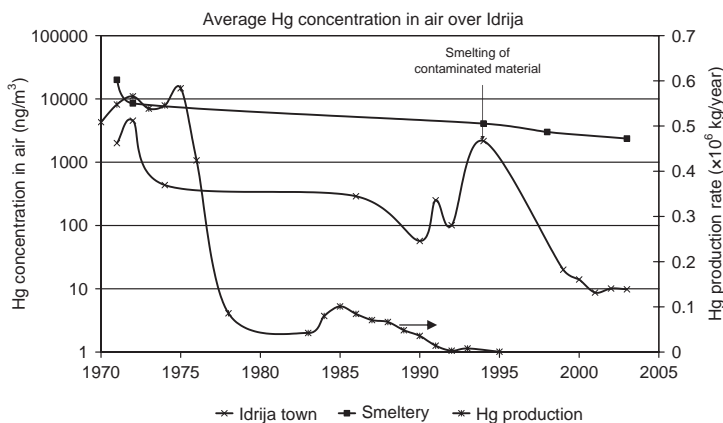


Fig. 2. Average Hg concentrations in air in Idrija Town (in ng m^{-3}) and Hg production rate (in kg year^{-1}) in the period 1970–2003.

vertical scanning of the measurement direction, a cross-section of the mercury plume can be found. The total flux can then be obtained by taking the wind speed into account.

The lidar system has previously been used in measurements at the two other main mercury mining areas, Abbadia San Salvatore (Italy) (Edner et al., 1993) and Almadén (Spain) (Ferrara et al., 1998). High concentrations, up to $5 \mu\text{g m}^{-3}$ were found and at Almadén a total flux of $600\text{--}1200 \text{ g h}^{-1}$ was determined in a September measurement campaign. At the Italian site, particularly high concentrations were found around the mercury distillation plant (Edner et al., 1993; Ferrara et al., 1999). Similar values have recently been reported by other authors (Gustin et al., 2003; Hylander and Meili, 2003; Rytuba, 2003). The present measurements at Idrija were concentrated to the area around the abandoned distillation plant, where high concentrations were expected from previous point-monitoring measurements.

2. Measurement systems

The Swedish mobile lidar system recently underwent an extensive upgrading process and is now equipped with an advanced optical parametric oscillator-based (OPO) transmitter system (Weibring et al., 2003). The earlier elemental mercury measurements were performed with a dye laser system. Mercury mapping with the upgraded system was recently demonstrated within the EC-funded EMECAP project where extensive flux determinations from chlor-alkali plants in Sweden, Italy, and Poland were performed (Sjöholm et al., 2004; Grönlund et al., to appear).

The radiation from the laser source is transmitted into the atmosphere via a roof-top dome, where a computer-

controlled mirror directs the laser beam into the measurement area. Elastically backscattered light from aerosol particles is collected by a 40 cm diameter optical telescope which views the measurement zone via the same mirror, leaving the transmitting and receiving optical axes always aligned. A photomultiplier tube converts the optical transient into an electronic signal which is captured by a transient digitizer and stored in the computer system. By firing the laser source alternately at the on- and off-resonance wavelengths and performing signal averaging for each wavelength, two raw data curves are obtained. By dividing the signal recorded at the absorption wavelength by the one obtained at the reference wavelength a curve is obtained, from the slope of which the range-resolved mercury concentration can be retrieved. Simultaneous measurements through gas cells of known concentrations ensure wavelength stability and internal calibration. The measurements are performed in a number of different vertical directions and interpolated to form a concentration map. Each such scan corresponds to approximately 5 min of measurement. The area-integrated concentration multiplied by the wind speed perpendicular to the area yields the flux through the area. An overview diagram of the mobile lidar system is given in Fig. 3.

Wind data were recorded with a vane anemometer placed at the top of a telescope pole attached to the lidar system. In this way the wind velocity and direction 10 m above the ground were continuously logged at the lidar site. A 40 kV A diesel power generator towed by the lidar truck provides electricity for the operation of the laser, the electronics and the cooling systems.

Simultaneous measurements were made by the IJS group, making concentration maps of the area using a Lumex RA-915+ Zeeman portable mercury point-monitor (Sholupov and Ganeyev, 1995). This system utilizes atomic absorption in a column of ambient air

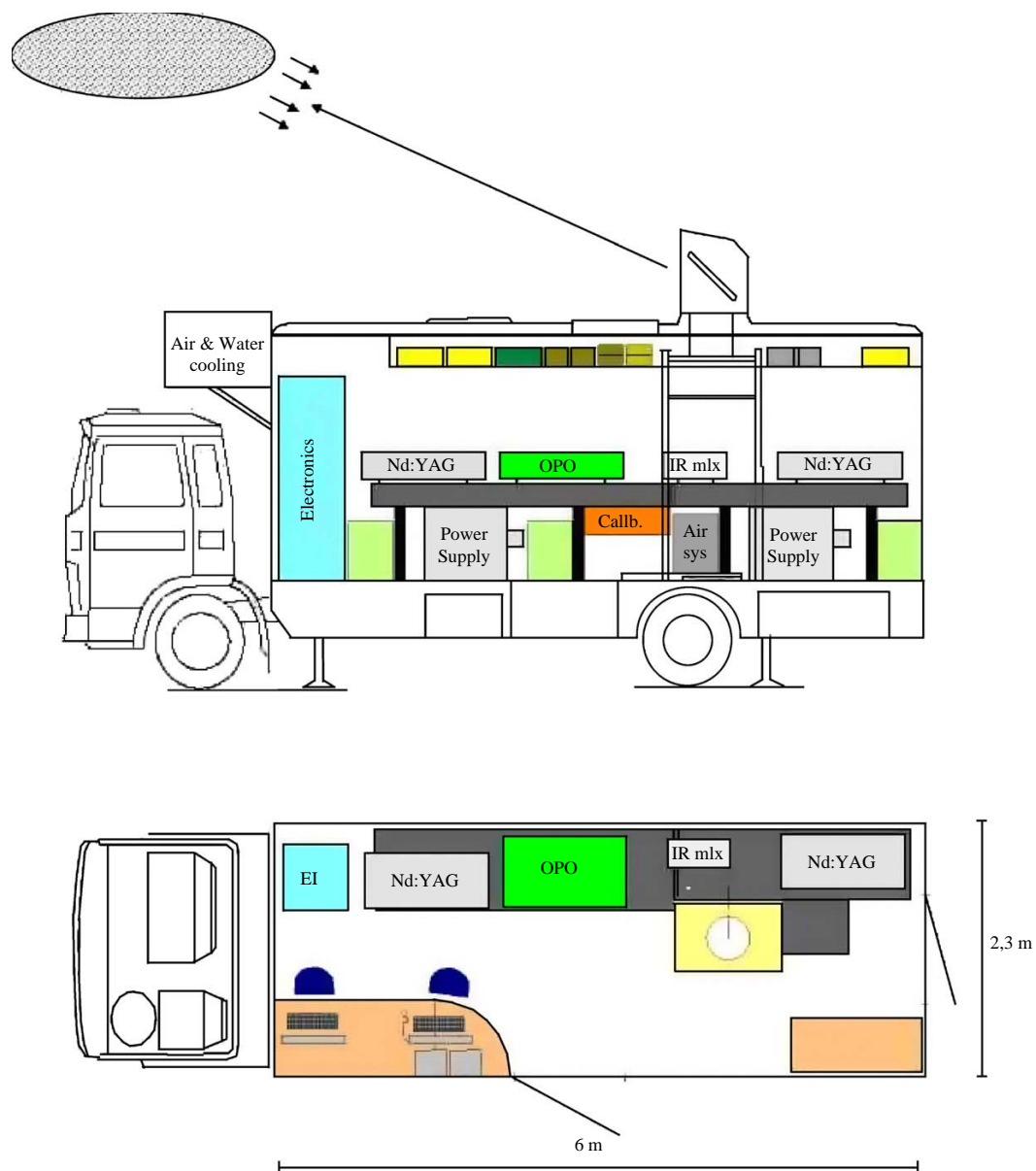


Fig. 3. Overview of the Lund mobile lidar system (Weibring et al., 2003). The laser radiation is sent through the roof-top dome and scattered by the atmosphere (represented by the grey ellipses). The back-scattered radiation is captured by the dome and directed to the detection system.

which is constantly replenished by a pump maintaining an air flow of 201min^{-1} through the system. By using Zeeman modulation techniques the system is particularly sensitive and real time measurements can be performed rather than relying on the customary gold

amalgamation technique for preconcentration before atomic absorption measurements. Spectra were collected and recorded by the computer every second as well as geographic position (the positions are shown in Fig. 1). Baseline correction time (period of time during which

the level corresponding to the zero mercury vapor concentration in the analytical cell) was set to be 30 s and was measured every 15 min. The calibration and function of the instrument was checked prior to every measurement by measuring known Hg vapor concentration in the test cell installed in the instrument. Relative deviation of the measured value of the Hg vapor concentration in the test cell from the tabulated value was within 10%. The accuracy of the instrument is $\pm 20\%$. The detection limit is 2 ng m^{-3} . The portable Hg spectrometer was installed in a vehicle together with a portable Magellan Meridian GPS system.

3. Measurements

The Idrija measurements were performed during the time 30 October–4 November 2003. The terrain in Idrija with a rather narrow valley along the Idrija river is somewhat complicated in view of positioning lidar scans for flux measurements. Wind conditions were not very favorable for flux measurements: frequently the wind speeds were very low, yielding relatively high uncertainties in the wind data. Heavy rainfall and associated low temperatures during most of the campaign decreased the mercury emission from the ground.

Lidar measurements were performed from two locations. The first one was located inside the city of Idrija at an elevation of about 30 m above the Idrija river, and close to the present visitors entrance to the mine (see Fig. 1). From here mostly horizontal scans over the city were made in directions where the beam was not

obstructed by vegetation or other structures. The second location was close to the Idrija river, about 300 m downstream (north) of the distillation plant and about 20 m above the river surface (Fig. 1). From here vertical scans downwind from the distillery were made, and also horizontal scans southwards over the valley in the direction towards the city of Idrija.

At the first position the measurements showed fairly low concentrations in all directions, too small to draw any conclusions from them. The horizontal scans showed maximum concentrations of around 50 ng m^{-3} . A vertical scan was also performed where the (low) concentration seemed to fall off at higher elevation.

The results of vertical scans downwind from the distillation plant and recorded from the second lidar site are shown in Figs. 4 and 5. In these figures, the lidar system is situated at the origin and interpolation between the measurement directions has been performed to create the concentration map. Note that these are raw measurements where the data has been gathered during a few minutes, during which time the concentration over this map is likely to change. This effect is considered to be levelled out over the measurement campaign. The line diagrams show the horizontally and vertically integrated concentrations. Strongly elevated concentrations of the order of a few hundred ng m^{-3} with a length resolution of 7.5 m are observed associated with the plant. The wind was blowing down the valley with a quite small and non-optimal angle between the wind and scan directions, which lowers the accuracy in a flux determination. Further, because of buildings blocking the lowest directions of interest some mercury flow escapes under

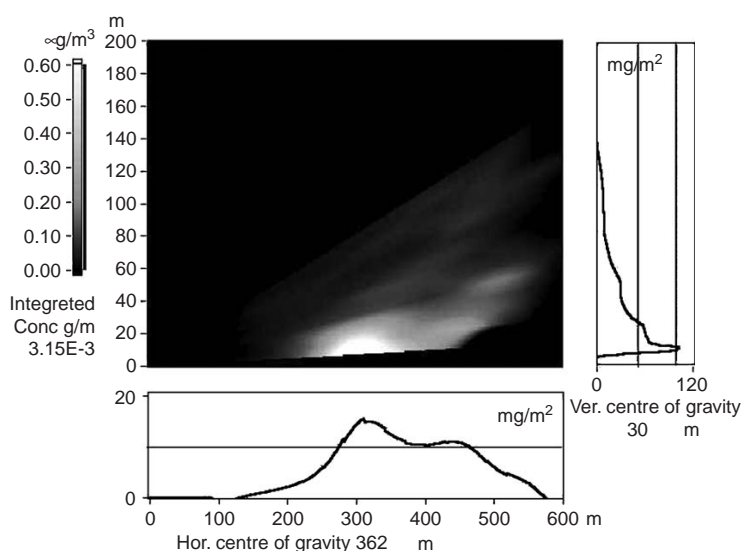


Fig. 4. Vertical scan, downwind from the distillation plant, yielding a flux of 2.4 g h^{-1} .

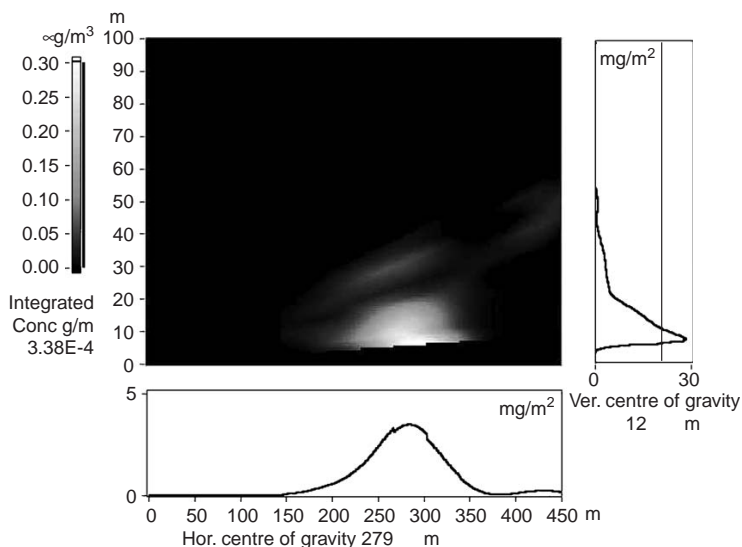


Fig. 5. Vertical scan, downwind from the distillation plant, yielding a flux of 4.7 g h^{-1} .

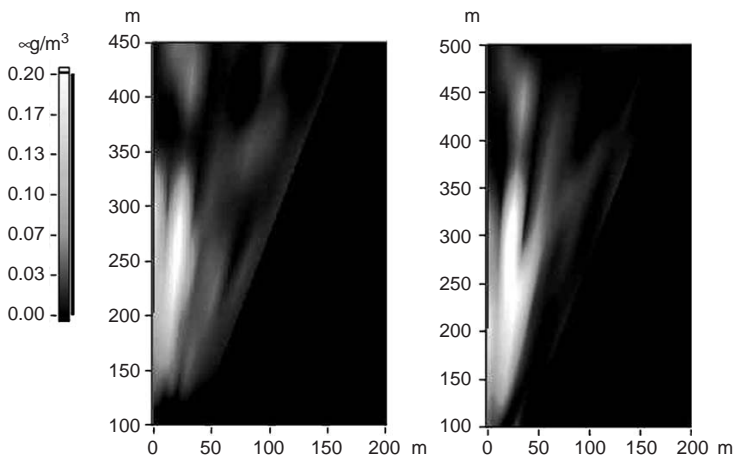


Fig. 6. Twenty degree horizontal scans southwards over the old distillation plant and river valley. The distillation plant was at the left in these pictures, at a range of $\sim 300 \text{ m}$.

the scan. However, from the two diagrams, measured flux values of 2.4 and 4.7 g h^{-1} can be evaluated. From evaluation of all flux data an average flux during the measurement time of 2 g h^{-1} was evaluated, with this value uncertain within a factor of 2, mainly due to uncertain wind assessment.

Horizontal scans starting at the distillery, which is quite close to the quickly rising valley side, and extending out over the Idrija river in a 20° sector are

shown in Fig. 6. Again, it can be seen that the concentrations rapidly fall off away from the plant. Lidar measurements were also performed in the opposite direction above the Idrija river as it continues on its way towards the Adriatic sea. An example from a vertical scan is shown in Fig. 7. It can be seen that the concentration falls off quite quickly at higher altitudes.

As mentioned above, mercury mapping over the area were also performed using the RA-915+ Zeeman

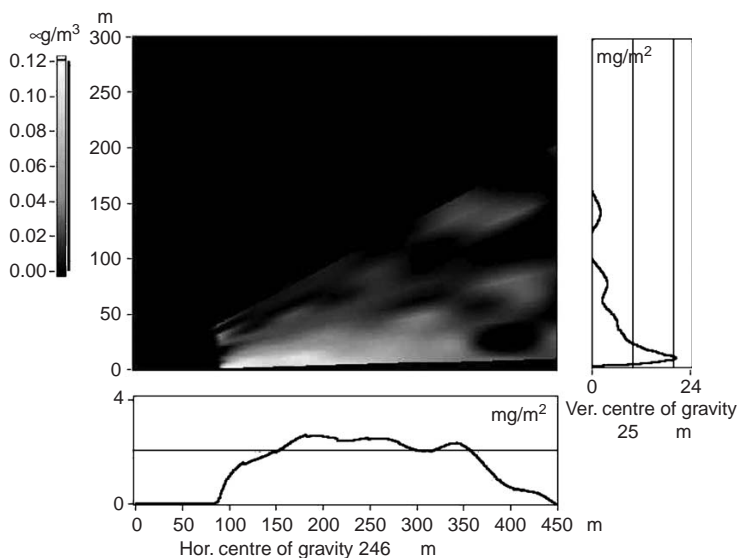


Fig. 7. Vertical scan above the Idrija river, away from the distillation plant.

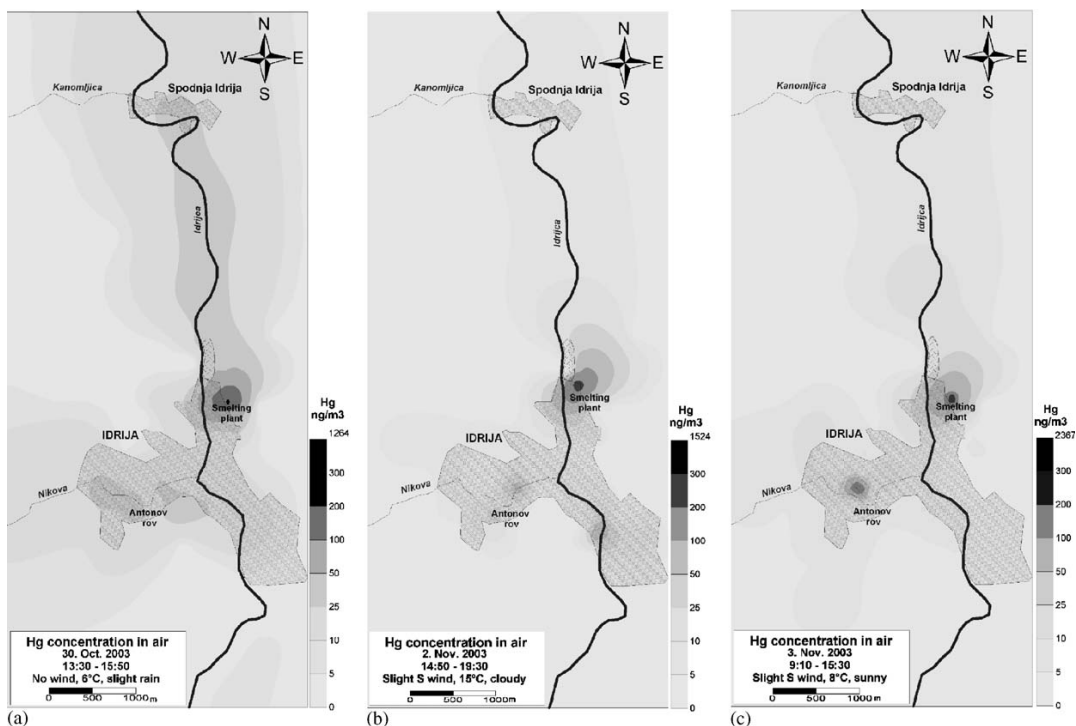


Fig. 8. Concentration maps obtained using a portable mercury point-monitor.

absorption spectrometer installed in a car traversing the roads of the area with the geometry given by GPS recordings. Results from 30 October, 2 and 3 November 2003 are given in Figs. 8a, b and c, respectively. The concentration values recorded in individual points are here smoothed into a map using the Golden Software program Surfer, version 8. The data sampling time varies between about 2 and 7 h. As can be seen, the distillery completely dominates the emission situation with values reaching above $2 \mu\text{g m}^{-3}$ being observed. It could be noted that such values corresponds to sampling 1.5 m above the road surface in direct vicinity to the plant. Average temperatures were 6, 15 and 8°C during the recordings of Figs. 8a, b and c, respectively.

4. Discussion

Lidar and point-monitoring data were found to be complementary in mapping the mercury distribution. Lidar provides a fast mapping and the potential for total flux measurements for favorable wind conditions. The mobile point monitor provided powerful large area mapping, but recording times are rather long which may influence mapping accuracy during changing wind and temperature conditions. Generally, comparatively low concentrations and fluxes were observed at Idrija due to reduced ambient temperatures and rainfall during the measurement campaign.

Acknowledgements

This work was supported by the Swedish Research Council, the Knut and Alice Wallenberg Foundation and the Jožef Stefan Institute. The Swedish team members would like to thank their Slovenian collaborators for great hospitality while in Slovenia.

References

Aldén, M., Edner, H., Svanberg, S., 1982. Remote measurement of atmospheric mercury using differential absorption lidar. *Optics Letters* 7 (5), 221–223.
Edner, H., Faris, G.W., Sunesson, A., Svanberg, S., 1989. Atmospheric atomic mercury monitoring using differential absorption lidar techniques. *Applied Optics* 28 (5), 921–930.
Edner, H., Ragnarson, P., Svanberg, S., Wallinder, E., Ferrara, R., Maserti, B.E., Bargagli, R., 1993. Atmospheric mercury

mapping in a cinnabar mining area. *Science of the Total Environment* 133 (1), 1–15.
Ferrara, R., Maserti, B.E., Andersson, M., Edner, H., Ragnarsson, P., Svanberg, S., Hernandez, A., 1998. Atmospheric mercury concentrations and fluxes in the Almadén District (Spain). *Atmospheric Environment* 32 (22), 3897–3904.
Ferrara, R., Maserti, B.E., Mazzolai, B., Di Francesco, F., Edner, H., Svanberg, S., Wallinder, E., 1999. Atmospheric mercury in abandoned mine structures and restored mine buildings at Mt. Amiata, Italy. In: Ebinghaus, R., Turner, R.R., de Lacerda, L.D., Vasiliev, O., Salomons, W. (Eds.), *Mercury Contaminated Sites*. Springer, Berlin, Heidelberg, pp. 249–257.
Gosar, M., Pirc, S., Šajn, R., Bidovec, M., Mashyanov, N.R., Sholupov, S.E., 1997. Distribution of mercury in the atmosphere over Idrija, Slovenia. *Environmental Geochemistry and Health* 19 (3), 101–110.
Grönlund, R., Sjöholm, M., Weibring, P., Edner, H., Svanberg, S., to appear. Elemental mercury emissions from chlor-alkali plants measured by lidar techniques. *Atmospheric Environment*.
Gustin, M.S., Coolbaugh, M.F., Engle, M.A., Fitzgerald, B.C., Keislar, R.E., Lindberg, S.E., Nacht, D.M., Quashnick, J., Rytuba, J.J., Sladek, C., Zhang, H., Zehner, R.E., 2003. Atmospheric mercury emissions from mine wastes and surrounding geologically enriched terrains. *Environmental Geology* 43 (3), 339–351.
Hylander, L.D., Meili, M., 2003. 500 years of mercury production: global annual inventory by region until 2000 and associated emissions. *Science of the Total Environment* 304 (1–3), 13–27.
Kosta, L., Byrne, A.R., Zelenko, V., Stegnar, P., Dermelj, M., Ravnik, V., 1974. Studies on uptake, distribution and transformations of mercury in living organisms in Idrija region and comparative areas. *Vestnik Slovenskega Kemijskega Društva* 21, 49–76.
Miklavčič, V. 1996. Mercury in the Idrija region. *Proceedings of the Meeting of Researchers on Idrija as a Natural and Anthropogenic Laboratory—Mercury as a Major Pollutant*, 24–25 May, Idrija Slovenia, pp. 6–10.
Rytuba, J.J., 2003. Mercury from mineral deposits and potential environmental impact. *Environmental Geology* 43 (3), 326–338.
Sholupov, S.E., Ganeyev, A.A., 1995. Zeeman atomic-absorption spectrometry using high-frequency modulated light polarization. *Spectrochimica Acta, Part B-Atomic Spectroscopy* 50 (10), 1227–1236.
Sjöholm, M., Weibring, P., Edner, H., Svanberg, S., 2004. Atomic mercury flux monitoring using an optical parametric oscillator based lidar system. *Optics Express* 12 (4), 551–556.
Weibring, P., Edner, H., Svanberg, S., 2003. Versatile mobile lidar system for environmental monitoring. *Applied Optics* 42 (18), 3583–3594.

PAPER III

Joint Application of Doppler Lidar and Differential Absorption Lidar to Estimate the Atomic Mercury Flux from a Chlor-Alkali Plant

M. Bennett, H. Edner, R. Grönlund, M. Sjöholm, S. Svanberg, and R. Ferrara.

Atmospheric Environment **40**, 664–673 (2006).



Joint application of Doppler Lidar and differential absorption lidar to estimate the atomic mercury flux from a chlor-alkali plant

M. Bennett^{a,*}, H. Edner^b, R. Grönlund^b, M. Sjöholm^b, S. Svanberg^b, R. Ferrara^c

^a*School of Chemical Engineering and Analytical Science, University of Manchester, Sackville Street, P.O. Box 88, Manchester, M60 1QD, UK*

^b*Department of Physics, Lund Institute of Technology, P.O. Box 118, S-221 00, Lund, Sweden*

^c*Istituto di Biofisica, Consiglio Nazionale di Ricerca, Pisa, Italy*

Received 8 April 2005; received in revised form 21 September 2005; accepted 28 September 2005

Abstract

We have combined differential absorption lidar (DIAL) measurements of mercury concentrations downwind of a chlor-alkali plant (Rosignano Solvay) with measurements of wind profiles made with a Doppler Lidar based on modern fibre-optic technology. Since the flux of pollutant is equal to the cross-wind integral of the product of concentration and wind speed, this should permit us to make a more precise estimate of the fugitive emission of mercury from the plant than could be obtained by using anemometer measurements of the wind. The flux was estimated to be 54 g Hg h^{-1} using an anemometer on the plant building; 49 g Hg h^{-1} using an anemometer on a nearby 10 m mast; and 48 g Hg h^{-1} using wind speed corrections estimated from the Doppler Lidar measurements. Because of difficulties with the range resolution of the Doppler Lidar, the precision of this estimate was not as good as it should have been, though the difference from the rooftop anemometer remains statistically significant. Corrections of this magnitude are irrelevant to the Rosignano plant, where the emission rate varies strongly with the meteorological conditions. Where a precise estimate of a steady flux is required, however, reliable measurements of the wind profile in the wake of the source are essential. Doppler Lidar provides a possible method for acquiring such measurements.

© 2005 Elsevier Ltd. All rights reserved.

Keywords: DIAL; Fibre-optics; Optical coherence tomography; OCT; Fugitive emissions; EMECAP; Building-affected flow; Wind measurements

1. Introduction

Mercury is a well-known toxic element (or pollutant), of significance even at very low levels in the environment. A recent study, initiated by the

European Union (EMECAP, European Mercury Emission from Chlor-Alkali Plants) has attempted to quantify the impact on the environment of one of the major artificial sources of mercury and to develop tools for estimating the risk to health that such emissions represent. As part of this study, the differential absorption lidar (DIAL) system developed by the Lund Institute of Technology in Sweden (Svanberg, 1994; Weibring et al., 2003)

*Corresponding author.

E-mail address: mike.bennett@manchester.ac.uk (M. Bennett).

undertook a programme of measurements of fugitive mercury flux at three European chlor-alkali plants (Wängberg et al., 2003; Sjöholm et al., 2004; Grönlund et al., 2005) between August 2001 and August 2003. In particular, a campaign of measurements was made at the Rosignano Solvay plant, near Livorno, Italy, in the period 1–10 July 2003.

The DIAL system remotely assesses range-resolved concentrations of an atmospheric pollutant from the ratio between the backscattered light on and off a spectroscopic absorption line of the pollutant. The range resolution is obtained by emitting short (a few nanoseconds long) pulses of light, combined with time-resolved acquisition of the elastically backscattered light. Emitting light pulses, produced by a Nd:YAG pumped optical parametric oscillator laser system, on and off the absorption line of mercury at 253.65 nm in different directions within a scanning plane renders a spatial map of the concentration distribution which, when combined with the wind speed, provides an estimate of the atmospheric flux of mercury (Sjöholm et al., 2004). Traditionally, the Lund group has installed a single anemometer and wind vane on the plant buildings (Ferrara et al., 1992) and used this to calculate the flux. We had some concern that such a wind speed measurement might be unrepresentative. For the summer measurements in Rosignano, therefore, the DIAL system was supplemented by a Doppler Lidar system being developed at UMIST in Manchester, UK (now a part of the University of Manchester). This should have been capable of remotely measuring the vertical profile of wind speed at right angles to the DIAL scanning plane, and should thus have allowed a more reliable estimate of the fugitive mercury flux.

The Doppler Lidar has been described previously by Bennett (2003). It is a continuous-wave (rather than a time-gated) device and has been constructed using mostly off-the-shelf components developed for fibre-optic communications. The operating wavelength is $\lambda = 1.55 \mu\text{m}$. This is generated by a distributed feedback (DFB) laser diode (GEC LD4204) and amplified to an output power of 1 W using a commercially available optical amplifier (IPG model EAM-1-C).

Conventional CW Doppler Lidars focus the output and return beams in the same volume of space in order to achieve range resolution (Karlsson et al., 2000; Harris et al., 2001). With our system, we attempt instead to define the target range using the finite coherence length of the laser source. If we

bleed off a reference signal of a few milliwatts and delay it in a single-mode fibre-optic cable before mixing it with scattered radiation returned from the sky, we should only see a narrow-band beats signal when the length of the delay line matches the path length in the atmosphere to within the coherence length of the source. Scattering from other distances will give a beats signal widened by twice the linewidth of the source (cf. Harris et al., 1998). In this case, the linewidth of our source is $\Delta\nu = 1.4 \text{ MHz}$; the coherence length for the beats signal is $\Delta r = c/(2\pi\Delta\nu) = 34 \text{ m}$, and this should be the effective range resolution of the system.

This principle of optical coherence tomography is now routinely applied in medical imaging (Fercher et al., 2003; Yang et al., 2003), for example of the retina. Our system is a form of Doppler OCT, but since we use a DFB laser source instead of a superluminescent diode, the physical scale of our measurement is a factor of order 10^7 greater. (In OCT, the source linewidth would be some tens of nm, to give a coherence length of a few μm). Note also that, in conventional OCT, fringes are generated by varying the length of the reference arm; in our system it is the effective length of the sample arm which is varied by the motion of atmospheric aerosol.

The system is controlled by a 1.3 GHz PC running under the Linux operating system, with the return beats signal being captured by a commercial 8-bit frame grabber card. This samples the signal at 28.6 MHz. Software has been written (Bennett, 2004) to calculate a 50-point 10 MHz power spectrum for each Msample of data. Each spectrum is then examined for a narrow-band ($\Delta f < 1 \text{ MHz}$) signal, with broad-band signals being rejected. The absolute radial velocity is given by $\lambda/2$ times the beats frequency, i.e. a frequency of 10 MHz corresponds to 7.75 m s^{-1} . The system can make in excess of 15 wind speed determinations per second, implying that it is fast enough to process more than half the signal presented to it.

With a focussed system, the optics are arranged so that the scattered signal is collected from as small a volume as possible. With our system, by contrast, we want scattered radiation over a considerable range to be returned to the instrument. This is achieved by arranging for output and return beams to be collimated and gently converging (i.e. the system is bistatic). The output optics are of 50 mm diameter (cf. Fig. 1(a)), being almost in contact at the instrument and arranged to overlap fully at a



Fig. 1. Optical head of Doppler Lidar system. The beam is normally directed at 60° to the horizon. In the image to the right, an angle of elevation of 11.9° has been improvised.

range of about 120 m. Within the overlapping range, the precise target range is defined by switching in fibre delay loops in a binary fashion. As configured at Rosignano, the system cycled around eight nominal ranges between 42 and 217 m.

A more reliable optical overlap could be achieved by using a monostatic system. That is, the output and return beams would follow the same external path, being separated within the instrument by an optical circulator. Within the constraints of our CW system, however, it would then have been impossible to distinguish our desired signal (i.e. from clear air) from unwanted scattering from the output optical surfaces and possibly from distant strong scatterers such as clouds.

Radiation of $\lambda = 1.55 \mu\text{m}$ is absorbed strongly by water. It thus cannot penetrate the cornea and a relatively relaxed maximum intensity of 1000 W m^{-2} is permissible for continuous ocular exposure. Integrated exposures of 10 kJ m^{-2} are permissible at higher intensities. Peak axial radiation intensity from our system is near the permissible limit for continuous viewing. It is thus inadvisable to stare into the beam while it is operating; but the system is effectively safe to the naked eye when directed above the horizon.

2. Methods

The layout of the site is given in Fig. 2. Previous experience at the plant (Ferrara et al., 1992) had shown that most of the fugitive mercury emission was released from the electrolytic cell rooms, indicated as C in the figure. The DIAL system was therefore installed at the point marked L (for 'Lund') 200 m to the N. For W winds, this permitted vertical scans to be made along the roadway between the plant and the administrative buildings (azimuth 174°). This was the most common arrangement during the period of the campaign. There were a few occasions when the wind was more NW. In that case the scanning azimuth was increased to 193° . A few scans were also made upwind of the cell house to check that there were no other significant sources.

Each DIAL 'sweep' consisted of concentration profiles along 10–15 directions, from as near the horizontal as possible to around 10° elevation. The site was deemed to be level, with the laser steering mirror being 4 m above site datum. Each sweep corresponded to a sampling time of 4–5 min, with measurements continuing where possible between 1100 and 2300 each day. Over the 10 days of the

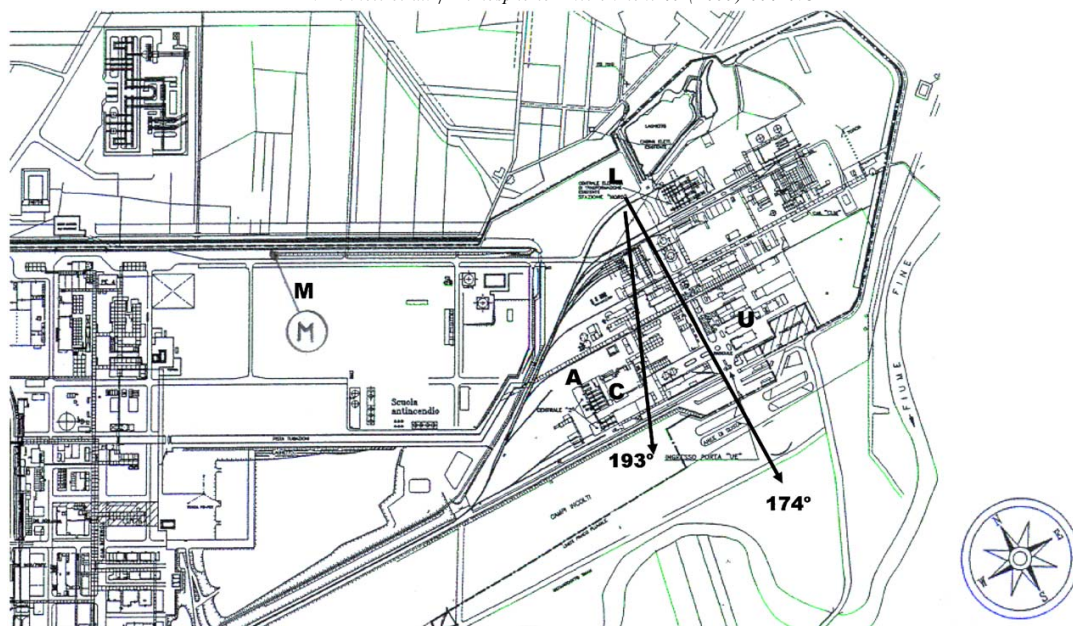


Fig. 2. Site map of western section of Rosignano plant. A designates the anemometer of the Lund group, C designates the cell house, L designates the DIAL, M designates the mast anemometer and U designates the Doppler Lidar.

campaign, 574 such sweeps were obtained. Details of these measurements are given in Grönlund et al. (2005).

The Solvay plant operates an anemometer and wind vane on a 10 m mast at the point marked M in Fig. 2, 400 m to the NW of the cell house. 5 min averages of wind speed and direction from this system for the entire period of the survey were made available to us.

The Lund group sited an anemometer and wind vane set (Nexus Wind Transducer manufactured by Silva Marine Electronics) 3.9 m above the roof on the NW side of the cell house (cf. Fig. 2). This was logged at 30 s intervals. These data were available for most of the survey, though the logging unfortunately failed between 1720 on 5 July and 0945 on 8 July.

The Doppler Lidar was installed in a laboratory building to the E of the cell house. This is marked U (for 'UMIST') in Fig. 2. The optical head was placed on the roof of the building (Fig. 1) at a height of 9.8 m above ground level: the operating electronics etc. could then be placed in an air-conditioned laboratory two floors beneath, with fibre-optic cables running outside up to the head. The default situation was that the optical head would be placed

on a fixed stand with an elevation of 60° from the horizontal and at an azimuth at right angles to the DIAL scanning plane. Assuming that the mean flow was approximately horizontal, the measured radial wind speed then merely had to be doubled to give the horizontal wind component normal to the DIAL scanning plane. Multiplying the wind component by the mercury concentration and integrating vertically should have given the mercury flux directly. It rapidly became evident that most of the mercury plume lay below the lowest nominal range of the Doppler Lidar. The angle of elevation of the Doppler Lidar was therefore gradually reduced (Fig. 1): over the final 5 days of measurements, the angle of elevation was varied between 1.9° , 11.9° and 27.9° . Note that, since the output beam of the Doppler Lidar is only 50 mm in diameter and is effectively eye-safe, it was perfectly feasible to direct it along gaps between plant structures.

3. Experimental results

The DIAL operated without significant problems for the period of the survey. Its measurements were combined with the wind measurements from the cell house anemometer to give a mean emission of

54 g Hg h⁻¹ (Grönlund et al., 2005). (Wind measurements from the 10 m mast were used for the 3 days when the cell house anemometer was not being logged).

Fig. 3 shows the ratio of the wind speeds measured by the anemometers on the roof of the cell house and on the 10 m mast as a function of wind direction. The large scatter is to be expected, since the rooftop measurements represent an averaging time of only 30 s, and is of little consequence since the ultimate calculation of flux is proportional to ~5000 such measurements. Rather more worrying is the mean bias, which varies between 0.88 in SSW winds and 1.27 in WSW winds. Such variation is to be expected: in SSW winds, the 10 m anemometer experiences a clear fetch over flat terrain, while in WSW winds it is in the wake of the polyethylene plant (Fig. 2). Equally, one would expect that in NW winds, the rooftop anemometer would experience some acceleration of the flow as the upwind streamlines are compressed over the building. Indeed, the limited number of measurements we obtained for NW winds (not shown in Fig. 3) suggested a wind speed ratio of about 1.5 for this direction.

The Doppler Lidar was started at 1634 on 1 July and subsequently ran on every day of the survey, typically between 0900 and 1830. The final measurements were made at 1000 on 9 July. Since the system relies on Mie scattering by atmospheric aerosol, a clear atmosphere gives a poor signal and in general we may only expect a reliable signal from our

system for atmospheric visibilities of less than 30 km. Visibility over the period of the survey was unfortunately much better than had been anticipated for a summer in Italy. On 7–8 July, the island of Elba was sometimes visible, 70 km away! In these conditions, very few measurements were obtained. At the beginning of the survey (2 July) horizontal wind speeds were in excess of 15 m s⁻¹, shifting the beats signal out of the calculated frequency window. The Doppler Lidar was then rotated 45° out of the wind so that a measurable radial component could still be obtained.

Fig. 4 shows the horizontal wind speeds measured with the Doppler Lidar (*numbers*) and with the rooftop anemometer (*solid line*) over the afternoon of 3 July 2003. Each Lidar measurement corresponds to a 1 min average with 1–8 corresponding to ranges 42–217 m in steps of 25 m. It may immediately be seen: (a) that there is a very good time correlation between the Lidar and the anemometer measurements; (b) that the Lidar consistently gives a wind speed about 50% larger than that given by the anemometer; but (c) that no consistent profile is observed, i.e. the wind speed at range 1 is not consistently much less than that for range 8. Overall, the measurements were consistent with the Lidar functioning well, but providing little range resolution.

Note that we can rely on the accuracy of radial wind speeds reported by the Doppler Lidar, since we know very accurately both the wavelength of the radiation and the sampling frequency of the frame

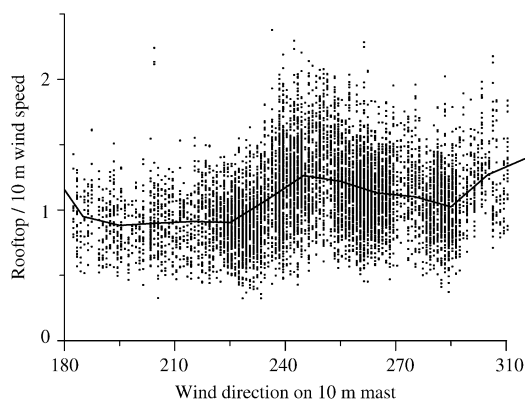


Fig. 3. Ratio of wind speed measured on cell house roof to that from the 10 m mast as a function of the wind direction on the 10 m mast. The solid line shows the mean ratio; dots show individual 30 s measurements.

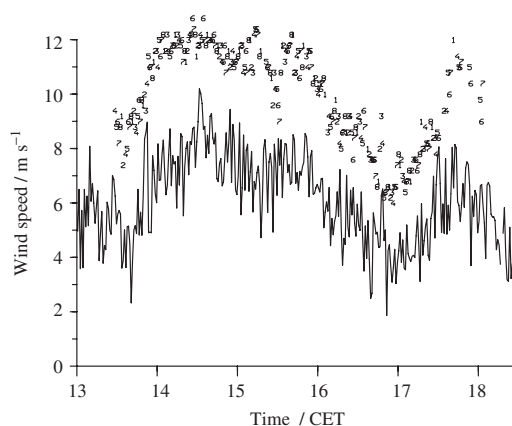


Fig. 4. Time series of Doppler Lidar wind speed at an average height of 130 m above ground level and of rooftop wind speed on the afternoon of 3 July 2003.

grabber. The timing of the power spectrum analysis has also been checked against a pulse generator (Bennett, 2004).

Subsequent measurements (Bennett et al., 2004) showed that the linewidth of the master oscillator was substantially less than that specified when the DFB laser oscillator was first purchased and tested. As implemented at Rosignano, the system appeared to have a linewidth of about 500 kHz, rather than the 1.4 MHz previously found. This would imply a range resolution of 95 m, greatly degrading the measurement of the wind profile.

It now appears that this narrowing was due to a small amount of back-reflection within the fibre-optic system. Effectively, such a reflection puts the laser diode within an external cavity, which narrows the line over which gain will take place (Morthier, 2002). The narrowing depends on the product of the path length to the reflector and the field strength of the reflection. Through an oversight, the fibre-optic tail to the first isolator in the system was 2 m, rather than the 20 cm specified. This meant that a back-reflection of as little as -60 dB of the signal power could have been enough to give the narrowing observed. This is within the specification of the isolator. The tail has now been reduced to a length 26 cm and it is found that the linewidth has been widened to about 1 MHz. This should be adequate for future measurements.

4. Analysis of wind speed measurements

In the light of the linewidth problem, we must regard the Doppler Lidar measurements of wind speed as accurate, but arising from a range of distances. It is probably simplest to take the effective distance of the measurement as being the centre of this range, i.e. at 129.5 m. For an angle of elevation of θ , this corresponds to a height of $9.8 + 129.5 \sin(\theta)$ m. Fortunately, since we have measurements for wind directions between 180° and 290° both from the 10 m anemometer and from the Doppler Lidar with $\theta = 60^\circ$, and similar measurements in westerly winds for θ between 1.9° and 60° , we should be able to calibrate the 10 m measurements to estimate the wind profile in the wake of the cell house down to a height of ~ 14 m.

Fig. 5 shows the ratio of the Lidar wind speed to that measured by the 10 m anemometer for the period over the first 4 days of the survey when the Lidar was at an angle of elevation of 60° . Note that we have corrected here for the angle between the

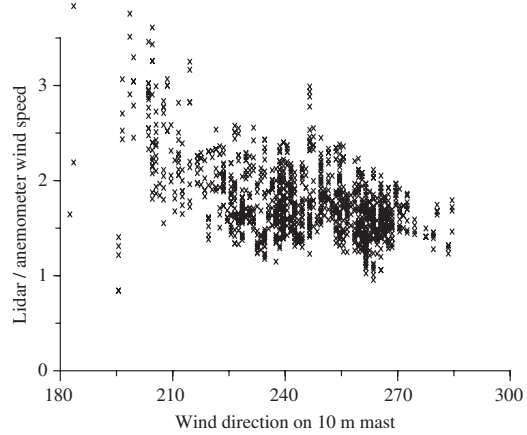


Fig. 5. Scatter plot of the ratio of Doppler Lidar wind speed to 10 m anemometer wind speed vs. wind direction at an angle of elevation of 60° .

azimuth of the Lidar (265°) and the wind direction as measured on the 10 m mast: the ratio is of the horizontal component along the azimuth of the Lidar. Mean ratios as a function of wind direction are listed in Table 1.

Several points may be noted from the scatter plot:

- For wind directions greater than 210° , the ratio is well defined. There are some suggestions of detailed structure, presumably arising from the exposure of the anemometer.
- An elevation of 60° implies that the mean height of measurement by the Doppler Lidar was 122 m. Assuming a $1/7$ power law of the wind speed with height (cf. e.g. Turner, 1970), we should then have expected the ratio of wind speeds to be $12.2^{1/7} = 1.43$. This is somewhat less than observed, suggesting that the anemometer is in the wake of plant buildings for most of these wind directions.
- The anemometer has a clear fetch in SSW winds, so we should have expected the ratio to fall off for wind directions of less than 210° (as we saw in Fig. 3). The large increase observed arises because of the *cosine* correction to the ratio as the angle between the wind direction and the azimuth of the Lidar approaches 90° . For southerly winds, the corrected ratio is very sensitive to this ratio: the asymmetry of Fig. 5 implies that there may have been a modest ($\sim 10^\circ$) offset in the measurement of the

Table 1
Wind speed corrections as a function of wind direction

Direction (deg)	<i>n</i>	DoLi/(10 m)	± SE
180	13	6.08	2.69
190	19	2.61	1.06
200	63	2.52	0.46
210	60	2.09	0.38
220	161	1.86	0.29
230	263	1.73	0.28
240	238	1.81	0.33
250	225	1.75	0.27
260	333	1.57	0.23
270	39	1.58	0.16
280	13	1.56	0.20
290			

n denotes the number of measurements. The Doppler Lidar was at an angle of elevation of 60°.

direction difference. Fortunately, since the Doppler Lidar was set up with an azimuth approximately at right angles to the scanning plane of the DIAL, the *cosine* correction cancels when calculating the flux.

On the basis of Table 1, we can thus extrapolate the wind speed observed on the 10 m mast (whether or not this is in the wake of a plant building) to the free stream flow at some height above the buildings. We now wish to extrapolate from the free stream flow to the wind speed in the wake of the cell house. For this, we can use the measurements from the second half of the survey, where the angle of elevation of the Doppler Lidar was gradually reduced. The wind direction over this period was mostly westerly. Fig. 5 displays the ratio of the Lidar to the anemometer wind speed for wind directions between 260° and 280° for four different angles of elevation of the Lidar. As may be seen, the ratio increases with the effective height of the measurement. For simplicity, we may fit the data to a linear regression:

$$\text{DoLi}/(10 \text{ m}) = 0.719 + 0.00683 \times \text{Height (m)}. \quad (1)$$

By implication, at a height of 122 m, we should have $\text{DoLi}/(10 \text{ m}) = 1.552$. This is slightly smaller than the values listed for these wind directions in Table 1, (i.e. about 1.578) though well within their 95% confidence limits.

It is also interesting to note that the scatter of the ratio is much larger at the lowest elevation: in this case the ratio's standard deviation was 0.373, while it lay in the range 0.186–0.220 for the other elevations. At the lowest elevation, the Lidar was directed between plant elements, so we should indeed have expected much higher levels of turbulence.

We now have the tools to extrapolate from the wind speed and direction measured by the Solvay anemometer to the wind component normal to the DIAL scanning plane at the height of the centre-of-gravity of the plume. Suppose that the DIAL azimuth is at 174°, that the plume centre-of-gravity is at 25 m and that the 10 m wind speed is 10 m s^{-1} with a direction of 225°. Then from Table 1, the wind speed at a nominal height of 122 m would be 18.62 m s^{-1} . Extrapolating to a height of 25 m, gives us a speed of $18.62 \times (0.719 + 0.00683 \times 25)/1.578 = 10.50 \text{ m s}^{-1}$. (Note that we have assumed that the vertical profile of wind speed within the wake is more or less independent of wind direction). Finally, the component at right angles to the scanning plane is given by $10.50 \sin(225^\circ - 174^\circ) = 8.16 \text{ m s}^{-1}$. It is this value which will be multiplied by the integrated concentration within the scanning plane to give the mercury flux.

Several points may be noted regarding this procedure:

- The final *sine* correction approximately cancels the *cosine* correction for the angle between the Doppler Lidar azimuth and the 10 m wind direction. The precise alignment of the wind vane is thus unimportant.
- The calculated flux is actually rather insensitive to the range of distances sampled by the Doppler Lidar. At low angles of elevation, the Doppler Lidar sampled the wind speed at rooftop height over a range of distances. This was also the height of the mercury plume. We are less certain of the distances sampled at high angles of elevation, but we do not really need to know the precise height of measurement: we have extrapolated our wind speed up to a nominal height of 122 m using Table 1, and then interpolated down to the plume height again using Eq. (1).

(c) The wind component as calculated above depends only on the calibration of the Doppler Lidar, not on that of the 10 m anemometer. As noted in the previous section, this calibration should be quite accurate.

5. Estimation of mercury flux

Ultimately, we obtained three possible estimates of the average mercury flux:

- That obtained using (mostly) the rooftop anemometer. This was calculated to be 54 g Hg h^{-1} (Grönlund et al., 2005).
- That obtained using the 10 m anemometer. We now calculate this to be 49 g Hg h^{-1} . It is not surprising that this should be 10% less than estimated using the rooftop anemometer, since the wind direction was mostly westerly over the period and, as we saw in Fig. 3, the rooftop anemometer could read 20–30% higher than the 10 m anemometer for winds in this sector.
- That obtained using the 10 m anemometer rescaled using Table 1 and Eq. (1). In this case, we obtained 48 g Hg h^{-1} .

Given the large scatters observed in Figs. 5 and 6, it might be reasonable to doubt whether such modest differences are of significance. It transpires that the most significant uncertainties arise not from the scatter of the measurements but from various inherent biases.

We may consider the scatter on individual wind determinations arising from Table 1 and Fig. 6. For wind directions lying between 260° and 280° , the weighted mean percentage standard deviation given by Table 1 (i.e. extrapolating from the 10 m anemometer to the Doppler Lidar at 60° elevation) is 14%. Similarly, the percentage standard deviation for a height of 14 m implicit in Fig. 6 (i.e. interpolating back to within the building wake) is $100 \times 0.373/1.578 \approx 24\%$. Adding the two errors in quadrature gives a rather large standard deviation of $\pm 27.4\%$ to the individual wind speed determinations. This scatter arises largely because of the difference in time and space between the anemometer measurement and the Lidar measurement. The two measurements are 400 m apart; the times of sampling do not necessarily match precisely; and the averaging times are different. The physical separa-

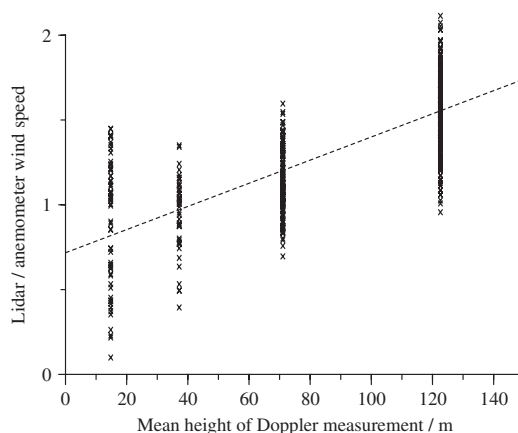


Fig. 6. Scatter plot of the ratio of Doppler Lidar wind speed to 10 m anemometer wind speed vs. nominal height for westerly winds.

tion between the two wind speed determinations is thus larger than the length- and time-scales of the convective turbulent elements passing across the test site. Instrumental inaccuracies may also contribute. Choosing a height of 14 m is, of course, the worst case, since the Lidar is then sampling within the turbulent wake of the buildings. Even above the wake, however, there would still be a scatter of $\pm 20\%$.

That said, we had 559 DIAL sweeps with usable wind directions from which to estimate the mean flux. Assuming errors are independent, the standard error on the mean arising from the Lidar wind speed determination is only $27.4/\sqrt{559} = 1.16\%$, i.e. a modest error relative to the differences between the three flux determinations.

We should consider now various sources of bias in the wind speed determination within the mercury plume. Firstly, there is the physical separation between the Doppler Lidar measurement and the 10 m anemometer. It should be noted that the terrain on which the plant is built is extremely flat and that the shoreline is several km distant. We should expect therefore that synoptic or micrometeorological differences between the two sites should be quite modest. Most of the difference in wind speed between the two sites should arise from their differing local exposure (in respect of buildings etc.) and from their independent sampling of convective turbulent elements as they advect past the site. The

latter effect should give rise mostly to scatter, as has been discussed above. The former will lead to large biases as a function of wind direction, and probably also as a function of stability. Table 1 attempts to capture these biases. Experience (e.g. Bennett, 1992) shows that at high Reynolds numbers in neutral conditions such biases are extremely repeatable. Allowing for them can improve the accuracy of the wind speed measurement by an order of magnitude. Since the relative bias shown in Fig. 5 ranges over about 30% between wind directions 210° and 280°, we should thus expect any residual bias after recalibration to be only a few percent of wind speed: a greater bias would have remained if many of our measurements had been made in stable conditions.

A second matter of concern is the true linearity of Fig. 6. Aside from simplicity, a linear regression to the data has the virtue that, with a linear wind profile, it is not necessary to calculate the integral of the product of mercury concentration and wind speed with height in order to calculate the flux: one need only multiply the height-integrated concentration by the wind speed at the height of the centre-of-gravity of the plume. This is especially advantageous with the plumes observed here (Grönlund et al., 2005) which tend to be vertically skewed: a high concentration is seen in the wake of the buildings and this then tails off vertically up to a height of 75–100 m. The overall centre-of-gravity is typically in the range 20–35 m. The linear fit in Fig. 6 appears to be adequate for heights above 30 m, but we do not have enough reliable measurements at lower heights to extend the line downwards as precisely as we might wish. Note that linear regression implies a Lidar/(10 m) ratio of 0.815 at 14 m, while the mean observed ratio is 0.920 at that height. If this offset is typical for (say) half the weight of the plume, then we shall have underestimated the mercury flux by 3.3%.

It should also be recognized, of course, that the wind speed may vary laterally across the plume. This would be a significant issue if the cell house were an isolated building. As may be seen, however, from Fig. 2, the plume from the cell house will be advected over an extended range of structures for all W and SW winds: dynamically, there is then nothing very special about the cell house wake. We have thus felt justified in treating the wind profile measured by the Doppler Lidar as being representative of the general flow through and over the plant.

6. Discussion and conclusions

Figs. 3, 5 and 6 illustrate clearly why wind measurements from a fixed-point monitor must be treated with caution when being combined with DIAL measurements to estimate fugitive fluxes.

There is the obvious issue that the wind speed at a given point is sensitively dependent on the location of nearby obstructions. We thus see in Fig. 3 that the ratio of the wind speeds from two anemometers on a complex site can vary over a range of 40% as a function of wind direction. Further, since the fugitive emission lies within the wake of plant buildings, we should really want information on the vertical profile of wind speed through the fugitive plume.

A more subtle issue is that to calculate the flux, we must multiply by the *sine* of the angle between the DIAL scanning plane and the wind direction. Where the two are approximately at right angles, there is not a problem. Inevitably, however, there are occasions when the angle becomes acute and the corrected value then becomes sensitively dependent on the precise wind direction (cf. Fig. 4). It is practically quite difficult to align a wind vane to better than a few degrees; and in addition the wind direction will vary across a complex site. The *sine* correction thus adds a further uncertainty to the calculated flux. Grönlund et al. (2005) indeed felt obliged to reject measurements when the measured wind direction was at too acute an angle to the scanning plane.

The use of a Doppler Lidar has side-stepped these difficulties. By setting up the system approximately at right angles to the DIAL scanning plane, the *sine* correction has been largely cancelled. And by using such remote sensing to estimate vertical wind speed profiles, we can allow for problems in the detailed exposure of the anemometers. Note that in this campaign the Doppler Lidar measurements were the only measurements of wind speed actually made within the wake. Clearly, the performance of the Doppler Lidar system on this particular campaign was not as it should have been. The lack of range resolution severely limited our ability to measure the velocity profile in the wake simultaneously with the DIAL measurements. This led to systematic errors which, although probably still significantly smaller than the difference between the Doppler Lidar and the rooftop anemometer, were still much larger than should in principle have been obtainable.

Overall, the corrections implied by our Doppler Lidar measurements imply a reduction of 12% in the estimated fugitive emission, to an accuracy of perhaps half of this amount. In the particular case of Rosignano, such a precision is probably not called for. As noted by Grönlund et al. (2005) the emission from the plant varied between 20 g Hg h^{-1} in a winter campaign and 54 g Hg h^{-1} in this summer one. This partly reflected the change in the mercury vapour pressure with temperature, but also the chance that the summer campaign had taken place in a period of relatively high wind speeds: a linear dependence was noted between the mercury flux and the rooftop wind speed. Given that the emission can vary strongly with the meteorological conditions, it does not seem profitable to put significant resources into measuring the wind profile to a precision of a few percent. Where fugitive emissions are believed to be much steadier, however, their precise determination will require wind profile measurements of this nature.

Acknowledgements

We are grateful to the management and staff of the Solvay plant at Rosignano for their permission to carry out this work; for their assistance in the course of it; and for the provision of the meteorological data from the 10 m mast. The Doppler Lidar was constructed with the help of grants from National Power and from the (UK) Engineering and Physical Sciences Research Council. Its application in this study was funded by the (UK) Natural Environment Research Council. The DIAL measurements were funded by the EMECAP programme, for which funding was principally provided by the European Commission but with additional sponsorship from the Regional Agency for Environmental Protection in Tuscany and from the Livorno Public Health Office. We are grateful to Ms Harriet Bennett and Mr. Charles Saunders for technical assistance.

References

Bennett, M., 1992. Wind statistics from the Belmont TV mast, 1983–89. *Weather* 47, 114–123.
Bennett, M., 2003. Doppler Lidar for boundary-layer measurements: must it be expensive? In: 12th International School on

Quantum Electronics, Varna (Bulgaria) September 2002, Proceedings of SPIE, 5226, 249–259.
Bennett, M., 2004. Fast algorithm for detecting a small signal in the presence of normally distributed noise. *IEE Proceedings-Vision Image and Signal Processing* 151, 264–270.
Bennett, M., Bradley, S.G., von Hünerbein, S., Pease, J., 2004. Comparison of wind profiles measured with Sodar and Doppler Lidar. In: 12th International Symposium on Acoustic Remote Sensing, Cambridge, UK.
Fercher, A.F., Drexler, W., Hitzinger, C.K., Lasser, T., 2003. Optical coherence tomography—principles and applications. *Reports on Progress in Physics* 66, 239–303.
Ferrara, R., Maserti, B.E., Edner, H., Ragnarson, P., Svanberg, S., Wallinder, E., 1992. Mercury emissions to the atmosphere from a chlor-alkali complex measured by the Lidar technique. *Atmospheric Environment* 26A, 1253–1258.
Grönlund, R., Sjöholm, M., Weibring, P., Edner, H., Svanberg, S., 2005. Elemental mercury emissions from chlor-alkali plants measured by lidar techniques. *Atmospheric Environment* 39, 7474–7480.
Harris, M., Pearson, G.N., Vaughan, J.M., Letalick, D., Karlsson, C., 1998. The role of laser coherence length in continuous-wave coherent laser radar. *Journal of Modern Optics* 45, 1567–1581.
Harris, M., Constant, G., Ward, C., 2001. Continuous-wave bistatic laser Doppler wind sensor. *Applied Optics* 40, 1501–1506.
Karlsson, C.J., Olsson, F.Å.A., Letalock, D., Harris, M., 2000. All-fiber multifunction continuous-wave coherent laser radar at $1.55 \mu\text{m}$ for range, speed, vibration and wind measurements. *Applied Optics* 39, 3716–3726.
Morthier, G., 2002. Feedback sensitivity of distributed-feedback laser diodes in terms of longitudinal field integrals. *Journal of Quantum Electronics* 38, 1395–1397.
Sjöholm, M., Weibring, P., Edner, H., Svanberg, S., 2004. Atomic mercury flux monitoring using an optical parametric oscillator based lidar system. *Optics Express* 12, 551–556.
Svanberg, S., 1994. Differential Absorption Lidar. In: Sigrist, M.W. (Ed.), *Air Monitoring by Spectroscopic Techniques*. Wiley, New York.
Turner, D.B., 1970. Workbook of Atmospheric Dispersion Estimates. PHS Publication no. 999-AP-26. US Department of Health, Education & Welfare, National Air Pollution Control Administration, Cincinnati, OH.
Wängberg, I., Edner, H., Ferrara, R., Lanzillotta, E., Munthe, J., Sommar, J., Svanberg, S., Sjöholm, M., Weibring, P., 2003. Atmospheric mercury near a chlor-alkali plant in Sweden. *Science of the Total Environment* 204, 29–41.
Weibring, P., Edner, H., Svanberg, S., 2003. Versatile mobile Lidar system for environmental monitoring. *Applied Optics* 42, 3583–3594.
Yang, V.X.D., Gordon, M.L., Seng-Yue, E., Lo, S., Qi, B., Pekar, J., Mok, A., Wilson, B.C., Vitkin, I.A., 2003. High speed, wide velocity dynamic range Doppler optical coherence tomography (Part II): imaging in vivo cardiac dynamics of *Xenopus laevis*. *Optics Express* 11, 1650–1658.

PAPER IV

Fluorescence Lidar Multispectral Imaging for Diagnosis of Historical Monuments – Övedskloster, a Swedish Case Study

R. Grönlund, J. Hällström, S. Svanberg, and K. Barup.

In *Lasers in the Conservation of Artworks: Lacona VI Proceedings, Vienna, Austria, Sept. 21–25, 2005* (J. Nimmrichter, W. Kautek, and M. Schreiner (Eds.)), pp. 583–592, (Springer, Berlin, Germany, 2007).

Fluorescence Lidar Multispectral Imaging for Diagnosis of Historical Monuments – Övedskloster, a Swedish Case Study

Rasmus Grönlund¹, Jenny Hällström², Sune Svanberg¹, and Kerstin Barup²

¹ Atomic Physics Division, Lund University, P.O. Box 118, SE-221 00 Lund, Sweden, Phone: +46-462-224138, Fax: +46-46-2224250
rasmus.gronlund@fysik.lth.se

² Department of Architecture and Built Environment, Lund University, P.O. Box 118, SE-221 00 Lund, Sweden, Phone: +46-46-2227272, Fax: +46-46-2220811
jenny.hallstrom@byggark.lth.se

Abstract A fluorescence lidar measurement has been performed on the castle Övedskloster in Sweden. A mobile system from the Lund University was placed at ~40 m distance from the sandstone façade. The lidar system, which uses a frequency-tripled Nd:YAG laser with a 355-nm pulsed beam, induces fluorescence in each target point. Areas were studied by using whisk-broom scans. The possibility of detecting biodeteriogens on the surface and characterization of materials was confirmed. The method can be a tool for conservation planning and status control of the architectural heritage where fluorescence light can point out features that are not normally visible under natural illumination.

1. Introduction

The possibility of in-situ optical remote investigations is an important instrument for the ongoing maintenance and care for our architectural heritage. Also, for future conservation and restoration projects, the non-destructive methods of investigation are vital. The fluorescence technique is well known in areas such as remote sensing of marine oil spills and medical diagnostics. The use of laser-induced fluorescence (LIF) for building investigation was introduced in field studies of, for example, the Lund Cathedral in Sweden and the Cathedral and Baptistery in Parma, Italy [1, 2].

The technique allows us to reveal aspects that are not evident to the naked eye or photography and makes it possible to extend the application of fluorescence spectroscopy to the outdoor environment with sometimes large distances and uncontrollable background light and with no need for scaffolding or taking samples. The aim of the fluorescence lidar method is to use both point monitoring and scanning of areas (whisk-broom technique) to provide multispectral images in order to distinguish and identify different materials and biodeteriogens and other substances not yet visible to the human eye. These colour-coded images could then form a basis for the decision-making and analysis of the historical building façade.

The possible application of the technique for the cultural heritage field includes: detection and identification of biodeteriogens on the façade,

characterization and identification of stone materials, and identification of treatments performed on the surface. Biodeteriogens can be identified through the presence of chlorophyll that has strong absorption bands in the UV-visible region and fluoresces in the near infrared. The fluorescence spectral features from stone materials can be used when identifying different lithotypes on a building surface and also for localizing past treatments. By processing of the spectra, the specific materials and their distribution can be pointed out in thematic maps or in images accessible for the cultural heritage sector.

A study of Övedskloster was performed during periods between May and October 2004. In May 2004, fluorescence lidar measurements were made with the mobile unit from Lund University over a period of three days and, in October 2004, an additional survey and measurements of the areas with traditional methods were carried out (Fig. 1). The study was divided into three main areas: the courtyard portal, the balustrade between the west pavilions and parts of the main façade facing the courtyard. The primary aim of the study was the possibility of identifying materials and phenomena on the surface, their origin, biodeteriogens present and their extent, and possible treatments used on the sandstone in previous conservation projects.



Fig. 1. The mobile system of Lund Institute of Technology parked in the Övedskloster courtyard for the field study in May 2004.

Övedskloster Castle

The Swedish Rococo style castle Övedskloster with its surroundings is a listed and entailed estate. It is situated in the province of Scania in the south of Sweden. A monastery from the Premonstratenser order, which was founded in the 12th century was previously on this site [3]. During the 18th century the estate came into the Ramel family possession and a new castle was built during 1763-1776, under the architects C. Hårleman and J. E. Rehn, of French model and with magnificent Rococo interior.

The castle, its pavilions and the courtyard portal are built of the red Swedish sandstone called Öved. The stone was quarried at a nearby opencast mine, which is now closed. The deposits form a 5-10 metres thick bank of red and soft stone of Upper Siluric sediment, with a porosity at about 10% [4]. By Swedish standards this is relatively young sandstone. The light red colour derives from oxidised iron compounds and, in addition to quartzite mineral, the stone contains feldspar, mica and calcite. The stone has a somewhat uneven quality and is vulnerable to

environmental exposure. The sandstone shows signs of algal growth, weathering, exfoliation and water rising through the capillary systems with salt efflorescence and, on some areas, greater damage causing parts of the stones to fall off. On some parts, the old Öved stone, being much weathered, has been replaced with new stones of Orsa sandstone, a similar red Swedish sandstone [5].

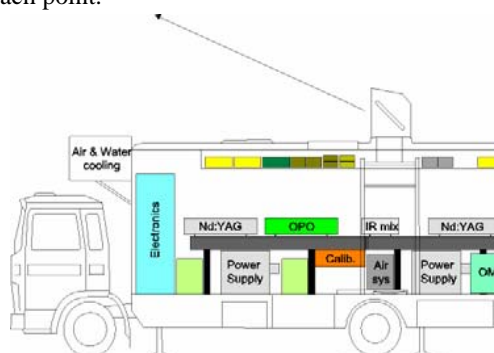
2. Methods

The technique used in these measurements was laser-induced fluorescence, where an ultra-violet laser pulse is directed to the point of interest. The laser excites atoms and molecules in the material which then relax and send out fluorescence light. The exciting wavelength is not critical in the sense that the atoms and molecules in the solid target have smeared-out energy levels, but the results may be different with different excitation wavelengths, and a combination of wavelengths may give extra information [6]. With an excitation pulse of 3-4 ns, the fluorescence is temporally confined which makes it possible to detect using a gated detector. In this way background light can be suppressed.

Measurement System

The measurements were performed using the mobile lidar system of Lund University (Fig. 2). The laser radiation from a tripled Nd:YAG laser at 355 nm was sent to the point of interest through a rooftop dome, with computer-controlled mirrors that can direct the light to the desired point. The laser light was used to induce fluorescence in the stone at ~40 m distance and the fluorescence radiation was collected using an on-axis Newtonian telescope. The radiation was filtered with a coloured glass filter which suppresses the elastic reflex. An Optical Multichannel Analyser (OMA) system with a time-gated image intensifier and a CCD camera captured the fluorescence radiation in the approximate wavelength range 400-800 nm for each measurement point, averaging over 40 laser shots. The laser beam, with a diameter of about 3 cm, was then swept over the area of interest to gather the spectrum in each point.

Fig. 2. Schematic of the mobile lidar system used in the study. Modified from [7]

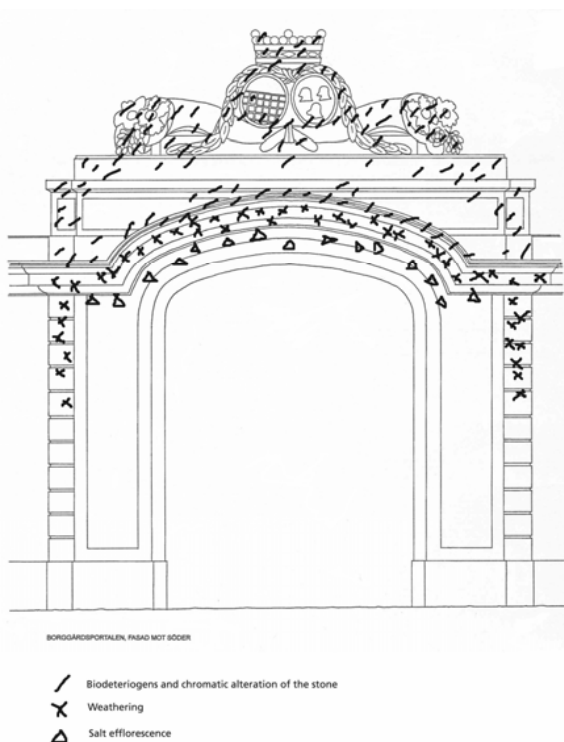


3. Measurements

The measurements performed on Övedskloster concerned three areas of the castle, where the material and analyses from two specific parts will be discussed in this article, namely the south side of the portal and one of the sandstone urns on the Attica on the main façade. The field study with the fluorescence lidar system from Lund took place during three days with relatively warm and sunny weather.

The mobile unit was parked on the inner courtyard where the possibility to move the dome vertically and horizontally enabled the measurements to be performed on the points and areas chosen. The distance to the main façade was 44 metres and, to the portal, 38 metres.

Fig. 3. To the right, a survey drawing and a sketch of the damage classification of the portal after ocular inspection indicating biodeteriogens, chromatic alteration, weathering and efflorescence.



The main portal chosen in the study has a core of bricks and is covered in Öved sandstone with a family coat-of-arms and two medallions surrounded by rich ornaments. The portal's north side is often in shadow from surrounding tall trees causing algal growth on the sandstone. The brick core draws the water high up through capillary action, which also causes many problems to the stone, for example, efflorescence and exfoliation. The portal has undergone conservation projects, the most recent in the middle of the 1990's including cleaning of the stone, consolidation and stone repair work [5]. Figure 3 shows the present status, after ocular inspections with indications of biodeteriogens, weathering and

efflorescence on the portal. The detection of chlorophyll from algae was shown with the fluorescence lidar technique and also the intensity of the growth (Fig. 4). The presence of a copper ledge on the portal was also detected, which indicates the distinction that can be made of different material due to their different spectra. The presence of earlier mending with mortar where the stone had fallen off or in joints between stones was also visible with the fluorescence lidar, Fig. 5.

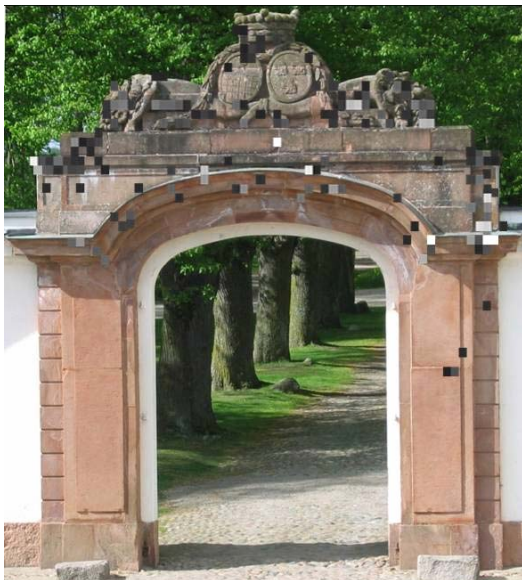
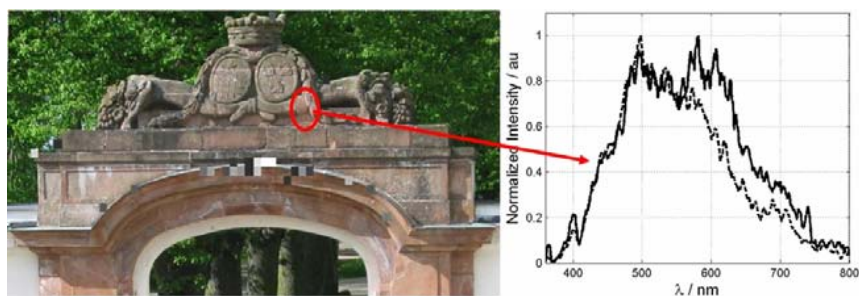


Fig. 4. To the left, a fluorescence image of the algae presence, indicating the chlorophyll and its intensity, the white spots have the highest intensity and the darker, lower

Fig. 5. Below, fluorescence of the copper ledge shown in grey-scale, and an indicated area showing presence of a mortar mending and its spectra together with a reference spectrum from the nearby stone in dotted line



Some old mending with cement was found to have red-shifted spectra and the areas are indicated in Fig. 6. The fluorescence lidar technique could also indicate the fluorescence from chlorophyll on the urns on the main façade (Figs. 7, 8). While the clean sandstone has a low fluorescence signal, the weathered stone with both visible and non-visible substances attached to the surface, give a stronger spectral signal. The fluorescence lidar could not easily distinguish between the red Öved and Orsa sandstone in this study, the data processing has shown a low

intensity in the signal from both clean Öved and Orsa sandstone which may derive from the little fluorescence emitted from the dominant part of quartz in the stone.

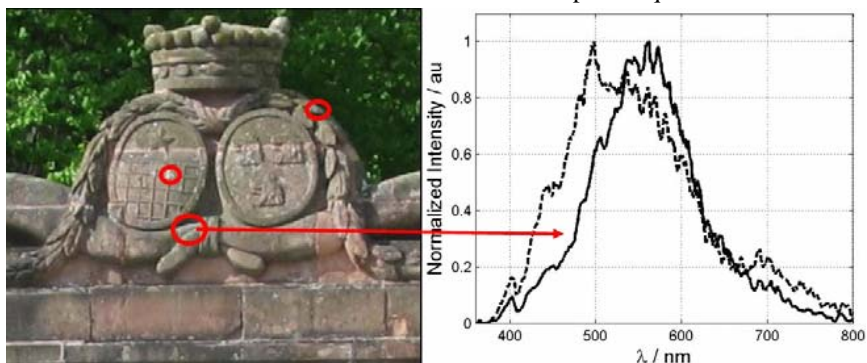


Fig. 6. Areas indicated refer to red-shifted spectra (while the reference stone spectrum is shown in a dotted line). The spectral anomaly is from earlier mending with cement

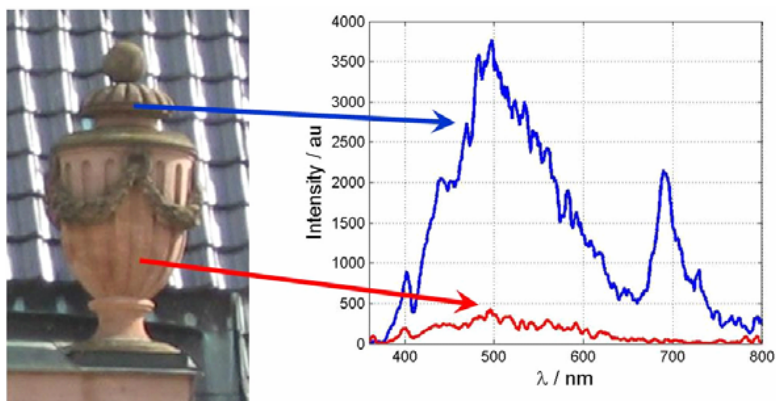


Fig. 7. An image of the far right urn on the Attica visualizing the much lower spectral signal from cleaned stone that also could be found in an associate experiment of clean and non-cleaned sandstone performed in Lund. The stronger, clear signal above the festoon is due to impurities and substances on the surface which emit fluorescence



Fig. 8. The urn on the main façade visualizing the presence of chlorophyll with fluorescence. A stronger algae presence is observed on the upper part and around the festoon while the stone is still clean below

4. Conclusions

The Övedskloster field study demonstrated that the use of fluorescence lidar makes it possible to perform non-destructive, in-situ, remote monitoring of stone building façades. It confirms previous results on identifying and remote mapping of biodeteriogens. It also gives the possibility of identifying the materials present, i.e. stone or previous mending with mortar and cement. Also, to some extent, it shows the sandstone condition after cleaning in a conservation project regarding to the differences of a clean sandstone surface and one affected by algae and particles present on the surface due to environmental conditions. The research on fluorescence lidar has shown good potential for the architectural conservation field concerning fluorescence identification and mapping, and could be a useful application supporting the status control of the monument and in planning for future interventions.

Very recently, the remote fluorescence imaging technique has been extended to remote imaging laser-induced breakdown spectroscopy (LIBS). Remote ablative cleaning of statues using the laser spark was also demonstrated [8, 9]. This opens the possibility of remote cleaning under spectroscopic control and guidance.

Acknowledgements. This work was supported by the Swedish Research Council for Environment, Agricultural Sciences and Spatial Planning (FORMAS) and the Knut and Alice Wallenberg Foundation.

References

1. P. Weibring, T. Johansson, H. Edner, S. Svanberg, B. Sundnér, V. Raimondi, G. Cecchi and L. Pantani, *Fluorescence lidar imaging of historical monuments*, Applied Optics **40**, 6111-6120, 2001
2. D. Lognoli, G. Cecchi, I. Mochi, L. Pantani, V. Raimondi, R. Chiari, T. Johansson, P. Weibring, H. Edner and S. Svanberg, *Fluorescence lidar imaging of the cathedral and baptistery of Parma*, Applied Physics B **76**, 453-465, 2003
3. G. Upmark, Övedskloster, in *Svenska slott och herresäten vid 1900-talets början, Skåne*, Stockholm, 266-268, 1909 (in Swedish)
4. *Natursten i byggnader, Stenen i tiden*, Stockholm, 95-96, 1996 (in Swedish).
5. M. Johansson, *Restaureringsrapport Övedskloster portal*, Dnr 5025, RAÄ, Stockholm, 1994 (in Swedish)
6. R. Grönlund, J. Hällström, A. Johansson, K. Barup and S. Svanberg, *Remote multicolor excitation laser-induced fluorescence imaging*, Submitted to Laser Chemistry, 2006
7. P. Weibring, H. Edner and S. Svanberg, *Versatile mobile lidar system for environmental monitoring*, Applied Optics **42**, 3583-3594, 2003
8. R. Grönlund, M. Lundqvist and S. Svanberg, *Remote imaging laser-induced breakdown spectroscopy and remote cultural heritage ablative cleaning*, Optics Letters **30**, 2882-2884, 2005
9. R. Grönlund, M. Lundqvist and S. Svanberg, *Remote imaging laser-induced breakdown spectroscopy and laser-induced fluorescence spectroscopy using nanosecond pulses from a mobile lidar system*, Applied Spectroscopy **60**, 853-859, 2006

PAPER V

Documentation of Soiled and Biodeteriorated Façades: A Case Study on the Coliseum, Rome, using Hyperspectral Imaging Fluorescence Lidars

J. Hällström, K. Barup, R. Grönlund, A. Johansson, S. Svanberg,
L. Palombi, D. Lognoli, V. Raimondi, G. Cecchi, and C. Conti.

Submitted, 2007.

Documentation of soiled and biodeteriorated façades: a case study on the Coliseum, Rome, using hyperspectral imaging fluorescence lidars

Jenny Hällström^{a*}, Kerstin Barup^a, Rasmus Grönlund^b, Ann Johansson^b, Sune Svanberg^b, Lorenzo Palombi^c, David Lognoli^c, Valentina Raimondi^c, Giovanna Cecchi^c, Cinzia Conti^d

^a Architectural Conservation and Restoration, Lund University, P.O. Box 118, SE-221 00 Lund, Sweden

^b Atomic Physics Division, Lund University, P.O. Box 118, SE-221 00 Lund, Sweden

^c Institute for Applied Physics 'Nello Carrara' - National Research Council, Via Madonna del Piano 10, I-50019 Sesto Fiorentino, Firenze, Italy

^d Soprintendenza Archeologica di Roma, Palazzo Altemps, Piazza di S. Apollinare 44, I-00186 Roma, Italy

Abstract

Non-invasive documentation of historic façades with fluorescence lidar techniques can provide helpful information for the cultural heritage sector, especially when large areas outdoors are to be examined. This paper presents a case study on the Coliseum, Rome, where both cleaned and heavily soiled areas of the monument were scanned and analysed with two fluorescence lidar systems. Biodeterioration processes have also been addressed during the experiment with the aim of assessing the colonisation extent on selected areas of the monument. Results show the usefulness of a mobile fluorescence lidar system for documentation and survey of large surfaces with complex conditions without limiting the public access to the monument.

Keywords: Coliseum, non-invasive, documentation, deterioration, soiling, UV fluorescence, lidar, remote sensing, hyperspectral imaging

1. Introduction

Assessment of soiling and progressing deterioration processes on historical façades is of great interest both to experts as well as to the general public. During recent years the growing interest in new ways of documenting the historical buildings using non-invasive techniques has resulted in a closer interdisciplinary collaboration in the conservation field. Furthermore, the increased awareness of the climate change impact on built heritage has improved the understanding that advances in monitoring and prediction technology will assist scientists and stakeholders with these evaluations. New techniques are being developed with the possibility of remote sensing as one of the characteristics. Use and application of different laser-based techniques as analytical tools, such as laser-induced fluorescence (LIF), laser-induced break-down spectroscopy (LIBS) and Raman techniques, are not unusual [1, 2].

Separating biological attacks from deterioration and patinas on the façade due to deposits of pollutants and production of chemical compounds can at first sight be troublesome. Detecting these deterioration processes is

central and often calls for a close contact and expert knowledge of biological attacks and their possible effects on stone [3].

The Flavian Amphitheatre, the Coliseum in Rome, has a unique history of documentation regarding its flora [4]. The soiling of porous stone, such as travertine, the main construction material of the monument, and the deterioration processes caused by natural ageing and environmental conditions have been thoroughly discussed regarding historical monuments [5]. The documentation of the effects is normally performed on samples from the site studied in the laboratory or in the field [6]. The non-movable heritage objects challenge the traditional analysis situation, hence the complexity of documentation methods.

The fluorescence LIDAR (Light Detection And Ranging) technique makes it possible to extend the application of the LIF technique to the outdoor environment, where considerable distances and uncontrollable background light have to be dealt with. Although the fluorescence lidar technique was initially developed for marine monitoring in the beginning of the 1970s, its application was

early extended to vegetation monitoring, where chlorophyll fluorescence in the red spectral region constituted a powerful tool for on-site eco-physiological studies [7-9]. Not until the last decade the technique has been applied to the monitoring of the cultural heritage: experiments were first conducted in the mid 1990s on the Cathedral of Parma, Italy [10], and then extended, thanks to the imaging fluorescence lidar technique, to the acquisition of hyperspectral fluorescence images on several monuments [11-13]. Main fields of investigation have been detection and characterisation of different lithotypes [10, 14, 15], of biodeteriogens [16] and of protective treatments [12, 17], showing good potential of the technique for an extensive monitoring and investigation of the stone cultural heritage.

The purpose of the fluorescence measurements presented in the current paper was to study particular chosen areas on the façade of the Coliseum in order to detect features not visible to the human eye and to assess the cleaned and the non-cleaned surfaces *in situ* on parts difficult to reach. Detecting chlorophyll through fluorescence can be applied as an analytical method to identify the deteriorated areas from longer distances. Furthermore, the technique gives the opportunity of early detection, i.e. identifying the problem before it is seen by visual inspection. The analysis could then be used together with other non-destructive investigation techniques for documentation and for sustainable conservation.

The study presented is a field campaign on the Coliseum in Rome, where fluorescence measurements in collaboration between Swedish and Italian researchers using mobile lidar systems were performed. The presence of chlorophyll was identified on parts of the cleaned façade. The possibility of using LIF to create thematic maps of the cleaned and weathered parts of the façade was also confirmed. Documentation of the surfaces can be performed without mounting scaffolding and taking samples and can provide the conservation sector with information where the human eye has its limitations.

Furthermore, documentation over time can also be obtained using remote LIF, as changes and the speed of the deterioration processes can be monitored through repeated scanning at regular intervals over time.

The present paper first describes the background and the set-up of the case study. Then the methods are outlined, followed by a section of results focusing on the documentation of deterioration and biodeterioration processes using two fluorescence lidar systems.

2. Background to the case study

Throughout the years there have been numerous surveys and observations of the amphitheatre Coliseum [18]. The fluorescence lidar study presented in this paper was initiated as a case study since the vast façades, including large areas for scanning and levels difficult to reach from the ground, could ideally be used for the survey using remote sensing techniques. The measurements could also benefit from previous studies of the monument.

The building was inaugurated in AD 80. Today little of the original Coliseum from the Flavian period is left, most of it being the supporting structure. The ongoing deterioration of the material, the historic interventions, the environment and microclimate of the building, and both natural disasters and excessive tourism contribute to the state of the monument and its subsequent conservation. From 1992, over a period of some years, a large research project involving different scientific disciplines was performed at the Coliseum. One of the research projects, led by the Soprintendenza Archeologica di Roma in cooperation with “La Sapienza” University of Rome and the International Centre for the Study of the Preservation and Restoration of Cultural Property (ICCROM), included a pilot study regarding the travertine at the outer ring, sections LI-LIIII, four arches northeast towards Via dei Fori Imperiali [19]. The study area was 28 m long and 50 m high, four out of eighty arcades. Besides cleaning, one of the main objectives of the study was to identify the materials of the area. The cleaning procedures on the travertine were done with a water mist,

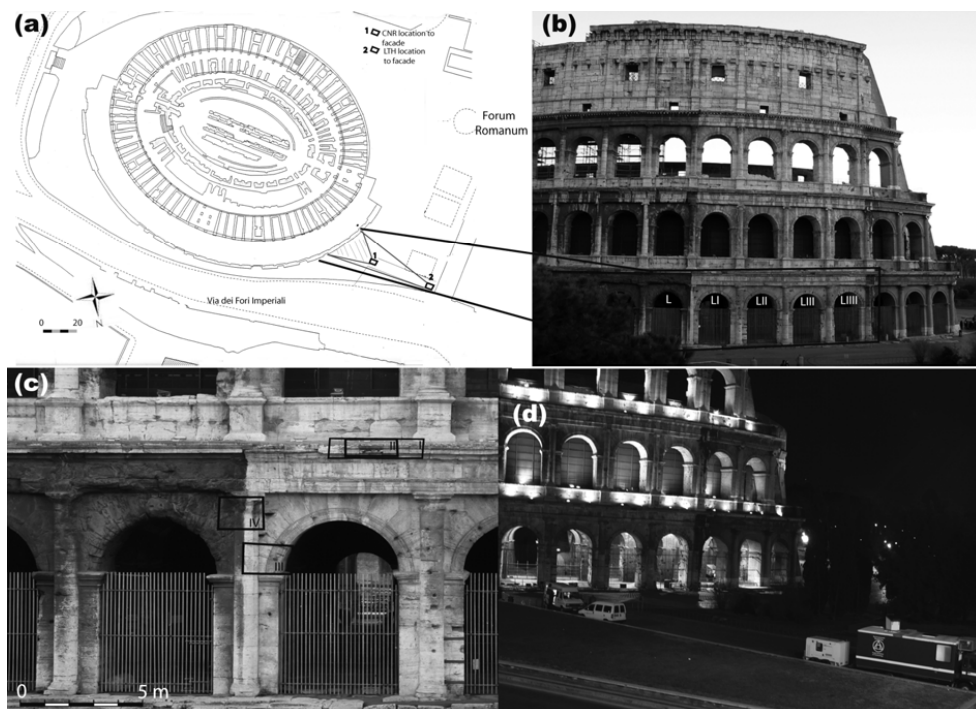


Figure 1. Plan over Coliseum and the area where measurements have been performed. The plan of the Coliseum valley and the amphitheatre is shown in (a), together with the location of the two systems and the area measured in the study. A photograph of the northeast façade with the section where measurements were performed is shown in (b). In (c) a part of the section of the northeast façade where fluorescence scans were performed is shown, with area I referring to Fig. 2, area II referring to Fig. 3, area III referring to Fig. 4, and area IV referring to Fig. 5. (d) is a photograph from the campaign performed during night-time with the CNR lidar system closer to the monument, 18 meters from the target, and the LTH lidar system at the far right, 65 meters from the target.

using a very low pressure at ambient temperature with no additives. The mist dissolved incoherent powders, black crusts, even strongly attached, and to some extent even inside the alveolars.

For the fluorescence lidar study in 2005, only parts of the vast monument was chosen, which was suitable for the extent of the study and the sequence of the work. These areas can easily be substituted for areas or parts situated at the top of the façade, nearly 50 meters up or higher if needed. Given sufficient time, the whole monument could have been realistically scanned at reduced spatial resolution. The surveyed area consisted of the sections L-LIIII of the façade, (a width of 33 m) situated northeast towards Via dei Fori Imperiali, where smaller areas were scanned, see Fig. 1. This

involved both cleaned and soiled travertine, thus giving fluorescence information from both types of surfaces.

The campaign was performed during night-time in order not to disturb those visiting the monument or the ongoing daily activities at the site. The two lidar vans were parked at the same location each night, with a distance to the façade of 18 and 65 meters, respectively, and they were driven away each morning. The location of the areas on the façade was not exactly identical for the two lidar systems, due to logistic planning and to reduce the time for each scanned area. The campaign was performed during a week in January-February 2005 (between 9.00 PM and 5.00 AM). No samples were taken for this study; the analysis consisted of the fluorescence data, visual

recordings and previous studies of the façades with written and image-based documentation.

3. Methods

The fluorescence lidar technique allows the detection of laser-induced fluorescence on a remote target [20]. Two different fluorescence lidar systems have been used for this study, though they operate in a similar manner. Both systems are fully mobile, as they are housed in vans and powered by motor generators. They both use ultraviolet laser pulses to excite fluorescence in the target. The laser pulses are remotely directed to the desired spot on the target; the fluorescence emitted is collected by a telescope, sent through a long-pass filter, and sent through an optical fiber to a spectrometer system coupled to a multi-channel detector. The long-pass filter is used to suppress the reflection at the excitation wavelength. By only detecting at the known arrival time of the fluorescence light pulse, the background signal level is efficiently reduced.

Depending on the target material, the fluorescence signal may differ. Fluorescence from natural stones is mainly due to impurities, such as exchanged ions (manganese, lead, dysprosium, europium, terbium), and lattice defects. Contaminations on the stone, e.g. biodeteriogens, have fluorescence features that contribute to the detected signal [14]. When measurements are performed with large spot diameters, as in our case of 2-5 cm diameter, the detected signal contains the fluorescence contributions from all the chemical compounds, including contaminations, contained in the whole area illuminated by the laser spot. The detected signal is then a superposition of these contributions, which can make the data difficult to interpret. However, comparison of fluorescence spectra referring to different areas can allow assessment of areas which are similar due to their compositional features, or affected by similar contaminations. In general, the comparison is carried out on the spectral shape of the fluorescence signals since the absolute intensity of remote sensed signals can be affected by several factors that are not dependent of the actual target fluorescence.

The fluorescence spectra can be recorded in single localized points, or by scanning a large area with the laser beam and collecting the spectrum in each point. Scanning over large areas gives the opportunity to perform thematic mapping, i.e. to obtain false-colour maps displaying the spatial pattern of a theme or series of attributes. For example, a thematic map can provide the spatial distribution of biodeterioration on a given surface. Visual inspection obviously also gives information on the state of the building and can be considered as a valuable integration to the information extracted from fluorescence-based analysis.

The lidar system used by the LTH team in the campaign is originally intended for atmospheric differential absorption lidar (DIAL) measurements, but is also well adapted for fluorescence measurements and has been employed in several fluorescence lidar campaigns [8, 9, 11-13]. The system is thoroughly described in [21]. Typical system-target distances are 40-100 m, in the current campaign the system was parked about 65 m from the target. The spot size on the target was about 5 cm and the resolution of the scans varied between 9 and 20 cm, depending on the purpose of the measurement, the features of the target and also the time required. The overall dimensions of the scanned area varied as well according to the issues to investigate. Fluorescence data were acquired with 355-nm excitation from a frequency-tripled Nd:YAG laser. The system acquired complete fluorescence spectra from 400 nm to 800 nm. Each spectrum was averaged over 100 or 200 shots, depending on the area considered and the accuracy needed. Measuring one spot, storing the spectrum and moving the dome to the next spot takes about 10 seconds.

An excimer-based mobile fluorescence lidar system (the FLIDAR) was deployed at the site by the CNR-IFAC team. Although initially developed for marine and agro-forestry lidar applications, the FLIDAR has been repeatedly used for fluorescence remote sensing of monuments since 1994 [8, 10, 12]. A general description of this system is given in [22, 23]. The system has been recently upgraded to perform also fluorescence imaging using an

automatic scanning system: two computer-controlled stepping motors allow scanning over the target for acquisition of a high-spectral resolution fluorescence spectrum at each position. In addition, the FLIDAR is equipped with a target pointing system using a coaxial laser pointer to reference the acquired fluorescence images on the target: the position of the pointing laser spot is recorded on a photo acquired at the same time. The final data is thus a referenced hyperspectral fluorescence image of the scanned surface.

During this campaign the FLIDAR was placed at about 18 m from the target. The dimension of the spot effectively measured on the target at this distance was about 2 cm in diameter. The horizontal and vertical spatial resolution of the acquired images (i.e. the distance between the centre of one measured spot and the following one) varied between 6 cm and 20 cm. Before every scan, the FLIDAR laser pointing system was used as a reference on the target for the definition of the area effectively measured by acquiring digital photos that were stored in the PC together with the relevant fluorescence data. Since the photos were taken at night they became of low quality. All data were acquired with 308-nm excitation from a XeCl excimer laser. A fluorescence spectrum (840 channels distributed over the 300-800 nm range) was acquired for each pixel of the fluorescence image. The complete fluorescence spectrum in the visible range was obtained by merging two separate fluorescence measurements, one from 300 nm to 600 nm and the other from 500 nm to 800 nm, to avoid second-order superimposition. Each fluorescence measurement is the result of an accumulation over 30 laser shots. The acquisition and storage of a spectrum takes about 1 min.

All spectra are corrected for the wavelength response of the respective optical systems.

4. Results

The fluorescence data from the study and the analysis of the surface have been presented in parts pertaining to the different lidar systems and the method of analysis.

4.1 Monitoring of biodeteriogens

The area where the fluorescence measurements were performed to detect the presence of chlorophyll content, area I in Fig. 1c is situated on the cornice above entrance LI, in the cleaned section near the supporting buttress raised by the architect Valadier in the 1820s. This section of the outer walls of Coliseum has been under reconstruction and conservation for many centuries. The most recent cleaning with pure water mist and the subsequent deterioration process that is visible to the eye has been used as a reference to the fluorescence analyses in this study. The colonization of organisms on and inside the walls of Coliseum is of numerous species, which is interesting because of the long-time surveys that have been undertaken as far back as in the XVII century (a study by Panaroli) [24].

The travertine of Coliseum, quarried from the nearby Tivoli, is a mono-mineral rock with more than 99% calcite content [25]. Up to present time, the cleaning and removal of the black crusts on the façade performed in the mid 1990s is still effective as to the visible perception of soiling, whereas biological growth on the surface has increased noticeably over time, particularly on travertine already affected by weathering processes. The speed of this biodeterioration can provide answers to a range of questions, climate and environmental strategies for sustainable conservation being one of them.

The pigment chlorophyll *a* (Chl *a*) shows a typical fluorescence band in the red with a maximum at about 685 nm. All photoautotrophic organisms such as algae, cyanobacteria, and higher plants, contains Chl *a* and thus its fluorescence peak in the red can be exploited to detect the presence of photoautotrophic biodeteriogens. In addition, some of them have additional pigments that can contribute with typical peaks to the fluorescence signal (e.g. phycocyanin, featuring a fluorescence band centred at 660 nm). UV-induced fluorescence of higher plants features a prominent red-far red band with maxima typically at 690 nm and 740 nm, which is due to Chl *a* (see, e.g., [26]). In addition there is a band in the blue-green region, typically with a

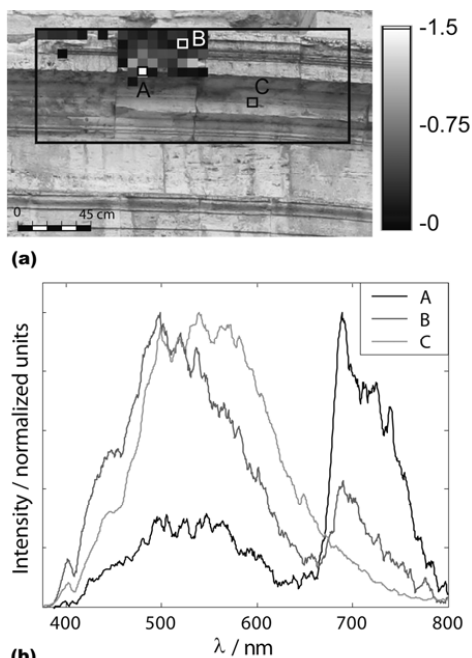


Figure 2. Classification of Chl content on Area I, $2.8 \times 1.3 \text{ m}^2$ studied in a distance of 65 m with a spot size diameter on the target of about 4 cm. In (a), the scanned area is indicated with the red frame, and the false-colour coded pixels correspond to the points containing Chl. The colour scale indicates the amount of Chl in the different points. In (b) the spectra from three points in the scan are shown. Spectrum A is a point containing heavy biodeteriogen growth, as indicated by the Chl peak at around 685 nm. Spectrum B is from a point with a weaker Chl signal, and spectrum C from a point without Chl signal.

maximum between 440 nm and a shoulder at 520 nm, mainly due to the compounds (e.g. ferulic acid) in the epidermal cell walls. The analysis of the fluorescence in the identified area is illustrated in Fig. 2 where one particular travertine block on the moulded cornice is shown to be colonized (Fig. 2a). The data show the feasibility of early remote detection even at a distance as large as 65 meters. The three spectra in Fig. 2b, taken from the area, indicate one of the most invaded points (A) of the Chl-rich area, showing the large peak at 685 nm. Point B exhibits a less intense Chl peak indicating a lower presence on the substrate. Point C is a reference point from travertine on the right side not affected by Chl and thus

representing a spectrum for travertine of the previously cleaned façade. In Fig. 2a the result from the fluorescence analysis showing the intensity of the Chl has been superimposed onto a photograph. The chlorophyll content was evaluated by creating three wavelength bands with central wavelengths at 700, 670 and 550 nm, respectively. The function of the intensities $(I_{700 \text{ nm}} - I_{670 \text{ nm}}) / I_{550 \text{ nm}}$ gives a measure of the chlorophyll content. The colorbar indicates the value of this function. The area, previously subjected to cleaning, was visually observed before the fluorescence measurement was performed. Some smaller areas were affected by biodeteriogens. The same area was studied one year later, in 2006, when the colonisation had spread and increased by visual analysis. There was also a perceived increase in the higher vegetation. The more affected travertine block which was analysed and surveyed in the area of Fig. 2, apart from being situated in a more sheltered environment beneath the protruding ledge, has many visual surface cavities and large material losses due to weathering. Colonization of these non-smooth surfaces often provides favourable growing conditions where pore size and distribution as well as transportation of water are one of the contributing factors. Surrounding stones also show signs of weathering with visual cavities. The identification of the organisms colonizing the surface has not been performed in this study, but has been thoroughly investigated in, e.g. [24].

Beside the detection of Chl-containing bio-organisms through the Chl *a* fluorescence peak at 685 nm, the fluorescence data can also be processed for a rough classification of the bio-organisms present on the examined surface. As an example, Fig. 3 shows a scan with the 308-nm excitation of a sub-set of the area illustrated in Fig. 2. In Fig. 3a, the measured area is shown together with the reference grid automatically generated by the FLIDAR software. The spatial resolution of the scan was 20 cm; the spot detected for each measurement is comparable in size to the dimension of each dot on the grid shown in Fig. 3a. In Fig. 3b, a Cluster Analysis (CA) based processing of the data [27] divides the examined spots into different classes for a first rough classification of biological growth.

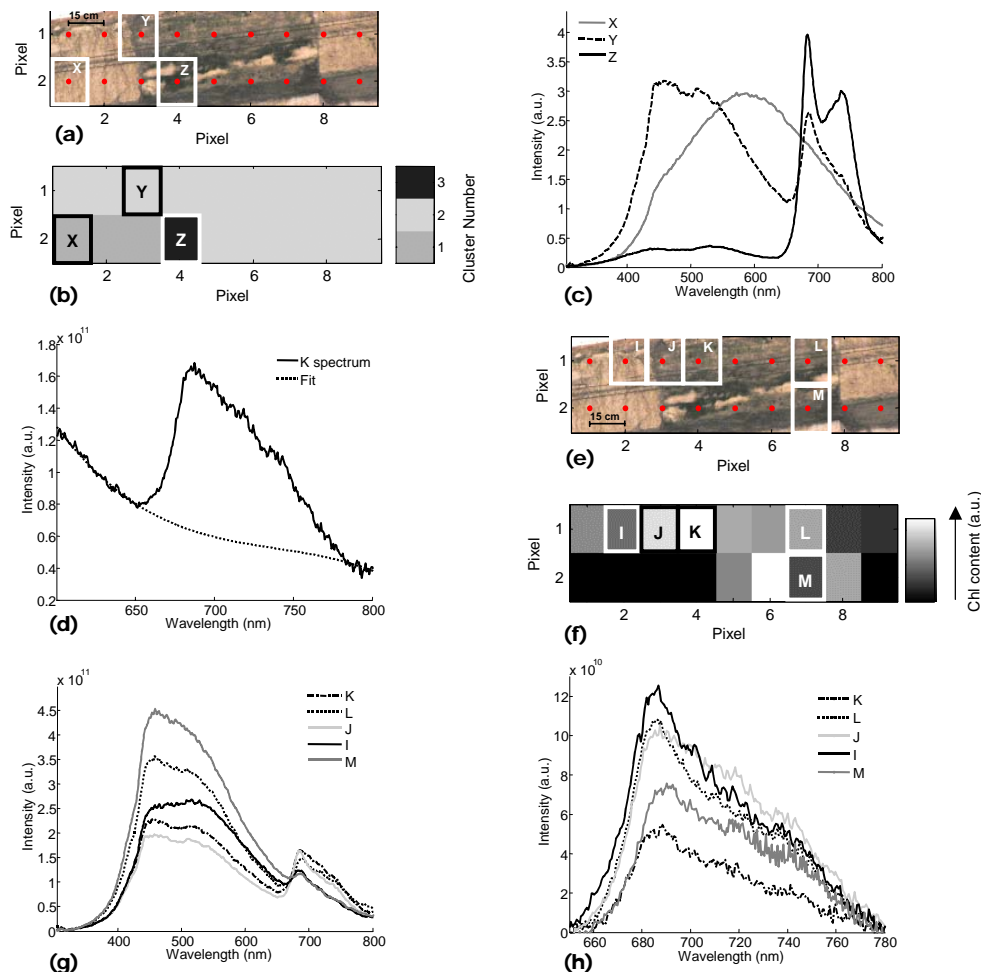


Figure 3. Determination of different types of biodeteriogens and Chl content assessment on a subset of Area I studied with the 308-nm excitation. The distance from the target was about 18 m and the spot size diameter on the target was about 2 cm. (a) shows the scanned area and the reference grid, automatically generated by the FLIDAR software, to position the fluorescence image on the target. The distance between the spot centres was 15 cm in the horizontal direction and 20 cm in the vertical one. (b) is a CA-based map with a preliminary classification of the biodeteriogens: grey pixels refer to stones, light-grey pixels highlight the presence of Chl-containing biodeteriogens while the black pixel points out the presence of higher vegetation. The CA analysis was performed using the ‘Standardized Euclidean’ distance and the ‘Average’ linkage method. (c) shows typical fluorescence spectra referring to the three identified classes (stone, Chl, higher vegetation). Spectra were STD normalised. The pixels referring to these spectra are white-squared in photo (a) and in map (b) and labelled as X, Y and Z for the stone, Chl-containing biodeteriogens and higher vegetation classes, respectively. (d) shows a fluorescence spectrum with the typical Chl fluorescence band (continuous line) and its fitting with a third degree polynomial curve to evaluate the travertine fluorescence background (dotted line). (e) is a map with an assessment of the Chl content distribution: light-coloured pixels refer to spots more heavily affected by biodeteriogens than dark-coloured pixels. The map was obtained by evaluating the integral of the Chl band after the subtraction of the travertine fluorescence background. (f) reports the fluorescence spectra referring to the white-squared pixels in map (e) and in photo (a). The spectra are labelled accordingly. (g) shows a close-up of the Chl a fluorescence bands of the same set of spectra shown in (f) after the subtraction of the stone fluorescence background.

The map was created by applying a CA to the set of data using the Euclidean distance and the average linkage method to measure the distance between clusters. Typical fluorescence spectra corresponding to the three classes are shown in Fig. 3c: for each spectrum the values of intensity are normalized to their standard deviation (STD normalization). This procedure makes the visual comparison of the profiles of different spectra easier in the figure. The Y spectrum shows the typical Chl *a* fluorescence peak at 685 nm so that light grey pixels (cluster #2) in the map of Fig. 3b highlight the presence of Chl-containing biodeteriogens such as algae. The Z spectrum, however, besides having the typical 685-nm Chl fluorescence peak, is also characterised by a very pronounced fluorescence contribution at 740 nm. This spectral band is typical for higher vegetation indicating that the dark pixel in the map (cluster #3) points out the presence of a small plant. The X spectrum shows instead the typical broad fluorescence band of the stone ashlars. The pixels referring to spectra shown in Fig. 3c are marked by squares in the photo (Fig. 3a) and in the map (Fig. 3b) and labelled as X, Y and Z, respectively, for the stone, the Chl-containing biodeteriogens and the higher vegetation classes. Spot Z, indicating the presence of higher vegetation is exactly in correspondence with a crevice in the travertine where it is likely to find higher water retention and debris accumulation which can favour the growth of a plant.

A further analysis, restricted to the Chl-containing biodeteriogens, can be used to evaluate the Chl content in these spots. The spectra were first processed with a third-order polynomial curve considering only the 600 - 650 nm and 780 - 806 nm spectral ranges to fit the background due to the fluorescence in the blue region. The fitted fluorescence background was then subtracted from the fluorescence spectra to evaluate the integral of the Chl *a* peak at 685 nm. A typical result of the fitting procedure is shown in Fig. 3d, where the fluorescence spectrum corresponding to pixel K in the photo (Fig. 3e) is shown together with the corresponding fitting curve. The integrals of the Chl *a* band corresponding to each pixel is reported in the grey-scale map shown in Fig. 3f:

the spots heavily affected by biological growth are represented by light colours; darker colours refer to spots characterised by a lower biological growth. The black pixels refer to the spots identified in Fig. 3b as corresponding to stone or higher vegetation features and were not considered in this analysis. A set of fluorescence spectra corresponding to different Chl contents is reported in Fig. 3g. The corresponding pixels are marked with squares in the map of Fig. 3f and in the photo (Fig. 3e) and labelled accordingly. In Fig. 3h, a close-up of this set of spectra is shown to highlight the details of the Chl *a* fluorescence band.

Microorganisms and organisms normally play an important role in the mechanisms of weathering and deterioration of inorganic materials. They can cause not only aesthetically non-desirable effects, but also, in some cases, act as indicators of loss of solidity and transformation of constituent materials. Different kinds of biodeterioration may also occur on materials of different chemical composition. Also, deteriorated stone, having a larger porosity, are more easily attacked by biodeteriogens than the same undamaged stone, due to its ability to retain water. Possible climate changes will also have an effect on the microclimate, which can produce significant changes in composition and structure of the community.

Deterioration occurs under different circumstances and may generate organic and/or inorganic acids, chelating substances, alkalis, enzymes and pigments. It is not always possible to separate biological damage from decomposition or disintegration of materials. This complexity arises from the fact that when a biological population grows on a surface, (even if the surface is not subject to nutrition) metabolism products or CO₂ from respiration is released, inducing some changes. The perception of aesthetic damage encompasses change due to chromatic alterations, development of biological patinas, or visual obstruction of the materials.

The correlation between stone deterioration and the chemical-physical characteristics of the material is evident, but differences in

mineralogy and stone homogeneity will also cause different colonization. Especially travertine has shown a correlation between the original pores and cavity formation [25] and their presence will support the presence of biological growth, due to the possibility to retain water and moisture and thus ensuring favourable growing conditions. The colonies of micro-organisms will also prefer the cavities within the travertine over those on the surface, as the microclimate of the surface will be more exposed to surrounding factors.

Knowledge of the effects of biofilms on the collection of dust, spores and particulate matter has led to a consideration of their effect of the micro-organisms and the substrate. Fluorescence techniques allow detection only of surface contaminants. No evidence about detecting endolithic biodeteriogens was demonstrated. The possibility of rating the speed of the biological surface growth and the deterioration by remote sensing will hence be important and can be made by fluorescence lidar monitoring. The visual observations confirmed the presence of biodeteriogens on parts of the area measured and also a noticeable increase over a one-year period, but need further expert analysis for characterization and integration in conservation plans for the monument. Chl not yet visible was also detected by fluorescence.

4.2 Monitoring of soiling

Patina that covers limestone and marble in a number of monuments is originating from natural ageing of the stone, biological activity and chemical-physical reactions between material and environment. The patina from this area has often consisted of calcite, calcium oxalates, gypsum, iron oxide pigments and various silicates. These, together with impurities of the mineral, compounds of soot particles and environmental impact will give the specific soiling of the stone surface and thus the differences in fluorescence spectra.

The external surface shows a rather thin deposit, which is rich in gypsum, iron oxides and carbonaceous particles, and was often found in the microscopic cavities underneath the deposited surface layers [28]. The crusts differ in thickness but have an average value of $\frac{1}{4}$ mm. A mix of calcite, quartz and pozzolana-like vitreous fragments were found in a previous study, with traces of calcium oxalate monohydrate (whewellite), mica, pyroxenes and iron oxides, all of which are normal constituents of soil deposits in Rome. Modern deposits may also have a different colour where oxidation processes may be induced by organic matter from Diesel soot.

The possibility to distinguish the effect of cleaning of a contaminated area through fluorescence imaging can be illustrated through thematic mapping as indicated in Fig. 4, where the fluorescence emission gives information not only due to the mineral present in the substrate but also due to impurities. The measured area, situated on the border of the cleaned and weathered façade gives the fluorescence image in Fig. 4, examined with the 355-nm excitation. The analysis illustrates diversity that is demonstrating variation in the ashlar due to emission from minerals, and to the microclimate of protruding parts as opposed to more sheltered ones. In Fig. 4a the area is framed on a photograph, and can be interpreted by visual inspection as constituted by travertine cleaned previously. This area (area IV in Fig. 1c) consists of the arch belonging to the opening of LI to the right and a semi-column to the left. The border of the cleaned section is situated just on the front of the column. Two titanium clamps from a conservation campaign in 1999 are visible on the travertine arch on the upper right. In this scanned area five points have been chosen to illustrate the diversity on the substrata.

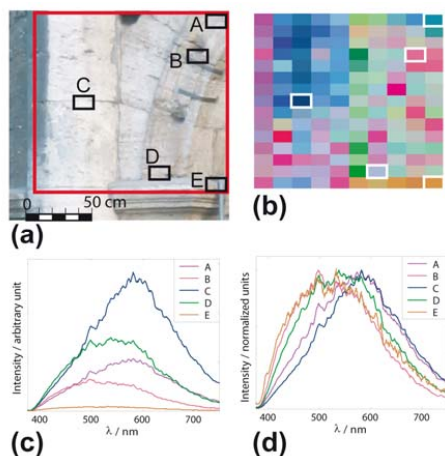


Figure 4. Scan over an area on part of the semicolumn and arch. The source-target distance was about 65 m, the spot size diameter on the target was about 4 cm and the measured area is about $1.9 \times 1.7 \text{ m}^2$. In (a) the measured area is indicated by the red frame and a few points are indicated, corresponding to the spectra in (c) and (d). In (b), a PCA-RGB analysis is seen, with PC1, PC2 and PC3. In (c), the chosen spectra are shown as they were measured, and (d) shows the same spectra, normalized with respect to the maximum value. In (b), differences in the area can be noted and the upper part of the left semicolumn seems to be different from the rest of the area. The lower right corner, as indicated by point E, shows very low intensities as seen in (c), but its shape is similar to B as seen in (d), and by their respective colour. It is also noted that the peak of the spectra are more and more shifted to the red for points D, C and A, respectively.

In Fig. 4b the Principal Component Analysis (PCA), [see, e.g. 27] analysis performed on the normalized spectra demonstrates that the area can be classified in zones. The scores of PC1, PC2 and PC3 have been assigned to red, green and blue colours, respectively. This was obtained without including information about the intensity of the spectra, which was definitely lower for the darker, soiled areas. To the right of the semicolumn, an area which belongs to the cleaned section is the visibly homogeneously cleaned surface indicated in green-red pixels in Fig. 4b. The lighter exterior of the semi-column is due to rain-washed travertine and the upper block exposes spectral differences compared to the lower one. The far

left of the semi-column, which has not been cleaned, is shown in purple colours, indicated by the vertical column to the far left in Fig. 4b. These pixels correspond to the darker more soiled areas of travertine and they may also be found in some points in the cleaned area, more notably in small non-smooth areas of the surface, or areas more secluded and hard to reach during cleaning. By visual inspection the area of the upper part of the column, illustrated in the pixels of column two and three from the left, is also corresponding to the perceived lightness of the stone. This is notable in the third column of pixels where point C and the spectrum (shown in Fig. 4c and Fig. 4d) shows the most sharp peak in fluorescence towards 600 nm.

The brown pixels in Fig. 4b, as well as the spectrum E in Fig. 4c (with very low intensity) and Fig. 4d refer to the part just above the ledge where cement has been applied for previous mending. This is also a secluded environment for accumulated debris of contamination and particles. Cement has also been smeared out on small areas on the lower part of the semi-column, identified by the intense red pixel in Fig. 4b. The scanning of the area detected no signal from Chl which gives us information of no current biological activity, which otherwise would be visible in fluorescence with this technique.

The area situated above the area of Fig. 4 was examined with the 308-nm excitation and the results are shown in Fig. 5. In Fig. 5a the measured area is shown together with the reference grid. A first rough classification of different areas is shown in Fig. 5b, where the soiled areas covered with dark patinas and crusts are shown in blue colours, while cleaned areas are marked with yellow-to-red colours. This map was obtained considering the intensity of the spectra that, as expected, was definitely lower for the black areas. Applying a CA-based evaluation, the spectra of the scanned area were divided into three classes, as shown in Fig. 5c: from a comparison with the photo in Fig. 5a it can be inferred that light blue pixels can be related to 'darker' heavily stained areas, brown pixels refer to 'lighter' areas and yellow pixels to 'grey' areas.

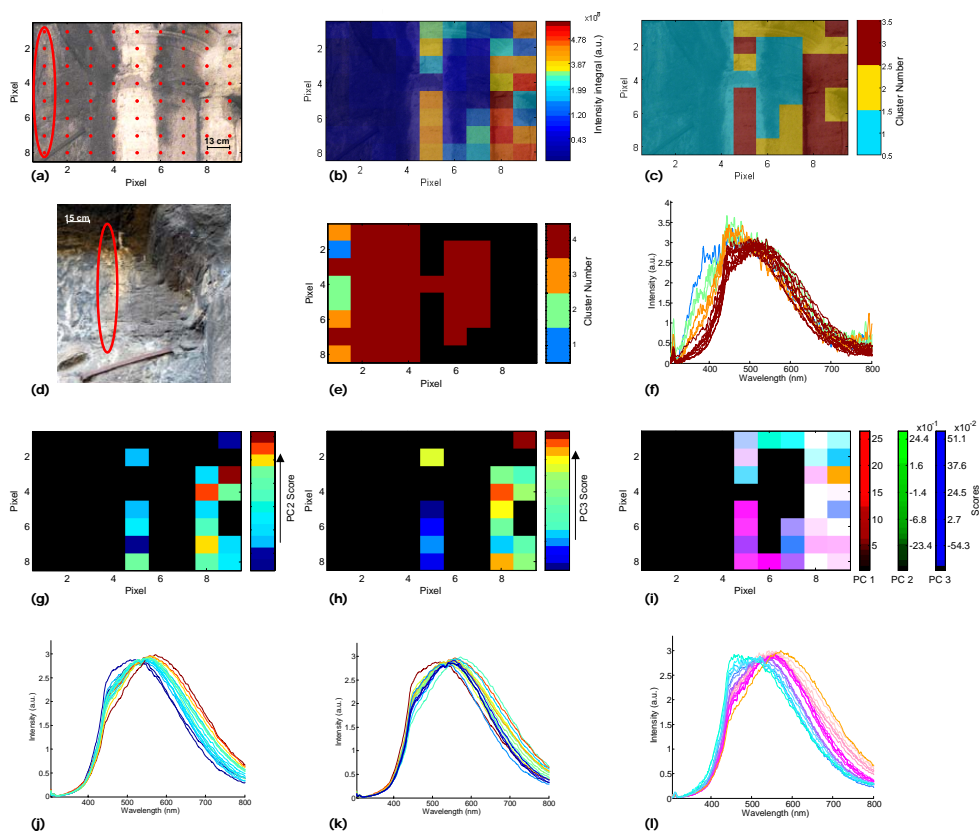


Figure 5. A scan with 308-nm excitation of a region containing both cleaned and non-cleaned parts. (a) shows the scanned area together with the reference grid and also the indicated area referred to in (d). In (b), a classification of different areas on the basis of the intensity of the spectra is displayed: areas covered with black patinas are identified by dark blue colours and white areas are marked with yellow-to red colours. The map has been superimposed to the photo shown in (a). (c) illustrates a CA-based evaluation that identifies three classes, which can be roughly identified with white, grey and black areas. The map has been superimposed to the photo shown in (a). (d) is a close-up of the scanned area, as marked in (a), taken in the sunlight, revealing the presence of a yellowish patina, maybe due to a prior presence of a metal clamp. (e) shows a CA-based evaluation of data applied to only the black areas (white and grey areas were excluded from the evaluation and are shown as black pixels). (f) is the STD normalised spectra of the black areas: the colour of each spectrum is the same as the corresponding pixel in map (e). (g) is the PC2-score map based on a PCA analysis applied to only the white areas (black and grey areas were excluded from the analysis and are shown as black pixels). (h) shows the PC3-score based on the same PCA evaluation. (i) is an PCA-RGB based map obtained on the STD normalised spectra referring to the grey and white areas. (j), (k) and (l) shows the STD normalised spectra corresponding to maps (g), (h) and (i) respectively. The colour of each spectrum is the same as the corresponding pixel in the map.

Further evaluation was separately performed on the two classes of spectra identified by the light-blue pixels and the brown pixels in map Fig. 5c corresponding, respectively, to the 'dark' and 'light' areas. Results for the black areas are shown in Fig 5e: a CA-based evaluation, applied to the 322 - 483 nm range, reveals that the black area on the right is quite homogeneous while a 'stripe' on the left shows a higher variability in its spectral features. This can also be inferred by the spectra shown in Fig. 5f, where the brown spectra (corresponding to the brown pixels in Fig. 5e) are quite similar, while the light blue/green/orange spectra (corresponding to the pixels of the corresponding colour in Fig. 5e) show a spectral behaviour characterised by a higher fluorescence contribution around 380-400 nm. Black pixels refer to the data not considered for this evaluation (grey and lighter, more cleaned areas). The photo in Fig. 5d shows a close-up of the non-cleaned area to the left of the capital in Fig. 5a with inhomogeneous surface of the travertine due to previous fires and also stress in the stone on the upper left: this photo was taken after data evaluation, in daylight, to check the presence of some peculiarity in the 'stripe' identified by the CA-based evaluation of the map in Fig. 5e: the close-up, in fact, reveals the presence of a yellowish patina just on the right of the measured 'stripe'. This is possibly due to the prior presence of an iron clamp, a nail or a transportation of ions from a covering of a ledge or the chemical reaction of the stone's own mineral, where oxidation of iron has led to transportation to the surface, or some other discoloration of the surface not identified by visual inspection.

On the right-hand side, where the crusts are more even and "grey" by visual inspection, the travertine has an even surface, although with small cavities and holes due to weathering and natural pore structure of the travertine. This presents a more even layer of patina on the surface. The chemical compounds of the patina on the surface have not been analysed in this study.

Less soiled areas, as identified by the brown pixels in Fig. 5c, were also analysed separately with the PCA technique. A first result is shown

in Fig. 5g where the PC2-score map, obtained on the non-normalised spectra, highlights some irregular spots in the cleaned ashlar on the right (yellow-red pixels in the map). The corresponding spectra are shown in Fig. 5j: for the sake of clarity, spectra are STD normalised and each spectrum has the same colour as the corresponding pixel in Fig. 5g. Comparing the shape of the spectra and the corresponding PC2 score in the map in Fig. 5g, it is apparent that the yellow-red pixels in the map are characterised by a higher contribution in the red region of the spectrum. Fig. 5h represents the PC3 score and highlights a homogeneous behaviour of the cleaned area on the column while the ashlar on the right are less homogeneous. This could be explained by the fact that the ashlar on the right have been cleaned with a low pressure water mist leaving some particles in the cavities, while the column, besides being cleaned, has been exposed to rain water. The corresponding spectra are shown in Fig. 5k.

A more comprehensive result is shown in Fig. 5i where 'cleaned' and 'grey-patina' areas (corresponding, respectively, to the brown and yellow pixels of Fig. 5c) were analysed with the PCA technique. In general, three areas can be identified in the following way: pink pixels correspond to the weathered section of the column, light-blue to blue pixels point out the capital and ashlar on the upper right, while white-grey pixels refer to cleaned ashlar on the right. Note that the capital shows a different behaviour with respect to the very column, maybe due to a different weathering process or compositional features. The spectra are shown in Fig. 5l and coloured as the corresponding pixels in Fig. 5i. The different behaviour is consistent with the fact that the light travertine ashlar on the right have been cleaned recently during a conservation intervention, whereas the lighter areas along the column are also subject to heavy weathering.

Assessing the amount of soiling and crusts can be a first documentation and, together with the perception, mapping the façade prior and after cleaning may be important to the presentation of a refurbished or redeveloped building. In the case of Coliseum the blackened surfaces may

contribute to the perception of patina and age-value of the monument. The public perception of soiling and the amount of blackening on the façades remains a difficult issue. There is both a need to consider the general patterns of soiling as well as the amount of soiling. It would be convenient to establish a hierarchy for fluorescence features to assess the soiling patterns. This development for the estimate of aesthetic damage to the surfaces in terms of distribution and reaction to the soiling would be an additional tool for the sustainable management and future decisions about selective cleaning.

5. Conclusions

Fluorescence lidar remote sensing is a non-invasive technique successfully used in the monitoring and documentation of deterioration of the façade of the Coliseum in Rome. The biological colonization on substrata present in the monitored areas gave information on the status after recent cleaning. Remote monitoring of parts of the façade which had been previously cleaned allowed us to point out Chl-containing bio-organisms and to perform a first rough classification of them. This was also carried out in areas where the biological activity was not visually apparent. Furthermore,

multivariate techniques applied to the fluorescence spectra characterized the soiling patterns on parts of the substrata. These patterns were confirmed by visual inspection as darker, more stained areas, less affected areas and areas perceived as being cleaned. This may point to the usefulness of remote monitoring where surfaces are hard to reach and to establish thresholds of perceived lightness of a building.

To establish the origin of the biological colonization and the diversified elements of the soiling, it would be necessary to carry out new and exhaustive studies using sampling. The usefulness of mobile fluorescence lidar for documentation and survey of large surfaces featuring complex conditions is shown in monuments such as Coliseum. The possibility of performing these analyses during night-time also permits the ongoing daily activities of a dynamic historical site.

Acknowledgements

This work was financially supported by the Swedish Research Council for Environment, Agricultural Sciences and Spatial Planning (FORMAS) and the Swedish Research Council (VR).

References

- [1] C. Fotakis, D. Angelos, V. Zafirooulos, S. Georgiou, V. Tornari, *Lasers in the preservation of cultural heritage: Principles and applications*, Taylor and Francis Group, New York, London, 2007.
- [2] K. Dickmann, Report on Session "Non-cleaning applications" (Analysis), *Journal of Cultural Heritage* 4 (2003) 287-288.
- [3] G. Caneva, M. P. Nugari, O. Salvadori, *Biology in the conservation of works of art*, ICCROM, Rome 1991.
- [4] G. Caneva, A. Pacini, L. Celesti Grapow, S. Ceschin, The Colosseum's use and state of abandonment as analysed through its flora, *International Biodeterioration & Biodegradation* 51 (2003) 211-219.
- [5] J. Ashurst, F. G. Dimes, *Conservation of building and decorative stone*, Elsevier Butterworth-Heinemann, Oxford, 2004.
- [6] C. Bläuer-Böhm, Techniques and Tools for Conservation Investigations, in: D. Kwiatkowski, R. Löfvendahl (Eds.), *Proceedings of the 10th International Congress of Deterioration and Conservation*, Volume 2, Stockholm, June 27-July 2, ICOMOS, Stockholm, 2004, pp. 549-559.
- [7] H.K. Lichtenthaler, U. Rinderle, The role of chlorophyll fluorescence in the detection of stress conditions in plants, *CRC Critical Reviews in Analytical Chemistry* 19 (1988) S29-S85.
- [8] H. Edner, J. Johansson, S. Svanberg, E. Wallinder, M. Bazzani, B. Breschi, G. Cecchi, L. Pantani, B. Radicati, V. Raimondi, D. Tirelli, G. Valmori, P. Mazzinghi, Laser-induced fluorescence monitoring of vegetation in Tuscany, *EARSeL Advances in Remote Sensing* 1 (1992) 119-130.
- [9] H. Edner, J. Johansson, S. Svanberg, E. Wallinder, *Fluorescence lidar multicolor*

- imaging of vegetation, *Applied Optics* 33 (1994) 2471-2479.
- [10] V. Raimondi, G. Cecchi, L. Pantani, R. Chiari, Fluorescence lidar monitoring of historic buildings, *Applied Optics* 37 (1998) 1089-1098.
- [11] P. Weibring, T. Johansson, H. Edner, S. Svanberg, B. Sundner, V. Raimondi, G. Cecchi, L. Pantani, Fluorescence lidar monitoring of historical monuments, *Applied Optics* 40 (2001) 6111-6120.
- [12] D. Lognoli, G. Cecchi, I. Mochi, L. Pantani, V. Raimondi, R. Chiari, T. Johansson, P. Weibring, H. Edner, S. Svanberg, Fluorescence Lidar Imaging of the Parma Cathedral and Baptistery, *Applied Physics B* 76 (2003) 457-465.
- [13] R. Grönlund, J. Hällström, S. Svanberg, K. Barup, Fluorescence lidar multispectral imaging for diagnosis of historical monuments – Övedskloster, a Swedish case study, in: J. Nimmrichter, W. Kautek and M. Schreiner, (Eds.), *Proceedings of the 6th International Congress on Lasers in the Conservation of Artworks LACONA VI, Vienna, Austria 2005*, Springer Berlin, Germany, 2006.
- [14] G. Cecchi, L. Pantani, V. Raimondi, L. Tomaselli, G. Lamenti, P. Tiano, R. Chiari, Fluorescence lidar technique for the remote sensing of stone monuments, *Journal of Cultural Heritage* 1 (2000) 29-36.
- [15] L. Pantani, G. Cecchi, D. Lognoli, I. Mocchi, V. Raimondi, D. Tirelli, M. Trambusti, G. Valmori, P. Weibring, H. Edner, T. Johansson, S. Svanberg, Lithotypes characterization with a fluorescence lidar imaging system using a multi-wavelength excitation source, *SPIE Proceedings* 4886 (2003) 151-159.
- [16] D. Lognoli, G. Lamenti, L. Pantani, D. Tirelli, P. Tiano, L. Tomaselli, Detection and characterisation of biodeteriogens on stone cultural heritage by fluorescence lidar, *Applied Optics* 41 (2002) 1780-1787.
- [17] G. Ballerini, S. Bracci, L. Pantani, P. Tiano, Lidar remote sensing of stone cultural heritage: detection of protective treatments, *Optical Engineering* 40 (2001) 1579-1583.
- [18] A. Gabucci, *The Colosseum*, Electa, Milan, 2000.
- [19] C. Conti, Anfiteatro Flavio: Il restauro delle superfici in travertino, *Arkos: Scienza e Restauro* 2 (2001) 22-27.
- [20] S. Svanberg, Fluorescence spectroscopy and imaging of Lidar targets, in: T. Fujii, T. Fukuchi (Eds.), *Laser Remote Sensing*, CRC Press, Boca Raton, 2005, pp. 433-467.
- [21] P. Weibring, H. Edner, S. Svanberg, Versatile mobile lidar system for environmental monitoring, *Applied Optics* 42 (2003) 3583-3594.
- [22] G. Cecchi, P. Mazzinghi, L. Pantani, R. Valentini, D. Tirelli, P. de Angelis, Remote sensing of Chl fluorescence on vegetation canopies: 1. Near and far field measurement techniques, *Remote Sensing of Environment* 47 (1994) 18-28.
- [23] G. Cecchi, L. Pantani, B. Breschi, D. Tirelli, G. Valmori, FLIDAR: a multipurpose fluorosensor-spectrometer, *EARSel Advances in Remote Sensing* 1 (1992) 72-78.
- [24] G. Caneva, *Amphitheatrum naturae, il Colosseo: Storia e ambiente letti attraverso la sua flora*, Electa Milano, Rome, 2004.
- [25] G. Caneva, D. Di Stefano, C. Giampolo, S. Ricci, Stone cavity and porosity as a limiting factor for biological colonisation: The travertine of Lungotevere, Rome, *Proceedings of the 10th International Congress of Deterioration and Conservation, Volume 1, Stockholm, June 27-July 2, ICOMOS, Stockholm, 2004*, pp. 227-233.
- [26] Z. G. Cerovic, G. Samson, F. Morales, N. Tremblay, I. Moya, Ultra-violet-induced fluorescence for plant monitoring: Present state and prospects, *Agronomie: Agriculture and Environment* 19 (1999) 543-578.
- [27] A. C. Rencher, *Methods of multivariate analysis*, Wiley Interscience, New York, 2002.
- [28] C. Cipriani, L. Franchi, Sulla presenza di whewellite fra le croste di alterazione di monumenti romani, *Bolletino del Servizio Geologico d'Italia* 79 (1957) 555-564.

PAPER VI

Hyperspectral Fluorescence Lidar Imaging at the Coliseum, Rome: Elucidating Past Conservation Interventions

L. Palombi, D. Lognoli, V. Raimondi, G. Cecchi, J. Hällström, K. Barup, C. Conti, R. Grönlund, A. Johansson, and S. Svanberg.

Manuscript, 2007.

Hyperspectral fluorescence lidar imaging at the Coliseum, Rome: Elucidating past conservation interventions

L. Palombi¹, D. Lognoli¹, V. Raimondi^{1*}, G. Cecchi¹, J. Hällström², K. Barup², C. Conti³, R. Grönlund⁴, A. Johansson⁴, and S. Svanberg⁴

¹*Institute for Applied Physics 'Nello Carrara' - National Research Council, Via Madonna del Piano 10, I- 50019 Sesto Fiorentino, Firenze, Italy*

²*Architectural Conservation and Restoration, Lund University, P.O. Box 118, SE- 221 00 Lund, Sweden*

³*Soprintendenza Archaeologica di Roma, Palazzo Altemps, Piazza di S. Apollinare 44, I- 00186 Roma, Italy*

⁴*Atomic Physics Division, Lund University, P.O. Box 118, SE- 221 00 Lund, Sweden*

*Corresponding author: v.raimondi@ifac.cnr.it

Abstract: Fluorescence lidar techniques offer considerable potential for remote, non-invasive diagnostics of stone cultural heritage in the outdoor environment. Here we present the results of a joint Italian-Swedish experiment, deploying two hyperspectral fluorescence lidar imaging systems, for the documentation of past conservation interventions on the Coliseum, Rome. Several portions of the monument were scanned and we show that it was possible to characterize masonry materials, reinforcement structures and protective treatments inserted during past conservation interventions, on the basis of their fluorescence signatures.

OCIS codes: (110.4234) Multispectral and hyperspectral imaging; (280.3640) Lidar; (300.2530) Fluorescence, laser-induced; (280.4788) Optical sensing and sensors; (300.6280) Spectroscopy, fluorescence and luminescence.

References and links

1. A. Moropoulou, N.P. Avdelidis, and E.T. Delegou, "NDT and planning on historical buildings and complexes for the protection of cultural heritage," in *Cultural Heritage Conservation and Environmental Impact Assessment by Non-Destructive Testing and Micro-Analysis*, R. Van Grieken, K. Janssens, eds. (Taylor & Francis Group, London, UK, 2005), pp. 67-76.
2. R. Dallas, *Guide for Practitioners 4: Measured Survey and Building Recording for Historic Buildings and Structures*, (Historic Scotland, Edinburgh, 2004).
3. A. Aldrovandi, E. Buzzegoli, A. Keller, and D. Kunzelman, "Investigation of painted surfaces with a reflected UV false color technique," in *Proceedings of Art'05 – 8th International Conference on Non Destructive Investigations and Microanalysis for the Diagnostics and Conservation of the Cultural and Environmental Heritage*, Lecce (2005), pp. 3-18.
4. C. Fischer and I. Kakoulli, "Multispectral and hyperspectral imaging technologies in conservation: current research and potential applications," *Reviews in Conservation* **7**, 3-16 (2006).
5. E. Ciliberto and G. Spoto, *Modern Analytical Methods in Art and Archaeology – Vol. 155 in Chemical Analyses*, (John Wiley & Sons, New York, 2000).
6. M. Laurenzi Tabasso and S. Simon, "Testing methods and criteria for the selection/evaluation of products for the conservation of porous building materials," *Reviews in Conservation* **7**, 67-82 (2006).
7. S. Svanberg, "Fluorescence spectroscopy and imaging of lidar targets," in *Laser Remote Sensing*, T. Fujii and T. Fukuchi, eds. (CRC Press, Boca Raton, 2005), pp. 433-467.
8. F.E. Hoge, "Oceanic and terrestrial lidar measurement," in *Laser Remote Chemical Analysis*, R.M. Measures, ed. (John Wiley&Sons, New York, 1988), pp. 409-503.
9. V. Raimondi, L. Masotti, G. Cecchi, and L. Pantani, "Remote sensing of cultural heritage: a new field for lidar fluorosensors," in *Proceedings of the 1st International Congress on Science and Technology for the Safeguard of Cultural Heritage in the Mediterranean Basin*, Catania (1995) pp. 935-938.
10. V. Raimondi, G. Cecchi, L. Pantani, and R. Chiari, "Fluorescence lidar monitoring of historic buildings," *Appl. Opt.* **37**, 1089-1098 (1998).
11. P. Weibring, T. Johansson, H. Edner, S. Svanberg, B. Sundnér, V. Raimondi, G. Cecchi, and L. Pantani, "Fluorescence lidar imaging of historical monuments," *Appl. Opt.* **40**, 6111-6120 (2001).

12. D. Lognoli, G. Cecchi, I. Mochi, L. Pantani, V. Raimondi, R. Chiari, Th. Johansson, P. Weibring, H. Edner, and S. Svanberg, "Fluorescence lidar imaging of the cathedral and baptistery of Parma," *Appl. Phys. B* **76**, 457-465 (2003).
 13. L. Pantani, G. Cecchi, D. Lognoli, I. Mochi, V. Raimondi, D. Tirelli, M. Trambusti, G. Valmori, P. Weibring, H. Edner, T. Johansson, and S. Svanberg, "Lithotypes characterization with a fluorescence lidar imaging system using a multi-wavelength excitation source," *Proc. SPIE* **4886**, 151-159 (2003).
 14. G. Cecchi, L. Pantani, V. Raimondi, L. Tomaselli, G. Lamenti, P. Tiano, and R. Chiari, "Fluorescence lidar technique for the remote sensing of stone monuments," *J. Cult. Heritage* **1**, 29-36 (2000).
 15. G. Cecchi, L. Pantani, V. Raimondi, D. Tirelli, L. Tomaselli, G. Lamenti, M. Bosco, and P. Tiano, "Fluorescence lidar technique for the monitoring of biodeteriogens on the cultural heritage," *Proc. SPIE* **2960**, 137-147 (1996).
 16. D. Lognoli, G. Lamenti, L. Pantani, D. Tirelli, P. Tiano, and L. Tomaselli, "Detection and characterisation of biodeteriogens on stone cultural heritage by fluorescence lidar," *Appl. Opt.* **41**, 1780-1787 (2002).
 17. G. Ballerini, S. Bracci, L. Pantani, and P. Tiano, "Lidar remote sensing of stone cultural heritage: Detection of protective treatments," *Opt. Eng.* **40**, 1579-1583 (2001).
 18. J. Hällström, K. Barup, R. Grönlund, A. Johansson, S. Svanberg, L. Palombi, D. Lognoli, V. Raimondi, G. Cecchi, and C. Conti, "Documentation of façades previously cleaned: A case study on the Coliseum, Rome, using hyperspectral imaging fluorescence lidars", submitted (2007).
 19. A. Gabucci, *The Colosseum*, (Electa, Milan, 2000).
 20. C. Conti, "Anfiteatro Flavio: Il restauro delle superfici in travertino," *Arkos: Scienza e Restauro* **2**, 22-27 (2001).
 21. G. Cecchi, P. Mazzinghi, L. Pantani, R. Valentini, D. Tirelli, and P. De Angelis, "Remote sensing of chlorophyll a fluorescence of vegetation canopies: 1. Near and far field measurement techniques," *Rem. Sens. of Environ.* **47**, 18-28 (1994).
 22. G. Cecchi, L. Pantani, B. Breschi, D. Tirelli, and G. Valmori, "FLIDAR: A multipurpose fluorosensor-spectrometer," *EARSeL Advances in Remote Sensing* **1**, 72-78 (1992).
 23. H. Edner, J. Johansson, S. Svanberg, E. Wallinder, M. Bazzani, B. Breschi, G. Cecchi, L. Pantani, B. Radicati, V. Raimondi, D. Tirelli, G. Valmori, and P. Mazzinghi, "Laser-induced fluorescence monitoring of vegetation in Tuscany," *EARSeL Advances in Remote Sensing* **1**, 119-130 (1992).
 24. H. Edner, J. Johansson, S. Svanberg, and E. Wallinder, "Fluorescence lidar multicolor imaging of vegetation," *Appl. Opt.* **33**, 2471-2479 (1994).
 25. R. Grönlund, J. Hällström, S. Svanberg, and K. Barup, "Fluorescence lidar imaging of historical monuments - Övedskloster, a Swedish case study," in *Lasers in the Conservation of Artworks: LACONA VI Proceedings, Vienna/Austria, Sept. 21-25, 2005*, J. Nimmrichter, W. Kautek, and M. Schreiner, eds. (Springer, Berlin, Germany, 2007) pp. 583-592.
 26. P. Weibring, H. Edner, and S. Svanberg, "Versatile mobile lidar system for environmental monitoring," *Appl. Opt.* **42**, 3583-3594 (2003).
 27. P. Weibring, J.N. Smith, H. Edner, and S. Svanberg, "Development and testing of a frequency-agile optical parametric oscillator system for differential absorption lidar," *Rev. Sci. Instrum.* **74**, 4478-4484 (2003).
 28. C. af Klinteberg, M. Andreasson, O. Sandström, S. Andersson-Engels, and S. Svanberg, "Compact medical fluorosensor for minimally invasive tissue characterization," *Rev. Sci. Instrum.* **76**, 034303 (2005).
 29. A.C. Rencher, *Methods of Multivariate Analysis* (Wiley Interscience, New York, 2002).
 30. P.F. Velleman and D.C. Hoaglin, *Applications, Basics, and Computing of Exploratory Data Analysis*, (Duxberry Press, Boston, 1981).
 31. Y. Hochberg and A.C. Tamhane, *Multiple Comparison Procedures*, (Wiley Interscience, New York, 1987).
-

1. Introduction

The documentation and scientific investigation of materials play a key role for the conservation and management of the cultural heritage worldwide [1]. The knowledge of the history of a monument and its status, together with the acquisition of information about previous conservation interventions with the subsequent introduction of new materials and chemicals, are all important factors for a thorough understanding of its present decay. Studying the behavior of a monument treated in the past gives us valuable information for its future conservation and also a good opportunity for a sound selection of suitable conservation solutions.

In this context, modern documentation methods based on new, non-invasive technologies are fundamental for the conservation sector. In the case of the immovable heritage, like buildings, methods to be used vary according to the category of documentation needed, which can range from an architectural survey to an in-depth analysis of pigments used in the paint applied on the surface [2,3].

Nowadays, the first assessment before intervention on both movable and immovable heritage is often an image-based evaluation. Besides traditional photographic methods, spectral imaging has also rapidly developed as a non-invasive technique within conservation science over the last decades [4,5]. However, when large surfaces in the outdoor environment must be tackled, the application of the spectral imaging methods are not as straightforward as for movable heritage and its application must often be limited to the analysis of samples in the laboratory [4,6].

The assessment of the status of a major monument, such as the Coliseum in Rome, regarding materials inserted during previous conservation interventions, chemicals and reinforcement structures, but also regarding new or re-worked travertine blocks, can be troublesome without extensive testing in a laboratory environment. On the other hand, porous building materials, as those employed for the Coliseum, exhibit a wide range of conservation problems as well as a great variety of different solutions for their conservation, so that great care must be taken in the selection of the most appropriate conservation method. In addition, the dimensions of the building and its height constitute a further difficulty, especially when preliminary survey information is needed. From this point of view, the use of fluorescence lidar imaging can play a crucial role to gain knowledge about the materials on the surface of the monument and thus provide the conservation sector with valuable, accessible information.

Fluorescence lidar (LIght Detection And Ranging) imaging is a non-invasive, remote sensing technique that extends the application of the LIF (Laser Induced Fluorescence) technique to the outdoor environment and combines it with the advantages offered by imaging. Although initially developed for marine and vegetation monitoring applications [7,8], fluorescence lidar remote sensing has already been applied to the monitoring of the cultural heritage for the last decade: first experiments date back to the mid 1990s, when characterization of biodeteriogens and lithotypes of stone monuments were performed in point measurements on the Cathedral and Baptistery of Parma, Italy [9,10]. These initial experiments have then been extended to fluorescence lidar imaging campaigns with acquisition of hyperspectral fluorescence maps on several targets [11-13]. Main fields of investigation have been the detection and characterization of different lithotypes [10,12,14], of biodeteriogens [15,16] and of protective treatments [12-17], showing good potential of the technique for an extensive monitoring and investigation of the stone cultural heritage. Up to now, no specific experiments were conducted for the analysis of past conservation interventions.

This paper illustrates main results of a joint Italian-Swedish measurement campaign carried out on the Coliseum, Rome, and focuses on the application of the fluorescence lidar imaging to the documentation of past conservation interventions and their consequences. Specifically, this paper addresses the following aspects:

- * Detection of masonry materials used in conservation interventions (e.g., mortar, cement), but also characterization of travertine blocks with the specific purpose to help identification of re-worked material.
- * Mapping of reinforcement structures on the surface, such as old and new clamps, and their characterization especially as far as their treatment with chemicals against degradation is concerned.

In an accompanying paper [18], aspects of biological contamination and soiling of surfaces are discussed separately.

2. Experimental

The measurements were conducted in January 2005 within the framework of a joint Italian-Swedish lidar campaign held at Coliseum, Rome. The measurements were carried out on selected areas of the monument, chosen in agreement with the *Soprintendenza Archeologica di Roma* to analyze interventions carried out in past and recent times for the external reinforcement and conservation of the monument. Measurements were performed at night to avoid interference with the intense diurnal activity at the site.

Two different fluorescence lidar systems were deployed for these measurements: the Italian CNR-IFAC fluorescence lidar system and the Swedish LTH lidar system. Both systems

are housed in vans used as mobile laboratories on site. The two lidar systems were placed at a distance of about 18 m and 60 m from the monument, respectively.

Hyperspectral fluorescence data were acquired on the selected areas and then analyzed with multivariate statistical techniques to investigate the spots on the monument's surface interesting with regard to past restoration or reinforcement interventions. Traditional documentation methods, such as digital photography, surveying and *in situ* studies, as well as the study of conservation reports and archive materials, have been exploited to complement hyperspectral fluorescence data.

The following subsections give a description of the investigated materials, the instrumentation, the experimental conditions and the data processing methods used in this paper.

2.1 The monument: examined areas and materials

The Flavian Amphitheatre, world-wide known as the Coliseum, is one of the best known historical monuments of its kind. The Flavian Emperor Vespasian (69-79 AD) planned and began the construction while his son Titus (79-81 AD) completed and inaugurated the arena in 80 AD [19]. The amphitheatre served as an arena for spectacular scenery with its famous gladiator games. In the 5th century the public interest in these games and the politics changed with the Christian emperors, leading to the suspension of the games in AD 438. The building that was then in the center of the city of Rome rapidly fell into abandonment and the centuries that followed included reuse of the valuable material in the building. The exterior of the arena, a typical example of extradosal arches framed by classical orders, is now best viewed from the north side (facing towards *Via dei Fori Imperiali*) with the external ring conserved in its entirety.

The amphitheatre suffered from demolitions, earthquakes, fires, and water drainage problems during the centuries. In Europe, a renewed interest in the Antiquity and the period of classical architecture led to a more systematic excavation and restoration of the arena, which was performed during the nineteenth and twentieth centuries. Due to its structural collapse, many reinforcements have been carried out on the façades, also including new materials and change of materials. Although many interventions and conservation projects have been undertaken with documentation in text and photographs, the knowledge of previous projects is sometimes hard to encompass.

The amphitheatre followed the fundamentals of Roman construction, based on the material involved - cut stone or brick and/or concrete structures. The calcite stone travertine was a widely used material for the Coliseum and was quarried in Tivoli. It covered most of the podium and perimeter walls, as well as public tiers, staircases and water channels. Three other kinds of stones were used in the construction, held together by metal clamps – Peperino stone, yellow and grey tufa. The section that was investigated during the lidar campaign also involved the previous restoration project and erection of the second buttress by the architect Giuseppe Valadier during 1823-1826.

The section of the monument selected for these fluorescence measurements is on its north side, facing *Via dei Fori Imperiali*, and is shown in Fig. 1d: it ranges from arch L to arch LIV and comprehends both heavily soiled areas (on the left of the picture) and areas cleaned recently with fine water mist, without any additive, during a restoration project [20]. In the latter areas black crusts and soiled parts have thus been removed from the travertine and the ageing of the stone has now left it with a browner staining on some parts.

This section of the external ring of Coliseum has undergone several reconstruction and conservation interventions in the last centuries. The main stone material is travertine, cut in large blocks. At first visual inspection, the travertine can be regarded as dating back to the first building phase, although there are indications suggesting that some parts of the lower half on the left side of the studied area contain blocks dating from a modern restoration period. In general, different techniques of craftsmanship forming the ashlar, tools used, boundaries, faces of the stone with different surface finish bearing the marks of the masons, etc., are considered as useful indicators to estimate the period to which the examined material dates back. However, the reuse of older blocks, widespread especially in the past, is hard to

distinguish on the basis of these methods, and its detection usually require collection of samples.

Besides areas undergone past restoration interventions, this section of the monument features also several mortar joints, holes filled up with cement due to previous conservation and several metal clamps used to prevent structural decay and to strengthen semi-columns and arches. These structural reinforcement interventions date from the last centuries (from the XIX to the XX century) and are located both in the soiled and in the cleaned areas.

The areas of this section that were mapped with the lidar systems are indicated in Fig. 1d with a summary of the main relevant features of each area. Besides hyperspectral fluorescence images of these areas, point fluorescence measurements were also acquired in some spots selected for their peculiar features, and their locations are specified in the *Results and Discussion* section as needed.

2.2 Instrumentation

The CNR-IFAC lidar system, the FLIDAR, is an excimer-based fluorescence lidar system that has been repeatedly used for fluorescence remote sensing of monuments since 1994 (see, e.g., [10,12]). It uses an excimer laser (XeCl @ 308 nm) as an excitation source. The signal is collected with a 25-cm diameter 1-m focal length Newtonian telescope. A fiber bundle conveys the signal from the telescope focal plane to the input slit of a 275-mm focal length spectrometer (Acton Research, 1235) coupled to an intensified gateable 512-photodiode array detector (EG&G, 1420R) which can detect a 300-nm wide spectrum in the 300-800 nm spectral range with an effective 2.4 nm spectral resolution. Long-pass optical filters are used to reject the laser line and spectrometer higher orders. Control electronics, data acquisition and storing are controlled via a personal computer. The system is housed inside a small van (FIAT, Ducato Maxi) whose dimensions (w×l×h) are 2.1 m×5.5 m×2.5 m. A detailed description of the system can be found in [10,21,22].

The FLIDAR has been recently upgraded with a automatic target scanning system to perform hyperspectral fluorescence imaging. In addition, the system is equipped with a target pointing system in the visible, coaxial with the lidar system, to reference the acquired fluorescence images on the target: the position of the pointing laser spot is recorded on a photo acquired at the same time. The final FLIDAR data is thus a referenced hyperspectral fluorescence image of the scanned surface.

The LTH lidar system was originally intended for atmospheric differential absorption lidar (DIAL) measurements, but is also well adapted for fluorescence measurements and has been employed in several fluorescence lidar campaigns [11-13,23-25]. The system is thoroughly described in [26]. The system can perform fluorescence imaging by scanning a folding mirror in a roof-top dome to direct the laser radiation where desired. The laser beam is sent out coaxially with the receiving telescope, so they are always aligned. The laser used is a frequency tripled Nd:YAG laser (Spectra Physics, GCR-290) at 355 nm running with 20 Hz repetition frequency. By Q-switched operation 4-5 ns pulses with high energy, in our case limited to about 30 mJ, are created. The beam is expanded to 5 cm diameter before it is transmitted to the target. Alternatively, radiation from a modified optical parametric oscillator (OPO) system (Spectra Physics, MOPO-730) [27], can be tuned to emit laser radiation in the wavelength range 220 nm-1.7 μ m. The receiver is a 40-cm-diameter Newtonian telescope which collects the fluorescence radiation. The collected signal is guided through a long-pass filter focused onto the tip of a 600 μ m optical fiber and connected to an optical multichannel analyzer (OMA) system [28]. The OMA is equipped with a spectrometer (Oriel, MS125) with a gated and intensified CCD detector (Andor Technology, DH501-25U-01), which can detect the spectrum in the wavelength range 280-810 nm with a 2.2 nm resolution. The system is housed in a Volvo F610 truck of dimensions (w×l×h) 2.5 m×8.0 m×3.1 m and is powered by a 40 kVA motor generator pulled by the truck.

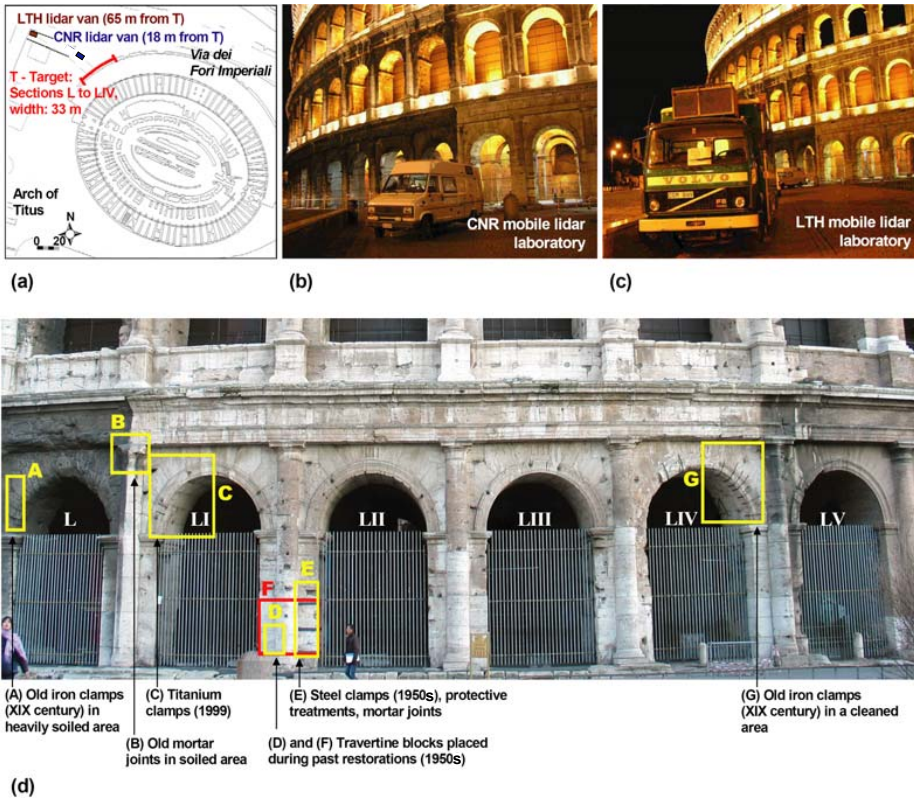


Fig. 1. Experimental conditions at the site location (Coliseum, Rome): (a) planimetry of the Coliseum with the section of the monument chosen for the measurements and the locations of the two lidar mobile laboratories; (b) on-site deployment of the CNR-IFAC and (c) of the LTH lidar systems; (d) areas selected for the analysis of past conservation interventions.

2.3 Experimental set-up

Fig. 1 shows the experimental conditions at the site: measurements were taken at night to avoid interference with the usual intense activity at the site during daytime. Fig. 1a shows the planimetry of the Coliseum and also indicates the section of the monument chosen for the experiment. The locations of the two mobile lidar laboratories with respect to the monument are also marked in the map. In Fig. 1b and Fig. 1c, the two mobile laboratories hosting the lidar systems are shown while deployed during the experiment.

The CNR-IFAC mobile lidar laboratory, shown in Fig. 1b, was placed at about 18 m from the target. At such distance the diameter of the spot effectively measured on the target was about 2 cm. The horizontal and vertical spatial resolution of the acquired images (i.e. the distance between the center of one measured spot and the following one) varied between 6 cm and 12 cm, depending on the purpose of the measurement, the features of the target and the time required to perform it. Fluorescence data were acquired with 308-nm excitation. A fluorescence spectrum (840 channels distributed over the 300-800 nm range) was acquired for each pixel of the fluorescence image. The fluorescence spectrum was obtained by merging two separate 300-nm wide fluorescence measurements, one from 300 nm to 600 nm and the other from 500 nm to 800 nm, to avoid second-order superimposition. Each fluorescence measurement was accumulated over 30 laser shots. The time required for the acquisition of the fluorescence spectrum, its storage and then aiming the next spot with the FLIDAR system takes about 1 min. Before the acquisition of each fluorescence map, the FLIDAR laser

pointing system in the visible was used to define the effective area where the fluorescence map would be acquired next; this is achieved by acquiring digital photos with the pointing system aiming in turn at each vertex of the area that will be scanned next and storing them in the computer together with the relevant fluorescence data.

The LTH mobile lidar laboratory, shown in Fig. 1c, was parked about 65 m from the target. The spot size on the target was about 5 cm and the resolution of the scans varied between 9 and 20 cm, depending on the purpose of the measurement, the features of the target and also the time required. The overall dimensions of the scanned area varied as well according to the issues to investigate. Fluorescence data were acquired with the 355-nm excitation. The LTH system acquired a complete fluorescence spectrum from 400 nm to 800 nm at each laser pulse. Each spectrum was averaged over 100 or 200 shots, depending on the area considered and the accuracy needed. Measuring one spot, storing the spectrum and moving the dome to the next spot takes about 10 seconds.

2.4 Data analysis

All fluorescence spectra from both lidar systems were corrected for the wavelength response of the relevant optical system.

Most evaluations were carried out using multivariate statistical techniques, specifically either Principal Component Analysis (PCA) or Cluster Analysis (CA). These techniques offer several advantages to extract information out of a complex set of data such as those obtained with hyperspectral fluorescence lidar imaging.

PCA offers the possibility to systematically extract the differences and similarities in the data set. The data are transferred onto a new set of orthogonal base vectors, called Principal Components (PCs), which maximize the variation in the data set onto the first PC, the remainder of the variation onto the second, and so on. Each spectrum is then described by its scores, i.e., its values along the different PCs. Usually, the data is thoroughly described with just a few PCs and thus it is easier to analyze the data.

CA is an unsupervised classification method used to arrange a set of data into clusters with the aim to establish a set of clusters such that all data within a cluster are more similar to each other than they are to data in other clusters. In particular, hierarchical CA differs from other classification methods since neither the number of clusters, nor the clusters themselves are known *a priori*. Several CA procedures can be applied and different *distance* and *linkage* methods, i.e., dissimilarity criteria, can be chosen for determining the clusters and the distance between them. In particular, the false-color maps shown in this paper were obtained applying a hierarchical agglomerative clustering to the data. A thorough description of multivariate techniques, such as the PCA and CA, can be found in, e.g., [29].

The thematic maps shown in the next section, i.e. false-color maps displaying the spatial pattern concerning a specific theme or specific target attributes (e.g., the spatial distribution of protective treatments over a surface), were obtained using one of the following methods:

- * calculating a ratio between two selected spectral bands of the fluorescence spectra and plotting the ratio values as a function of the corresponding (x,y) positions in a false-color coded map;
- * applying the PCA technique to the fluorescence data set of a given area and plotting either a PC score or the ratio between two PC scores as a function of the corresponding (x,y) position in a false-color coded map;
- * applying the PCA technique to the fluorescence data set of a given area, selecting three PC scores (usually the first three) and associating to each of them one of the three channels of an Red-Green-Blue (RGB) coded image; in this way the final RGB map will contain information referring to all the three selected PCs;
- * applying a CA method to a fluorescence data set of a given area, associating to each identified cluster a specific color and plotting them as a function of the corresponding (x,y) position in a false-color coded map.

Spectra were usually normalized either to their maximum or to their standard deviation before the PCA or CA-based evaluation, as specified, if needed, in the next section. This procedure is consistent with the fact that, in remote sensing, absolute fluorescence intensities are usually

affected by many factors that cannot be easily controlled and thus methods based on spectral shape analysis are preferred to those based on the fluorescence intensities.

3. Results and discussion

This section is organized in two parts: the first part focuses on the characterization of masonry materials inserted during restorations carried out in the past, such as travertine blocks and joints of mortar or cement. The second part deals with the identification of strengthening elements, such as metal clamps, on the surface and their characterization in terms of protective treatments.

3.1 Characterisation of masonry materials

The analysis of the surface concerning the historical background of the building and the time aspect of the initial construction and later reconstructions may be a troublesome process when it comes to the interpretation of the stones being used. When observing the surfaces, interpretation of techniques used by the masons, geological identification, mortars and other information from archives are all useful indicators but often need additional documentation and scientific investigations on site and in the laboratory. The fluorescence lidar technique as a completely non-invasive technique can provide additional data without requiring samples or even the use of scaffolds or lift, as required by a thorough visual inspection or any sampling procedure.

To demonstrate the potential of the fluorescence technique to support experts in the identification of non-original blocks, an area (D in Fig. 1d) containing both original blocks, dating back to the Roman period, and blocks placed during past restorations, was selected and measured with 308 nm excitation. However, due to the practice, widespread in the past, of re-working original blocks, a visual inspection of these blocks by experts could not univocally determine if some of the blocks inserted during the restorations were in fact original blocks processed again by craftsmen.

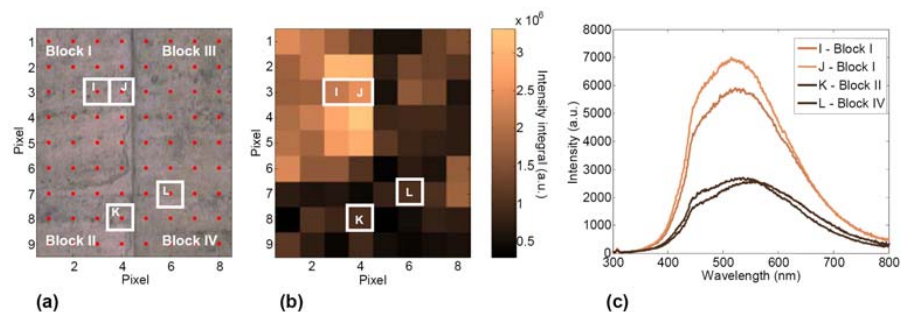


Fig. 2. Analysis of an area (Area D in Fig. 1d) containing original Roman blocks and blocks placed later, during conservation interventions. The excitation wavelength was 308 nm. The distance of the sensor from the target was about 18 m and the spot size diameter on the target was about 2 cm. The spatial resolution (i.e. the distance between the centers of two following spots) was 12 cm both in horizontal and vertical directions. (a) Scanned area and reference grid automatically generated by the FLIDAR software. (b) Map obtained from the integrals of the spectral intensity of the non normalized fluorescence spectra in the 410 nm-750 nm spectral range. (c) Typical non-normalized fluorescence spectra of the scanned area.

Fig. 2a shows the scanned area together with the grid automatically generated by the FLIDAR software to reference the fluorescence data on the target. This area comprehends four blocks: Blocks I and II were probably placed in the present position during a restoration intervention carried out in the 1950s; Blocks III and IV were original blocks dating back to the Roman period. However, Block II, although inserted only in recent times as inferred from its new joints, the finish of the stone surface and its sharp edges together with a patina different from that of the surrounding blocks, could also be an original Roman block that was re-

worked by restorers to harmonize the other newly inserted blocks. All the four blocks are in travertine.

Fig. 2b shows a map with the spectral integrals of the intensity of the non-normalized fluorescence spectra: the map highlights a different spectral behavior of Block I with respect to the other three blocks (Blocks II, III, IV), as pointed out by a prominence of lighter colors for Block I, indicating a definitely higher fluorescence intensity with respect to the other three blocks. On the other hand, Block II shows a spectral behavior very similar to Blocks III and IV. This leads to believe that Block II, although placed in this position in recent times, is in fact an original Roman block. This is further supported by the comparison of the fluorescence spectra shown in Fig. 2c: spectra belonging to Block I (labeled as I and J) have similar profiles and are definitely more intense than the spectra of Block II and IV (labeled as K and L). The spatial locations of these fluorescence spectra are indicated in the map of Fig. 2b and labeled accordingly.

An extended portion (Area F in Fig. 1d), containing the same area as discussed in Fig. 2b (Area D in Fig. 1d), was analyzed with the 355-nm excitation, from a greater distance (65 m). The map of Fig. 3a, superimposed to the photo of the examined area was obtained from the mean values of the fluorescence spectral intensity in the 410-750 nm spectral range. Also in this case, the spectral behavior of Block II is very similar to that of the blocks belonging to the central column, identified by the experts as being original Roman blocks. On the contrary, all the other blocks on the left part of this area generally show a more intense fluorescence intensity, as indicated by the lighter colors in the map. Fig. 3b shows some typical fluorescence spectra referring to different spots of the scanned area: the relevant pixels are squared with the corresponding colors in the map of Fig. 3a. Note that also with the 355-nm

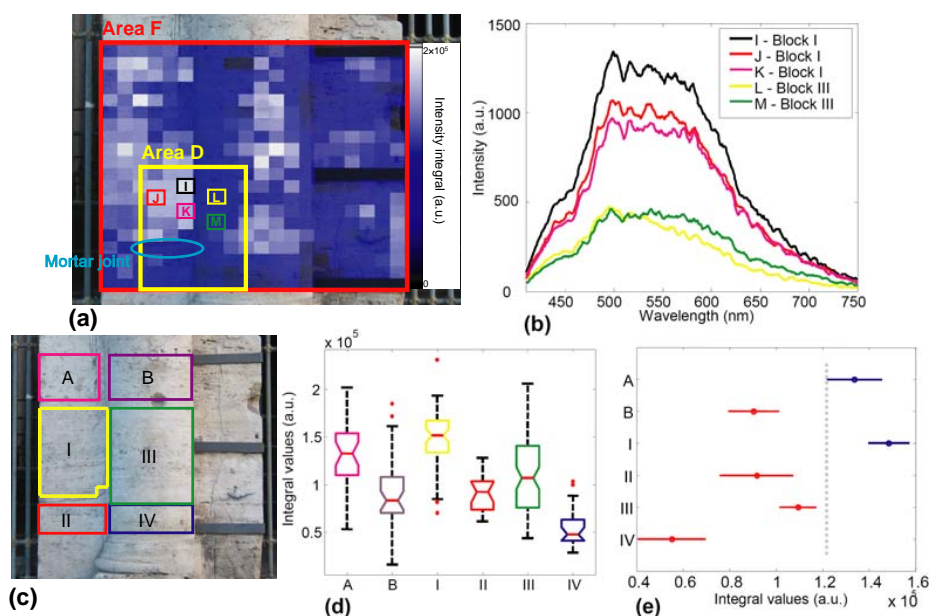


Fig. 3. Analysis of an extended portion (Area F in Fig. 1d) containing Area D. The excitation wavelength was 355 nm. The distance from the sensor to the target was 65 m and the spot size diameter on the target was about 5 cm. The horizontal and vertical spatial resolutions were 12 cm and 10 cm, respectively. (a) shows a fluorescence map obtained by integrating the spectral intensity between 410 nm and 750 nm of the non-normalized fluorescence spectra. (b) illustrates some typical non-normalized fluorescence spectra of the scanned area. (c) indicates the positions of the different blocks in the examined area: blocks on the left (blocks A, I, II) present characteristics typical of new or re-worked blocks inserted during conservation interventions; blocks along the column (blocks B, II, IV) are original Roman blocks. (d) is a box and whisker diagram illustrating mean values and standard deviations for the fluorescence intensity for each block. (e) shows the results of a multiple comparison test with mean values and uncertainties for the six blocks.

excitation Block I (upper left in area D) showed a high fluorescence intensity with respect to all the other blocks, as also found with 308-nm excitation (see Fig. 2).

The fluorescence spectral integrals, in fact, feature a certain variance also within a single block. This is clear by comparing the map in Fig. 3a with the photo in Fig. 3c where the different blocks are marked in different colors: Blocks A, I and II were new or re-worked blocks inserted during the interventions carried out in the 1950s; Blocks B, II and IV are original Roman blocks. Fig. 3d reports a box and whisker plot for the data set of fluorescence integrals grouped by different blocks. The notches in the boxes represent a robust estimate of the uncertainty about the medians for box-to-box comparison [30]. The graph in Fig. 3d indicates that the true medians of Block A and I differ, with 95% confidence, from those referring to Blocks B, II and IV, since their notches do not overlap. Block III has a greater spread and its notches slightly overlap with those of block A. To further investigate the feasibility to distinguish the blocks on the basis of their fluorescence spectral intensity integrals, the data set has been analyzed with a multiple comparison test using the Tukey-Kramer method [31]. The mean values and corresponding uncertainties were evaluated for each block and reported in Fig. 3e: Blocks A and I (blue markers in the graph) can be considered different from the other blocks (red markers in the graph), with a 95% confidence, since their bars do not overlap.

Area D, a detail of which is shown in Fig. 4a, also features an apparent mortar joint: the joint is located between Block I and Block II of Area D (Fig. 2a), in correspondence of line 7 (first four pixels) of the map of Fig. 2b. The same joint has also been scanned in Area F with the 355-nm excitation as shown in Fig. 3a where it corresponds to line 17 (first six pixels) of the map.

Fig. 4b shows the fluorescence spectra of the first four pixels of line 7 of the map in Fig. 2b: the spectra are compared with some reference point fluorescence spectra acquired separately in a selected spot of the joint and with the fluorescence spectra corresponding to the lines above and below the joint in the map. In general, the mortar shows a higher fluorescence contribution at lower wavelengths than the spectra of stone. This is also confirmed by the 355-nm excited fluorescence spectra shown in Fig. 4c: these are the fluorescence spectra corresponding to the first six pixels of line 17 of the map on Area F shown in Fig. 3a: according to their shape, the first two spectra (dotted lines) refer to the stone rather than to the mortar. This can be inferred also from the photo in Fig. 4a. The 355-nm excited fluorescence spectra are noisier than the 308-nm excited spectra also because of the greater distance from the target (65 m instead of 18 m).

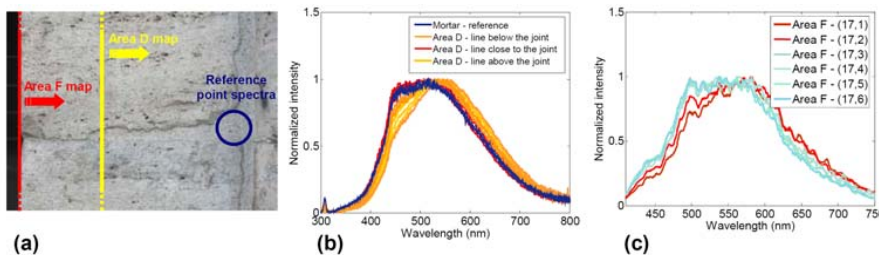


Fig. 4. Fluorescence spectra, acquired on the mortar joint between Block I and Block II, and fluorescence spectra from scans over Area D and Area F. (a) Detail showing the mortar joint and the spot where reference spectra were acquired. (b) 308-nm excitation: reference point fluorescence spectra (blue) acquired on the mortar joint are compared with a set of spectra from the map of Fig. 2 (Area D). (c) 355-nm excitation: fluorescence spectra from line 17 of the map of Fig. 3a (Area F); the line was acquired along the mortar joint. Note that the first two pixels of line 17 refer to stone rather than to mortar, as can be inferred also from the photo in (a).

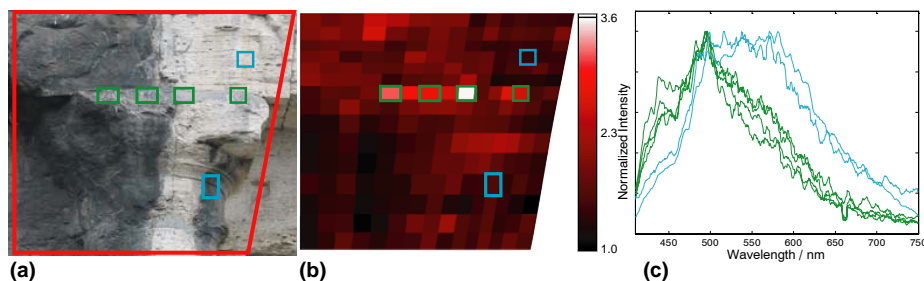


Fig. 5. Scanning of an area with mortar joints on both cleaned and non-cleaned portions of the monument (Area B in Fig. 1d). The excitation wavelength was 355 nm. The distance of the sensor from the target was 65 m and the spot size diameter on the target was about 4 cm. Spatial resolutions were 17 cm and 11 cm along the horizontal and the vertical direction, respectively. (a) the red frame indicates the measured area and (b) shows the ratio between the intensities in the wavelength range 485-505 nm divided by the intensity in the wavelength range 525-735 nm. The highest values correspond to a mortar joint, possibly with cement content, present on the top of the capital. The normalized spectra in (c) correspond to cement (green curves) and travertine stone (cyan curves), corresponding to the squares in (a) and (b).

The feasibility of detecting historic joints with the fluorescence lidar technique was also investigated in heavily soiled areas, as that shown in Fig. 5a. The area to scan was chosen on the border of a recently cleaned section of the monument. This region, corresponding to Area B in Fig. 1d, features an extensive, old smeared cement joint and comprehends both a heavily soiled portion of the façade and a portion of travertine recently cleaned. The soiled portion has a very rough surface due to weathering and natural ageing of the travertine, but also due to previous fire incidents, that caused stress to the stone. Fig. 5b shows a false-color map obtained by a ratio of the intensity value in the wavelength range 485-505 nm divided by the intensity value in the wavelength range 525-735 nm. Comparing the map in Fig. 5b with the photo in Fig. 5a it is clear that the brightest pixels correspond to an old smeared mortar joint which most likely contains cement. This is further confirmed by the fact that the fluorescence spectra relative to the mortar joint have a remarkably different spectral shape with respect to the fluorescence spectra of both the non-cleaned, soiled travertine and the cleaned one, as shown in Fig. 5c. The green curves correspond to spectra from the mortar joints, while the cyan curves are reference spectra from the underlying stone as marked by the squares of the same colors in Figs 5a and 5b.

3.2 Detection and characterization of metal reinforcement structures

The section of the monument selected for the fluorescence campaign included the presence of several past and recent interventions for the reinforcement of the original structure with metal clamps. During the measurements, it was noted that some of the metal clamps gave characteristic spectral signals, including a sharp peak in the ultraviolet region (around 380 nm), interpreted as an anti-corrosion chemical applied to the clamps.

An example is shown in Fig. 6. Fig. 6a shows a photograph of the measured area and indicates two measured points, on different metal clamps. Both clamps belong to the same period, dating back to the consolidation interventions carried out by Valadier in 19th century. In Fig. 6b, their corresponding fluorescence spectra are shown. The sharp peak in the ultraviolet region is clearly seen in point A, while it does not occur in point B, indicating that the clamp in B has not been recently treated with the anti-corrosion chemical.

A scan over a cleaned area containing metal clamps was performed with the 308 nm excitation and results are reported in Fig. 7. This area corresponds to Area E in Fig. 1d. In Fig. 7a, the area with the measured points is shown. In Fig. 7b a CA has been performed, and it is clearly seen that points on the metal clamps are different from the surrounding travertine stone. The same feature can be seen by plotting the integral values in the wavelength range 360-400 nm, as can be seen in Fig 7c. The metal clamps have been treated, so they are clearly identified by the peak at around 380 nm, and the spectra corresponding to the colored points are seen in Fig. 7e. The curves have the same color as the corresponding pixels in Fig. 7c.

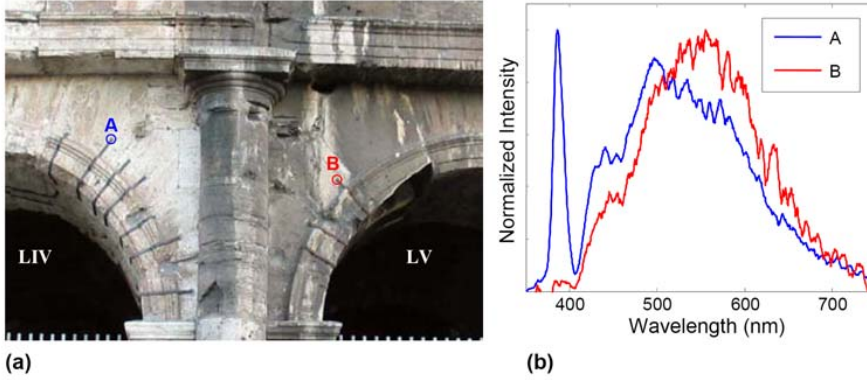


Fig. 6. Comparison between fluorescence spectra from two old iron clamps. The excitation wavelength was 355 nm. The distance of the sensor from the target was 65 m and the spot size diameter on the target was about 5 cm. (a) The spots where the fluorescence spectra were acquired. (b) Fluorescence spectra, normalized to their maximum, from the two clamps: Spectrum A shows the typical narrow peak due to the anti-corrosion treatment chemicals; Spectrum B does not show this feature and hence this metal clamp was not treated recently.

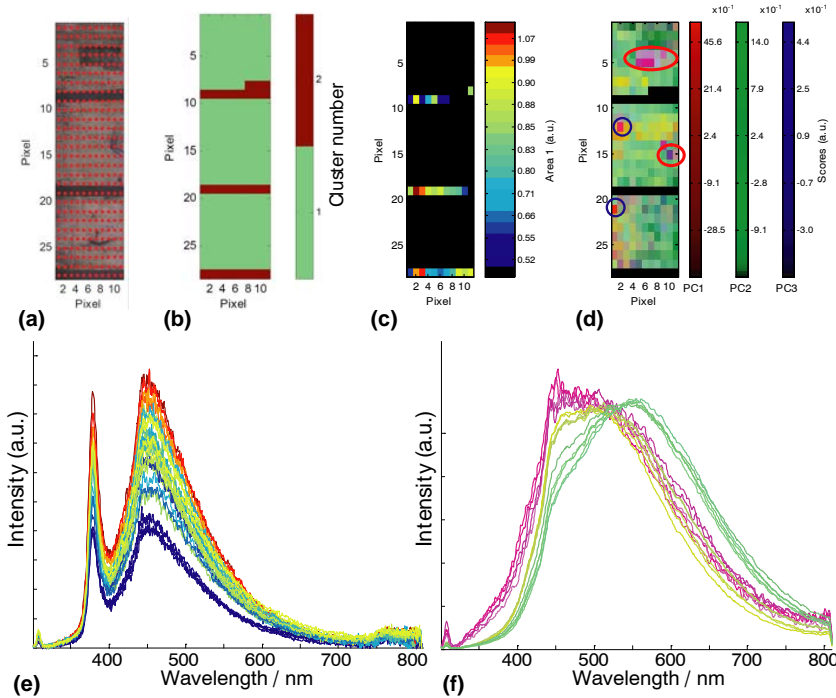


Fig. 7. Analysis of an area (Area E in Fig. 1d) containing steel clamps inserted during an intervention interpreted as dating back to the 1950s conservation project. There are also several joints made of cement/mortar. The excitation wavelength was 308 nm and the distance to the target was about 18 m. The spot size diameter on the target was about 2 cm and the spatial resolution was 6 cm both in horizontal and vertical directions. (a) shows a picture of the area with the measured points indicated. (b) shows a CA of the area, where the metal clamps can be clearly discriminated. In (c), the integral of the values in the wavelength range 360-400 nm. (d) shows a PCA-RGB map of the points on the travertine stone, with PC1 as red, PC2 as green and PC3 as blue. In (e), spectra from metal clamps are shown, in the same color as the color of the pixels in (c), and in (f), spectra from travertine are shown, in the same color as the color in (d).

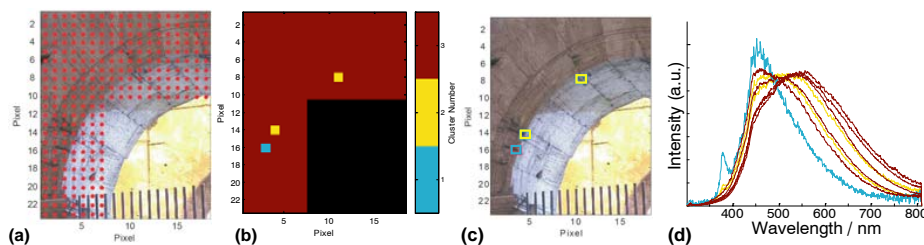


Fig. 8. Analysis of an area (Area C in Fig. 1d) containing titanium clamps inserted during a restoration carried out recently (1999) and treated with anti-corrosive chemicals. Excitation wavelength was 308 nm. The distance of the sensor from the target was about 18 m and the spot size diameter on the target was about 2 cm. The spatial resolution was 10 cm both in horizontal and vertical directions. (a) shows the area with the measured points. In (b), a CA has been performed and the points where the beam has hit the metal clamps are identified as different from the surrounding travertine stone. (c) shows the three points on the metal clamps in the area. In (d) the corresponding spectra are shown together with representative spectra from the travertine areas. The cyan point is identified as a point on a treated metal clamp, as indicated by the peak at 380 nm. The yellow points indicate points which are partly stone and partly metal clamp. These have only a slight indication of a peak at 380 nm.

In Fig. 7d, a PCA-RGB analysis has been applied to the spectra from cluster 1 in Fig. 7b, i.e., the ones corresponding to stone points. One can notice two areas with purple points, which seem to differ from the surrounding stone, marked by red circles. By comparison with Fig. 7a, it is possible to assign these points to damaged pits in the wall, possibly containing mortar. Also, a few red pixels are seen, circled with blue. These are identified as mortar joints. Examples of spectra from the area are given in Fig. 7f, where the colors of the spectra are the same as the colors of the pixels in Fig. 7d.

The section of the monument considered in the measurement campaign comprises several other portions where metal clamps were applied to strengthen its structure. Fig. 8 shows an area (Area C in Fig. 1d) where titanium clamps were applied during a restoration carried out recently, in 1999. This area has also been cleaned with fine water mist during the recent restoration project mentioned previously. The area was measured using 308 nm excitation and is shown in Fig. 8a together with the measured points. This area comprehends three titanium clamps placed in different positions, even under the arch. Fig. 8b shows a CA-based map where three pixels (light blue and yellow pixels) clearly stand out against the vast majority of the brown-marked pixels referring to the travertine. The positions of the former on the scanned area are shown in Fig. 8c where it is clear that they correspond to the position of the clamps. The relevant fluorescence spectra are shown in Fig. 8d together with typical fluorescence spectra from the travertine (brown): the distinctive feature of the spectra referring to the clamps (spectra marked in light blue and yellow) is the 380-nm peak due to the anti-corrosive chemicals, which is present both in the blue and the yellow spectra. In addition, while the blue fluorescence spectrum clearly refers to a spot largely centered on the metal clamp, the other two spectra marked in yellow show an intermediate behavior between the fluorescence features of the anti-corrosive chemicals and those of the travertine. Another consideration can be done about the spatial resolution adopted for the scan of the area: in this case, a resolution of 10 cm was enough to detect the position of the clamps and to assess the presence of the anti-corrosive protective treatment on them.

The method has been applied also in heavily soiled areas to check the feasibility of detecting metal clamps on them. Fig. 9 reports the results of fluorescence lidar mapping on an area characterized by heavily soiled and weathered travertine (area A in Fig. 1d). Iron clamps were attached during a past external reinforcement intervention, carried out by Valadier in the early 19th century, to strengthen stressed and affected stones. The area has an exceptionally irregular surface indicated by cavities and large material losses, where soot and different deposits on the surface have created a very dark crust and patina which covers not only the travertine but also the iron clamps. The scanned area is shown in Fig. 9a, together with the

grid indicating the spots where fluorescence measurements were taken. Data were acquired with the 308 nm excitation from a distance of about 18 m. The spot diameter on the target was about 2 cm. The spatial resolution was 8 cm both in horizontal and vertical directions.

An analysis of the fluorescence data with the CA technique to extract the position of the iron clamps in the scanned area provided the map shown in Fig. 9b. Light blue pixels identify the vast majority of spots corresponding to soiled and weathered travertine, while the presence of the soiled iron clamps is highlighted by the blue pixels in the map. A set of fluorescence spectra corresponding to the identified classes are shown in Fig. 9c, where the colors of the spectra correspond to the color of the relevant class as shown in Fig. 9b. Here fluorescence spectra are not normalized. From this graph it is clear that the spectra corresponding to the iron clamps (blue spectra) are characterized by a very low intensity with respect to all the other fluorescence spectra. In addition, the iron clamp spectra, which are shown separately and rescaled in Fig. 9d, show a spectral shape that is considerably different from those referring to the soiled stones (see Fig. 9c), being characterized by a sharp fluorescence contribution around 450 nm. Such spectral shape is very different from the fluorescence spectra obtained from the travertine. Also in a heavily soiled area, such as this one, where there is a higher variability of the spectral shape of the fluorescence due to the presence of many contaminants on the surface, it is not a shape expected for travertine stone. Since the scanned area was relatively easy to be observed from the ground (about 6 m above the ground level), the position of the iron clamps could be also verified by visual inspection (yellow circles in Fig. 9a; the green circle, on the contrary, refers to a deep crack and spalling of the stone). However, the fluorescence imaging can give the same information from any portion of the façade, where visual inspection is limited unless scaffolding or lifts are used. Another piece of information that can be retrieved from the spectra shown in Fig. 9d is that the clamps are not treated with the anti-corrosive chemicals detected on those previously analyzed because of the lack of the typical fluorescence peak centered at about 380 nm.

A further aspect to be considered for the detection and characterization of metal clamps on a monument's façade is a proper choice of the scanning spatial resolution. In this case, the adopted 8-cm spatial resolution was quite coarse for a thorough detection of the clamps, as points easily miss the narrow features. Only a few points on the clamps were found, as can be inferred from the comparison of Fig. 9a and Fig. 9b. On the other hand, a trade-off between spatial resolution and time required for the scanning must often be achieved, especially for a first screening of an extensive surface. Further detailed analysis could be then carried out on specific areas selected on the basis of a first screening and adopting a higher spatial resolution such as that of Fig. 7.

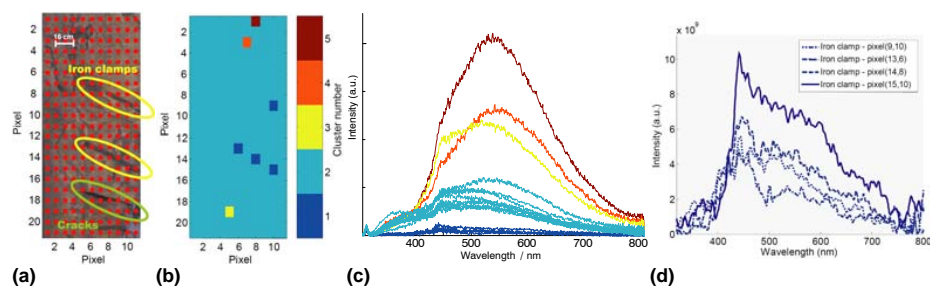


Fig. 9. Detection of iron clamps in a heavily soiled and weathered area (Area A in Fig. 1d). The excitation wavelength was 308 nm. The distance of the sensor from the target was about 18 m and the spot size diameter on the target was about 2 cm. The spatial resolution was 8 cm both in horizontal and vertical directions. (a) the scanned area with the measurement reference grid. (b) CA-based classification of the fluorescence spectra pointing out the position of the iron clamps (blue pixels). For this CA analysis the 'Euclidean' distance and the 'single' linkage method were used. (c) typical spectra referring to the five different classes identified in (b). The color of each spectrum corresponds to the color of the relative class in map (b); the iron clamps (blue spectra) show remarkably low fluorescence intensity with respect to the spectra of the other classes. (d) shows rescaled fluorescence spectra of the iron clamps.

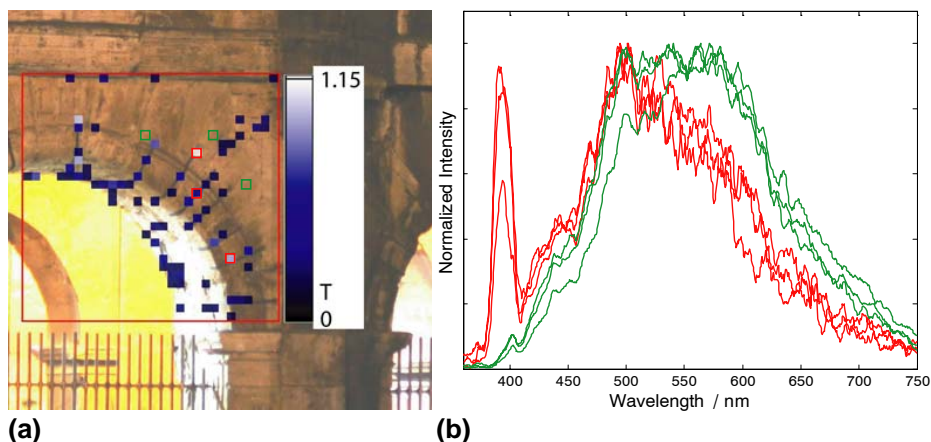


Fig. 10. Scanning of a recently cleaned area featuring old iron clamps (Area G in Fig. 1d). The excitation wavelength was 355 nm. The distance of the sensor from the target was 65 m and the spot size diameter on the target was about 4 cm. The spatial resolution was 12 cm both in horizontal and vertical directions. (a) shows the area with a superimposed evaluation to find the metal clamps. (b) shows some characteristic spectra, as indicated by the squares in (a). The squares in (a) have the same color as the curves in (b).

A further area containing metal clamps was scanned and the result can be seen in Fig. 10. Fig 10a indicates the measured area with a red frame and an analysis to single out the treated metal clamps has been superimposed. The values were obtained by using a ratio between the mean value in the 385-405 nm and the mean value in the 480-625 nm wavelength band. The color scale indicates the value of this ratio. The T indicates the applied threshold, which was used to suppress low-value spectra. Some example spectra are given in Fig. 10b, and these points are marked with squares in Fig. 10a. The red squares correspond to the points on metal clamps, and these spectra are drawn as red curves. Similarly, the green squares correspond to travertine points, and these are drawn as green curves in Fig. 10b.

4. Conclusions

The fluorescence lidar study presented in this paper clearly shows the potential of the technique to identify historical conservation interventions. One aspect refers to the insertion of new stone blocks of a restoration. A further aspect is to assess the status of protective anti-corrosion treatments on applied metal clamps placed to reinforce the structure.

A specific advantage of the fluorescence lidar techniques is that they operate on the remote-sensing principle and thus make areas of high elevation accessible without using scaffolding. Such arrangements are traditionally needed to collect samples for laboratory analysis – fluorescence lidar, on the contrary, provides a completely non-invasive investigation of large façade areas.

Acknowledgments

The authors wish to acknowledge the Swedish Research Council for Environment, Agricultural Sciences and Spatial Planning (FORMAS) and the Swedish Research Council (VR) as well as the Swedish Institute in Rome for supporting this study.

PAPER VII

Laser-Induced Fluorescence for Assessment of Cultural Heritage

R. Grönlund, J. Hällström, A. Johansson, L. Palombi, D. Lognoli, V. Raimondi, G. Cecchi, K. Barup, C. Conti, O. Brandt, B. Santillo Frizell, and S. Svanberg.

Reviewed and Revised Papers Presented at the 23rd International Laser Radar Conference, Nara, Japan, 723–726 (2006).

LASER-INDUCED FLUORESCENCE FOR ASSESSMENT OF CULTURAL HERITAGE

Rasmus Grönlund⁽¹⁾, Jenny Hällström⁽²⁾, Ann Johansson⁽¹⁾, Lorenzo Palombi⁽³⁾, David Lognoli⁽³⁾,
Valentina Raimondi⁽³⁾, Giovanna Cecchi⁽³⁾, Kerstin Barup⁽²⁾, Cinzia Conti⁽⁴⁾, Olof Brandt⁽⁵⁾,
Barbro Santillo Frizell⁽⁵⁾, Sune Svanberg⁽¹⁾

⁽¹⁾ Atomic Physics Division, Lund Institute of Technology, P.O. Box 118, SE-221 00 Lund, Sweden,
E-mail: rasmus.gronlund@fysik.lth.se, sune.svanberg@fysik.lth.se

⁽²⁾ Division of Architectural Conservation and Restoration, Lund Institute of Technology, P.O. Box 118, SE-221 00 Lund,
Sweden

⁽³⁾ CNR-IFAC, Via Madonna del Piano 10, I-50019 Sesto Fiorentino (FI), Italy

⁽⁴⁾ Soprintendenza Archaeologica di Roma, Palazzo Altemps, Piazza di S. Apollinare 44, I-00186 Roma, Italy

⁽⁵⁾ Istituto Svedese di Studi Classici a Roma, Via Omero 14, I-00197 Roma, Italy

ABSTRACT

Remote imaging measurements of laser-induced fluorescence have been performed, with application towards cultural heritage. Measurement campaigns have been performed at, e.g., the Coliseum in Rome. Differences in fluorescence spectra from different points were found and images corresponding to different features could be produced for thematic mapping.

1. INTRODUCTION

Laser-induced fluorescence can be used in diverse applications. It is used in laser medicine [1], but can also be applied remotely [2] to study, e.g., vegetation status [3] or cultural heritage [4-5].

2. MEASUREMENT SET-UP

Measurements are performed using the mobile lidar system of the Lund Institute of Technology [6] and the mobile lidar system of CNR-IFAC [7].

Pulsed laser radiation is directed to the target spot, where fluorescence is induced. The laser beam can be steered wherever desired. When it hits the target, molecules are excited to higher energy levels. When they relax, they emit fluorescence light, which may show different features dependent on the material. Since the target is a solid material, the energy levels are smeared out and the return signal does not show any sharp features. Instead, small differences in the spectra have to be analyzed.

The fluorescence light is gathered by a receiving telescope, on the same optical axis as the transmitting optics. The signal is sent through a long-pass filter to block the exciting wavelength and guided by an optical

fiber to a spectrometer with a gated CCD camera which records the spectrum. The measurement is averaged over a number of laser shots to reduce the noise.

When the spectrum in a point is gathered, the laser spot is directed to the next point. The spectrum from this spot is recorded and the laser beam is moved again, and so on. In this way, an area is scanned and imaging is accomplished.

The Swedish system is originally intended for differential absorption lidar measurements, but is also well suited for remote fluorescence. The system is built inside the cargo compartment of a Volvo F610 truck and is thus fully mobile. A motor generator, towed by the truck, ensures that measurements can be performed at any location. The laser source is a frequency tripled Q-switched Nd:YAG laser at 355 nm or alternatively an optical parametric oscillator system, which can produce wavelengths between 220 nm and 1.7 μm , although usually only the ultraviolet wavelengths are used.

The laser beam is directed through a beam expander and to the air through a roof-top dome, where a computer-controlled folding mirror can be used to direct the radiation to the desired spot. The spot size on the target, 50-100 m away, is typically about 5 cm. The fluorescence light is gathered by the same folding mirror and directed to a 40-cm-diameter Newtonian telescope which focuses the radiation onto the tip of an optical fiber, connected to the spectrometer. The spectrum in the wavelength range 280-810 nm can be detected. The measurement is averaged over a number of laser shots (typically 100 shots, corresponding to 5 seconds) to reduce the noise.

The Italian system is a dedicated fluorescence lidar system (FLIDAR), housed in a Fiat Ducato van and powered by a motor generator. Pulsed laser radiation from a 10 Hz XeCl excimer laser at 308 nm is used, with a spot size on target of 2 cm at a typical range to

the target of about 20 m. The fluorescence light is gathered with a 25-cm-diameter Newtonian telescope and directed through an optical fiber to a spectrometer and a 512 channel linear photodiode array detector. The spectrum in the wavelength range 300-800 nm is gathered by merging two acquisitions, one in the range 300-600 nm and the other in the 500-800 nm range. A spectrum is recorded in about 1 minute (averaging over 30 laser shots).

3. MEASUREMENT CAMPAIGNS

Measurements have been performed at sites of importance for the cultural heritage. Recent measurements include the castle Övedskloster in southern Sweden [8], the amphitheater Coliseum in Rome (see Fig. 1) and the Lateran Baptistery in Rome.

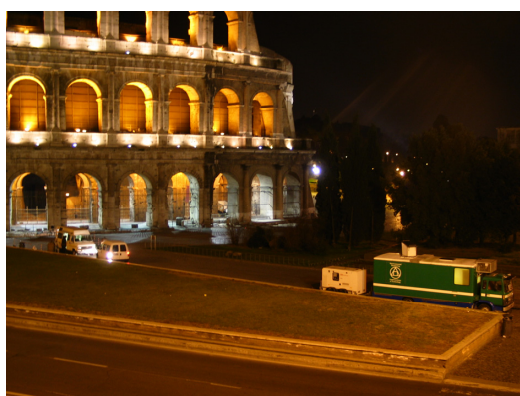


Fig. 1. Measurements at Coliseum. The Swedish lidar system is seen on the right and the Italian system is on the left, closer to the monument.

The measurement campaign in Rome was performed over a two week period in February 2005. Measurements were performed at night, not to disturb the daytime activities, e.g. tourism, at the sites. Note that the gating of the detectors is efficient enough to suppress the ambient light, so technically the measurements could have been performed in daytime, as has been done in most previous campaigns.

The Coliseum, officially known as the Flavian amphitheater, was inaugurated in year 80 A.D. It is mainly constructed with travertine, quarried in nearby Tivoli. The stone has in many parts deteriorated and the need for ongoing control and analysis of the material is vital for the conservation and maintenance of the monument, which is now also a great tourist attraction.

The Lateran baptistery is connected to San Giovanni in Laterano, the cathedral of Rome and the oldest church

of Christianity. It was constructed in the 4th century A.D. and is a brick building. It has been rebuilt many times and the façades thus consist of many construction phases. The building is the property of the Vatican state, and is part of the Laterano territory.

4. ANALYSIS

The resulting data from a scan is three-dimensional (two spatial dimensions and wavelength). To create easy-to-understand images the data must be reduced to two dimensions. This can be done by applying some sort of function to each spectrum, so that the wavelength dimension is reduced to a single value. Then it is possible to create a false-color coded image that can show differences between different regions in the studied area (thematic mapping).

The function applied to the spectra can be chosen in several ways. By choosing, e.g., the mean value in a certain wavelength band, the wavelength dimension is reduced to a single value. However, this is generally not enough to describe the differences in the spectra. By choosing more wavelength bands and combining them (e.g. one band divided by another) more subtle variations can be focused on. Also, instead of the mean value in a band, one may choose the maximum value in the band or the minimum value, the integral over that band or the slope of the curve in the band. It is always desired to use dimensionless quantities, since all outer factors that may affect the absolute value of the detected fluorescence, such as laser intensity fluctuations, angle of incidence, etc. are then divided away. Only the shape of the spectrum is then evaluated, the absolute intensities are neglected. In some cases this is not desired, so special care has to be taken in each case.

Normalizing the spectra is another way of disregarding absolute intensities. This can be done in several ways, e.g. each spectrum may be divided by its maximum value (max-normalization) or the area under the spectrum (integral-normalization). Another way may be to regard each wavelength as a sample and normalize with regards to the maximum value for that wavelength in the data set (lambda-normalization).

It is also possible to make correlations between different spectra and thus find points with similar spectral features.

Usually, the spectra have only small differences, although certain materials have characteristic fluorescence features. Chlorophyll has strong fluorescence features in the near infrared area, around 700 nm.

In this context, it is important to have collaborations between physicists and partners from architectural conservation science and the archeological fields, who can interpret the results and draw relevant conclusions.

4.1 Principal Component Analysis

Principal component analysis (PCA) is a systematic way to find the most significant differences between (in this case) the spectra. Each spectrum has 1024 channels, which means that there are 1024 different variables. Then there are a number of samples, represented by the spectra that have been taken in the scan. Each sample has a certain value for each variable.

The PCA algorithm projects the data onto a new set of variables, called principal components (PCs). This is done such that the variance in the data along the first PC is maximized. Then the second PC is created, orthogonal to the first one, maximizing the residual variance, and so on. Each PC has a set of values for the wavelengths, called loadings. Each spectrum can be expressed as a linear combination of the PC loadings, and the factors are called the score values for the sample. This procedure reduces the complexity of the samples, because usually no more than 4-5 PCs are needed to describe the data, the rest is noise. By forming functions of the scores for the different PCs, new information can be extracted from the data.

5. RESULTS

In Fig. 2 the fluorescence spectrum from four different points on a part of the northern façade of Coliseum is shown for 355 nm excitation.

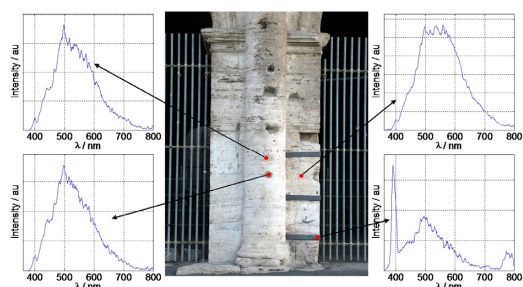


Fig. 2. Fluorescence spectra from different points on the northern façade of Coliseum.

Differences between the spectra can be seen. The lower right spectrum is taken from a steel clamp where the sharp peak at 390 nm is due to an anti-corrosion treatment chemical applied to the surface. In the other three spectra, the differences are more subtle. The upper

right spectrum shows a broader structure than the two on the left. The two left ones are very similar, although still some difference may be noticed, e.g. studying the slope of the curve between 500 and 600 nm.

With an area analysis of a scan over this area, it is easy to find the metal points, as these are clearly different than the other points. The result is seen in the left part of Fig. 3. On the right in Fig. 3, points with a strong positive slope in the region 500-550 nm are shown. Some distinct areas can be recognized as similar in this aspect.

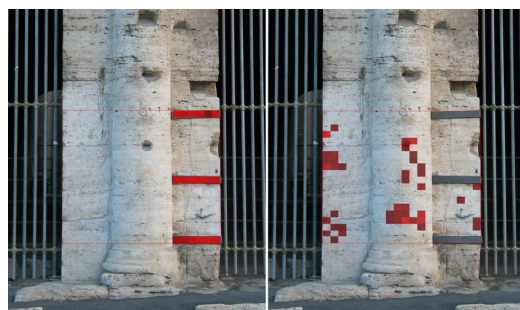


Fig. 3. The left picture shows that the metal bars are easily singled out and in the right picture the points with a large positive slope at 500-550 nm. The frames correspond to the measured area and the brightest pixels correspond to the points with the largest values.

As mentioned above, chlorophyll has characteristic fluorescence features. In Fig. 4 the spectrum from a point on Coliseum with algal growth is shown for 355 nm excitation. There is a large peak at around 700 nm which corresponds to the presence of chlorophyll.

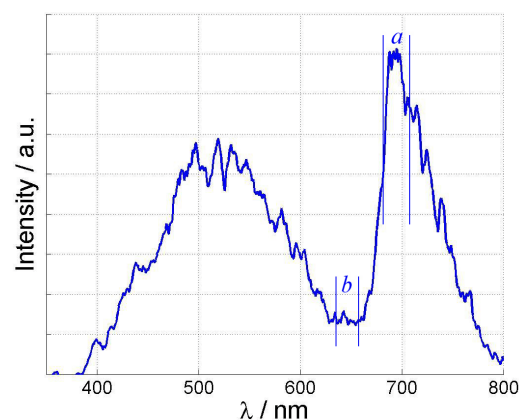


Fig. 4. The spectrum from a point with algal growth.

The points with algal growth are thus easily singled out and an image showing points with algal growth can be

produced. Here, the intensity value in the wavelength region 680-705 nm (*a*) is compared to the intensity in the region 635-655 nm (*b*). As can be seen from Fig. 4, a point with chlorophyll content will have a higher intensity in the *a*-band than in the *b*-band, whereas the opposite will be true for a spectrum without chlorophyll. The result can be seen in Fig. 5. It is noted that the most intense chlorophyll signal is detected from a stone with rough surface and large cavities, giving good living conditions for the biodeteriogens.

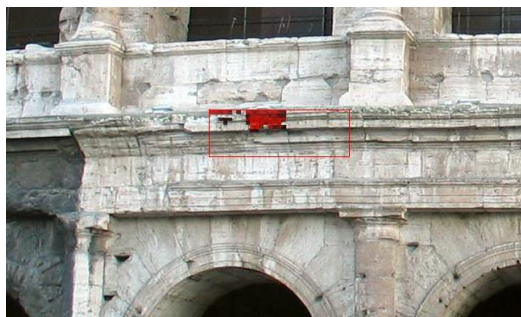


Fig. 5. Chlorophyll on an area on Coliseum. The frame indicates the measured area and the brightest pixels correspond to the points with highest chlorophyll signal.

In Figs. 6 and 7 areas on the Lateran baptistry are shown. In these pictures, differences can be seen, due to the presence of different types of bricks. There is also difference between the bricks and the surrounding mortar. In both Figs. 6 and 7, the pixels indicated have spectra with a slightly wider structure, that do not fall off as fast towards longer wavelengths.



Fig. 6. An area on the Lateran baptistry. The mineralogical composition of the bricks in the window arch differ from the re-used bricks within.

6. CONCLUSIONS

Our measurements show that laser-induced fluorescence is an efficient method for conservation assessment. Measurements are made remotely and are completely non-destructive. Information that can be extracted

include detection of biodeteriogens and characterization of different materials. The data from our Rome campaign is now in the process of being fully analyzed.

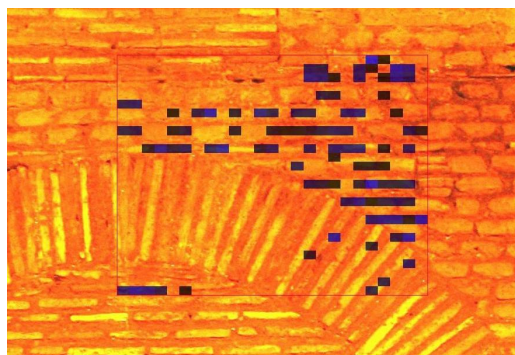


Fig. 7. An area on the Lateran baptistry. Differences between different types of bricks can be detected and bricks can be distinguished from mortar.

REFERENCES

1. Svanberg, S., New Developments in Laser Medicine, *Physica Scripta*, Vol. T72, 69-75, 1997.
2. Svanberg, S., Fluorescence Spectroscopy and Imaging of Lidar Targets, Chap. 6 in T. Fujii and T. Fukuchi (eds.), *Laser Remote Sensing*, CRC Press, Boca Raton, Florida, 2005.
3. Svanberg, S., Fluorescence Lidar Monitoring of Vegetation Status, *Physica Scripta*, Vol. T58, 79-85, 1995.
4. Weibring, P., et al., Fluorescence Lidar Imaging of Historical Monuments, *Applied Optics*, Vol. 40, 6111-6120, 2001.
5. Lognoli, D., et al., Fluorescence Lidar Imaging of the Cathedral and Baptistry of Parma, *Applied Physics B*, Vol. 76, 457-465, 2003.
6. Weibring, P., et al., Versatile Mobile Lidar System for Environmental Monitoring, *Applied Optics*, Vol. 42, 3583-3594, 2003.
7. Cecchi, G., et al., Remote Sensing of Chlorophyll *a* Fluorescence of Vegetation Canopies: 1. Near and Far Field Measurement Techniques, *Remote Sensing of Environment*, Vol. 47, 18-28, 1994.
8. Grönlund, R., et al., Fluorescence Lidar Multispectral Imaging of Historical Monuments – Övedskloster, a Swedish Case Study, proceedings of Lacona VI, Vienna, Austria, 21-25 September 2005, to appear.

PAPER VIII

Remote Multicolor Excitation Laser-Induced Fluorescence Imaging

R. Grönlund, J. Hällström, A. Johansson, K. Barup, and S. Svanberg.
Laser Chemistry **2006**, Article ID 57934 (2006).

Research Article

Remote Multicolor Excitation Laser-Induced Fluorescence Imaging

Rasmus Grönlund,¹ Jenny Hällström,² Ann Johansson,¹ Kerstin Barup,² and Sune Svanberg¹

¹Atomic Physics Division, Lund University, P.O. Box 118, SE-221 00 Lund, Sweden

²Architectural Conservation and Restoration, Lund University, P.O. Box 118, SE-221 00 Lund, Sweden

Received 15 September 2006; Revised 31 October 2006; Accepted 3 November 2006

Recommended by Costas Fotakis

Remote laser-induced fluorescence of stone materials was performed with application towards cultural heritage. Fluorescence was induced in targets 60 m from a mobile lidar laboratory by ultraviolet laser light, either from a frequency-tripled Nd:YAG laser or from an optical parametric oscillator system. Analysis was performed on combined spectra from the different excitation wavelengths and it was noted that important additional information can be gained when using several excitation wavelengths.

Copyright © 2006 Rasmus Grönlund et al. This is an open access article distributed under the Creative Commons Attribution License, which permits unrestricted use, distribution, and reproduction in any medium, provided the original work is properly cited.

1. INTRODUCTION

Laser-induced fluorescence (LIF) can be used to distinguish different areas on surfaces in numerous applications, for example, tissue diagnostics [1]. Laser light illuminating a surface excites the material which reemits fluorescence light when relaxing. Different molecules have different fluorescence features, and thus areas containing different materials give different signals. From stone materials, typically the fluorescence spectra have little features and only small variations occur. The fluorescence usually peaks in the blue/green wavelength region and falls off towards red wavelengths. Variations between materials may be displayed as differences in the slopes and wavelength for the maximum fluorescence. Certain molecules may give more specific fluorescence signals, such as chlorophyll, which shows two sharp peaks in the near infrared [2]. Due to the limited penetration depth of ultraviolet light, only the superficial layer of the target can be investigated.

By studying details in the fluorescence spectra from different parts of a building, it may, for example, be possible to assess surface damage and detect traces of chemicals previously used for restoration purposes, which are often unnoticed in visual inspections. These signals can aid in understanding the effects of earlier restoration techniques and could ultimately form a basis for future maintenance and intervention.

Remote laser-induced fluorescence, also known as fluorescence lidar [3], has earlier been applied by our group to aquatic monitoring [4], studies of vegetation status [5] and surfaces of historical buildings [6, 7]. In these measurements, performed with single wavelength excitation, we have illustrated that chlorophyll-rich areas, regions previously exposed to chemical treatment, as well as different stone types can be demarcated.

Remote fluorescence spectra can be gathered by transmitting a powerful laser pulse onto the target and collecting the induced fluorescence with a telescope and a spectrometer system. To perform measurements at daytime, gating of the detector is usually required to suppress background light. By scanning the laser beam over a target area and recording the fluorescence spectrum in each spot, imaging can be achieved.

In this paper, we present remote fluorescence imaging measurement results from measurement campaigns in both laboratory and field settings. Although much information can be extracted from a single excitation wavelength, the use of two or more excitation wavelengths is demonstrated to add significant information to the analysis, improving the possibilities to discriminate between areas with different fluorescent/physical characteristics. Furthermore, we discuss different analysis methods for extracting useful information from huge fluorescence data sets.

2. EXPERIMENT

Laser-induced fluorescence was used to remotely study stone surfaces. Some measurements were performed in a laboratory environment, while others were performed as field campaigns at cultural heritage sites. By excitation of the material using ultraviolet laser pulses, fluorescence was induced from a distance of about 60 m. The signal was remotely gathered by a telescope and the spectral shape was analyzed. By scanning the laser beam over the building and detecting the fluorescence from each spot, imaging could be performed. When performing measurements on buildings with historical value, it is important to note that the surfaces of buildings are not at all affected by the measurement, which is not the case for many other building investigation methods.

The measurements presented in this paper are from a campaign with brick samples measured in Lund, Sweden, a field campaign at Övedskloster castle in southern Sweden and a field campaign at Coliseum in Rome, Italy. More information on the Övedskloster campaign is presented in [8] and on the Coliseum campaign in [9, 10].

3. MATERIAL AND METHODS

A mobile lidar laboratory [11], which is primarily adapted for atmospheric monitoring by the differential absorption lidar technique, was employed for the experiments. The system has a flexible design and is well suited for monitoring remote fluorescence as has been previously reported [4–7]. The fluorescence lidar transmitter was a frequency-tripled Nd:YAG laser generating radiation at 355 nm in 5-nanosecond-long pulses at a repetition rate of 20 Hz. Typically the transmitted pulse energy was limited to 25 mJ in these experiments. Also, an optical parametric oscillator (OPO) could be used as the excitation source, where the laser wavelength could be selected in a wide range from ultraviolet to infrared. Only ultraviolet wavelengths were used, as fluorescence induction is particularly efficient using these wavelengths, and also due to eye-safety reasons. From the OPO, the transmitted pulse energy was typically 5 mJ. Over a scan, the output integrated over a particular measurement spot was stable to ~20%.

The vertically looking receiving optics was a Newtonian telescope with 40 cm diameter. A 40 cm × 80 cm folding mirror placed over the telescope in a dome above the vehicle roof can be steered to direct the laser beam onto the desired spot. As the laser beam is coaxial to the field of view of the telescope, the detected radiation is gathered from the correct area. A gated and intensified optical multichannel analyzer, more closely described in [12], detected the fluorescence radiation from 280 to 810 nm with a spectral resolution of ~3 nm. The laser beam expander, which was coaxial with the receiving telescope, was normally adjusted to give a 5-cm-diameter laser spot on the target. For a typical distance of 60 m between the lidar and the target, the diameter of the image spot in the telescope focal plane was ~1.3 mm. The radiation was transmitted through a high-pass filter to suppress

the specular reflection and collected using a 600 μm diameter optical fibre connected to the optical multichannel analyzer system. With the computer-controlled folding mirror the lidar was pointed at selected locations for spectral data collection, or scanned row by row over the façades for image generation. A signal integration of 100 laser shots was normally used. To suppress background interference, time-gated detection was used, with a 100 nanosecond gate set to open at the arrival time of the fluorescence pulse.

From each spot investigated a fluorescence spectrum is collected, and as the laser is scanned over an area, a three-dimensional data set is obtained. To extract useful information from this huge amount of data, efficient data processing is necessary. Different aspects of the fluorescence features can be focused on by forming ratios of intensities in different wavelength bands, by performing correlation between spectra or by principal component analysis. In this study, mainly the correlation technique has been used, where a linear correlation between one reference spectrum and all other spectra within the scan is performed. The result is then a single number for each point, between -1 and +1, corresponding to the similarity to the reference spectrum, where +1 corresponds to identical spectra and -1 corresponds to negatively correlated spectra. A zero value would indicate totally uncorrelated spectra, as would be expected when correlating two sets of white noise. In this way, areas with similar fluorescence features can quickly be found and delineated. Different analysis methods for these types of data are further discussed in [13].

The measurement campaign on brick samples was performed in a laboratory setting. The lidar system was docked to the Physics Department building at Lund University, and the bricks were set up on the roof of a building 60 m away. The measurement was performed using five different excitation wavelengths: 250 nm, 290 nm, 337 nm, 355 nm, and 375 nm. Spectra from the same point, with different excitation wavelengths, can be combined to make it possible to analyze the results, taking all the excitation wavelengths into account simultaneously. This is done by creating an artificial spectrum for each measured spot, by simply assigning one excitation wavelength to the first 1024 data points, another to the next 1024 data points, and so on. If not all 1024 recorded data points contain significant information, some parts can be excluded [11]. Although some features may be appearing only with a certain excitation wavelength, the main advantage is gained when spectra are combined. In this way, all features appear simultaneously and can easily be presented.

In the measurement campaign at Övedskloster, areas on the façade of the building and on the courtyard portal were scanned using 355 nm excitation from the Nd:YAG laser. Different fluorescence features could be observed and much information could be extracted, even though only this one excitation wavelength was used.

During the Coliseum campaign, different areas on the Coliseum façade were scanned. In particular, one area was scanned using two different excitation wavelengths, 355 nm from the Nd:YAG laser and 250 nm from the OPO.

4. RESULTS

As mentioned, the measurements on the brick samples were performed using five different excitation wavelengths. In the analysis, the spectra for the 355 nm excitation have been divided by 5 to compensate for its greater output energy. After combining the spectra, each resulting spectrum has been normalized with respect to its greatest value. The spectra have not been normalized within each excitation wavelength, as the relative intensities hold information that would otherwise be lost. Spectra from six arbitrary spots, each on a different brick sample, have been plotted in Figure 1. By correlating all spectra with an arbitrarily chosen reference spot, different stones could be isolated, as indicated in Figure 2. This was not possible using data from only one excitation wavelength. We note that none of the neighboring pixels is white, the reason for this being that the noise in the different spectra would have to be identical.

One of the areas studied at Övedskloster castle was an ornamental urn on the roof of the main building. This part of the building is very difficult to reach for close-up examination, and thus remote fluorescence imaging is a good method to study such parts. Despite the use of a single excitation wavelength, several aspects of the fluorescence features could be studied, and other examples are given in [7]. It was noted that the spectra from the base of the urn were quite different from the rest of it. In Figure 3(a), a correlation between the spot marked with a red circle and all other spectra in the scan has been performed. The blue pixels correspond to the degree of similarity, and it can clearly be seen that the parts on the base of the urn are similar to each other and different from the rest. A few points on the upper part of the urn appear as similar, but with low correlation values. Figure 3(b) shows the spectra from two points in the scan, marked by the red and cyan circles in Figure 3(a). It is evident that the red spectrum shows a stronger fluorescence towards longer wavelengths.

One area on the Coliseum was scanned using both 250 nm and 355 nm excitation light. In the analysis, the two spectra from each point were combined to yield a combined spectrum containing information from both scans. Figure 4(a) shows the two spectra from a certain point in the scan. The red spectrum indicates the 250 nm excitation and the blue one the 355 nm excitation. In Figure 4(b), the combined spectrum is shown, where data from both excitation wavelengths have been used.

Figure 5(a) shows the area on the Coliseum which has been scanned. In Figures 5(b)–5(d), correlation has been performed with one of the spectra in the scan (marked by an oval) as the reference point. However, in Figure 5(b), only the 250 nm excitation data and in Figure 5(c), only the 355 nm excitation data have been used. In contrast, the result when using the combined spectra is shown in Figure 5(d). The correlation values in the range 0.96–1.0 have been mapped out. Values below 0.96 are not indicated in the figures. All correlation values are relatively high, which is expected, as all spectra are similar and display only subtle differences. Comparing Figures 5(b)–5(d), it is clear that spectra on the block

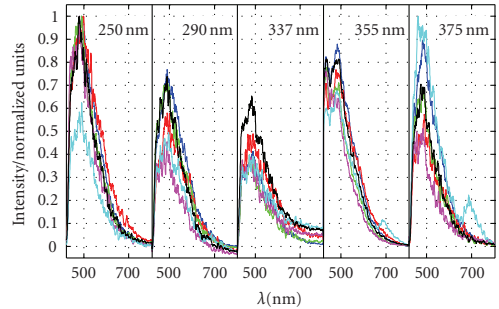


FIGURE 1: Spectra from six different brick samples, measured using five different excitation wavelengths. The spectra have been combined to make analysis of all data possible simultaneously. The different excitation wavelengths are indicated in the figure. Studying the spectra, it is difficult to distinguish them by using only one excitation wavelength, but with the combined spectra differences can be seen. One spectrum contains the characteristic chlorophyll peak at ~ 690 nm, but this fluorescence feature can only be seen with the 355 nm and 375 nm excitation.



FIGURE 2: The brick samples measured, with an analysis superimposed. It was possible to delineate one of the brick samples by correlating all spectra in the scan with one spectrum on this particular brick. The white spot corresponds to the chosen reference spectrum and the blue points display the correlation coefficient value. Values below a certain threshold value have not been displayed. The scan was performed over all the bricks and contained 26×22 points, as indicated by the red frame. As can be seen, the points on the particular brick have high correlation values and only a few points in the rest of the scan have values above the threshold.

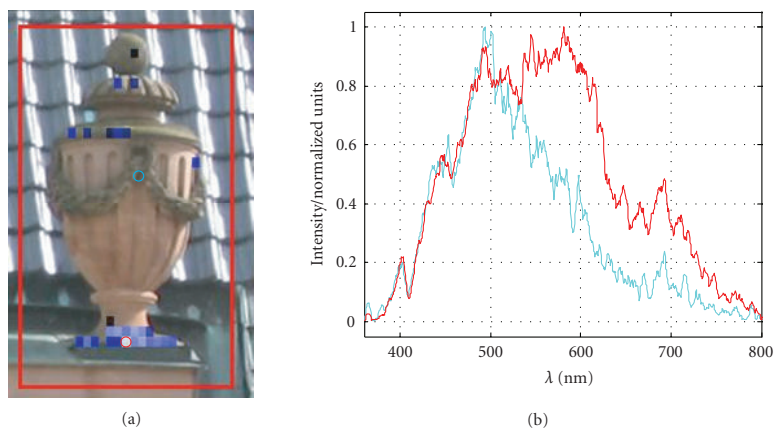


FIGURE 3: An ornamental urn on the roof of Övedskloster castle. Part (a) shows the correlation between a point on the base of the urn (marked by a red circle) and all other spectra. The frame indicates the measured area. In part (b), the spectra from the selected point and a further point (marked by a cyan circle) are shown, and there is an obvious difference between them. The red spectrum corresponds to the red circle in part (a), and the cyan spectrum to the cyan circle.

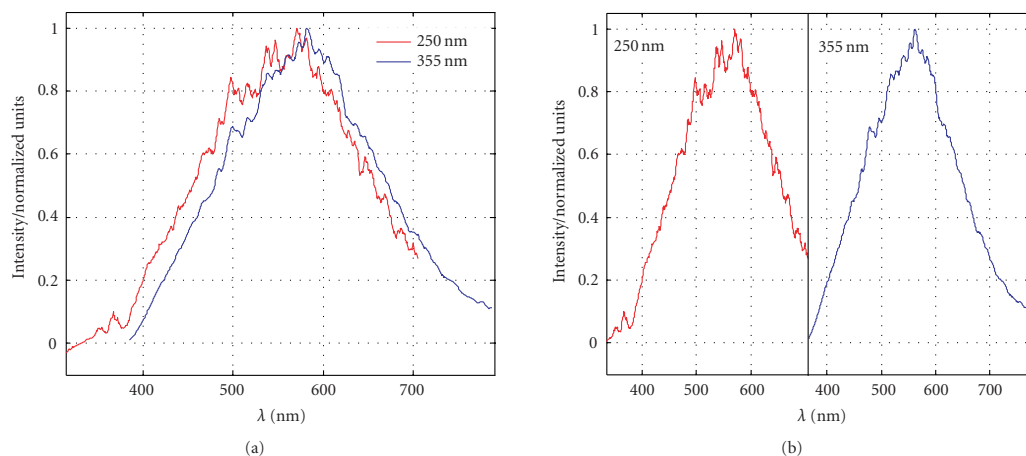


FIGURE 4: Spectra from a point in a scan on the Coliseum. (a) Shows the two different spectra and (b) shows the combined spectrum. The latter can be used in the analysis to simultaneously use information from both excitation wavelengths.

in the upper part of the pillar and in the bottom line of the scan (corresponding to the edge of a stone further down) are similar. Also, it is seen that these have different fluorescence features than the block between them. It is noted that the correlation using combined spectra discriminates more effectively than the same analysis using only the spectra from one excitation wavelength. In Figure 5(d), only a few points outside the area of interest are above the threshold, and all of them have values within the lower part of the allowed range.

5. DISCUSSION

Our studies show that laser-induced fluorescence is a useful method for studying stone surfaces with application towards cultural heritage. The method is particularly useful when applied remotely, which makes it possible to scan large areas and to reach parts of a building that are not easily accessible to methods that require close-up examination. Further, we would like to emphasize that multicolor excitation

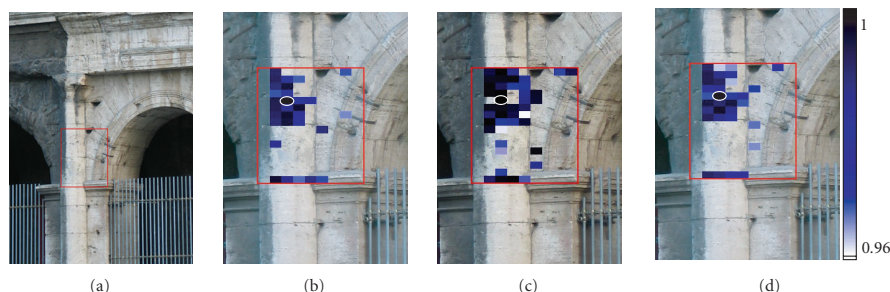


FIGURE 5: An area on the Coliseum façade, marked in part (a). The close-ups in parts (b)–(d) show correlation between one spectrum (marked by an oval) and all other spectra. In part (b), data from the 250 nm excitation measurement have been used, in part (c), data from the 355 nm excitation have been used, and in part (d), the data from both measurements have been combined. The color scale indicates the correlation value. Note that, since the background stone is light, high correlation values are here demarcated with dark colors, in contrast with Figures 2 and 3. Values lower than 0.96 are not indicated in the figure.

provides more information to the analysis. As different excitation wavelengths are used, different molecules are interrogated or excited to different degrees, thereby causing the observed differences in the radiated fluorescence. As was illustrated in Figures 2 and 5, utilizing the combined data resulting from inducing fluorescence at multiple wavelengths, different regions could be better discriminated and distinguished. The use of correlation analysis was demonstrated to be an efficient tool in extracting relevant information from a large amount of data and by this method it was easy to distinguish areas with similar fluorescence characteristics.

To implement analysis of the fluorescence spectra as a useful tool within the field of cultural heritage, collaborations with building restoration scientists are of utmost importance in the data extraction from fluorescence imaging experiments.

ACKNOWLEDGMENTS

The authors would like to acknowledge important contributions from Dr. Petter Weibring and Dr. Magnus Bengtsson in the brick-measurement campaign. Also, we would like to thank the CNR-IFAC Flidar group of Dr. Giovanna Cecchi for nice collaboration on the Coliseum campaign and Dottorssa Cinzia Conti for great help in practical arrangements and background information on the Coliseum campaign. This work was supported by FORMAS—The Swedish Research Council for Environment, Agricultural Sciences, and Spatial Planning, the Swedish Research Council, and the Knut and Alice Wallenberg Foundation.

REFERENCES

- [1] S. Svanberg, “Tissue diagnostics using lasers,” in *Lasers in Medicine*, R. Waynant, Ed., pp. 135–169, CRC Press, Boca Raton, Fla, USA, 2002.
- [2] H. K. Lichtenthaler and U. Rinderle, “The role of chlorophyll fluorescence in the detection of stress conditions in plants,” *CRC Critical Reviews in Analytical Chemistry*, vol. 19, supplement 1, p. S29, 1988.
- [3] S. Svanberg, “Fluorescence spectroscopy and imaging of lidar targets,” in *Laser Remote Sensing*, T. Fujii and T. Fukuchi, Eds., CRC Press, Boca Raton, Fla, USA, 2005.
- [4] H. Edner, J. Johansson, S. Svanberg, E. Wallinder, G. Cecchi, and L. Pantani, “Fluorescence lidar monitoring of the Arno River,” *EARSel Advances in Remote Sensing*, vol. 1, no. 2, pp. 42–45, 1992.
- [5] H. Edner, J. Johansson, S. Svanberg, and E. Wallinder, “Fluorescence lidar multicolor imaging of vegetation,” *Applied Optics*, vol. 33, no. 13, pp. 2471–2479, 1994.
- [6] P. Weibring, T. Johansson, H. Edner, et al., “Fluorescence lidar imaging of historical monuments,” *Applied Optics*, vol. 40, no. 33, pp. 6111–6120, 2001.
- [7] D. Lognoli, G. Cecchi, I. Mochi, et al., “Fluorescence lidar imaging of the cathedral and baptistry of Parma,” *Applied Physics B: Lasers and Optics*, vol. 76, no. 4, pp. 457–465, 2003.
- [8] R. Grönlund, J. Hällström, S. Svanberg, and K. Barup, “Fluorescence lidar imaging of historical monuments - Övedskloster, a Swedish case study,” in *Proceedings of The 6th International Congress on Lasers in the Conservation of Artworks (LACONA '05)*, J. Nimmrichter, W. Kautek, and M. Schreiner, Eds., Vienna, Austria, September 2005, Springer, Berlin, Germany, 2006 (in press).
- [9] CNR-IFAC-SAR Collaboration, “Remote monitoring of conservation status of the Coliseum by laser-induced fluorescence imaging. Part I,” manuscript in preparation for *Journal of Cultural Heritage*.
- [10] CNR-IFAC-SAR Collaboration, “Remote monitoring of conservation status of the Coliseum by laser-induced fluorescence imaging. Part II,” manuscript in preparation for *Journal of Cultural Heritage*.
- [11] P. Weibring, H. Edner, and S. Svanberg, “Versatile mobile lidar system for environmental monitoring,” *Applied Optics*, vol. 42, no. 18, pp. 3583–3594, 2003.
- [12] C. Af Klinteberg, M. Andreasson, O. Sandström, S. Andersson-Engels, and S. Svanberg, “Compact medical fluorosensor for minimally invasive tissue characterization,” *Review of Scientific Instruments*, vol. 76, no. 3, Article ID 034303, 6 pages, 2005.

- [13] R. Grönlund, M. Lundqvist, and S. Svanberg, "Remote imaging laser-induced breakdown spectroscopy and laser-induced fluorescence spectroscopy using nanosecond pulses from a mobile lidar system," *Applied Spectroscopy*, vol. 60, no. 8, pp. 853–859, 2006.

PAPER IX

Laser-Induced Fluorescence Spectroscopy for Detection of Biological Contamination on Composite Insulators

A. Dernfalk, M. Bengtsson, R. Grönlund, M. Sjöholm, P. Weibring,
H. Edner, S. Gubanski, S. Kröll, and S. Svanberg.

*Proceedings of XIIIth International Symposium on High Voltage
Engineering*, Netherlands, O.15.01 (2003).

Laser-induced fluorescence spectroscopy for detection of biological contamination on composite insulators

A.D. Dernfalk¹, M. Bengtsson², R. Grönlund², M. Sjöholm², P. Weibring²,
H. Edner², S.M. Gubanski¹, S. Kröll² and S. Svanberg²

¹Chalmers University of Technology, Gothenburg, Sweden

²Lund Institute of Technology, Lund, Sweden

Abstract: A new technique for remote detection of biological contamination on high-voltage outdoor insulators has been investigated. The technique, which is based on laser-induced fluorescence (LIF) spectroscopy, has been applied to study surfaces of real silicon rubber insulators from a distance of approximately 60 m. Measurements were performed outdoors on a number of clean, as well as, biologically contaminated insulators. Several types of biological contamination were included, as five of the studied insulators had become covered when installed in Sweden, and another three had been contaminated by fungal growth in laboratory. Fluorescence spectra obtained from the surfaces of the described insulators are presented and the applicability of the technique is discussed and compared with photographic methods.

1. Introduction

Reports on biological growth on outdoor insulators reveal that microbiological colonization of ceramic as well as composite insulators can take place in all parts of the world [1-14]. Since the impact of biological growth on insulator performance is not fully understood, it makes utility engineers concerned [14, 15]. The fact that microorganisms grow on composite insulators is of special concern. Silicone rubbers are known to exhibit high resistance to biological degradation. One of the reasons is that the material consists of both organic as well as inorganic components, and that microorganisms like fungi cannot digest the inorganic parts [16]. However, it is believed that in service, composite insulators are mostly attacked by fungi [8, 17].

There is a number of reports on biological contamination of composite insulators [1, 2, 4-13, 15, 18], about half of them from tropical climate [2, 6-8, 11, 15, 18]. Different types of silicon rubber (SIR) insulators, epoxies and blends of silicone and ethylene-propylene-diene monomer rubber (EPDM) have been found to support growth of bacteria, algae, fungi and lichen. However, so far there is not much information published on the growth on EPDM insulators.

This study is a step in a process of investigating the influence of biological growth on insulator performance. More specifically, the aim is to develop a method that can be used to remotely detect and measure/characterize growth and growth distributions.

At close distance, presence of for instance algae on an insulator surface can be detected through visual inspection. However, in order to get a measure of its "severity", more refined techniques have to be used. An example of such a diagnostic technique is photography followed by digital image analysis, which has been proposed by one of the authors [19, 20]. Using this technique, it is possible to get measures of area covered by the growth and its distribution. However, it is difficult to differentiate between regions covered by contamination similar to other microorganisms.

The technique investigated in this study, laser-induced fluorescence (LIF) spectroscopy, has e.g. been utilized for imaging of historical monuments [21] and previously been suggested for insulator diagnostics [22]. In the latter report, the authors presented fluorescence spectra obtained in laboratory from different SIR and EPDM materials and from SIR surfaces where its hydrophobic properties had been reduced through water immersion. In the present study, LIF spectra have been obtained from real insulators partly covered by biological growth using a mobile measuring system. To simulate a real situation, i.e. studying insulators installed in a HV-system, measurements were performed outdoors at a distance of about 60 m.

2. Experimental set-up

The used mobile Light Detection And Ranging (LIDAR) system, housed in a Volvo F610 truck, is based on all solid-state laser technology, and can be used for multi-wavelength excitation and detection in fluorescence imaging, gas concentration- and flux measurements [23]. The system is self-contained, with a diesel powered electrical generator, making it well-suited for field measurements.

In the present experiment, only a part of the laser system, a frequency tripled Nd:YAG laser (Quanta-Ray) was used. This laser delivers pulses with a duration of 4-5 ns at a repetition rate of 20 Hz and a wavelength of 355 nm. The laser beam is passed through an aperture to produce a better mode, rendering a beam diameter of 5 mm and a pulse energy of around 25 mJ. After a totally reflecting 90 degree prism, the laser beam is expanded in a vertically mounted Galilean quartz telescope to 3 cm in diameter. This gives sufficiently low laser intensity

on the computer controlled output folding mirror mounted in a dome, Figure 1, not to damage the mirror. The transmitted excitation light is directed towards a remote target, which in the present work was a number of insulators.

From a control computer, the dome can be rotated 360 degrees (resolution of 0.0035 degrees) with a stepper motor in the azimuthal angle and the folding mirror can be tilted from -10 to $+55$ degrees (resolution of 0.011 degrees) in the polar angle. At the target located 60 m from the laser source, this corresponds to a resolution of 3.7 mm and 12 mm respectively. However, if using this resolution the time for acquiring spectra from the complete insulator surface would be very long. Therefore, a beam diameter of ~ 20 mm and a separation between adjacent measurement points of ~ 20 mm at the insulator were used. The change of position of the laser beam at the target due to mechanical instability of the whole truck was estimated to 5 mm.

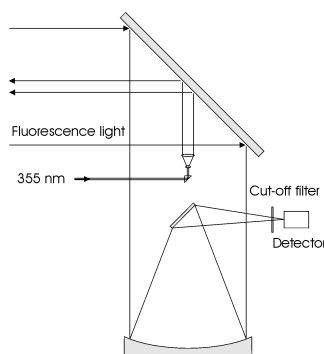


Figure 1. Dome and light receiving unit.

The remotely emitted fluorescence light is received by a 40 cm diameter Newtonian telescope ($f=1\text{m}$), coaxially mounted with the Galilean telescope. By using a cut-off filter in front of the focus of the telescope, the excitation light is discriminated. An optical fibre, 600 μm core diameter and numerical aperture 0.22, guides the fluorescence light to a compact time-gated Optical Multi-channel Analyser system (OMA) designed for medical use. It consists of a spectrometer, a charge coupled device (CCD) camera. In the OMA system a beamsplitter and a cut-off filter selects only wavelengths longer than approximately 385 nm, effectively suppressing the dominating excitation light which is still of appreciable intensity.

A crossed Czerny-Turner spectrograph diffracts the fluorescence light to the image intensified CCD. The thermo-electrically cooled detector has a CCD array with 1024x128 pixels where the 128 pixels are binned. The resulting resolution for the OMA system, set by the slit width (100 μm), is 2.2 nm up to 805 nm. Ambient daylight is suppressed by using a time-gate

of 100 ns, positioned in time by a properly delayed trigger signal from the laser. Spectra from the OMA-system are acquired by a data collection computer that stores the spectrum together with information about the measurement coordinates.

Studied insulators

The present study included eight insulators partly covered by biological contamination and one clean reference insulator. The insulators have been divided into three categories, A-C, according to their design. Type A and B are of line suspension type, while insulators of type C are of apparatus type and have a hollow core. All insulators have sheds and sheath of SIR. However, the formulation differs between the three categories.

The three insulators A have been installed in a 10 kV distribution system in Sweden for approximately 12 years, where they have become covered by a rather thick green growth. However, at the time of the measurement, the growth had turned brown/grey, as the insulators had been kept in laboratory for 6 months. Three of the four insulators B had been exposed to fungal spores and kept in a climate chamber for approximately two years [19]. This treatment led to colonisation of the insulator surfaces by fungi in spot-like manner. The insulators of the third type, C, have been installed in a test station 30 km south of Gothenburg, Sweden, since 1995. They had become covered by a greenish growth on the surfaces shaded from direct sunlight.

During the measurements, the insulators were placed about 60 m away from the truck. To get a better view of the growth, which mainly were located on the upper side of the sheds, the insulators had to be turned up-side-down, tilting away from the point of observation. The insulators C were supported by a wooden structure, and tilted an angle of 30 degrees. Type A and B were fixed using horizontal metal rods and tilted 60 and 50 degrees, respectively. As a safety precaution, a board covered with black paper was put behind the insulators, hindering the laser beam to propagate further.

3. Results

LIF spectra were obtained from characteristic points on the insulators. A typical region with thick, green growth located on a shed of one of insulators C gave the spectrum shown in Figure 2. As seen, there is a large peak located around 680-690 nm, corresponding to the well-known fluorescence peak of chlorophyll *a* at 685 nm [23]. Further, the shoulder on the right probably corresponds to another smaller fluorescence peak of chlorophyll at 735 nm.

Comparison of the obtained spectra gave that the fluorescence peak of chlorophyll around 685 nm is significant for the region covered by growth. The parts

of the insulator, which are not covered by algae, show a low and decaying fluorescence above 600 nm. The spectra obtained from measurements on insulators of type B were more difficult to interpret due to several reasons. First, these insulators were covered by fungi, which do not utilize photosynthesis, and thus not contain any chlorophyll. Second, the growth was more or less evenly distributed over the surface in the form of small isolated spots. As the spatial resolution of the measurements was in the order of 20 mm, spectra could not be obtained from regions completely without growth or regions totally covered by growth. However, comparison of typical spectra from a clean reference insulator and from insulators with growth shows that the total fluorescence of the contaminated insulator is lower, compared to the clean insulator, Figure 3. Further, if the amplitudes are normalized, it is revealed that the contaminated insulator has a slightly higher relative fluorescence in the wavelength band 520-600 nm.

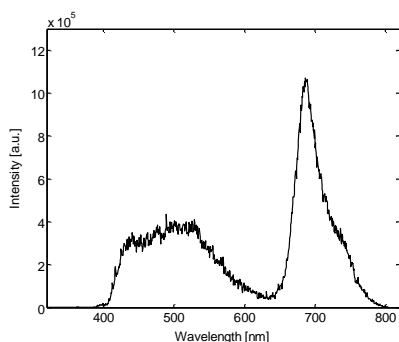


Figure 2. Typical spectra obtained from a region with green growth on one of the insulators C.

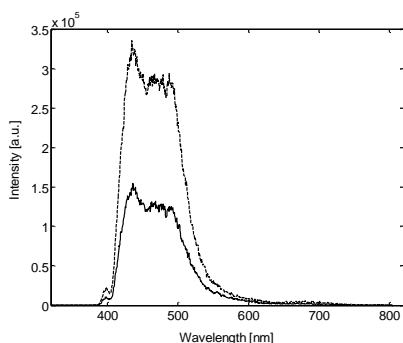


Figure 3. Spectra from clean reference insulator B (dashed) and an insulator B with growth (solid).

Measurements on insulators A revealed that these had a low fluorescence compared to the other insulators studied. As the insulators of type B, the intensity of fluoresced light was much lower from regions covered by growth, than from clean regions, Figure 4. Further, regions covered by growth showed

an increased fluorescence in an interval around 685 nm. However, the difference was very small compared to the insulators of type C. The reason for the low response was probably that the algae had died, due to lack of sun radiation and desiccation, when stored in laboratory.

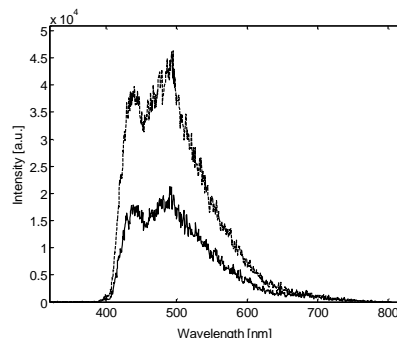


Figure 4. Spectra from a region covered by growth (solid) and a region without visible growth (dashed), on one of the type A insulators.

As the aim was to study distributions of biological contamination, the dome was programmed to scan a window covering a substantial part of the insulator surface. The data were presented as gray level images where the intensity was proportional to the intensity of the fluorescence light within a specific wavelength band. The result of a scan of one of the insulators C is presented in Figure 5, together with a photograph (left) taken from the roof of the truck using a system camera equipped with a 300 mm telephoto lens. In the center image, depicting the average overall fluorescence intensity, it can be seen that the supporting wooden structure has a strong fluorescence (black) compared to the other materials present. However, when only studying the fluorescence peak of chlorophyll, i.e. the intensity in a range from 670-700 nm, the chlorophyll becomes clearly visible (right). As stated above, this is interpreted as presence of algae cells on the surface of the insulator.

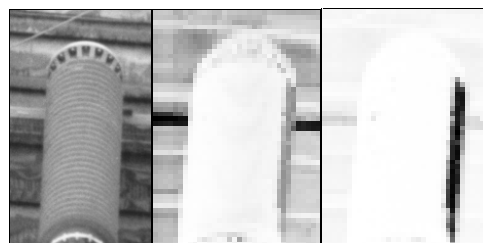


Figure 5. Type C insulator with algae on the right side. Left to right: Photo, mean intensity in 400-800 nm band and in 670-700 nm band.

In order to improve sensitivity and avoid incorrect classification of regions, the obtained spectral data were processed. Average intensities were calculated

for two different wavelength bands, B_1 and B_2 , and the intensity ratio $I(B_2)/I(B_1)$ were formed. The main advantage of these types of dimensionless ratios is that they eliminate the influence of geometrical artifacts, i.e. intensity differences due to different directions of studied surfaces. An example is shown in Figure 6. Image a) shows a photograph taken from close distance, b) shows the average fluorescence intensity in the 410-500 nm band, while c) shows the average intensity in the 670-690 nm band. The ratio of the light fluoresced in the two bands is shown in d), where the dark areas are well corresponding to the regions covered by green growth.

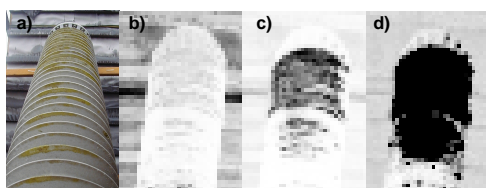


Figure 6. a) Photograph of an insulator of type C, b) average intensity in 410-500 nm band, c) in 670-690 nm band and d) ratio of intensities in 670-690 nm band and 410-500 nm band.

4. Discussion and Conclusions

In comparison with photography, LIF can be used to get a higher sensitivity, especially when there is a large difference in fluorescence between insulator material and contamination. Further, as collection of fluorescence light only is performed under a short period of time, ~100 ns, measurements are not affected by sun radiation.

Comparison of the obtained spectra shows that the fluorescence peak of chlorophyll around 685 nm is significant for the regions covered by algae, while regions with no algae showed low fluorescence in the same wavelength interval. Presence of growth without chlorophyll, i.e. fungi and bacteria, did only cause small changes in the shape of the spectra, compared to the ones of clean surfaces. The most apparent difference here was an amplitude reduction. However, it is not unlikely that a good detection sensitivity of growth without chlorophyll can be obtained using other excitation wavelengths and more extensive data analysis. In conclusion, it has been shown that remote LIF measurements can be used to detect and measure distribution of biological contamination on composite insulators.

5. References

[1] K. Kunde, R. Hennings, M. Kuhl, A. Schütz, H. Jansses, and U. Stietzal, "New experience with composite insulators", Cigré, Paper No. 15-206, 1998
 [2] M. A. R. M. Fernando, "Performance of non-ceramic insulators in tropical environments", Ph.D. Thesis, Chalmers University of Technology, Goteborg, Sweden, 1999

[3] R. D. McAfee, R. D. Heaton, J. M. King, and A. U. Falster, "A study of biological contaminants on HV porcelain insulators", *Electric Power System Research*, Vol. 42, No. 1, pp. 35-39, July, 1997
 [4] G. B. Rackliffe, R. E. Lee, D. E. Fritz, and R. W. Harmon, "Performance evaluation of 15-kV polymeric insulators for dead-end type applications on distribution systems", *IEEE Trans. on P. D.*, Vol. 4, No. 2, pp. 1223-1231, April, 1989
 [5] I. Gutman, R. Hartings, and W. L. Vosloo, "Field testing of composite insulators at natural test stations in South Africa", 11th ISH, London, UK, pp. 50-53, 1999
 [6] M. A. R. M. Fernando and S. M. Gubanski, "Performance of nonceramic insulators under tropical field conditions", *IEEE Trans on P. D.*, Vol. 15, No. 1, pp. 355-360, January, 2000
 [7] S. M. Gubanski, M. A. R. M. Fernando, S. J. Pietr, J. Matula, and A. Kyaruzi, "Effects of biological contamination on insulator performance", Proceedings of the 6th Int. Conf. on Properties and Applications of Dielectric Materials, Xi'an, China, pp. 797-801, 2000
 [8] Research findings comparing performance of different insulator designs on distribution lines in tropical environments", *INMR*, Vol. 7, No. 6, pp. 46-53, 1999
 [9] Research at Chalmers focusing and promoting developments in outdoor electrical insulation", *INMR*, Vol. 8, No. 2, pp. 28-36, 2000
 [10] Growing interest at Entergy to assess techniques for in service monitoring of composite insulators", *INMR*, Vol. 7, No. 2, pp. 30-34, 1999
 [11] R. S. Gorur, J. Montesinos, R. Roberson, J. Burnham, and R. Hill, "Mold growth on nonceramic insulators and its impact on electrical performance", *IEEE Transmission and Distribution Conf.*, New Orleans, USA, pp. 818-822, 1999
 [12] R. S. Gorur and B. S. Bernstein, "Field and laboratory aging of polymeric distribution cable terminations. I. Field aging", *IEEE Trans. on P. D.*, Vol. 13, No. 2, pp. 316-322, 1998
 [13] M. Josho, H. Miyakawa, M. Sakata, K. Arakawa, K. Tsuge, D. Usami, T. Kondo, and Y. Utsumi, "Long term field test of polymer insulators at the Yonezawa Test Site", *IEEJ Trans. on HV*, Paper No. HV-01-72, 2001
 [14] F. Coowar and P. R. P. Hoole, "Discharge characteristics of alga-contaminated string insulators in the tropics", *Electric Power System Research*, Vol. 5, No. 3, pp. 215-218, 1988
 [15] Experience with non-ceramic bushings at Florida-based utility", *INMR*, Vol. 5, No. 6, pp. 30-35, 1997
 [16] A. Wolf, "Mould fungus growth on sanitary sealants", *Constr. and building materials*, Vol. 3, pp. 145-151, 1998
 [17] F. Schmuck and R. Bärsch, "Electrochemical and microbiological phenomena during accelerated ageing tests of polymeric insulators", 8th ISH, Yokohama, Japan, Paper No. 41.02, 1993
 [18] M. A. Mbwana, "Laboratory and field performance of polymeric insulators and RTV coatings", Lic. Thesis, Royal Institute of Technology, Stockholm, Sweden, 1997
 [19] A. Dornfalk, "Image analysis for diagnostics of insulators with biological contamination", Lic. Thesis, Chalmers University of Technology, Gothenburg, Sweden, 2002
 [20] A. Dornfalk and S. M. Gubanski, "Use of digital image analysis for studying biological contamination on nonceramic insulators", 12th ISH, Bangalore, India, pp. 599-602, 2001
 [21] P. Weibring, T. Johansson, H. Edner, S. Svanberg, B. Sundner, V. Raimondi, G. Cecchi, and L. Pantani, "Fluorescence lidar imaging of historical monuments", *Applied Optics*, Vol. 40, No. 33, pp. 6111-6120, 2001
 [22] A. Larsson, S. Kröll, A. D. Dornfalk, and S. M. Gubanski, "In-situ diagnostics of high-voltage insulation using laser-induced fluorescence spectroscopy", *IEEE Trans. on Dielectrics and Electrical Insul.*, Vol. 9, pp. 274-281, 2002
 [23] P. Weibring, "Environmental Monitoring by Multi-Spectral Lidar Techniques", Ph.D. Thesis, Lund Institute of Technology, Lund, Sweden, 2002

Author address: Andreas Dornfalk, Department of Electrical Engineering, Chalmers University of Technology, 412 96 Goteborg, Sweden. Email: andreas.dornfalk@eltek.chalmers.se

PAPER X

Fluorescence Lidar Imaging of Fungal Growth on High Voltage Outdoor Composite Insulators

M. Bengtsson, R. Grönlund, M. Sjöholm, C. Abrahamsson, A. Dernfalk, S. Wallström, A. Larsson, P. Weibring, S. Kröll, and S. Svanberg.

Optics and Lasers in Engineering **43**, 624–632 (2005).



Fluorescence lidar imaging of fungal growth on high-voltage outdoor composite insulators

M. Bengtsson^{a,*}, R. Grönlund^a, M. Sjöholm^a,
Ch. Abrahamsson^a, A.D. Dernfalk^b, S. Wallström^c,
A. Larsson^d, P. Weibring^e, S. Karlsson^c, S.M. Gubanski^b,
S. Kröll^a, S. Svanberg^a

^aDepartment of Atomic Physics, Lund Institute of Technology, P.O. Box 118, SE-221 00 Lund, Sweden

^bDepartment of Electric Power Engineering, Chalmers University of Technology,
SE-412 96 Gothenburg, Sweden

^cDepartment of Fibre and Polymer Technology, The Royal Institute of Technology,
SE-100 44 Stockholm, Sweden

^dWeapons and Protection Division, FOI – Swedish Defence Research Agency, SE-147 25 TUMBA, Sweden

^eThe National Center for Atmospheric Research, Atmospheric Technology Division, 3450 Mitchell Lane,
Boulder, Colorado 80301, USA

Received 4 June 2004; accepted 17 September 2004

Available online 8 December 2004

Abstract

Remote fluorescence imaging of fungal growth on polymeric high-voltage insulators was performed using a mobile lidar system with a laser wavelength of 355 nm. Insulator areas contaminated by fungal growth could be distinguished from clean surfaces and readily be imaged. The experiments were supported by detailed spectral studies performed in laboratory using a fibre-optic fluorosensor incorporating an optical multi-channel analyser system (OMA) and a nitrogen laser emitting radiation at 337 nm.

© 2004 Elsevier Ltd. All rights reserved.

Keywords: Lidar; Fungal growth; Polymeric insulators; Fluorescence; Remote sensing

*Corresponding author. Tel.: +46 46 2224595; fax: +46 46 2224250.

E-mail address: magnus.bengtsson@fysik.lth.se (M. Bengtsson).

1. Introduction

Modern society is increasingly dependent upon electric power and a reliable electric power transmission is of paramount importance. Thus, when developing new high-voltage outdoor insulators, for instance for support of power lines, these must be proven to withstand the impact from the surrounding environment and have a sufficient lifetime. Over the years, the use of polymeric materials in outdoor insulation has increased steadily [1]. One of the advantages of the polymeric, or composite, insulators over traditional ceramic ones is their light weight, making them easier and cheaper to store, transport, handle and install [2]. Another major advantage of these composite insulators is their low surface-free energy, making their surface hydrophobic and thereby, suppresses the development of a continuous layer of water on their surfaces. Such water layers can trigger a process leading to a surface flashover, which will lead to disconnection and possibly a power outage. As a consequence, a composite insulator has superior electric withstand performance compared to ceramic ones in polluted environments [2].

However, composite insulator performance can possibly be affected by biological growth, such as algae, fungi or lichen, which have been found to colonize insulators all over the world [3]. The presence of algae and fungi have, for instance, been found to decrease wet flashover withstand voltage [4]. Chlorophyll fluorescence from algae on insulators has been investigated remotely in earlier studies [5]. Algal growth, exhibiting a characteristic fluorescence peak due to chlorophyll *a* at about 685 nm, could readily be detected from a surface by a frequency-tripled Nd:YAG laser generating radiation at 355 nm. The imaging of algae on insulators [5] followed similar previous investigations, such as fluorescence imaging of vegetation status [6] and the monitoring of vegetation on historical monuments [7,8]. In the present paper, we report on remote fluorescence studies of the fungal growth on insulator surfaces.

2. Instrumentation

A mobile and self-contained light detection and ranging (lidar) system [9], based on all solid-state laser technology and housed in Volvo F610 truck was used. Although the system has multi-wavelength excitation capabilities [10], the present fluorescence experiments were conducted at a single wavelength. The light source used was a frequency-tripled Nd:YAG laser operating at 355 nm with a pulse energy of about 12 mJ. The laser light pulses had a duration of about 4–5 ns and were delivered at a 20 Hz repetition rate.

The light was sent out from the lidar truck, by a roof-top transmission and receiving an optical dome that could be horizontally rotated at 360° using a computer-controlled stepper motor with a resolution of 0.0035°. Similarly, a folding mirror could handle the vertical directionality of the light in the range of –10° to +55° with a resolution of 0.011 deg. That corresponds to a resolution of 3.7 and 12 mm, respectively, at the target insulators which were mounted at a 60 m distance

from the lidar system. The beam diameter at the target was 3 cm as adjusted with a Galilean transmitting telescope and the separation between adjacent measurement points was 3 cm. The change in position of the laser beam at the target due to mechanical instability of the whole truck was estimated to be about 1 cm. The transmitter, dome and light receiving unit are illustrated in Fig. 1.

Part of the laser-induced fluorescence light was captured by a 40-cm-diameter Newtonian telescope via the roof-top transmission and receiving an optical dome and focused into an optical fibre. A BG 385 coloured-glass cut-off filter was inserted in the optical path to block the elastically scattered laser light while passing most of the fluorescence light for wavelengths longer than 385 nm. An optical fibre with a 600 μm core diameter and a numerical aperture of 0.22 guided the fluorescence light to an optical multi-channel analyser system (OMA), consisting of a crossed Czerny–Turner spectrometer, a time-gated image intensifier, and a charge-coupled device (CCD) camera. The Peltier-cooled detector had a CCD array of 1024×128 pixels where the 128 vertical pixels were binned. The resolution of the OMA system, set by the 100 μm slit width, was 2.2 nm, and the spectrum could be recorded up to 805 nm. A time gate of 40–50 ns was utilized during the experiments

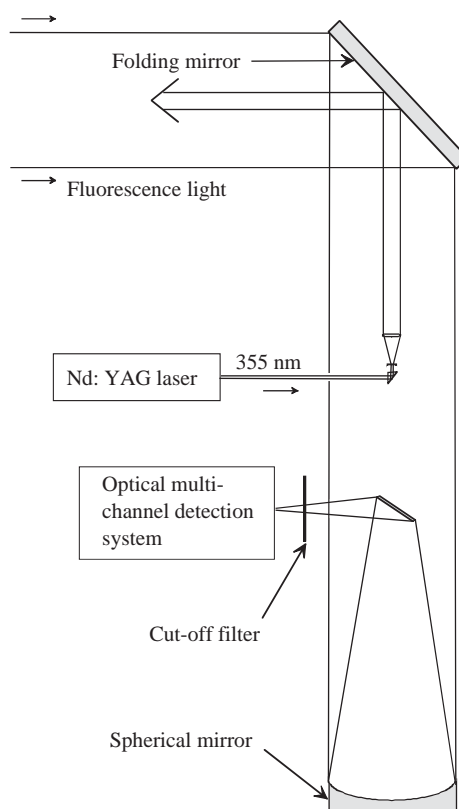


Fig. 1. Transmitter, dome and light receiving unit.

to suppress ambient light. The time gate was delayed with respect to the transmission of the laser pulse, to match the arrival of the fluorescence burst, some 400 ns later. Spectra from the OMA system were gathered by a data collection computer that stored the spectrum together with information about the measurement coordinates.

The OMA system could also be used separately, without the lidar system, and in that case a nitrogen laser, generating radiation at 337 nm was used as an excitation source. An optical fibre led the light to the target and also guided the fluorescence light back to the OMA system. This set-up has enabled the detailed laboratory studies of fungal growth on the small pieces of silicone rubber insulator material.

The extent of fungal growth on the material samples were estimated using a Jeol JSM-5400 scanning electron microscope (SEM) at an acceleration of 10 kV. Samples were dried in vacuum over night and sputtered with palladium/gold (60%/40%) for 30 s under an argon pressure of 0.5 kp/cm² (49 kPa) and a loading of 45 mA before the analysis.

3. Measurements, analysis and results

Several measurements have been performed, both remotely outdoors using the Nd:YAG laser-equipped lidar system combined with the OMA system and locally using the nitrogen laser-equipped OMA system in the laboratory. First small material samples (diameter ~5 cm) of silicone rubber, where one side of the samples was heavily colonized by fungal growth, were studied in the laboratory. It was observed that the intensity of the fluorescence light was substantially higher from clean surfaces compared to surfaces covered by fungal growth. This observation was previously noticed in an attempt to estimate fungal coverage [5]. However, the absolute intensity recorded in remote measurements is dependent on several factors such as laser pulse energy, laser spot size compared to the area of the sample studied and angle between the studied surface and incident laser beam. Thus, absolute intensity can be difficult to utilize for retrieving an unambiguous information. A more promising approach is to use the spectral shape of the fluorescence spectrum.

An example from the laboratory measurements is displayed in Fig. 2, where it can be seen that the fluorescence spectrum from a fungus-covered sample surface is much wider than the spectrum from a clean sample surface. Only a small variation in the spectral shapes between more or less fungus-covered areas (determined by the naked eye) was observed, indicating that the fluorescence imaging can reveal additional information compared to photographic imaging. Some parts of the rubber surface looked clean, but still showed the response of a fungus-covered area. When these parts were studied under SEM it was found that the studied areas were still infected. This shows that a fungus-covered surface can be partly cleaned but still show the same spectrum, even if it looks clean to the naked eye.

The difference between the fluorescence spectrum of a fungus-covered surface and a clean sample surface is smaller in the remote measurements made by the frequency-tripled Nd:YAG laser-equipped lidar system than in the case of the laboratory measurements, as can be seen when comparing Fig. 3 with Fig. 2. This is probably

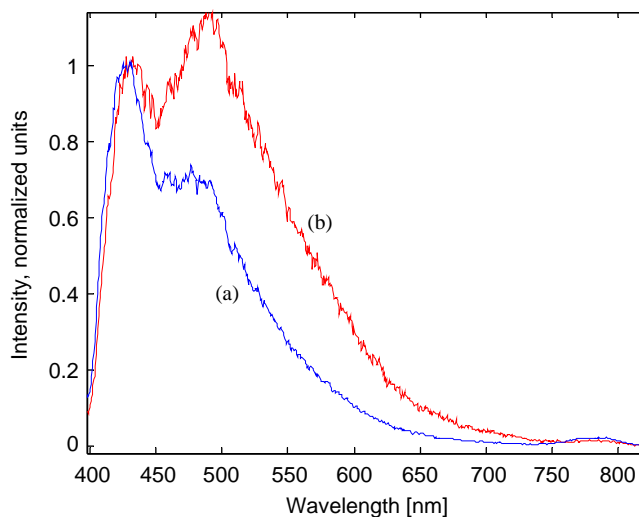


Fig. 2. Spectra from a clean; (a) and fungus-covered; (b) sample surface, respectively. The mixed culture originated from an insulator installed in Gothenburg, Sweden, and consisted of *Epicoccum nigrum* (34%), *Cladosporium cladosporides* (26%) and *Microsphaeriopsis 1* (20%) [11]. The spectra are normalized to have the same intensity around 430 nm. The experiment has been performed by using the nitrogen laser-equipped OMA system.

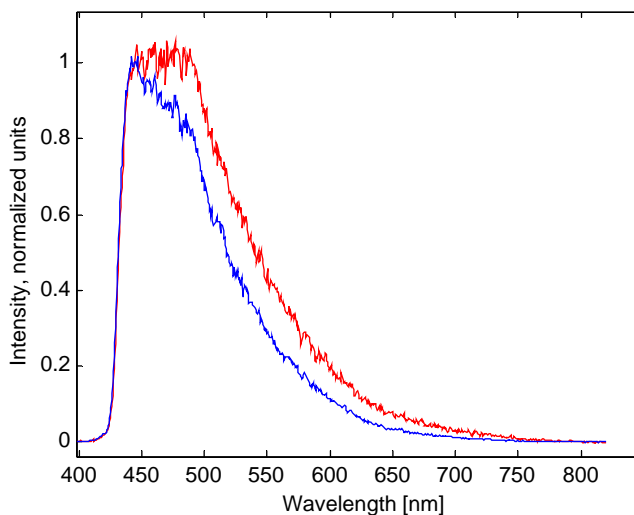


Fig. 3. Spectra from a clean sample surface and a fungus-covered sample surface can easily be distinguished due to the difference in fluorescence fall-off for longer wavelengths. The wider spectrum originated from the fungal growth. The experiment has been performed by using the lidar system together with the OMA system. Data was obtained by averaging over 200 laser pulses for each sample.

due to the relatively large beam spot size (~ 3 cm) from the lidar system, which will capture the fluorescence from both clean and fungus-contaminated areas simultaneously. Moreover, the intensities of fluorescence light from the colonized areas are lower than the corresponding intensities from the clean areas, which means that the clean areas are given a higher weight in the surface average. It should also be noted that there was a difference in the excitation wavelength between the laboratory and the remote measurements, which also might have an influence on the spectral shape. To focus on the interesting spectral features of the fluorescence spectra, these have to be intensity normalized in an appropriate way. The fluorescence spectra shown in Figs. 2 and 3 are normalized to have the same intensity in a 10 nm broad interval around 430 nm. However, this is a somewhat arbitrary choice and to more objectively study the spectral shape, a principal component analysis (PCA) [12,13] was performed.

To imitate a real-field measurement, naturally aged insulators were placed at a 60 m distance from the lidar system and fluorescence spectral recordings and imaging were performed remotely. The insulators that were covered by fungal growth were made of silicone rubber (SIR) and ethylene-propylene-diene monomer (EPDM) rubber.

In the PCA, one of the principal components could be used to distinguish a clean surface from a fungus-covered surface. That principal component mainly captures the difference in the fluorescence fall-off towards longer wavelengths between areas with and without fungal growth. However, this fall-off is different for different materials. This means that an obtained spectrum has to be compared to reference spectra from a clean surface and a fungus-covered surface of the same material in order to make it possible to discriminate between fungal growth and clean surface.

Results from imaging fluorescence measurements are presented in Figs. 4 and 5. Fig. 4 shows a fluorescence image of the insulators where the fungus-covered

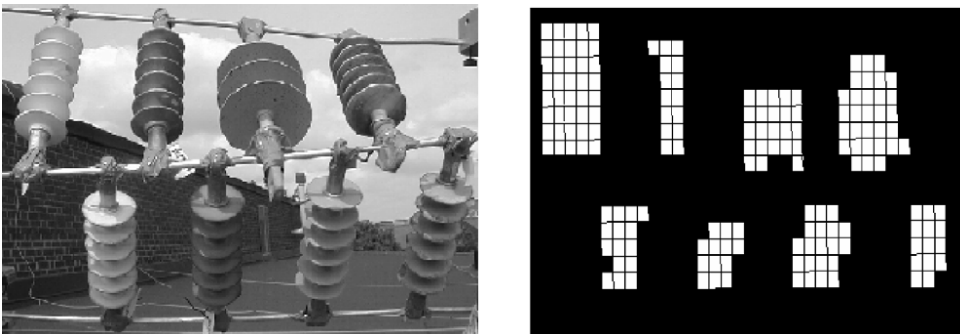


Fig. 4. Two insulators were partly covered by fungal growth, the third SIR and the fourth EPDM from the top-left. The corresponding fluorescence image of the insulators is shown on the right. Spectra were recorded remotely, from a slightly different angle of observation, using the lidar system. The image size is about 0.8×1.1 m. For each image point, data from 50 laser pulses were averaged. The total recording time for the image was about 50 min.

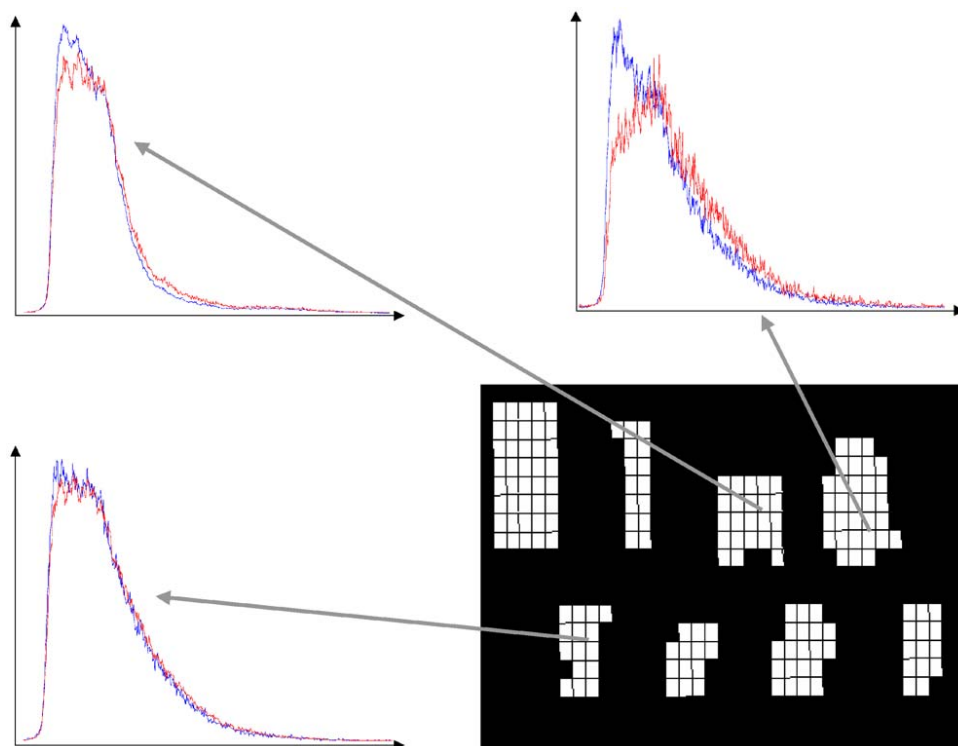


Fig. 5. Fluorescence spectra from the fungus-covered SIR and EPDM insulators in the upper row and a SIR insulator that has been exposed to weather and wind in the lower row. In each diagram, the spectra have been normalized to have the same area. Spectra were collected using the lidar system remotely (light-grey graphs) and compared to spectra collected from clean surfaces in the laboratory (dark-grey graphs) using the same excitation wavelength (355 nm).

insulators made of SIR and EPDM are located as the third and the fourth from the top-left. Here, only the average intensity is displayed outlining the insulators. Mean normalized fluorescence spectra obtained from three insulators utilizing the lidar system and spectra collected in the laboratory from clean surfaces (rinsed by water) are shown in Fig. 5. It was found that it was possible to image the fungus-covered insulators using a soft independent modeling of class analogy (SIMCA) classification analysis to assess the presence of fungal growth [13,14].

To calculate the change in the spectra, PCA data from the fungus-covered SIR insulator and clean surfaces was mean normalized and mean centered. Each spectrum can then be expressed as a sum of the average spectrum, shown in Fig. 6, and the contribution of a principal component, corresponding to the deviation in the spectral shape, shown in Fig. 7. A spectrum from a fungus-covered surface is expressed by a negative contribution of the principal component, but a spectrum from a clean surface adds a positive contribution.

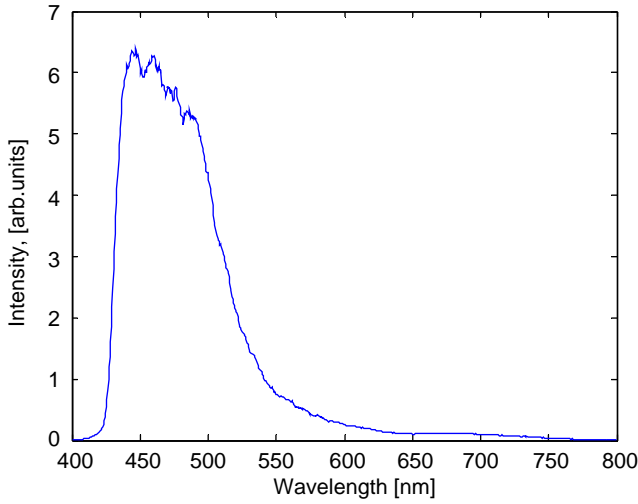


Fig. 6. The average spectrum calculated from all spectra obtained from the clean surface and the fungus-covered SIR surface.

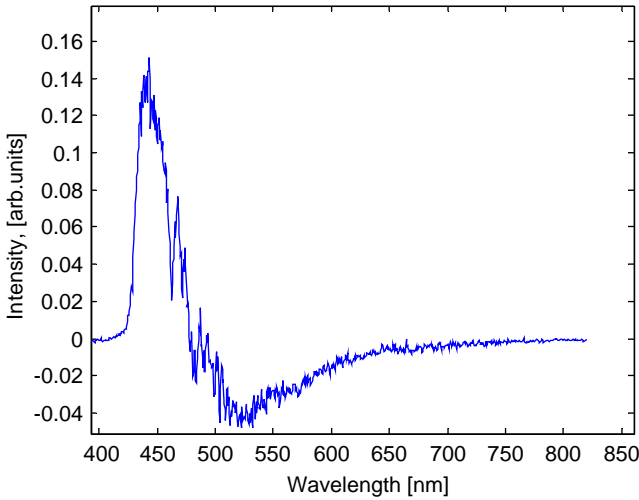


Fig. 7. The principal component which corresponds to the change in the spectral shape.

4. Discussion and conclusions

The main goal with this experiment has been to extract information about a potential method for remotely assessing the fungal coverage of insulators. It was found that a fungus-covered surface could be readily detected, imaged and distinguished from a clean surface. Future experiments will include both

algae- and fungus-covered insulator surfaces in the investigations aiming at finding the excitation wavelength giving the best demarcation between algae and fungal growth. The final goal is to perform remote fluorescence imaging in order to get a full status of the insulators and possibly identify the signs of future insulator failure.

Acknowledgements

This work has been partially supported by the Swedish Research Council, FORMAS, Elforsk AB and the Knut and Alice Wallenberg Foundation.

References

- [1] Gubanski SM. Modern outdoor electrical insulation. *IEEE Trans Dielectrics Electr Insul* 1999;6:517.
- [2] Hackam R. Outdoor HV composite polymeric insulators. *IEEE Trans Dielectrics Electr Insul* 1999;6:557.
- [3] Dernfalk AD. Image analysis for diagnostics of insulators with biological contamination. Lic. thesis, Department of Electric Power Engineering, CTH, Gothenburg, Sweden, 2002.
- [4] Gubanski SM, Fernando MARM, Pietr SJ, Matula J, Kyaruzi A. Effects of biological contamination on insulator performance. Proceedings of the sixth international conference on properties and applications of dielectric materials, Xi'an, China; 2000.
- [5] Dernfalk AD, Bengtsson M, Grönlund R, Sjöholm M, Weibring P, Edner H, et al. Laser-induced fluorescence spectroscopy for detection of biological contaminations on composite insulators. XIIIth international symposium on high voltage engineering, Netherlands; 2003. contribution O.15.01.
- [6] Svanberg S. Fluorescence lidar monitoring of vegetation status. *Phys Scr* 1995;T58:79.
- [7] Weibring P, Johansson Th, Edner H, Svanberg S, Sundnér B, Raimondi V, et al. Fluorescence lidar imaging of historical monuments. *Appl Opt* 2001;40:6111.
- [8] Lognoli D, Cecchi G, Mochi I, Pantani L, Raimondi V, Chiari R, et al. Fluorescence lidar imaging of the cathedral and baptistery of Parma. *Appl Phys B* 2003;76:457.
- [9] Weibring P, Edner H, Svanberg S. Versatile mobile lidar system for environmental monitoring. *Appl Opt* 2003;42:3583.
- [10] Weibring P, Smith JN, Edner H, Svanberg S. Development and testing of a frequency-agile optical parametric oscillator system for differential absorption lidar. *Rev Sci Instrum* 2003;74:4478.
- [11] Wallström S, Karlsson S. Biofilms on silicone rubber insulators; microbial composition and diagnostics of removal by use of ESEM/EDS. *Polymer Degradation and Stability* 2004;85(2):841–6.
- [12] Geladi P. Chemometrics in spectroscopy. Part I. Classical chemometrics. *Spectrochim Acta Part B* 2003;58:767.
- [13] Esbensen K. *Multivariate data analysis—in practice*, 5th ed. Oslo: Camo Process AS; 2002.
- [14] Wold S. Pattern recognition by means of disjoint principal components models. *Patt Recog* 1976;8:127.

PAPER XI

Remote Imaging Laser-Induced Breakdown Spectroscopy and Remote Cultural Heritage Ablative Cleaning

R. Grönlund, M. Lundqvist, and S. Svanberg.

Optics Letters **30**, 2882–2884 (2005).

Remote imaging laser-induced breakdown spectroscopy and remote cultural heritage ablative cleaning

Rasmus Grönlund, Mats Lundqvist, and Sune Svanberg

Atomic Physics Division, Lund Institute of Technology, P.O. Box 118, S-221 00 Lund, Sweden

Received July 11, 2005

We report, for what we believe to be the first time, on remote imaging laser-induced breakdown spectroscopy (LIBS). Measurements have been performed by using a tripled Nd:YAG laser working at 355 nm with 170 mJ pulse energy, with an expanded beam that is focused onto a target at 60 m distance. The LIBS signal is detected by using an on-axis Newtonian telescope and an optical multichannel analyzer. The imaging is performed by scanning the laser beam on the target. The same setup is also used in demonstrations of remote laser ablation for cleaning of contaminated objects with applications toward cultural heritage.

© 2005 Optical Society of America

OCIS codes: 280.3640, 300.6360, 240.6490.

Laser-induced breakdown spectroscopy (LIBS) is a powerful method for material elemental analysis based on emission spectroscopy.^{1,2} It has been widely applied in analytical chemistry.³ LIBS can be applied remotely, as demonstrated in early Russian work^{4,5} and more recently by Palanco *et al.*,⁶ Rohwetter *et al.*,⁷ and our group.⁸ Lidar techniques were employed using CO₂, Nd:YAG, and short-pulse femtosecond laser systems. Remote detection from selected spots has been demonstrated, but imaging has not been performed previously. In a parallel development, remote LIBS is now being developed for deployment on remotely operated Mars landing vehicles.⁹

Laser ablation, where laser pulses are employed for explosive evaporation of small amounts of surface materials, is a technique widely used for micromachining and thin-film fabrication. It is also used for surface cleaning in the field of cultural heritage management, e.g., of paintings or statues,¹⁰ over short ranges.

Remote-imaging LIBS and remote ablative cleaning of stone surfaces are described in the present Letter, we believe for the first time. The Lund mobile lidar system, which was recently thoroughly upgraded,¹¹ was used in the present work. The experiments were performed with a system–target distance of 60 m. The important aspects of the lidar system regarding the present work on LIBS and remote ablation are noted in Fig. 1. We use frequency-tripled radiation (355 nm) from a 20 Hz pulsed Nd:YAG laser, and the radiation is transmitted toward the target via a 10 cm diameter specially designed refractive transmission telescope placed coaxially with the receiving 40 cm diameter reflective Newtonian telescope. The transmission and receiving beam paths are folded via a roof-top 40 × 80 cm first-surface aluminized mirror, which is controlled by stepper motors for precision scanning of the target.

A key aspect of remote LIBS and remote surface ablation is to ensure that a sufficiently high optical field strength can be achieved in the remote focus to induce a plasma breakdown at the solid target

surface. Clearly, because of diffraction, the laser beam must first be expanded and transmitted through a low-aberration telescope, which was designed with the aid of a ray-tracing program (Linos Photonics, WinLens 4.3). One plano–concave and two plano–convex lenses with focal lengths of, −25, 500, and 1000 mm and spaced by ~20 and ~25 cm were employed. The beam diameter and the laser pulse energy chosen must be matched in such a way that a laser spark is induced at the target without causing optical damage in the transmission system, especially damage of the aluminized folding mirror. We normally employed 170 mJ, 4–5 ns long pulses at 355 nm, generated by a Spectra-Physics Model GCR-290 Nd:YAG laser. While a focal-spot diameter of about 0.7 mm at a 60 m distant target is calculated, in practice we noted burn marks with a diameter of about 5 mm. The selection of tripled Nd:YAG radiation instead of doubled (532 nm) or fundamental (1064 nm) radiation is governed by eye-safety considerations (outside the focus, the UV beam reaches eye-safe intensity levels comparatively fast). Further, the

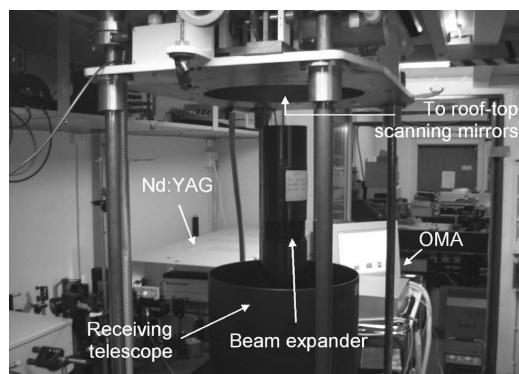


Fig. 1. Measurement setup with the important parts of the interior of the lidar system labeled. Detailed diagrams of the optical and electronic arrangements of the lidar system can be found in Ref. 11.

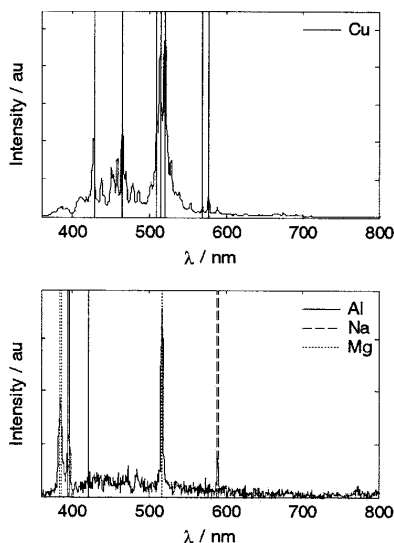


Fig. 2. Remote LIBS spectra from metal plates of copper and aluminum. The vertical lines correspond to tabular values of prominent emission peaks.¹² Note that magnesium and sodium contamination can be clearly seen in the aluminum case.

use of UV radiation allows plasma light to be detected throughout the visible region, and fluorescence can also be efficiently induced.

The plasma light collected by the lidar receiving telescope is focused into a 600 μm diameter optical fiber, which is connected to the entrance slit of an Oriel Corporation MS125 400 lines mm^{-1} grating spectrometer equipped with an Andor DH50125U-01 gated and intensified ccd detector. The 360–800 nm spectral region is detected with a spectral resolution of 2.2 nm. The intensifier is activated with a temporal window typically of 150 ns, which can be temporally located to match the arrival of the prompt target emission or delayed to allow observation of the plasma afterglow.

The present measurements were performed in Lund with the lidar system parked at the Physics Department, with the target area located on an easily accessible roof and with a brick wall terminating any stray laser pulses. Laser pulses are transmitted from the lidar roof-top mirror 4 m above the ground level in a completely safe manner. The lidar system is equipped with two TV cameras surveying the target area through the roof-top transmission dome, with clear marking of the exact target spot. As targets, arrangements of metal plates made of different elements were used. In addition, stone samples and even statues were utilized.

As an example of remote LIBS spectra, in Fig. 2 we show emission lines from copper and aluminum targets, recorded 300 ns after ablation with a 150 ns gate. The vertical lines correspond to tabular values of prominent emission lines of different elements.¹² Note that magnesium and sodium contamination can be seen in the case of aluminum.

By scanning the laser beam under computer control, it was possible to generate LIBS images such as shown in Fig. 3. A photograph of the target is included. By image processing, looking at the characteristic lines of different elements, it was possible to identify the target materials as shown in the figure.

The energy deposited in the plasma is sufficient to perform ablation and surface layer removal. On metal targets clear ablation marks could be seen. Oxide layers could be removed; even the green copper hydroxide typical of copper roofs at coastline locations could be ablated, and spectral differences could be noted as the surface was cleaned. Surface layer removal from stone surfaces has considerable value in terms of cultural heritage management. Thus, biodegenerative layers on weathered mortar surfaces could be removed as well as corresponding coatings on granite rock [Fig. 4(a)]. Pencil and marker-pen blackened areas on white alabaster slabs (Volterra, Italy) could be readily removed [Fig. 4(b)] at a working speed of about $10 \text{ cm}^2 \text{ min}^{-1}$. Ablation speeds were similar for all the substances. The ablation process is basically self-terminating when the white substrate is reached. Here the samples were manually moved in a fixed beam. For a realistic remote cleaning of a statue, a 1 m tall white Italian garden replica statue partially covered by dirt and algal growth after ten years of weather exposure was used as a target. The remote cleaning of the statue with computerized beam scanning is illustrated in Fig. 4(c). Finally, an Italian replica statue head, made of white Carrara marble, was exposed, and an area heavily blackened by a soft pencil was cleaned [Fig. 4(d)]. No detectable surface damage could be observed by the naked eye.

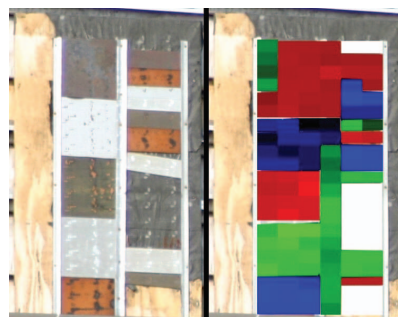


Fig. 3. LIBS imaging of metal plates, with the target on the left and a false-color coded identification image on the right with copper (red), aluminum (green) and iron (blue). The classification has good correspondence to the spots where the laser has hit the target. The big plates on the left are (from top to bottom) copper, stainless steel, brass, aluminum, and iron. The stainless steel is classified as iron and the brass as copper, as they contain large amounts of these substances. The vertical profiles holding the plates are made of aluminum and are classified accordingly. Note that the pixels are much larger than the spot size and that the scanning resolution is quite low. The beam scanning has been slightly tilted, and the middle spot in the upper rows does not hit the aluminum profile but instead hits the metal plates. White parts correspond to nonmetallic surfaces.

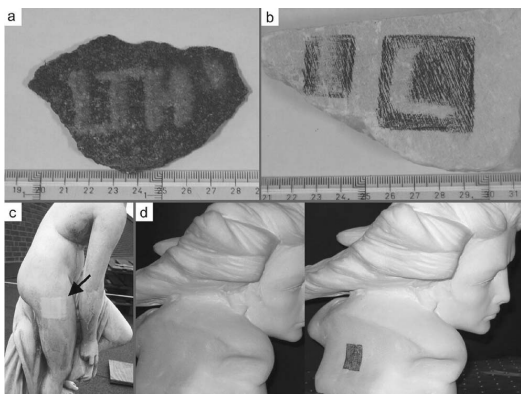


Fig. 4. Remote laser ablative cleaning of, a, mortar; b, alabaster; c, a replica of an Italian statue with the arrow indicating the 100 cm² cleaned area; d, a statue made of Carrara marble after and before cleaning.

Fluorescence and line emission spectra could be expected to change as the ablation of the surface layer proceeds and the substrate is reached. Thus the spectroscopic signals might be used to control the ablation in a similar way as coronary artery ablation can be supervised by a spectroscopic signal recorded through the fiber used as discussed, e.g., in Ref. 13.

It should be noted that the experiment described could, as in earlier laser-induced fluorescence lidar campaigns,^{14,15} have been performed at any historical monument, since the mobile lidar system is fully self-contained and is equipped with a 40 kVA motor generator towed by the lidar truck.

The present work shows that remote imaging LIBS can be used for surface assessment at considerable standoff distance and thus constitutes a complement to remote fluorescence imaging, e.g., in the assessment of historical monuments. Further, remote laser ablation with spectroscopic guidance seems to be a realistic possibility, which could reduce the cost of very expensive scaffolding in restoration work. Clearly, only areas directly seen from the ablation lidar system can be cleaned; however, on the other hand, these are the only ones that are visible to the spectator.

This work was supported by the Swedish Research Council for Environment, Agricultural Sciences and Spatial Planning (FORMAS) and by the Knut and Alice Wallenberg Foundation. Valuable assistance from Gabriel Somesfalean, Magnus Bengtsson, and Hans Edner in the early stage of the experiment is gratefully acknowledged.

References

1. L. J. Radziemski, T. R. Loree, D. A. Cremers, and N. M. Hoffman, *Anal. Chem.* **55**, 1246 (1983).
2. D. A. Cremers and L. J. Radziemski, in *Laser Spectroscopy and its Applications*, L. J. Radziemski, R. W. Solarz, and J. A. Paisner, eds. (Dekker, 1989), p. 351.
3. Special issue on LIBS, *Spectrochim. Acta, Part B* **56**, 565 (2002).
4. Iu. V. Akhtyrchenko, E. B. Beliaev, Iu. P. Vysotskii, O. V. Garin, A. P. Godlevskii, V. E. Zuev, Iu. D. Kopytin, A. I. Kuriapin, V. A. Pogodaev, and V. V. Pokasov, *Fizika (Alma Ata)* **26**, 5 (1983).
5. V. E. Zuev, Y. D. Kopytin, V. A. Korolkov, M. E. Levitskii, M. F. Nebolsin, B. G. Sidorov, and N. P. Soldatkin, in *Proceedings of the 13th International Laser Radar Conference* (NASA Langley Research Center, 1986).
6. S. Palanco, J. M. Baena, and J. J. Laserna, *Spectrochim. Acta, Part B* **57**, 591 (2002).
7. Ph. Rohwetter, J. Yu, G. Méjean, K. Stelmaszczyk, E. Salmon, J. Kasparian, J. P. Wolf, and L. Wöste, *J. Anal. At. Spectrom.* **19**, 437 (2004).
8. R. Grönlund, M. Bengtsson, M. Sjöholm, G. Somesfalean, T. Johansson, P. Weibring, H. Edner, S. Svanberg, J. Hällström, and K. Barup, in *Air Pollution and Cultural Heritage*, C. Saiz-Jimenez, ed. (A. A. Balkema, 2004).
9. R. C. Wiens, S. Maurice, D. A. Cremers, and S. Chevrel, *Lunar Planet. Sci.* **34**, 1646 (2003).
10. C. Fotakis, S. Georgiou, V. Zafropoulos, and V. Tornari, in *Proc. SPIE* **4402**, 8 (2001).
11. P. Weibring, H. Edner, and S. Svanberg, *Appl. Opt.* **42**, 3583 (2003).
12. D. R. Lide, ed., *CRC Handbook of Chemistry and Physics*, 74th ed. (CRC Press, 1993).
13. S. Svanberg, *Phys. Scr.* **T72**, 69 (1997).
14. P. Weibring, Th. Johansson, H. Edner, S. Svanberg, B. Sundnér, V. Raimondi, G. Cecchi, and L. Pantani, *Appl. Opt.* **40**, 6111 (2001).
15. D. Lognoli, G. Cecchi, I. Mochi, L. Pantani, V. Raimondi, R. Chiari, Th. Johansson, P. Weibring, H. Edner, and S. Svanberg, *Appl. Phys. B* **76**, 457 (2003).

PAPER XII

**Remote Imaging Laser-Induced Breakdown
Spectroscopy and Laser-Induced Fluorescence
Spectroscopy using Nanosecond Pulses from a
Mobile Lidar System**

R. Grönlund, M. Lundqvist, and S. Svanberg.

Applied Spectroscopy **60**, 853–859 (2006).

Remote Imaging Laser-Induced Breakdown Spectroscopy and Laser-Induced Fluorescence Spectroscopy Using Nanosecond Pulses from a Mobile Lidar System

RASMUS GRÖNLUND,* MATS LUNDQVIST, and SUNE SVANBERG

Atomic Physics Division, Lund Institute of Technology, P.O. Box 118, SE-221 00 Lund, Sweden

A mobile lidar system was used in remote imaging laser-induced breakdown spectroscopy (LIBS) and laser-induced fluorescence (LIF) experiments. Also, computer-controlled remote ablation of a chosen area was demonstrated, relevant to cleaning of cultural heritage items. Nanosecond frequency-tripled Nd:YAG laser pulses at 355 nm were employed in experiments with a stand-off distance of 60 meters using pulse energies of up to 170 mJ. By coaxial transmission and common folding of the transmission and reception optical paths using a large computer-controlled mirror, full elemental imaging capability was achieved on composite targets. Different spectral identification algorithms were compared in producing thematic data based on plasma or fluorescence light.

Index Headings: Laser-induced breakdown spectroscopy; LIBS; Laser-induced fluorescence; LIF; Lidar; Remote sensing.

INTRODUCTION

Laser-induced breakdown spectroscopy (LIBS) is a minimally invasive elemental analysis method in which the characteristic line emission from free atoms and ions is used.^{1,2} LIBS has numerous applications in analytical chemistry.³⁻⁵ Normally, LIBS is performed in a laboratory environment, but it can also be applied remotely. Early LIBS lidar (light detection and ranging) used multi-Joule CO₂ lasers for elemental analysis of airborne particulates.^{6,7} More recently Palanco et al.⁸ used infrared nanosecond Nd:YAG radiation on remote solid targets and could demonstrate a measurement range up to 120 m,⁹ and a range of 300 m is anticipated.¹⁰ Rohwetter et al.¹¹ and Stelmaszczyk et al.¹² demonstrated remote LIBS using a high-power femtosecond lidar system employing filamentation in the air for sustaining the high energy density at target needed for plasma breakdown. Recently, a range of 180 meters could be demonstrated, and schemes for extending the range to 1 km are discussed.¹³ Remote LIBS is now being developed for deployment on Mars landing vehicles.¹⁴

Our group has performed extensive remote target laser-induced fluorescence (LIF) imaging using lidar techniques¹⁵ regarding vegetation¹⁶ and power-line insulators¹⁷ as well as historical buildings including the Lund Cathedral,¹⁸ the Parma Cathedral and Baptistery¹⁹ as well as the Rome Coliseum and Lateran Baptistery.²⁰ Fluorescence is useful for complete nonintrusive mapping of complex organic molecules such as chlorophyll and façade conservation agents, and by using multivariate analysis of the multispectral images, thematic maps can be produced. LIBS, on the other hand, is useful for elemental composition determination, since a hot dissociative plasma is formed. Since only a small amount of material is

ablated off, little damage to the target is inflicted. However, controlled ablation can be very useful for removing surface layers, providing powerful close-range cleaning means in the cultural heritage sector.²¹

Based on our experience in imaging remote LIF we recently extended lidar imaging capability to LIBS, demonstrated at a range of 60 meters.²² Challenging issues here are to achieve coordinated target irradiation and detection of lobe movements for swiftly selecting arbitrary target points to achieve general-purpose imaging using LIBS as well as LIF. This is possible using nanosecond laser pulses while retaining eye-safety outside the immediate target area. In the present paper we will describe our experiments with special regard to achieving useful images and remote cleaning of fouled surfaces in the cultural heritage sector. We also discuss the relative advantages of long- and short-pulse remote LIBS/surface cleaning/LIF.

MEASUREMENT SYSTEM

The measurements were performed using the mobile lidar system developed at Lund Institute of Technology.²³ The system, fully mobile as it is housed in the cargo compartment of a Volvo F610 truck, is a multi-purpose lidar for atmospheric trace gas monitoring, as well as maritime measurements, and solid target interrogation. For the LIBS measurements discussed in the present paper, the frequency-tripled laser radiation from the 20 Hz Nd:YAG laser with a pulse energy at 355 nm of 170 mJ, limited by the tolerance of the transmitting optics, is used. The radiation is guided through a beam expander and sent into the atmosphere via the roof-top dome, where a motor-controlled mirror can direct the radiation to the desired target spot. Imaging can be performed by steering the radiation onto different spots and scanning over an area.

To perform laser-induced breakdown one key aspect is to be able to focus the laser radiation tightly to a small enough spot. Thus, a beam expander has been developed by which the laser beam is expanded with a negative lens and focused using two 10-cm-diameter positive lenses. Using two positive lenses instead of one to focus the radiation reduces the spherical aberration and thus a tighter focus can be achieved. Also, the lens diameter is chosen to minimize the focus with regards to both aberrations and diffraction. Although ray-tracing simulations yield a focal diameter of 0.7 mm at 60 m distance, in reality burn-marks show a focus with about 5 mm diameter.

The plasma radiation was gathered with a 40-cm-diameter Newtonian telescope and focused onto the tip of an optical fiber, connected to an optical multichannel analyzer (OMA) system²⁴ where the spectrum in the wavelength range 280–800 nm was gathered. The detection is gated to suppress background light, and the gate can be adjusted to gather the radiation from different times. Each point is averaged over

Received 2 February 2006; accepted 24 May 2006.

* Author to whom correspondence should be sent. E-mail: rasmus.gronlund@fysik.lth.se.

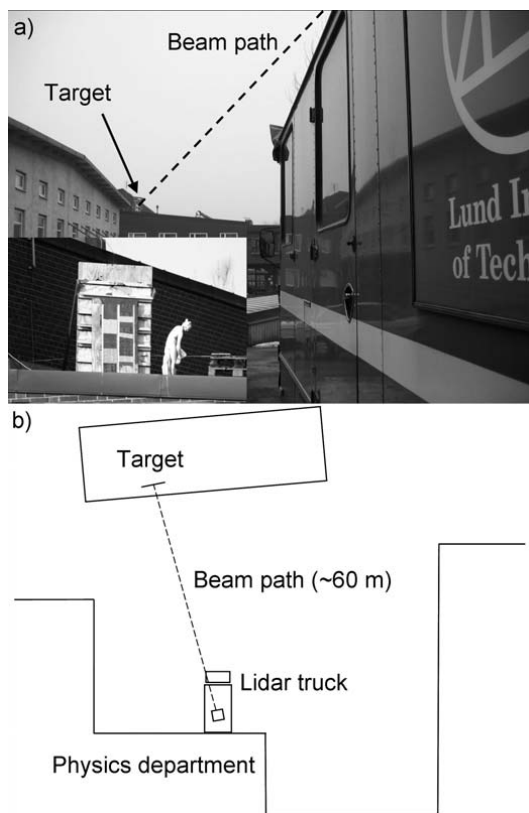


Fig. 1. Overview of the measurement setup. (a) Picture of the target area with the lidar truck on the right and a close-up of the target area on the lower left; (b) an overview map of the measurement situation.

a number of laser shots, typically about 500, which corresponds to an integration time of half a minute. The OMA system has a quite limited resolution (2.2 nm), but still different peaks can be identified and different materials can be classified.

For LIF measurements, the same setup is utilized, using a larger spot size and a lower pulse energy. A 30 mJ laser pulse is sent through a 5 cm diameter beam expander to the target and hits with a diameter of approximately 5 cm. Since the excitation wavelength is at a convenient UV wavelength (355 nm), laser-induced fluorescence is efficiently generated and is collected with the same OMA system and with the same configuration as in the LIBS measurements.

MEASUREMENTS

Laser-induced breakdown spectroscopy measurements were performed in Lund on some test samples, with the mobile laser-radar system docked to the Physics Department building and the target area at a roof of a nearby building, about 60 m from the system (see Fig. 1). Although the measurements were performed in a laboratory-like environment, they could as well

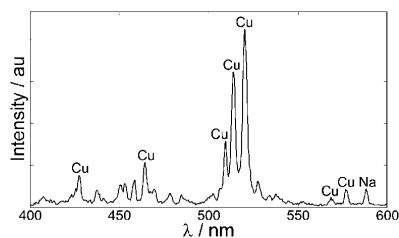


Fig. 2. A LIBS spectrum from a copper plate with identification of the strongest peaks. Some sodium contamination can be noted.

have been performed at any place, since the system is fully self-contained with a motor generator powering it.

Measurements were performed on different metal targets and a few mineral samples. A vertical scan over five different metal plates was performed and the spectrum from each point was registered. Also, tests with different delay times were tried to examine the time dependence of the plasma.

Tests were also performed on remote ablative cleaning, where the laser beam was directed onto a contaminated object. The laser beam could then be scanned over the object to clean the entire area.

Laser-induced fluorescence measurements were performed at Övedskloster, a castle in southern Sweden, in a 3-day field campaign. Different areas on the main façade of the building and on the courtyard portal were scanned at typical ranges of 40 meters.

RESULTS AND ANALYSIS

An example of a spectrum from a copper plate is shown in Fig. 2. The spectrum was gathered with pulse energy of 150 mJ and was integrated over 10 seconds. Spectral lines are found in tables²⁵ and the measured spectrum corresponds well to the tabular lines.

Time Dependence. With different delays for the detector gate it is possible to study the temporal development of the spectrum. In Fig. 3, the temporal development of a lead spectrum is shown. It is clearly seen that at early times the continuous plasma background is quite intense and at later times the peaks will become narrower, but at the same time weaker.

Classification. For the vertical scan (total length: 0.9 m) a set of spectra (more precisely 22 different points) was gathered. In each spectrum peaks can be identified and the material can be classified. Analysis of the spectra can be performed in several different ways. Here, we will discuss three different algorithms that can be applied.

A first, obvious choice would be to examine the highest peak in each spectrum. However, we want to work with dimensionless quantities to avoid influences due to different absolute values, so it is advantageous to divide the maximum value in a narrow wavelength region (where the top peak is) by the average value over a broad wavelength range. This is done for copper and the result can be seen in Fig. 4. The maximum value in the wavelength range 504–513 nm has been divided by the average value between 380 and 710 nm. As can be seen, the points on the copper plate and on the brass plate yield high values, whereas the other points give much lower values. However, with this method it may be difficult to discriminate

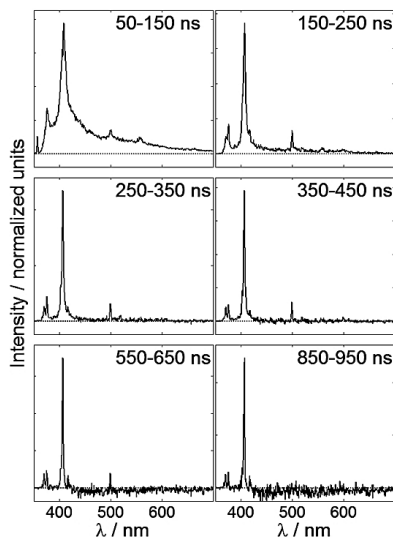


Fig. 3. Temporal development of the LIBS signal in a lead target. At early times, the continuous plasma light is clearly seen, but at later times the substance-specific lines dominate. At even later times the signal starts to disappear and the picture becomes more and more noisy. Time delays indicated start from the lidar round-trip time lapse for the light.

copper from brass, as they both have this copper emission line. Also, one has to be very careful when choosing the wavelength region for the peak, to avoid coincidences with emission peaks for any other substance in the current experiment, which sometimes may be a difficult task. This is why the sharp 522 nm copper line was excluded from the analysis in Fig. 4, since both Cr and Mg (present as trace elements in some of the metal plates) have sharp lines in its close vicinity.

Although several peaks may have coincidences with peaks from other substances, the total spectral shape serves as

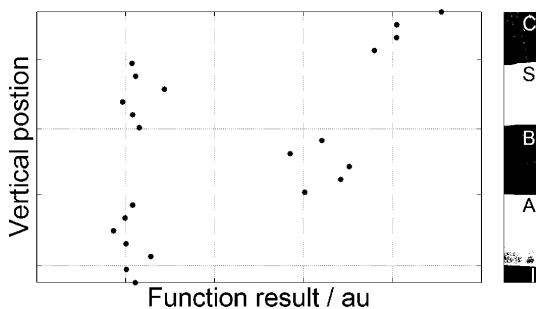


Fig. 4. In a first analysis, a function has been produced to single out the points containing copper. On the right is a picture of the metal plates that have been scanned over (C: Copper, S: Stainless steel, B: Brass, A: Aluminum, and I: Iron). The evaluation was carried out by taking the maximum value in the 504–513 nm range (where copper has a large peak, see Fig. 2) and dividing by the average value in the 380–710 nm range to get a dimensionless quantity. As can be seen, the points containing copper are successfully singled out, although it is difficult to discriminate copper from brass (as both contain copper and thus have high values at ~510 nm).

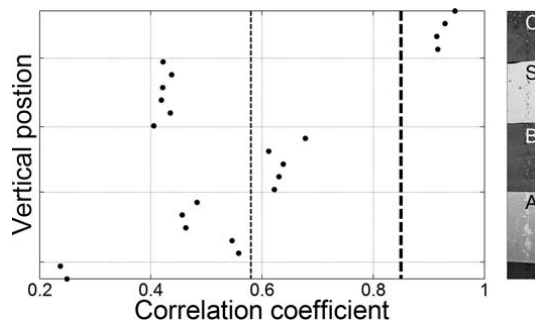


Fig. 5. The correlation coefficient when compared with a copper spectrum. On the right is a picture of the target metals (C: Copper, S: Stainless steel, B: Brass, A: Aluminum, and I: Iron) and the y-scale corresponds to the vertical measurement position. The curve clearly has the largest value for the copper points (about 0.9) but also quite high values for the brass points (which, of course, contain copper). It is seen that a threshold can easily be applied to discriminate copper points from non-copper points, either at 0.85, as the thick dashed line indicates, or at a lower value (around 0.55) as the thinner dashed line indicates, where the brass points are included.

a fingerprint for the material. Thus, taking more peaks into account will give a more certain classification of the different materials. One could, of course, take the sum of the values for all the substance-specific lines that can be found and divide by the integrated value over a larger range to get a dimensionless quantity, but then it is probably easier to compare each spectrum with a reference spectrum. This can be done using linear correlation between the reference spectrum, \mathbf{X} , and each spectrum in the sample set, \mathbf{Y} . Each point will then give one numerical value, r , called the correlation coefficient.²⁶

$$r = \frac{\sum_i (\mathbf{X}_i - \bar{\mathbf{X}})(\mathbf{Y}_i - \bar{\mathbf{Y}})}{\sqrt{\sum_i (\mathbf{X}_i - \bar{\mathbf{X}})^2 \sum_i (\mathbf{Y}_i - \bar{\mathbf{Y}})^2}} \quad (1)$$

Here, $\bar{\mathbf{X}}$ and $\bar{\mathbf{Y}}$ denote the average intensity value over the entire wavelength region for \mathbf{X} and \mathbf{Y} , respectively. The correlation coefficient will have a value between -1 and $+1$; the closer to $+1$ the value is, the more similar the two spectra are. Practically, however, for spectral values the correlation coefficient is almost always larger than 0. Equation 1 is applied to all spectra \mathbf{Y} in the scan with one reference spectrum \mathbf{X} giving each point one value, and by applying a threshold the points of the same material can be found. In Fig. 5 the linear correlation with a copper spectrum is shown. It is clearly seen that the largest values are obtained for the points on the copper plate. These points are easily discriminated from the rest as indicated by the thick dashed threshold level in Fig. 5. It is also noted that relatively high values result for the brass points, as they contain copper, and a threshold level could be applied to discriminate these points as well. Performing this function with several different reference spectra, a number of graphs like the one in Fig. 5 are found, to each of which a threshold can be applied and then a classification can be made. Even with a universal threshold level, it is possible to assign each point to the correct material, and the result is shown in Fig. 6. Of course, this method requires that a set of reference spectra is known.

Another interesting way to interpret the results is to use

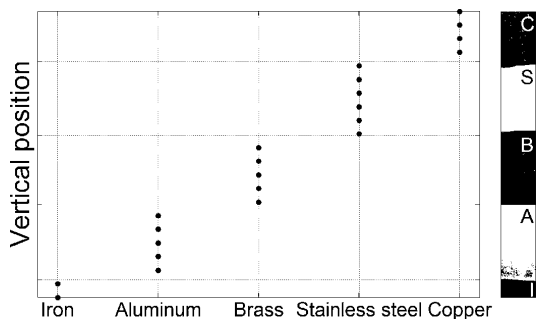


FIG. 6. Classification of different metals by linear correlation with reference spectra. On the right is a picture of the target metals where the vertical scan is performed (C: Copper, S: Stainless steel, B: Brass, A: Aluminum, and I: Iron)

principal component analysis (PCA). Here, we call each measurement point a sample and each wavelength where we have a value is called a variable. Our data is then a matrix of (in this case) 22 samples and 1024 variables. The PCA algorithm projects the data onto a new set of variables, called principal components (PCs), such that the variance along the first direction is maximized. A second PC is then created perpendicular to the first one, including as much of the remaining variance in the data as possible. PCs can be added until the residual consists of only noise. Each sample will now have a certain value along each PC, called the score value. A commercial program package called Unscrambler²⁷ was used. Looking at the scores along the first and the third PC, as seen in Fig. 7, it is noted that there are five distinct groups, corresponding to the five different materials. It is also noted that copper and brass are quite close to each other (as both contain copper) and that iron and stainless steel are also close to each other.

Minerals. Remote measurements on a few different stones and minerals were also tried. This could be interesting for mining applications, where the results can guide the mining operations to the areas of highest mineral content. The spectrum from a stone containing a mixture of calcite (CaCO_3) and quartz (SiO_2) is shown in Fig. 8a. There is also some contamination of clay minerals that contain some aluminum. Peaks of Ca and Si^+ are seen in the spectrum and also a weak Al^+ line can be identified. Figure 8b shows parts of the

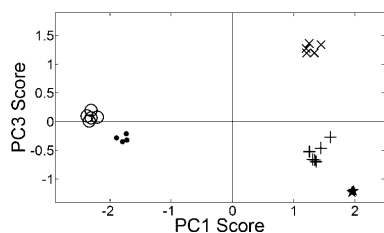


FIG. 7. PC scores for the vertical scan, PC1 vs. PC3. The different symbols correspond to the different materials (●, Copper; +, Stainless steel; ○, Brass; ×, Aluminum; and ★, Iron). The samples divide into five distinct groups corresponding to the different materials in the scan. It is also noted that copper and brass are situated close to each other and that iron and stainless steel are close to each other, indicating similarities, as expected.

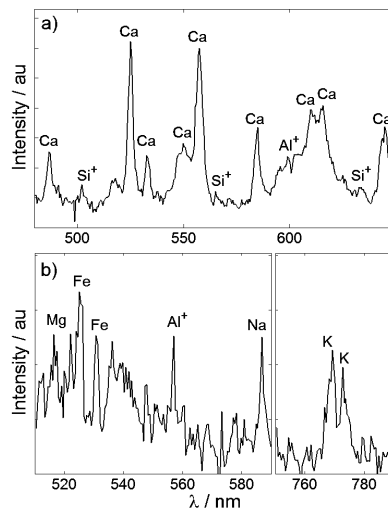


FIG. 8. Parts of LIBS spectra from (a) a calcite stone (CaCO_3) containing quartz (SiO_2) and clay minerals (containing aluminum), and (b) a biotite stone ($\text{K}(\text{Mg,Fe})_3\text{AlSi}_3\text{O}_{10}(\text{OH})_2$) with a rusty surface.

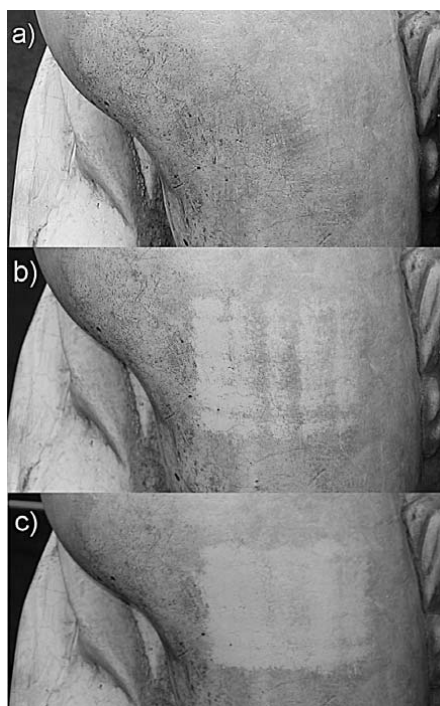


FIG. 9. A part of an Italian garden statue, (a) before cleaning, (b) after cleaning in the spots that the stepper motors could reach, and (c) after cleaning with fast movement of the laser beam. The cleaned area has a size of $6 \times 4 \text{ cm}^2$.

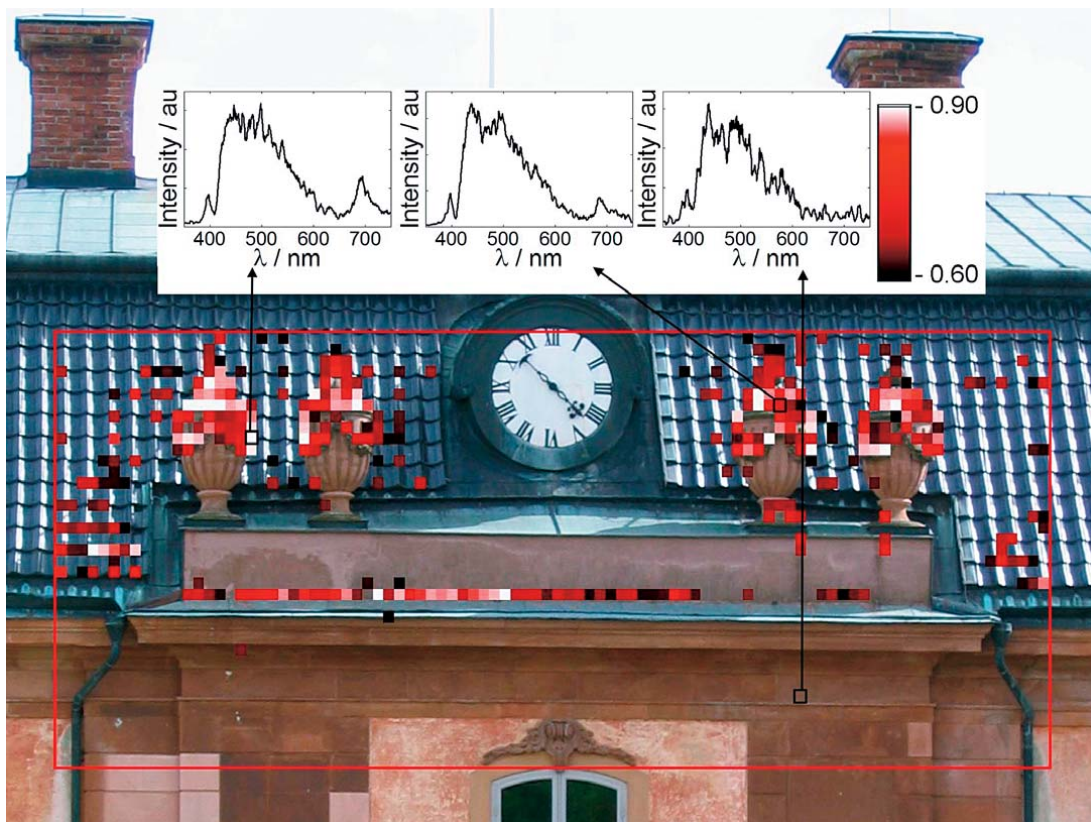


Fig. 10. Points on the main façade of the Övedskloster castle containing chlorophyll. The false-color coded pixels correspond to the correlation value with a reference spectrum and bright pixels indicate a strong chlorophyll signal, as indicated by the color scale. It can be noted that the chlorophyll is present mainly in the upper part of the ornamental urns, on the edges of the roof tiles and in a horizontal line along the metal plate. The spectra show the detected signal from the indicated points with different amounts of chlorophyll as estimated from the peak at 690 nm.

spectrum from a biotite stone ($\text{K}(\text{Mg},\text{Fe})_3\text{AlSi}_3\text{O}_{10}(\text{OH})_2$). Peaks from Fe, Mg, Al, Na, and K could be identified. Only the most interesting parts of the spectra are shown.²⁸

Cleaning. Remote ablative cleaning was performed on an Italian garden statue by scanning the laser beam on the target. The laser intensity was enough to ablate the contamination but not the underlying substance, making the process self-terminating. When moving the laser beam, the stepper motors can only move to certain points, thus leaving a few points uncleaned. This can, however, be overcome by quickly moving the beam over the area several times, spending more time moving the spot than in the spot it can be placed. Results are shown in Fig. 9, where Fig. 9a is the original state, Fig. 9b is after cleaning the spots the stepper motors could reach, and Fig. 9c is after several iterations of quickly moving the beam over the area. Another way would be to look at the LIBS signal while performing the cleaning and thus control the cleaning spectroscopically. However, in these measurements, the signal-to-noise ratio was not enough for this to be possible.

Fluorescence. Fluorescence data does not exhibit features as distinct as those in LIBS spectra and thus they are more difficult

to classify. The same analysis methods can be used, i.e., constructing functions to focus on certain features, correlating spectra with a reference spectrum, and performing PCA. The thematic maps that can be constructed then show spectra with similar features, but it may not be obvious what feature is shown, as it often is in the case of LIBS. Hence, it is good to have collaborations with, e.g., building conservationists, who can correlate the thematic maps with physical phenomena.

An example of a thematic map is shown in Fig. 10, where the chlorophyll content on an area on the main façade of the building has been evaluated. As chlorophyll has strong fluorescence at around 690 nm, as seen in the inset in Fig. 10, the points containing chlorophyll can be mapped out. Figure 10 has been constructed by linear correlation with a reference spectrum in the wavelength interval 580–750 nm and the brightest points correspond to the highest values. Further LIF results from Övedskloster castle are given in Ref. 29.

DISCUSSION

Remote LIBS performed with a lidar system has substantial analytical power, especially when adapted with full and

straight-forward selectivity of the target point. Then multi-spectral imaging can also be achieved as demonstrated in the present paper. Full steerability of the laser beam is also necessary for remote ablative cleaning, e.g., of the cultural heritage, but also for possible specific tasks such as salt removal from high-voltage insulators.³⁰ The inherent capability of a LIBS system to use the emitted plasma light for controlling and terminating the process is a further attractive feature. Range capability is an important aspect for a remotely operating LIBS system. In the present work 60 m was achieved, but this could easily be increased by optimizing the optical components to achieve a smaller spot size. A coaxial modified Galilean refractive telescope with a beam diameter of 10 cm was used, limiting the transmitted pulse energy to about 170 mJ for safe-guarding the folding mirror. Lidar systems, such as ours, are frequently mostly intended for atmospheric work where a reduced-cost spherical main telescope mirror is sufficient at a received beam diameter of 40 cm, as in our case. However, this mirror, with major spherical aberration, is totally unsuitable for transmitting a correspondingly expanded high-energy pulsed laser beam for LIBS. Clearly, by replacing the lidar telescope main mirror with a parabolic one with strongly reduced aberration, two very desirable effects are achieved simultaneously: (1) the attainable focused spot size will be strongly reduced for this high-aperture optics, and (2) the full laser power (presently about 500 mJ at 355 nm) can be employed without running the risk of damage to the folding mirror. A range capability of at least 300 m could be anticipated for the present, fully steerable system equipped with a modified telescope mirror. However, for most civil applications, including the cultural heritage sector, a range of 100 m would suffice and would also allow for convenient target inspection. A corresponding down-scaling of transmitter and/or telescope is then possible.

Femtosecond high-power transmitters cause laser beam filamentation and long-range self-focused propagation,³¹ an effect that was innovatively utilized for lidar applications by the Teramobile team.^{11,12,32} Performing remote LIBS by this scheme is advantageous not only for transmittance of high laser powers over long distances but also due to the insensitivity on target distance—the beam hitting the target is always properly focused. However, eye safety with a high-power laser beam, with essentially white light due to the self-phase-modulation, is a challenging issue. In contrast, a 355 nm strongly focused laser beam will, outside the direct target, expand (if missing) or diffusely scatter radiation that is absorbed by the human cornea. Of course, laser goggles fully absorbing 355 nm can be made completely transparent throughout the visible region and would be a default and convenient eye protection for persons at risk. It should also be noted that an increased range for a laser spark on the target still calls for a correspondingly larger detection telescope, because of the $1/r^2$ intensity fall-off for the solid target plasma light. A short-pulse system operating in the white-light filamentation mode is not suited for LIF measurements since the scattered white light completely drowns the faint fluorescence. In contrast, the 355 nm nanosecond pulse system is also perfectly functioning in LIF applications.

CONCLUSION

In this paper, a system able to perform remote laser-induced fluorescence and remote laser-induced breakdown spectroscopy measurements with the same setup is presented. LIBS

measurements have been performed and could be complementary to LIF measurements, e.g., in cultural heritage applications. As this system can perform both types of measurements with the same setup, it is easy to quickly switch between the two modes and thus be able to gain more information on the studied area.

In conclusion, a nanosecond LIBS lidar system operating in the UV region offers many possibilities for moderate-range stand-off diagnostics, complementing LIF measurements, while also offering remote ablation.

ACKNOWLEDGMENTS

This work was supported by the Swedish Research Council (VR), the Swedish Research Council for Environment, Agricultural Sciences and Spatial Planning (FORMAS), and the Knut and Alice Wallenberg Foundation. Building restoration specialists Jenny Hällström and Kerstin Barup are acknowledged for excellent cooperation and aid in the LIF measurement campaign. Valuable assistance from Gabriel Somesfalean, Magnus Bengtsson, and Hans Edner in the early stage of the experiment is gratefully acknowledged.

1. L. J. Radziemski, T. R. Loree, D. A. Cremers, and N. M. Hoffman, *Anal. Chem.* **55**, 1246 (1983).
2. D. A. Cremers and L. J. Radziemski, "Laser Plasmas for Chemical Analysis", in *Laser Spectroscopy and Its Applications*, L. J. Radziemski, R. W. Solarz, and J. A. Paisner, Eds. (Marcel Dekker, New York, 1989), Chap. 5, p. 351.
3. Special issue on laser-induced breakdown spectroscopy: *Spectrochim. Acta, Part B* **56**, 565 (2002).
4. Special issue on laser-induced breakdown spectroscopy: *J. Anal. At. Spectrom.* **19**, 419 (2004).
5. Special issue on laser-induced breakdown spectroscopy: *Spectrochim. Acta, Part B* **60**, 877 (2005).
6. I. V. Akhtyrchenko, E. B. Beliaev, I. P. Vysotskii, O. V. Garin, A. P. Godlevskii, V. E. Zuev, I. D. Kopytin, A. I. Kuriapin, V. A. Pogodaev, and V. V. Pokasov, *Fizika* **26**, 5 (1983).
7. V. E. Zuev, Y. D. Kopytin, V. A. Korolkov, M. E. Levitskii, M. F. Nebolsin, B. G. Sidorov, and N. P. Soldatkin, in *Proc. 13th International Laser Radar Conference* (1986).
8. S. Palanco, J. M. Baena, and J. J. Laserna, *Spectrochim. Acta, Part B* **57**, 591 (2002).
9. S. Palanco, S. Conesa, and J. Laserna, "Pulse energy requirements for remote analysis with LIBS beyond the 100 meter range", paper W3-2, *3rd International Conference, LIBS 2004* (September 28–October 1 2004, Torremolinos (Malaga), Spain, 2004).
10. S. Palanco and J. Laserna, *Rev. Sci. Instrum.* **75**, 2068 (2004).
11. Ph. Rohwetter, J. Yu, G. Méjean, K. Stelmasczyk, E. Salmon, J. Kasparian, J.-P. Wolf, and L. Wöste, *J. Anal. At. Spectrom.* **19**, 437 (2004).
12. K. Stelmasczyk, P. Rohwetter, G. Méjean, J. Yu, E. Salmon, J. Kasparian, R. Ackermann, J.-P. Wolf, and L. Wöste, *Appl. Phys. Lett.* **85**, 3977 (2004).
13. Ph. Rohwetter, K. Stelmasczyk, L. Wöste, R. Ackermann, G. Méjean, E. Salmon, J. Kasparian, J. Yu, and J.-P. Wolf, *Spectrochim. Acta, Part B* **60**, 1025 (2005).
14. R. C. Wiens, S. Maurice, D. A. Cremers, and S. Chevrel, *Lunar and Planetary Science XXXIV*, 1646 (2003).
15. S. Svanberg, "Fluorescence spectroscopy and imaging of LIDAR targets", in *Laser Remote Sensing*, T. Fujii and T. Fukuchi, Eds. (CRC Press, Boca Raton, FL, 2005), Chap. 6, pp. 433–467.
16. S. Svanberg, *Phys. Scr. T* **58**, 79 (1995).
17. M. Bengtsson, R. Grönlund, M. Sjöholm, Ch. Abrahamsson, A. D. Dornfalk, S. Wallström, A. Larsson, P. Weibring, S. Karlsson, S. M. Gubanski, S. Kröll, and S. Svanberg, *Opt. Laser Eng.* **43**, 624 (2005).
18. P. Weibring, Th. Johansson, H. Edner, S. Svanberg, B. Sundner, V. Raimondi, G. Cecchi, and L. Pantani, *Appl. Opt.* **40**, 6111 (2001).
19. D. Lognoli, G. Cecchi, I. Mochi, L. Pantani, V. Raimondi, R. Chiari, Th. Johansson, P. Weibring, H. Edner, and S. Svanberg, *Appl. Phys. B* **76**, 457 (2003).
20. J. Hällström, K. Barup, R. Grönlund, A. Johansson, S. Svanberg, G. Cecchi, D. Lognoli, L. Palombi, V. Reimondi, and C. Conti, "Remote Monitoring of Conservation Status of the Coliseum by Laser-Induced Fluorescence Imaging", paper in preparation (2006).

21. C. Fotakis, S. Georgiou, V. Zafirooulos, and V. Tormari, [Proc. SPIE-Int. Soc. Opt. Eng.](#) **4402**, 8 (2001).
22. R. Grönlund, M. Lundqvist, and S. Svanberg, [Opt. Lett.](#) **30**, 2882 (2005).
23. P. Weibring, H. Edner, and S. Svanberg, [Appl. Opt.](#) **42**, 3583 (2003).
24. C. Klinteberg, M. Andreasson, O. Sandström, S. Andersson-Engels, and S. Svanberg, [Rev. Sci. Instrum.](#) **76**, 034303-1 (2005).
25. D. R. Lide, Ed. *CRC Handbook of Chemistry and Physics* (CRC Press, Boca Raton, FL, 1993), 74th ed.
26. T. Tong, J. Li, and J. P. Longtin, [Appl. Opt.](#) **43**, 1971 (2004).
27. K. H. Esbensen, *Multivariate Data Analysis – in practice* (CAMO Process AS, Oslo, Norway, 2002), 5th ed.
28. M. Lundqvist, M.Sc. Thesis, Lund Institute of Technology, Lund Reports on Atomic Physics LRAP-341 (Sweden, 2005).
29. R. Grönlund, J. Hällström, S. Svanberg, and K. Barup, “Fluorescence Lidar Multispectral Imaging for Diagnosis of Historical Monuments—Övedskloster, a Swedish Case Study”, LACONA VI: Lasers in the Conservation of Artworks (Vienna, Austria, September 2005), paper accepted (2006).
30. M. Bengtsson, R. Grönlund, M. Lundqvist, A. Larsson, S. Kröll, and S. Svanberg, “Remote Laser-induced Breakdown Spectroscopy for the Detection and Removal of Salt on Metal and Polymeric Surfaces”, *Appl. Spectrosc.*, paper submitted (2005).
31. A. Braun, G. Korn, X. Liu, D. Du, J. Squier, and G. Mourou, [Opt. Lett.](#) **20**, 73 (1995).
32. <http://www.teramobile.org>.

PAPER XIII

Laser Spectroscopy of Gas in Scattering Media at Scales Ranging from Kilometers to Millimeters

M. Andersson, R. Grönlund, L. Persson, M. Sjöholm, K. Svanberg,
and S. Svanberg.

Laser Physics **17**, 893–902 (2007).

Laser Spectroscopy of Gas in Scattering Media at Scales Ranging from Kilometers to Millimeters

M. Andersson^a, R. Grönlund^a, L. Persson^a, M. Sjöholm^a, K. Svanberg^b, and S. Svanberg^{a,*}

^a Division of Atomic Physics, Lund University, P.O. Box 118, SE-221 00 Lund, Sweden

^b Oncology Department, Lund University Hospital, SE-221 85 Lund, Sweden

*e-mail: sune.svanberg@fysik.lth.se

Received January 10, 2007

Abstract—Free gases are characterized by their narrow line width, and they can conveniently be studied by laser spectroscopy. The present paper discusses the monitoring of such ambient pressure gases, which are dispersed in scattering media such as aerosol-laden atmospheres, solids, or liquids. Atmospheric work basically constitutes the well-known field of differential absorption lidar (DIAL), while the study of free gas in solids and liquids was initiated more recently under the name of GASMAS (GAs in Scattering Media Absorption Spectroscopy). We discuss the connections between the two techniques, which are extensively used in our laboratory. Thus, we span the field from trace-gas mapping of gases in the lower atmosphere to gas studies in construction materials, food products, and the human body. We show that the basic ideas are very similar, while the spatial and temporal scales vary greatly.

PACS numbers: 87.64.Je, 89.60.-k, 87.80.-y, 34.50.-s, 81.05.Rm

DOI: 10.1134/S1054660X07070018

1. INTRODUCTION

Media with strong optical scattering are extremely common in the real world, and are often encountered in everyday life. Examples of scattering media are clouds, fog, ice, snow, foams, food products, wood, and human tissue. Two major aspects pertain when light is propagating in such media. First, the light path traveled by the light becomes undefined with a distribution of path lengths, which results in the absence of a well-defined Beer–Lambertian law, directly applicable for determining the concentration of an absorbing species in the scattering material. Secondly, imaging through scattering media becomes blurred. Many techniques have been developed to alleviate the detrimental effects of scattering as discussed, e.g., in [1–3].

The influence of scattered light in imaging can be removed, e.g., by gated viewing and coherent gating, where the unique feature of the shortest traveling time, and the preserved coherence, respectively, for nonscattered light is taken advantage of [4, 5]. The problem of concentration evaluation can be addressed by using time-resolved measurements, where a histogram of the path lengths of individual photons is recorded, allowing a modified Beer–Lambertian law to be established [6]. In this way, it becomes possible to determine the concentration of molecular species, e.g., in tissue related to sensitizer concentration evaluation in photodynamic therapy [7], for breast tissue characterization in optical mammography [8], or for the concentration evaluation of active components in pharmaceutical tablets [9, 10].

These types of measurements were extended to the study of free gas in scattering media using a technique which was named GASMAS (GAs in Scattering Media

Absorption Spectroscopy) [11]. The technique, although operating on samples on millimeter to centimeter scales, has a clear resemblance to laser radar (lidar, or light detection and ranging) measurements in the atmosphere, where the scales are up to several kilometers [12–14]. Single-scattering events strongly dominate in clear air, allowing a straight-forward evaluation of gas concentrations to be performed using the so-called differential absorption lidar (DIAL) technique [15, 16], which, for air pollution studies, was pioneered by Walther and collaborators [17] and Grant and collaborators [18]. However, in the presence of fog or clouds, multiple scattering frequently occurs, especially when operating at short wavelengths. The field of multiple-scattering lidar is extensive and has been covered in a series of international conferences (see, e.g., [19]). The situation in multiple-scattering lidar is very similar to GASMAS measurements, except that the spatial scale is different. In our group, DIAL as well as GASMAS studies are being pursued, and, in the present paper, we show their close connection. Laser spectroscopy applied to environmental and medical research has much in common [20], which is also illuminated, as is the power of multidisciplinary multispectral imaging [21].

The present paper is organized in the following way. Experimental arrangements for lidar and GASMAS measurements are presented in the next section. Then, some results from different types of experiments are presented. Finally, in a concluding section, the techniques are discussed and new fields of investigation are proposed.

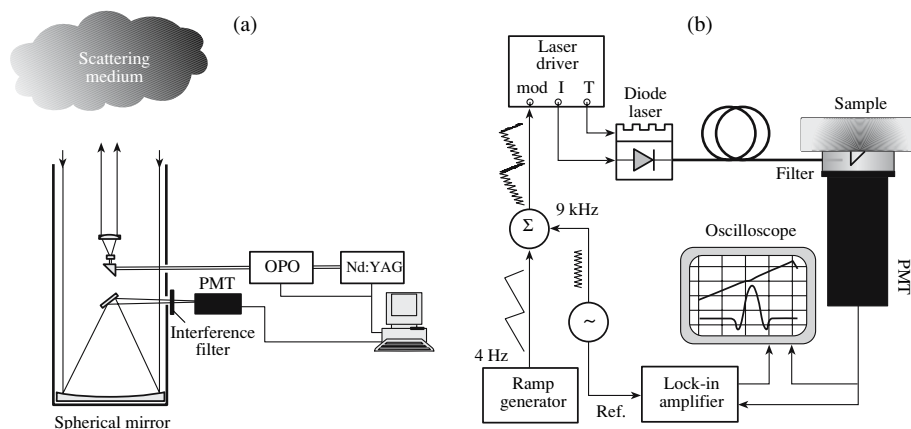


Fig. 1. (a) Schematic arrangement for lidar monitoring of atmospheric gases (left) and (b) the schematic arrangement for measurements of gases in solid or liquid scattering media (right) (from [3]).

2. EXPERIMENTAL ARRANGEMENTS

2.1. Lidar

A schematic diagram of the Lund lidar system used for range-resolved trace-gas element mapping in the atmosphere is shown in Fig. 1a. Short pulses from a tunable high-power laser are transmitted into the atmosphere, and the laser is switched between two different wavelengths—one on an absorption peak and one slightly off. The laser radiation is scattered by particles and molecules in the atmosphere and backscattered light is collected with a 40-cm-diameter Newtonian telescope and directed to a detector. The telescope has a very small viewing angle (about 1 mrad) defined by an aperture stop in the focal plane. The viewing angle matches the divergence of the laser beam, which is transmitted through a beam expander, and is mounted on the same optical axis as the receiving telescope. With this “tunnel-vision” arrangement, the probability of multiply scattered photons is strongly reduced—to the extent it is possible to be neglected in the absence of fog or clouds. The detected laser-radar signals will, for a uniform atmosphere, show a typical $1/r^2$ dependence, reflecting the diminishing solid angle of the receiving telescope presented to the scatterers along the propagating beam. This is true for the off-resonance wavelength, whereas the on-resonance signal will be additionally attenuated by absorption related to the gas of interest. Division of the on-resonance by the off-resonance curve will also eliminate the influence of nonuniform scattering particle distributions, and the slope of the ratio curve indicates the gas concentration.

The Lund lidar system [22] is housed in the cargo compartment of a Volvo truck and can easily be transported to measurement sites. The system is fully self-contained with an autonomous source of electricity. A 20 Hz Nd:YAG-pumped optical parametric oscillator

(OPO) system (Spectra Physics MOPO-730), modified to make fast wavelength switching possible is used as the lidar transmitter. The OPO can be widely tuned, and, in combination with nonlinear frequency conversion techniques, the spectral range 220 nm to 3.4 μm can be covered. The vertically looking arrangement in Fig. 1a is normally complemented by a rooftop dome with a computer-controllable folding mirror to direct the radiation in any direction desired. Collected backscattered light is passed through a narrow-band interference filter, which transmits only the elastically scattered radiation onto a photomultiplier tube (PMT), while suppressing most of the ambient light.

Ultraviolet laser radiation is preferably used, since these wavelengths are essentially eye safe (below 400 nm) and a sufficiently strong backscattering is attained, which is not necessarily true in the infrared region, which otherwise is also eye safe beyond 1.4 μm .

Our group has performed measurements on several pollutants, including sulphur dioxide (SO_2), nitrogen dioxide (NO_2), nitric oxide (NO), and mercury (Hg), the last of which was recently studied in a major interdisciplinary project concerning chlor-alkali factories [23]. During these measurements, the absorption peak for Hg at 253.65 nm was used, where 5 mJ laser pulses with 4–5-ns length could be produced. The laser wavelength is switched on a shot-to-shot basis, such that there is not time for the atmosphere to change appreciably between the on- and off-resonance measurements.

2.2. GASMAS

A schematic setup for GASMAS is shown in Fig. 1b. It is employed to measure molecular gases inside scattering media by using tunable diode laser absorption spectroscopy. The laser is scanned across an absorption line of the gas to be studied by repetitively

modifying the laser driver current by supplying a sawtooth ramp. Our work has been focused on molecular oxygen [11, 24–26], which has its conveniently located A-band around 760 nm. Furthermore, water vapor around 980 nm [27] has been studied for moisture assessment. In principle, any gas with absorption lines situated at a wavelength available with a suitable laser can be investigated, provided that the bulk material is sufficiently transparent. Thus, there is a practical limitation to the optical region below 1400 nm for samples containing large concentrations of liquid water (biological tissue, fruits, foods, etc.), and from 600–1400 nm for human tissue due to the additional absorption of hemoglobin at lower wavelength.

In order to achieve sensitive detection, lock-in detection techniques are used. The laser driver current is, then, modulated by a 10-kHz sine wave. The light is fiber optically guided to the sample, which, for oxygen monitoring, has the additional advantage of suppressing a strong background signal from ambient air. In the arrangement shown in Fig. 1b, a right-angle prism is positioned in front of the fiber, centrally located over a large area photomultiplier tube (PMT) detector. The backscattered light from the sample is collected through an annular aperture, which has the function of suppressing the strong light backscattered close to the injection point of the sample, allowing deeper levels of the sample to be probed. A high-pass filter with a cut-off wavelength at 715 nm is mounted on the detector in order to reduce the influence of background light. The sharp sensitivity cut off of the PMT towards the IR region provides the matching low-pass filter function. The signal from the detector is split into two parts. One part is directly connected to a digital oscilloscope, while the other part is fed to a lock-in amplifier, where the amplitude at twice the modulation frequency is phase sensitively detected and fed to a second channel of the oscilloscope. The lock-in signal normalized to the amount of light reaching the detector is used as a measure of the gas content. The standard-addition method, where known pathlengths of ambient air are added into the laser beam, is used to calibrate the system. By doing so, a so-called equivalent mean pathlength, L_{eq} , can be estimated for the sample, corresponding to the distance light has to travel in ambient air to obtain the same signal as in the sample, where multiple scattering produces a distribution of pathlengths. We note that L_{eq} depends on both the sample scattering properties and the concentration of the distributed gas.

2.3. Comparison

By comparing Figs. 1a and 1b, we notice the close resemblance between the lidar and GASMAS techniques, which typically operate at kilometer and millimeter ranges, respectively. In the second case, strong multiple scattering can cause the effective pathlengths to be centimeters up to meters in rare cases. Thus, while

a lidar system operates at photon travel times on the order of microseconds, the latter system is characterized by pico- and nanosecond time scales. Both systems can, in principle, be operated in pulsed mode yielding time resolution, or in a continuous-wave (CW) mode. The former system is normally a pulsed one, while the latter is frequently a continuous one. In continuous operation, the overwhelming signal at short range must be suppressed by a ring-shaped aperture arrangement suppressing the on-axis signal. Pulsed operation in short-range applications (high temporal resolution) is not compatible with a high spectral resolution, due to Fourier broadening. However, the phase-shift method, where a CW laser is amplitude modulated, may be compatible with spectral as well as spatial resolution in a certain parameter range.

The CW detection scheme can also be seen as a long-path absorption arrangement where the range resolution is lost. Two scenarios are depicted in Figs. 2a and 2b. An arrangement for long-path absorption measurements of air pollutants is shown in Fig. 2a, where a retroreflecting mirror, placed at a distance far away is used to effectively throw the light back to the receiver. In Fig. 2b, a magnetic resonance image (MRI) indicating the frontal human sinus cavities is shown together with a light path for probing the gas content in the sinuses. This can be considered as equivalent to a long-path absorption measurement. Here, the very nonoptimal laser transmitting optics is the frontal bone, the retroreflector is the diffusely scattering underlying tissue (i.e., the brain), and the receiving optics, again, correspond to the inefficient “frontal-bone” telescope followed by the large-area detector. Still, it is possible to measure the pathlength traveled through air in the sinuses. As compared to the atmospheric monitoring case, a huge amount of light is wasted in the sinus case due to diffuse scattering.

3. MEASUREMENT EXAMPLES

Many different aspects of applied molecular spectroscopy are pursued in our research group. Different techniques are used; however, they are frequently closely related, as pointed out in this paper. Atmospheric long-path absorption measurements can be performed using single-mode diode lasers. Frequently, cheap and easily accessible diode lasers do not necessarily emit light at wavelengths corresponding to the strongest gas absorption lines, but rather, at weak overtone or combination spectral bands. To compensate for this, sensitive frequency-modulation techniques can be used, bringing down the sensitivity to the shot-noise limit. As an example, we performed road traffic measurements of nitrogen dioxide concentrations with a cheap laser emitting around 635 nm, rather than employing the commonly used blue spectral region [28]. The two-tone frequency modulation technique, which combines a large frequency modulation, matching the pressure-broadened lines, with convenient elec-

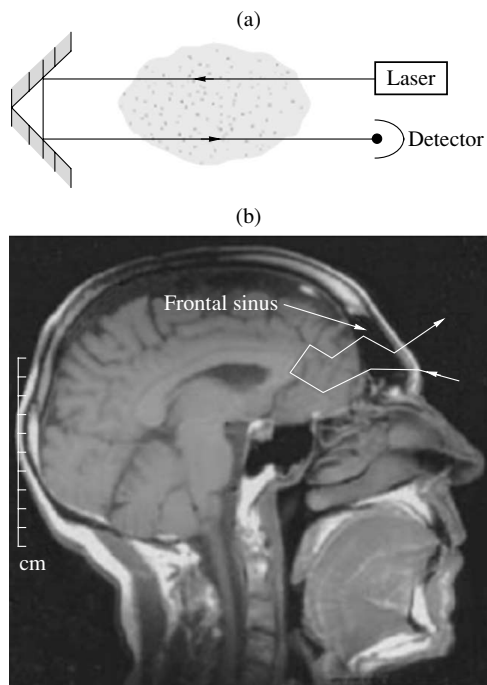


Fig. 2. The upper part (a) shows a schematic setup for a long-path absorption measurement employing a retroreflector. The lower part (b) shows an MRI image of the senior author indicating the location of the frontal sinuses. A light path illustrating the GASMAS technique measurement is also included (from [3]).

tronic detection around 10 MHz, was employed. A well-known problem with diode lasers is their tendency to mode hop if not accurately controlled. We have developed a new temporal correlation technique, where an uncontrolled multimode laser can be employed for gas concentration measurements. Observed intensity spikes related to modes hitting absorption lines of the atmospheric gas are correlated to the spikes observed from a laboratory cell containing the same gas [29].

As an example of a typical DIAL measurement, the signals received from a DIAL measurement on atmospheric mercury are shown in Fig. 3. The lidar beam was directed downwind from a chlor-alkali plant intersecting the atomic mercury plume. The upper part shows the on- and off-resonance lidar signals as a function of the range. We note that the signals are equal at short distances, indicating that no pollutant has been encountered. The curves run apart at about the 300-m range, indicating that the on-resonance light has been attenuated. The absolute intensity of the recorded signals depends on many different factors, including non-uniform distributions of scattering particles as discussed above, and range-modulated amplification of

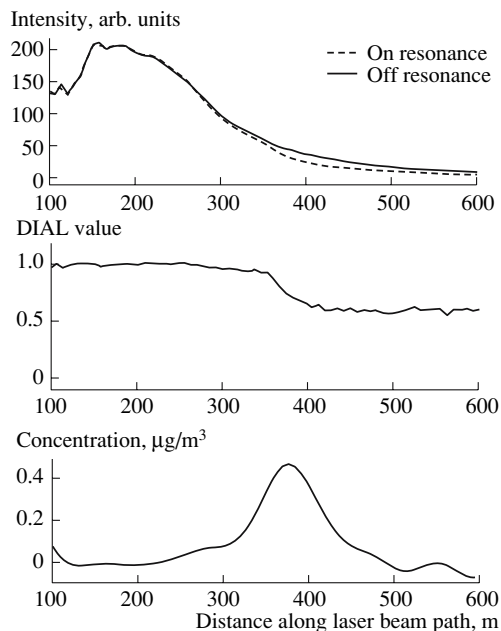


Fig. 3. Results from an atomic Hg lidar measurement: the top part shows the raw data for on- and off-resonance wavelengths, the middle part is the ratio between the two curves, and the bottom part is the evaluated range-resolved concentration (from [3]).

the detector. However, these factors are cancelled when forming the ratio between the on- and off-resonance signals, as can be seen in the middle part of Fig. 3. From the slope of the ratio curve, the range-resolved concentration shown in the bottom part of the figure can be calculated. Data from any measurement direction obtained in a fan-like scan through the plume can be merged into a cross-section image, such as the one shown in Fig. 4. Here, vertically and horizontally integrated values are also shown. By multiplying the area-integrated value by wind speed perpendicular to the cross section, the total flux of mercury from the plant can be evaluated. This was done in an extensive project at different European plants [23].

As a further DIAL example, we show data from ship-borne vertically sounding measurements of sulphur dioxide at the Italian volcano Mt. Etna in Fig. 5. Examples of on- and off-resonance lidar recordings around 300 nm are shown, and, also, the extension of the SO₂ plume from the volcano, recorded in a traverse under the plume. Passive measurements of the integrated SO₂ absorption using the blue-sky radiation as the light source were also performed. Due to the extended light source, passive measurement can be influenced by multiple scattering. Actually, the passive measurements were compared with nonaffected lidar

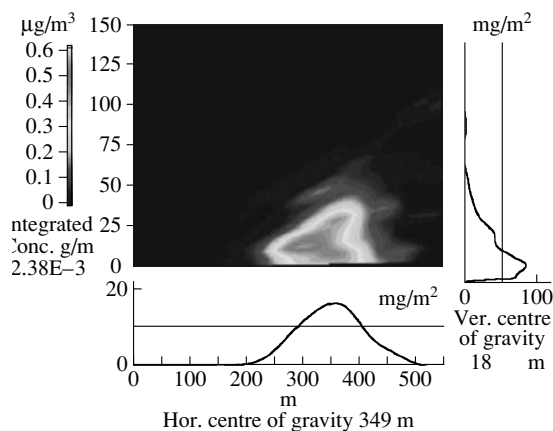


Fig. 4. Cross section of atomic mercury concentration through the emission plume from a chlor-alkali plant. Vertically and horizontally integrated values are also shown. By multiplying the total integrated value with the wind velocity perpendicular to the cross section, the total flux from the plant can be evaluated. Typical values for the case shown are around 70 g/h (from [23]).

data, and the scattering situation was also theoretically modeled [30].

The examples given constitute “conventional” single-scattering lidar cases. The data analysis is based on the time of the arrival of a photon, which is interpreted as a distance—that is, to and from its only scattering event. However, measurements through fog or clouds would be affected by multiple scattering. Multiple scattering lidar measurements—which, in fact, could be considered as large-scale GASMAS experiments—could be performed by spatially resolved measurements. In such a case, the lidar transmitter and receiver optical axes would not be aligned, but translated with respect to each other. Alternatively, the central part of the detector could be blocked with an annular aperture being left open as discussed above. In such a measurement arrangement, only the multiply scattered photons could be detected. If a DIAL measurement would be made on oxygen, the concentration is known and, thus, the optical pathlength could be calculated. Of particular interest would be to perform such measurements both at an A-band transition at about 760 nm, as mostly discussed in this paper, and at a transition around 254 nm, as encountered in [31]. Due to the strong wavelength dependence of both the dominant Mie scattering and the Rayleigh scattering, quite different behavior can be expected and the influence of multiple scattering could be further elucidated.

We will now discuss short-range lidar measurements of free gas, i.e., GASMAS experiments. The general principle is shown in Fig. 6, where transillumination and backscattering geometries are shown. Furthermore, the very narrow gas signal on a spectrally

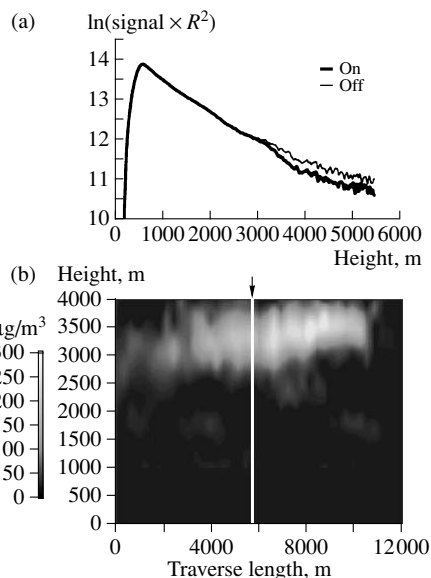


Fig. 5. Data from vertical lidar sounding of the sulphur dioxide flux from Mt. Etna, Italy. Examples of on- and off-resonance lidar curves are shown, illustrating the onset of SO₂ absorption at a height of about 3 km. The evaluated data from a ship-borne full scan under the volcanic plume are also shown (from [22, 30]).

broad background absorption is highlighted. As a first example, a recording of molecular oxygen inside an apple is shown in Fig. 7 [25]. Here, an arrangement of the kind shown in Fig. 1b was used. The directly recorded backscattered light is shown, and the scanned absorption line around 760 nm is too weak to show up. However, the corresponding 2f-lock-in signal (resembling the second derivative of the true absorption line shape) is clearly seen.

Gas transport can be studied by first immersing the sample, in this case an apple, in an atmosphere of pure nitrogen (e.g., in a sealed-off plastic bag). The reinvasion of normal air (with oxygen) can then be studied as shown in Fig. 8 [25]. We note that the invasion is faster when the apple is peeled, and that the final concentration value, then, becomes almost double, illustrating the active functioning of the skin. Theoretical considerations regarding the GASMAS-based measurement of gas diffusion are given in [32].

Wood is a complex material with cellulose cells, which are partially water-filled and partially air-filled, depending of the state of drying (Fig. 9, upper part). We have studied wood-drying processes by measurements of gaseous water molecules and oxygen. In addition, liquid water, characterized by much broader absorption bands, was studied. Soaking wet balsa wood, placed on scales during the entire drying process, was used and GASMAS signals were recorded in transmission for

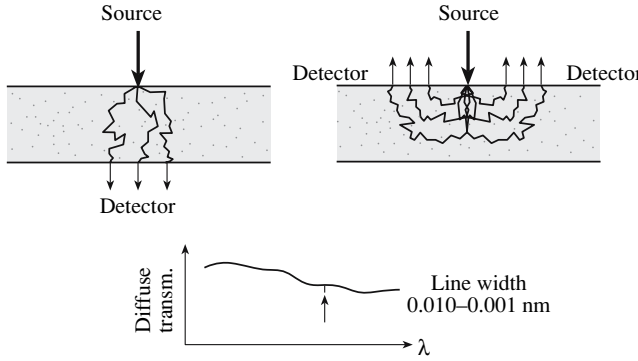


Fig. 6. The principles of GASMAS. The sharp absorptive features of free gas and the transmission and reflection measurement geometries are illustrated.

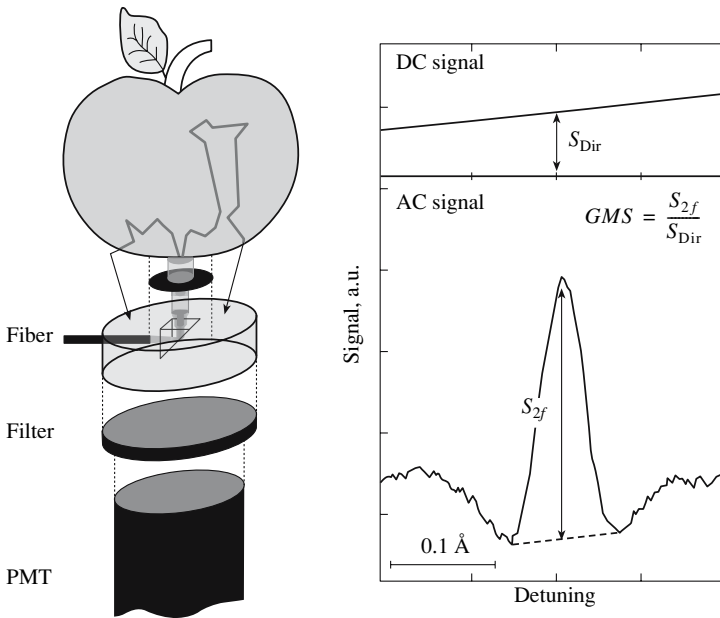


Fig. 7. GASMAS measurement of oxygen in an apple using backscattering geometry. Please note that the separations of the components are heavily exaggerated for clarity; in practice, they are touching each other. Direct transmission and 2f lock-in recordings of an oxygen line are also shown (from [25]).

both gases. The results are shown in the middle part of Fig. 9 [27]. The oxygen signal is seen to increase up to a maximum value reached when the wood is completely dry. The gaseous water signal is also increasing, because of the larger pore volumes where saturated water vapor builds up. However, when no more liquid water is available (the wood is dry), the saturation value cannot be maintained and the humidity gradually

reaches that of the surrounding air. The ratio between the water and oxygen molecule signals is partly compensated for by the scattering effects and provides a useful drying diagnostic.

The lower part of the figure shows the total intensity curves for 980 and 760 nm, placed on- and off-resonance, respectively, of a broad liquid water peak. The

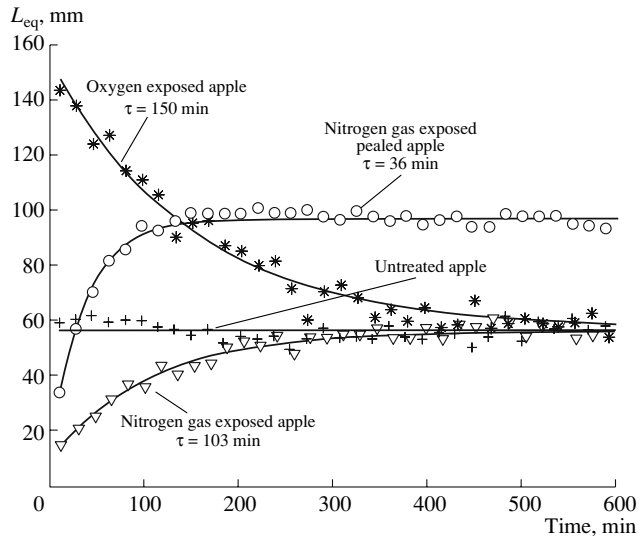


Fig. 8. Gas diffusion temporal curves are shown for apples previously exposed to pure nitrogen or oxygen (from [25]).

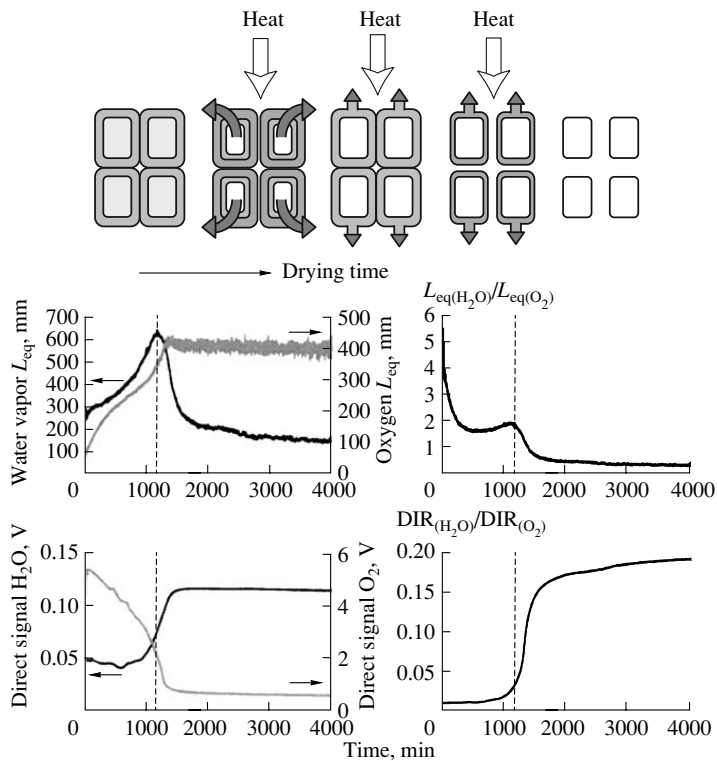


Fig. 9. Spectroscopic study of the drying of wood. Top: Schematic diagram of wood cells with different amounts of liquid water during the drying process. Middle: Recording of water vapor and oxygen GASMAS curves during drying and ratio curve (right). Bottom: Recording of total light transmission at 980 and 760 nm, corresponding to liquid water absorption and a reference wavelength, respectively. The ratio curve is also displayed (right) (from [27]).

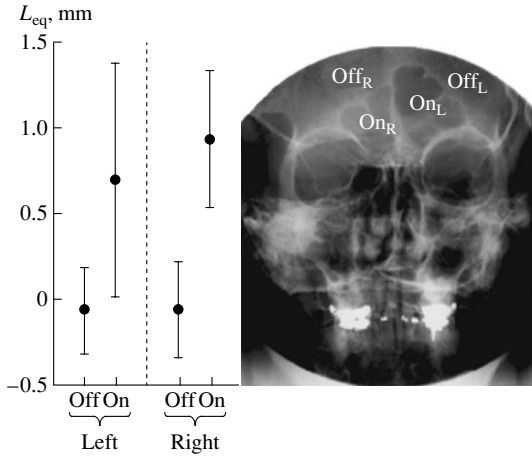


Fig. 10. Recording of molecular oxygen from the frontal sinuses of a healthy volunteer. The positions of the measurement points are indicated in the X-ray image (from [33]).

ratio curve is the differential absorption curve with partial compensation for scattering.

We will finish this section by showing how oxygen in the sinus cavities, as shown in Fig. 2b, can be

detected. Here, the gas is not distributed in pores like it is in, e.g., wood, but rather a localized cavity, surrounded by strongly scattering tissue, is probed. A setup of the kind shown in Fig. 1b was used. Figure 10 shows an X-ray radiogram of the senior author with the frontal sinuses clearly visible. Recordings show the presence of oxygen in both cavities and a zero signal outside the sinus areas [33]. The case can be seen as a short-range lidar experiment, where, however, time resolution was not utilized. Instead, it was ensured that the signal was sampled from sufficient depth by blocking the close-range signal with the annular aperture.

Below the floor of the orbital cavity, the maxillary sinuses are located. They can be studied in backscattering, but also in transillumination, because of their locations. Thus, diode laser radiation can be launched through the mouth into the chin from a fiber held against the mucosa. Now, the PMT detector is placed on the outside against the cheek bone. Very distinct signals can be observed on a healthy volunteer as shown in Fig. 11 [34]. A stable amplitude is observed in repeated measurements. However, when the ipsilateral nostril is briefly flushed with nitrogen gas, a fast reduction of the signal is observed, showing that the sinus is connected to the nasal cavity by an open venting channel. When the nitrogen is taken away after 20 s, the sinus again “charges up” with oxygen. Clearly, an interesting new type of ear-nose-throat (ENT) diagnostic tool is in sight.

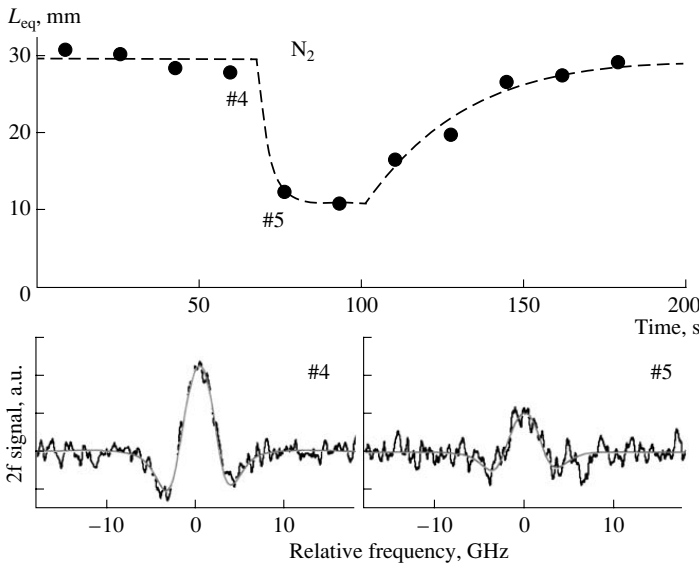


Fig. 11. Oxygen signal from the maxillary sinus of a healthy volunteer recorded in transmission. The laser light was launched fiber optically from the mouth, while the PMT detector was placed against the cheek bone. The signal change following a 20-s flushing of the nasal cavity with nitrogen is shown together with signal recordings (from [34]).

4. DISCUSSION AND OUTLOOK

Several examples showing the close connection between the lidar and GASMAS techniques were given. Multiple scattering differential absorption lidar (DIAL) measurements, i.e., large-scale GASMAS measurements, are of interest for many applications. For example, they could closely relate to studies of the Earth's radiation budget. As solar radiation passes through a cloud, it is multiply scattered. This leads to a larger gas absorptive imprint than otherwise expected. If a lidar beam is directed into a mass of distant snow or ice, the internally scattered radiation will emerge diffusely and can be picked up at a distant point, where the receiving telescope can be directed in a large-scale variety of the geometry shown in the right hand-side of Fig. 6. In particular, an annular detection geometry, such as that in the frontal sinus example, could be adopted. Gas composition in aged polar ice might be studied noninvasively. Furthermore, and more concretely, avalanche victims might be located from a helicopter-borne or stationary remote-sensing GASMAS system, detecting with high contrast exhaled carbon dioxide distributed in the strongly scattering snow.

Returning to small-scale GASMAS applications, the field of food packaging and food inspection appears interesting, in particular, since much of the considerations in this field regard the assurance that oxygen is kept away from foodstuffs. Modified atmosphere packaging is widespread. Gas penetration through plastic enclosures could readily be studied. Likewise, gas penetration through surface coatings, such as paints and veneers, could be studied for the characterization of products.

In the medical field, non-ENT applications might include nonintrusive monitoring of lung function in premature and neonatal infants. Pharmaceutical applications of GASMAS have already been demonstrated [35].

It could be noted that, by monitoring the ratio between the GASMAS signals for two gases, the influence of scattering may be eliminated and absolute concentration values for one gas may be given if the concentration of the other gas is known. Thus, water vapor might be normalized on oxygen in moisture measurements, and oxygen might be normalized on water vapor, having a known concentration in a naturally thermostated human sinus cavity.

As already pointed out in the introduction, the interplay between absorption and scattering, and gas analysis on different spatial scales, constitute an exceedingly rich field of phenomena of both basic and practical interest. In particular, environmental and biomedical applications are very closely related, and differences mainly pertain to the spatial scales and to the mindset of the investigator. Further research and developmental efforts within the field of study in the present paper should be worthwhile.

DEDICATION

This paper is dedicated to the memory of Professor Herbert Walther, who passed away on July 22, 2006. He served as the Faculty opponent at the senior author's dissertation in Göteborg in 1972. As one of the pioneers in laser spectroscopy, he provided great stimulus to the initiation of this field in Sweden in 1973, and, through his early work on laser radar, published in 1974, he also gave stimulus to the lidar work initiated in the senior author's group in 1975. Out of this program, laser applications in the fields of combustion diagnostics and medicine were also developed, and are now vigorously pursued at the Lund Laser Center.

ACKNOWLEDGMENTS

This work was supported by the Swedish Research Council and the Knut and Alice Wallenberg Foundation, and is based on the dedicated and extremely competent work of a large number of additional graduate students and collaborators.

REFERENCES

1. S. Svanberg, "Electromagnetic Radiation in Scattering Media—Spectroscopic Aspects," in *Progress in Nonlinear Science*, Ed. by A. G. Litvak (Univ. of Nizhny Novgorod, Nizhny Novgorod, 2002), Vol. 2, p. 429.
2. S. Svanberg, "Some Applications of Ultrashort Laser Pulses in Biology and Medicine," *Meas. Sci. Technol.* **12**, 1777 (2001).
3. R. Grönlund., L. Persson, M. Sjöholm, et al., "Studies of Free Gas in Scattering Media at Micro- and Macroscopic Scales," *Proceedings of the International Symposium on Biophotonics, Nanophotonics and Metamaterials, Hangzhou, China, 2006*, p. 51.
4. S. Andersson-Engels, R. Berg, S. Svanberg, and O. Jarlman, "Time-Resolved Transillumination for Medical Diagnostics," *Opt. Lett.* **15**, 1179 (1990).
5. R. Berg, S. Andersson-Engels, and S. Svanberg, "Time-Resolved Transillumination Imaging," in *Medical Optical Tomography, Functional Imaging and Monitoring*, Ed. by G. Müller et al. (SPIE, Bellingham, 1993), SPIE Institute Series, Vol. 11, p. 397.
6. M. S. Patterson, B. Chance, and B. C. Wilson, "Time Resolved Reflectance and Transmittance for the Non-Invasive Measurement of Optical Properties," *Appl. Opt.* **28**, 2331 (1989).
7. C. af Klinteberg, A. Pifferi, S. Andersson-Engels, et al., "In Vivo Absorption Spectroscopy of Tumor Sensitizers with Femtosecond White Light," *Appl. Opt.* **44**, 2213 (2005).
8. T. Svensson, J. Swartling, P. Taroni, et al., "Characterization of Normal Breast Tissue Heterogeneity Using Time-Resolved Near-Infrared Spectroscopy," *Phys. Med. Biol.* **50**, 2559 (2005).
9. J. Johansson, S. Folestad, M. Josefson, et al., "Time-Resolved NIR/VIS Spectroscopy for Analysis of Solids: Pharmaceutical Tablets," *Appl. Spectrosc.* **56**, 725 (2002).

10. Ch. Abrahamsson, T. Svensson, S. Svanberg, et al., "Time and Wavelength Resolved Spectroscopy of Turbid Media Using Light Continuum Generated in a Crystal Fibre," *Opt. Express* **12**, 4103 (2004).
11. M. Sjöholm, G. Somesfalean, J. Alnis, et al., "Analysis of Gas Dispersed in Scattering Media," *Opt. Lett.* **26**, 16 (2001).
12. G. Fiocco and L. D. Smullin, "Detection of Scattering Layers in the Upper Atmosphere (60–140 km) by Optical Radars," *Nature* **199**, 1275 (1963).
13. *Laser Remote Sensing*, Ed. by T. Fujii and T. Fukuchi (CRC, Fla, 2005).
14. S. Svanberg, "LIDAR," in *Springer Handbook of Lasers and Optics* Springer, Ed. by F. Träger (Springer, New York, 2007).
15. R. M. Shotland, "Some Observation of the Vertical Profile of Water Vapour by a Laser Optical Radar," *Proceedings of the 4th Symposium on Remote Sensitive Environment, Univ. Mich. Ann Arbor, 1966*, p. 273.
16. S. Svanberg, "Differential Absorption Lidar," in *Air Pollution Monitoring with Optical Techniques*, Ed. by M. Sigrist (Wiley, New York, 1993), Chap. 3.
17. K. W. Rothe, U. Brinkman, and H. Walther, "Applications of Tuneable Dye Lasers to Air Pollution Detection: Measurements of Atmospheric NO₂ Concentrations by Differential Absorption," *Appl. Phys.* **3**, 115 (1974); *Appl. Phys.* **4**, 181 (1974).
18. W. B. Grant, R. D. Hake, Jr., E. M. Liston, et al., "Calibrated Remote Measurements of NO₂ Using Differential Absorption Backscattering Technique," *Appl. Phys. Lett.* **24**, 550 (1974).
19. *12th International Workshop on Lidar Multiple Scattering Experiments*, Ed. by C. Werner, U. Ooppel, and T. Rother (SPIE, Bellingham, WA, 2003).
20. S. Svanberg, "Environmental and Medical Applications of Photonic Interactions," *Phys. Scr.*, T **110**, 39 (2004).
21. S. Svanberg, *Multi-Spectral Imaging—From Astronomy to Microscopy—from Radiowaves to Gamma-rays* (2007) (to appear).
22. P. Weibring, H. Edner, and S. Svanberg, "Versatile Mobile Lidar System for Environmental Monitoring," *Appl. Opt.* **42**, 3583 (2003).
23. R. Grönlund, M. Sjöholm, P. Weibring, et al., "Elemental Mercury Emissions from Chlor-Alkali Plants Measured by Lidar Techniques," *Atmos. Environ.* **39**, 7474 (2005).
24. G. Somesfalean, M. Sjöholm, J. Alnis, et al., "Concentration Measurement of Gas Embedded in Scattering Media by Employing Absorption and Time-Resolved Laser Spectroscopy," *Appl. Opt.* **41**, 3538 (2002).
25. L. Persson, B. Andersson, M. Sjöholm, and S. Svanberg, "Studies of Gas Exchange in Fruits Using Laser Spectroscopic Techniques," *Proceedings of FRUITIC 05, Information and Technology for Sustainable Fruit and Vegetable Production, Montpellier, France, 2005*, pp. 543–552.
26. L. Persson, H. Gao, M. Sjöholm, and S. Svanberg, "Diode Laser Absorption Spectroscopy for Studies of Gas Exchange in Fruits," *Opt. Lasers Eng.* **44**, 688 (2006).
27. M. Andersson, L. Persson, M. Sjöholm, and S. Svanberg, "Spectroscopic Studies of Wood-Drying Processes," *Opt. Express* **14**, 3641 (2006).
28. G. Somesfalean, J. Alnis, U. Gustafsson, and S. Svanberg, "Long-Path Monitoring of NO₂ with a 635 nm Diode Laser Using Frequency Modulation Spectroscopy," *Appl. Opt.* **44**, 5148 (2005).
29. G. Somesfalean, M. Sjöholm, L. Persson, et al., "Temporal Norrelation Scheme for Spectroscopic Gas Analysis Using Multimode Diode Lasers," *Appl. Phys. Lett.* **86**, 184102 (2005).
30. P. Weibring, J. Swartling, H. Edner, et al., "Optical Monitoring of Volcanic Sulphur Dioxide Emissions—Comparison between Four Different Remote Sensing Techniques," *Opt. Lasers Eng.* **37**, 267 (2002).
31. H. Edner, G.W. Faris, A. Sunesson, et al., "Lidar Search for Atomic Mercury in Icelandic Geothermal Fields," *J. Geophys. Res.* **96**, 2977 (1991).
32. M. Sjöholm, L. Persson and S. Svanberg, "Gas Diffusion Measurements in Porous Media by the Use of a Laser Spectroscopic Technique" (in preparation).
33. L. Persson, K. Svanberg, and S. Svanberg, "On the Potential of Human Sinus Cavity Diagnostics Using Diode Laser Gas Spectroscopy," *Appl. Phys. B* **82**, 313 (2006).
34. L. Persson, M. Andersson, T. Svensson, et al., "Non-Intrusive Optical Study of Gas and its Exchange in Human Maxillary Sinuses," *Proc. ECBO, Paper Number: 6628-3* (2007).
35. T. Svensson, L. Persson, M. Andersson, et al., "Non-Invasive Characterization of Pharmaceutical Solids Using Diode Laser Oxygen Spectroscopy," *Appl. Spectroscopy* (in press).